

STUDIES OF THE ELASTIC, DIELECTRIC AND THERMAL EXPANSION PROPERTIES
OF CsH_2PO_4

Steven Prawer

B.Sc. (Hons.)

Physics Department Monash University March 1985

A thesis submitted for the degree of Doctor of Philosophy

C4998960

To
the women in my life:
Mum
Michelle
and my brand new daughter
Ronit

TABLE OF CONTENTS

	PAGE
<u>Summary</u>	7
<u>Acknowledgements</u>	10
<u>Chapter 1</u> Introduction	12
1.1 Background	12
1.2 Crystal Structure of CDP	14
1.3 The Present Study	17
1.3.1 Room Temperature Studies	17
1.3.2 Studies Closer to the Transition	18
1.3.3 Structure of the Thesis	18
<u>Chapter 2</u> Theoretical Background	20
2.1 Theory of Elastic Wave Propagation in Crystals of General Symmetry	20
2.1.1 Wave Velocity and Polarization	21
2.1.2 The Energy Flow Vector	25
2.2 Determination of the Elastic Constants of a Monoclinic System	33
2.2.1 Form of the Elastic Constant Matrix for a Monoclinic System	33
2.2.2 Determination of the Elastic Constant Matrix via Velocity Measurements	35
<u>Chapter 3</u> Materials Preparation	38
3.1 Crystal Preparation	38

	PAGE
3.2 Materials Verification	41
3.2.1 Electron Microprobe	41
3.2.2 Powder X-ray Diffraction	42
3.3 Crystal Properties	44
3.3.1 Crystal Habit and Multiple Growth Planes	44
3.3.2 Other Physical Properties	51
3.4 Sample Preparation for Ultrasonic Velocity Measurements	51
3.4.1 Requirements	51
3.4.2 Polishing Technique	54
3.4.3 Orientation	58
3.5 Preparation of Deuterated Samples	61
 <u>Chapter 4</u> Experimental Details	 63
4.1 The Measurement of Ultrasonic Phase Velocity	63
4.1.1 Introduction	63
4.1.2 The Pulse Echo Overlap Method	67
4.1.3 Sample Limitations on Accuracy	80
4.2 Attenuation Measurements	83
4.2.1 Introduction	83
4.2.2 Methods of Measurement	83
4.3 Equipment	88
4.3.1 Overview	88
4.3.2 Transducers	88
4.3.3 Room Temperature Measurements	90
4.3.4 Low Temperature Measurements	93

	PAGE
<u>Chapter 5</u> The Room Temperature Elastic Behaviour of CDP	100
5.1 Determination of the Elastic Constant Matrix	100
5.1.1 Velocity Measurements	100
5.1.2 Density Determination	102
5.1.3 Method of Calculation	102
5.2 Calculation of the Elastic Properties	113
5.2.1 Wave Velocity Surfaces	113
5.2.2 Ray Directions	116
5.2.3 Bulk Modulus, Linear Compressibility and Young's Modulus	118
5.2.4 Debye Temperature	122
5.3 Relationship to Crystal Structure	122
5.4 Summary	128
 <u>Chapter 6</u> Investigation of the Ferroelectric Transition	 131
6.1 Introduction	131
6.2 Velocity and Attenuation Measurements as a Function of Temperature	132
6.2.1 Introduction	132
6.2.2 Experimental Details	133
6.2.2.1 Bonding Considerations	133
6.2.3 Results	137
6.2.3.1 CDP	137
6.2.3.2 CDDP	150
6.2.4 Discussion	154
6.2.4.1 General Features of the Critical Region	154
6.2.4.2 Critical Point Analysis	162

	PAGE
6.3 Thermal Expansion Measurements on CDP	178
6.3.1 Introduction	178
6.3.2 Theory	178
6.3.3 Experimental Details	180
6.3.4 Results	180
6.3.5 Calculation of the Grüneisen Parameters	182
6.3.6 Discussion	188
6.4 Dielectric Measurements on CDDP	194
6.4.1 Introduction	194
6.4.2 Experimental Method	194
6.4.3 Results	195
6.4.4 Discussion	202
6.4.4.1 $T > T_c^d$: Deviations From Curie-Weiss Behaviour	202
6.4.4.2 $T < T_c^d$: Relaxation Effects	209
6.5 Summary	211
<u>Chapter 7</u> Conclusion	214
7.1 The Present Study	214
7.2 Future Work	215
<u>References</u>	217
<u>Publications</u>	222

SUMMARY

Cesium dihydrogen phosphate CsH_2PO_4 (CDP) is a ferroelectric with ordering temperature $T_c = 154$ K. In many respects CDP is a unique material, displaying a chain and layer-like structure and a pseudo-one-dimensional ordering of the hydrogen ions at T_c , making it an attractive candidate for the application of a pseudo-one-dimensional Ising model.

The elastic constants of a material completely describe its elastic behaviour. As a first step in the understanding of the lattice dynamics of CDP, the room temperature elastic constants have been determined using ultrasonic velocity measurements. The constants have been used to calculate a number of elastic properties: the phase and group velocities, Young's modulus, the bulk modulus, linear compressibilities, and the elastic Debye temperature. The calculations showed a marked elastic anisotropy which has been correlated with the chain and layer-like structure of this material.

The one-dimensional nature of the ordering of the hydrogen ions can be expected to be evident in a wide range of critical phenomena. In an attempt to elucidate further the transition mechanism of CDP, the temperature dependences of the velocity and attenuation, thermal expansion, and dielectric constant were measured in the critical region. The critical point analyses of the dielectric and ultrasonic anomalies showed evidence of a temperature region above T_c in which one-dimensional, short-range forces were dominant. However, very close to T_c , the usual 3-D, long-range, dipole-dipole interaction was found to be dominant.

Calculations of the Grüneisen parameters based on the expansion measurements have revealed that, from the thermodynamic point of view,

the degree of "one-dimensionality" of CDP increases as the transition is approached. However, despite the one-dimensional nature of the transition, a significant anomaly was observed in the dielectric constant measured orthogonal to the ferroelectric axis.

Whilst most of the analysis of this study was for $T > T_c$, a very long term relaxation effect in the dielectric constant was observed below T_c , which suggested that CDP has a very "soft" domain structure in the ferroelectric state. Several suggestions are made as to possible further investigations into these domain effects.

The findings of this study constitute one more step in the overall understanding of the lattice dynamics of CDP. Directions for future research based on these findings are also presented.

This thesis contains no work which has been presented for any other degree or diploma, and to the best of my knowledge contains no material previously published or written by another person except where due reference is made in the text of the thesis.

[REDACTED]

[REDACTED] (March 1985)

ACKNOWLEDGEMENTS

I would like to express my deep gratitude to my supervisor Professor T.F. Smith, and to Dr. T.R. Finlayson for their help, patience, practical advice and invaluable insights into the "physics of the situation". Their expert guidance and unfailing confidence in my ability, even when progress was slow, were of immeasurable help to me in bringing this work to completion.

Many thanks are also due Professor H.C. Bolton who gave freely of his time in leading a novice into the deep waters of critical point phenomena. I would also like to thank Dr. J.G. Collins and Dr. F. Ninio for many useful discussions.

My fellow research students in Lab. 17 deserve special thanks for their day-to-day advice and practical help, and in particular for providing a "sounding board" on which to try new ideas. Their co-operative spirit has helped make Lab. 17 a stimulating, friendly, and encouraging place in which to work.

Almost none of the results described in this thesis would have been obtained without the expert assistance of Mr. R. Horan and his staff in the mechanical workshop, and Mr. I. Lecis and his staff in the electronics workshop. Many thanks go to them for patiently extracting practical designs from a rough sketch and an "amorphous" idea.

In the presentation of this thesis I would like to thank Mr. S. McCausland for drawing the figures, Mr. S. Morton for the photography, and Mrs. L. Macdonald and Mrs. C. Kratzmann for typing a portion of the text. Very special thanks are due to Mr. P. Zamek for his expert proof-reading of the entire thesis.

Without the support and encouragement of my wife, Michelle, and my parents I could not have undertaken, let alone completed, this work. I

can never thank them enough for their wonderful understanding and tolerance of the long hours, late nights and many frustrations inherent in research.

This work was undertaken with support of the Australian Research Grants Scheme and the Monash University Special Grants Scheme. I would like to gratefully acknowledge the support provided by the Vera Moore Junior Research Fellowship which I held during the period of my candidature.

CHAPTER 1

INTRODUCTION

1.1 BACKGROUND

The family of ferroelectric hydrogen-bonded phosphates and arsenates, of which KH_2PO_4 (KDP) is the well known prototype, has attracted considerable interest over the past 30 years (see for example Scott 1974, Jona and Shirane 1962). From the large effect deuteration has on the Curie temperature of these materials, it is clear that the occurrence of ferroelectricity is, to a large degree, associated with the hydrogen bonding. At T_c , the hydrogen ions undergo an order-disorder transition, whilst the metal ions undergo a displacive transition associated with the transformation from the paraelectric tetragonal state to the ferroelectric orthorhombic state.

Prior to 1975, almost no interest was shown in CsH_2PO_4 (CDP) or its isomorphic deuterate CsD_2PO_4 (CDDP) despite the fact that ferroelectricity in CDP had been reported as early as 1950 (Seidl 1950). The ferroelectric transition was confirmed by the dielectric measurements of Levstik *et al.* (1975) ($T_c = 154$ K for CDP and 267 K for CDDP), who concluded that the ferroelectric transition mechanism was "not very different" from that in tetragonal KDP.

Unlike most of the members of the KDP family, which are tetragonal in the paraelectric phase, CDP was initially reported to be orthorhombic in the room temperature paraelectric state (Fellner-Feldegg, 1952). However, in a further X-ray study, Uesu and Kobayashi (1976) re-examined the crystal structure of CDP and unambiguously determined that the room temperature paraelectric phase was monoclinic ($P2_1/m$). They also determined the positions of the P, Cs, and O atoms and found that the structure was very different from that of KDP with regard to the

configuration of the hydrogen bonds, the coordination number of the O atoms, and the sequence of the Cs and P atoms along the polar axis. Their dielectric measurements showed that the anomaly in the dielectric constant was only present for measurements taken along the ferroelectric b axis, and that the Curie constant for CDP was ten times as large as that for KDP. On the basis of these findings, they concluded that ferroelectricity in CDP takes place through a different mechanism from that in KDP.

The neutron diffraction studies of Frazer et al. (1979), Nelmes and Choudhary (1978) and Iwata et al. (1980), and the detailed X-ray study of Matsunaga et al. (1980) showed that the sites for the two hydrogens in the unit cell are inequivalent. The hydrogen ions associated with the hydrogen bonding along the c axis are ordered at room temperature, whereas the ions along the a axis are disordered (see next section below and Figure 1.1). Since one hydrogen is already ordered in the paraelectric state, the ferroelectric transition has been described as pseudo-one-dimensional, in marked contrast to the three-dimensional behaviour noted in the case of KDP (Frazer et al. 1979). Thus, at the commencement of this study in 1980, it was known that the ferroelectric ordering in CDP was substantially different from that in KDP, although little was understood about the mechanism of this ordering.

Following the discovery of the 1-D nature of the ferroelectric ordering, there was a marked increase in the interest shown in CDP. Since the neutron studies had also suggested that the bonding is much stronger in the direction of the polar axis than orthogonal to it, many authors were prompted to attempt to explain a wide range of critical point phenomena in terms of the pseudo-one-dimensional Ising model. For example, the model has had some success in explaining (a) the deviations

from Curie-Weiss behaviour of the dielectric constant (Blinc et al. 1979), (b) the short spin-relaxation time found by deuteron magnetic resonance (Topic et al. 1980), (c) the long relaxation time of the polarization found by dynamic dielectric measurements (Kanda et al. 1982(a)), (d) the anomalous behaviour of the specific heat (Kanda et al. 1982(b)), (e) the anomalies in the ultrasonic velocity and attenuation (Kanda et al. 1983) and (f) the anomalous behaviour of the b axis expansion coefficient (Nakamura et al. 1984). The antiferroelectric state induced by a pressure of 3.3 kbar (Yasuda et al. 1979) was also reasonably understood in terms of this model (Youngblood et al. 1980).

During the course of this study many other papers appeared in which the authors attempted to elucidate further the transition mechanism. Some of the most significant were: an investigation of anomalies in the dielectric constant and hysteresis curves (Baranov et al. 1980); a study of the ultrasonic velocity and attenuation anomalies (Yakushkin et al. 1981), the findings of which differ considerably from those of Kanda et al. (1983); an investigation of the dependence of the ultrasonic velocity anomalies on the applied electric field (Baranov et al. 1983); a specific heat study by Imai (1983), which reported results considerably different from those reported by Kanda et al. (1982(b)); and a measurement of the thermal conductivity close to the transition (Spörl et al. 1984).

1.2 CRYSTAL STRUCTURE OF CDP

Figures 1.1 and 1.2 show the structure of CDP based on the X-ray and neutron studies discussed above. The hydrogen bonds along the a axis link the PO_4 groups into chains running along the ferroelectric b axis. These chains are cross-linked by the hydrogen bonds along the c axis to

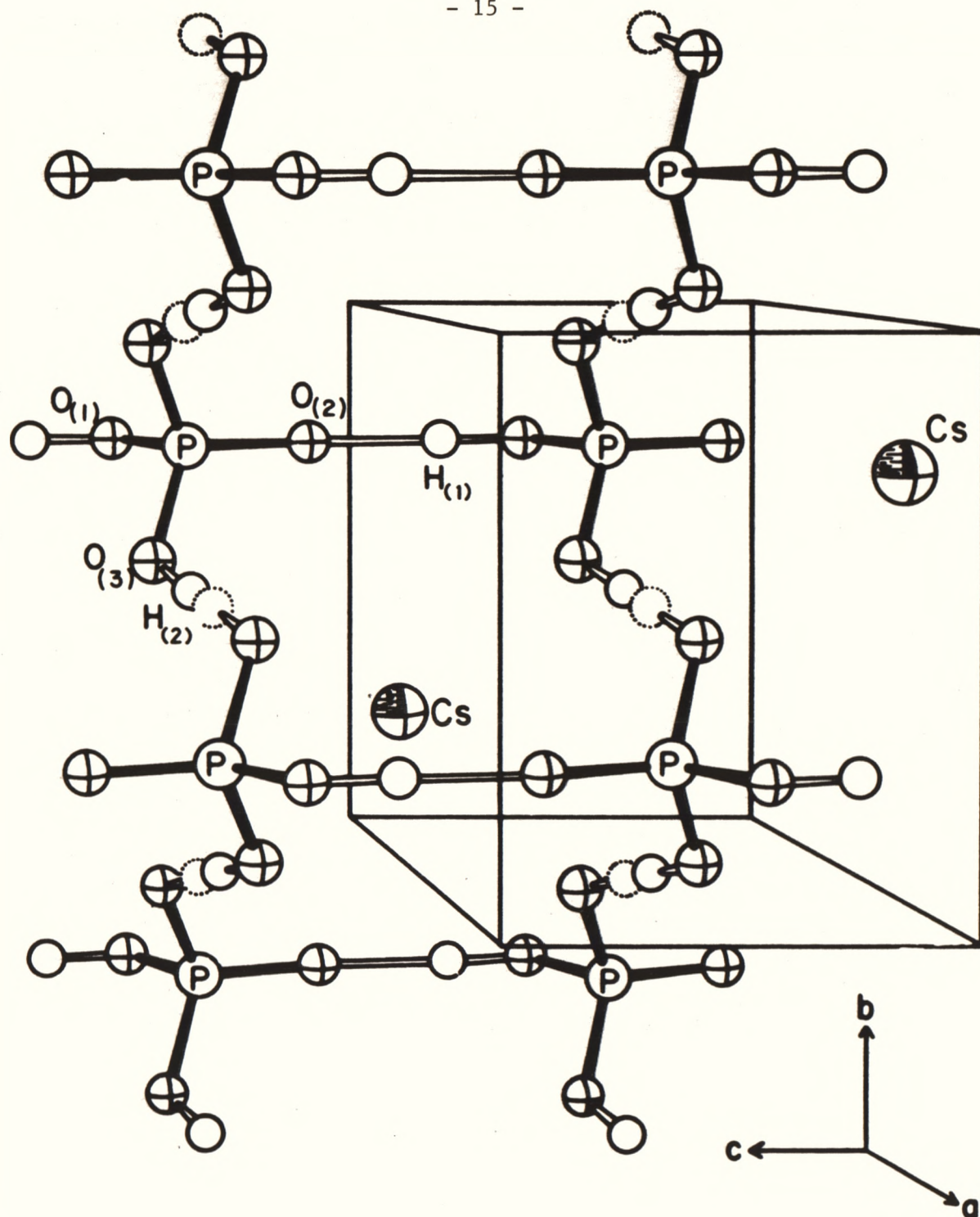


Figure 1.1. Crystal Structure of CDP. Disorder in the hydrogen bonds along the a axis involved in chain formation is indicated by the neighbouring solid and dotted circles used to represent the proton positions. Note that adjacent PO_4 groups in the b axis chain are not in the same cell. (From Frazer et al. 1979).

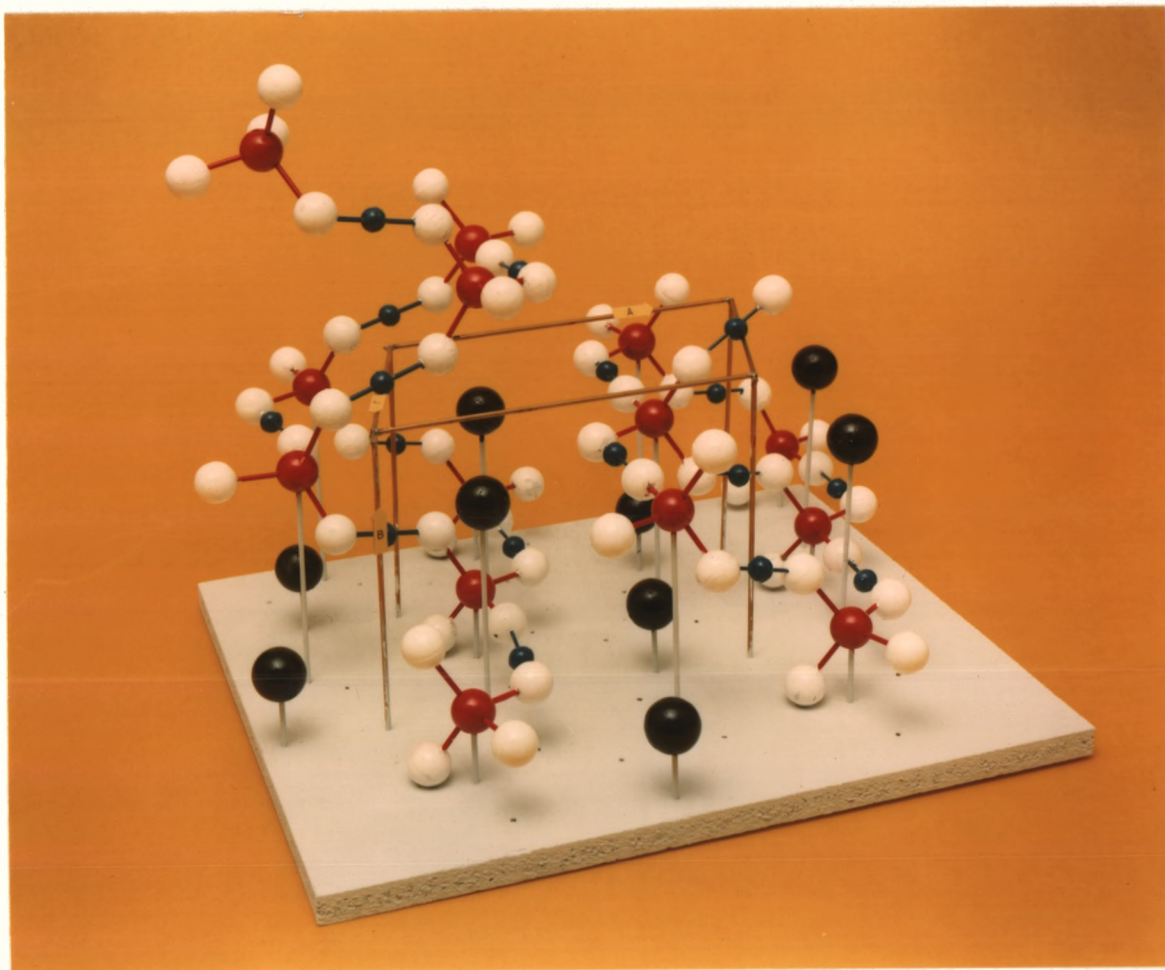


Figure 1.2. A Scale Model of CDP. The model was constructed using the lattice parameters and atomic positions of Uesu and Kobayashi (1976) and Matsunaga et al. (1980) with $a = 7.90 \text{ \AA}$, $b = 6.37 \text{ \AA}$, $c = 4.87 \text{ \AA}$, and $\beta = 107.7^\circ$. The colour code is: black-cesium, red-phosphorous, white-oxygen and blue-hydrogen. Note the "zig-zag" chains of PO_4 groups running up the ferroelectric b axis.

form (100) layers which are bonded to each other by ionic forces involving the Cs^+ ion. The relative weakness of the interlayer forces is evident from the perfect cleavage which occurs along the (100) plane. Above the transition, the disordered hydrogen ions ($\text{H}_{(2)}$ in Figure 1.1) occupy one of two off-centre equivalent sites in a double well potential, but at T_c these hydrogen ions move co-operatively to one side of the double well giving rise to a permanent dipole moment along the b axis. Iwata et al. (1980) have found that this process is accompanied by a 3° rotation of the PO_4 tetrahedron, a 0.06 Å displacement of the P atom in the b direction, and a 0.04 Å displacement of the Cs atom in the c direction. In the ordering process the centre of inversion is lost and the $\text{P2}_1/\text{m}$ space group transforms to P2_1 .

1.3 THE PRESENT STUDY

1.3.1 Room Temperature Studies

As the elastic constants are given by the second derivative with respect to strain of the free energy, the nature of the chain and layer-like bonding in CDP can be expected to be reflected in the elastic properties of the crystal. Hence, as a first step in the understanding of the lattice dynamics of CDP, a determination of the room temperature elastic constants was undertaken using measurements of the ultrasonic sound velocities in different crystallographic directions. The elastic constants completely describe the elastic behaviour of the crystal so that having determined the elastic constant matrix it was possible calculate a range of properties such as linear compressibility, Young's modulus, bulk modulus and the elastic Debye temperature and to relate these to the crystal structure.

There are 13 independent non-zero elastic constants for a monoclinic system (Nye 1967). Direct, simple relationships between the

measured velocities and the elastic constants are only possible for C_{22} , C_{66} , and C_{44} . All the other constants occur coupled together in much more complicated relationships. Also, only measurements along the b axis yield pure waves (i.e. pure transverse or pure longitudinal particle motion). Hence, the determination of all 13 elastic constants of monoclinic CDP was demanding both experimentally and computationally.

1.3.2 Studies Closer to the Transition

The one-dimensional type ordering should be reflected in the critical point phenomena. In an attempt to elucidate further the ferroelectric transition mechanism, ultrasonic velocity and attenuation measurements were undertaken close to T_c . Of particular interest were (a) a comparison of the ultrasonic anomalies in different directions as an indication of which modes are dominant in the transition mechanism, and (b) the application of a critical point analysis to the velocity and attenuation anomalies in an attempt to gain information about the nature of the dominant interaction forces in the system close to T_c .

Thermal expansion and dielectric measurements were also undertaken in conjunction with the ultrasonic measurements. The expansion measurements were directed at providing important thermodynamic information about the nature of the transition via a calculation of the directional Grüneisen parameters. The focus of the dielectric measurements was a study of deviations from Curie-Weiss behaviour of the dielectric constant, and an investigation as to whether any dielectric anomaly exists orthogonal to the ferroelectric b axis.

1.3.3 Structure of the Thesis

This thesis is set out as follows. Chapter 2 reviews the theory of elastic wave propagation in crystals of general symmetry and provides

the necessary framework for the calculation of the elastic constants from the measured velocities. The techniques used in growing, characterizing, polishing and orienting the CDP and CDDP crystals used in this study are described in Chapter 3. The next chapter describes the pulse-echo-overlap technique for ultrasonic measurements and the equipment used in the experiments. The velocity measurements and the calculations leading to the determination of the room temperature elastic constants of CDP are presented in Chapter 5. In Chapter 6, the investigation of the critical point region using ultrasonic, dielectric, and expansion measurements is presented, and in the final chapter the current work is reviewed and suggestions are made as to possible future directions for investigations into CDP and CDDP.

CHAPTER 2

THEORETICAL BACKGROUND

2.1 THEORY OF ELASTIC WAVE PROPAGATION IN CRYSTALS OF GENERAL SYMMETRY

A force applied to a small cubic volume element of a crystal is specified by the stress tensor $\underline{\sigma}$, where σ_{ij} is the component of force in the x_i direction transmitted across that face of the volume element which is perpendicular to x_j (Nye 1967). As this tensor is symmetric, it has only six independent elements. Strain is the response, in terms of the fractional change of lattice dimensions, of a crystal to an applied or internal stress. If the displacements of particles from their mean positions are given by u_i , then the strain is given by

$$\epsilon_{ij} = \frac{1}{2} \left(\frac{\partial u_i}{\partial x_j} + \frac{\partial u_j}{\partial x_i} \right) \quad (2.1).$$

This definition ensures that the strain tensor is symmetric and that rotations of the crystal as a whole are not included.

For small strains, for which the displacements are reversible, a linear relationship exists between stress and strain. This is often referred to as Hooke's Law and in the repeated suffix notation (which is used throughout this work) is given by

$$\sigma_{ij} = C_{ijkl} \epsilon_{kl} \quad (2.2)$$

where i, j, k , and l take the values 1, 2, or 3 and where C_{ijkl} are the components of the elastic constant tensor. The subscripts i and j , k and l may be interchanged so that $C_{ijkl} = C_{jikl}$ and $C_{ijkl} = C_{ijlk}$. Further it can be shown that (Nye 1967)

$$C_{ijkl} = \frac{\partial^2 U}{\partial \epsilon_{ij} \partial \epsilon_{kl}} \quad (2.3)$$

where U is the elastic strain energy of the crystal. Since the order of differentiation is immaterial, it follows that $C_{ijkl} = C_{klij}$. These relationships reduce the 81 possible components of the elastic constant tensor to a maximum of 21 independent components.

The symmetry properties of the elastic constant tensor may be used to contract the tensor to a six by six matrix by using the Voigt notation (Nye 1967). The scheme is :

Tensor notation	i, j	11	22	33	23,32	13,31	12,21
Voigt matrix notation	i	1	2	3	4	5	6

Hence the tensor C_{ijkl} is reduced to the elastic constant matrix C_{ij} . In this notation Hooke's law becomes

$$\sigma_i = C_{ij} \epsilon_j \quad \text{for } j=1 \text{ to } 6 \quad (2.4).$$

Equation (2.3) implies that $C_{ij} = C_{ji}$, and therefore there is a maximum of 21 independent elements of the C_{ij} matrix. The elements of this matrix, which are referred to as the elastic constants of the crystal, are sufficient to describe completely the elastic behaviour of the material.

2.1.1 Wave Velocity and Polarization

If a small element of crystal of density ρ is subjected to a stress wave, the particles in such a volume will respond according to the equation of motion (Brown 1967)

$$\rho \frac{\partial^2 u_i}{\partial t^2} = \frac{\partial \sigma_{ij}}{\partial x_j} \quad (2.5).$$

Substituting for σ_{ij} from equation (2.1) and (2.2) yields

$$\rho \frac{\partial^2 u_i}{\partial t^2} = C_{ijkl} \frac{\partial^2 u_k}{\partial x_j \partial x_l} \quad (2.6).$$

The material is assumed to be homogeneous so that the elastic constants are independent of position.

A travelling wave solution to equation (2.6)

$$u_i = A_i \sin(\omega t - k_j x_j) \quad (2.7)$$

is assumed. Here \underline{k} is the wave vector and ω is the radial frequency. \underline{A} is the polarization or particle displacement vector.

Substituting this solution into the equation of motion (2.6) yields

$$\rho \omega^2 A_i = C_{ijkl} k_j A_k k_l$$

$$\text{or} \quad (C_{ijkl} k_j k_l - \rho \omega^2 \delta_{ik}) A_k = 0 \quad (2.8).$$

The continuum approximation is now made which states that in the long wavelength limit, where the wavelength is much longer than the interatomic spacings, dispersion is negligible. Typical ultrasonic waves have frequencies of 1-100 MHz and velocities of about 10^3 m s^{-1} . Therefore wavelengths are typically of the order of $10^{-3} - 10^{-5}$ metres. Interatomic spacings are usually less than $10 \text{ \AA} = 10^{-9}$ metres. Hence the continuum approximation is justified. In terms of the dispersion curves ultrasonic measurements lie very close to the zone centre ($\underline{k} = 0$) where ω versus k is generally linear. Under these conditions the wave

velocity, V , is given by

$$V = \omega |\underline{k}|^{-1} \text{ where } |\underline{k}|^2 = k_1^2 + k_2^2 + k_3^2 \quad (2.9).$$

Then on dividing equation (2.8) by $|\underline{k}|^2$ we obtain

$$(\lambda_{ik} - \rho V^2 \delta_{ik}) A_k = 0$$

or $\underline{\lambda} \underline{A} = \rho V^2 \underline{A} \quad (2.10).$

where $\lambda_{ik} = C_{ijkl} n_j n_l$ and $n_j = k_j |\underline{k}|^{-1}$ are the direction cosines of the wave vector \underline{k} . The notation l, m, n will also be used to denote these direction cosines.

Equation (2.10) indicates that ρV^2 are the eigenvalues of the matrix $\underline{\lambda}$ whilst \underline{A} (the polarizations) are the corresponding eigenvectors. Since $\underline{\lambda}$ is real and symmetric, it possesses three mutually orthogonal eigenvectors. Hence waves with different phase velocities will have mutually orthogonal polarization directions.

In general the eigenvectors do not constitute purely transverse or purely longitudinal particle motion. In the special cases that the longitudinal mode is pure, the two transverse modes must also be pure. However, if only one transverse mode is pure, the remaining transverse and longitudinal modes are not pure, but their eigenvectors are constrained to lie in a plane perpendicular to the eigenvector of the pure transverse mode, and are therefore referred to as semi-pure modes of vibration.

Using the contracted Voigt notation it is possible to obtain explicit expressions for the elements of the $\underline{\lambda}$ matrix.

Specifically, if

$$\underline{Q} = \begin{bmatrix} c_{11} & c_{66} & c_{55} & c_{56} & c_{15} & c_{16} \\ c_{66} & c_{22} & c_{44} & c_{24} & c_{46} & c_{26} \\ c_{55} & c_{44} & c_{33} & c_{34} & c_{35} & c_{45} \\ c_{56} & c_{24} & c_{34} & \frac{1}{2}(c_{44} + c_{23}) & \frac{1}{2}(c_{36} + c_{45}) & \frac{1}{2}(c_{46} + c_{25}) \\ c_{15} & c_{46} & c_{35} & \frac{1}{2}(c_{36} + c_{45}) & \frac{1}{2}(c_{55} + c_{13}) & \frac{1}{2}(c_{14} + c_{56}) \\ c_{16} & c_{26} & c_{45} & \frac{1}{2}(c_{25} + c_{46}) & \frac{1}{2}(c_{14} + c_{56}) & \frac{1}{2}(c_{66} + c_{12}) \end{bmatrix}$$

and

$$\underline{L} = \begin{bmatrix} \ell^2 \\ m^2 \\ n^2 \\ 2mn \\ 2n\ell \\ 2\ell m \end{bmatrix}$$

then the components of $\underline{\lambda}$ become

$$\begin{aligned} \lambda_{11} &= Q_{1j} L_j & \lambda_{22} &= Q_{2j} L_j & \lambda_{33} &= Q_{3j} L_j \\ & & & & & (2.11) \end{aligned}$$

$$\begin{aligned} \lambda_{23} &= Q_{4j} L_j & \lambda_{13} &= Q_{5j} L_j & \lambda_{12} &= Q_{6j} L_j \end{aligned}$$

where $j = 1$ to 6 .

For a given propagation vector $[\ell, m, n]$ in a crystal the components of the $\underline{\lambda}$ matrix may be calculated via equation (2.11) if the elastic constants of the material are known. The velocities and directions for the polarizations of the three possible modes for this propagation

direction will be given by the eigenvalues and eigenvectors of $\underline{\lambda}$. For computational purposes the eigenvalues of $\underline{\lambda}$ may be calculated via the characteristic (sometimes referred to as secular) equation

$$| \lambda_{ik} - \rho V^2 \delta_{ik} | = 0 \quad (2.12)$$

and the corresponding eigenvectors, \underline{A} , by solving equation (2.10) for each eigenvalue.

2.1.2 The Energy Flow Vector

In the above section it was shown that the phase velocity depends on the direction of propagation in the crystal. Therefore the velocity surface will not be spherical, and hence the ray or energy flux vector is expected to deviate from the wave normal. The situation is similar to the optical case of birefringence and extraordinary refraction.

Whilst the electromagnetic energy flow vector (the Poynting vector) is well studied, the energy carried by ultrasonic waves has received little attention. Neighbours (1973) has given expressions for calculating the deviation angle between the energy flow vector and propagation vector for crystals of general symmetry. However, he accomplishes this by a complicated transformation of the elastic constant matrix to a reference frame such that the direction of propagation is always along the x axis. Below, the theory is reviewed and expressions for the deviation angle are presented without the aid of the transformations used by Neighbours (1973). This approach is more direct, and computationally simpler. The reader is referred to the texts by Musgrave (1970) and Federov (1968) for a more complete treatment of the general theory of ultrasonic wave propagation in crystals.

It is reasonable to assume that the total energy density in a small volume of material is the sum of the elastic potential and kinetic

energies. This total energy is given by

$$E_{\text{tot}} = \frac{1}{2} \int_V \left(\rho \dot{u}_i \dot{u}_i + C_{ijkl} \frac{\partial u_i}{\partial x_j} \frac{\partial u_k}{\partial x_l} \right) dv \quad (2.13).$$

The total outward energy flow per unit time is given by the integral of the energy flow vector, \underline{P} , over the surface bounded by the wave fronts. Thus, this energy flow is given by

$$\int_S \underline{P} \cdot d\underline{s}.$$

But the outward energy flow per unit time must also be equal to the rate change of energy density within the volume contained by the wave front. Hence,

$$\int_S \underline{P} \cdot d\underline{s} = \frac{d}{dt} \left\{ \frac{1}{2} \int_V \left(\rho \dot{u}_i \dot{u}_i + C_{ijkl} \frac{\partial u_i}{\partial x_j} \frac{\partial u_k}{\partial x_l} \right) dv \right\}.$$

Using the divergence theorem $\int_S \underline{P} \cdot d\underline{s} = \int_V (\nabla \cdot \underline{P}) dv$ it follows that

$$\begin{aligned} \nabla \cdot \underline{P} &= \frac{1}{2} \frac{\partial}{\partial t} \left[\rho \dot{u}_i \dot{u}_i + C_{ijkl} \frac{\partial u_i}{\partial x_j} \frac{\partial u_k}{\partial x_l} \right] \\ &= \frac{1}{2} \left[\rho \dot{u}_i \ddot{u}_i + \rho \ddot{u}_i \dot{u}_i + C_{ijkl} \left\{ \frac{\partial \dot{u}_i}{\partial x_j} \frac{\partial u_k}{\partial x_l} + \frac{\partial u_i}{\partial x_j} \frac{\partial \dot{u}_k}{\partial x_l} \right\} \right] \\ &= \rho \dot{u}_i \ddot{u}_i + C_{ijkl} \frac{\partial \dot{u}_i}{\partial x_j} \frac{\partial u_k}{\partial x_l} \end{aligned} \quad (2.14).$$

When the equation of motion (2.6) is substituted into (2.14) we obtain

$$\begin{aligned} \nabla \cdot \underline{P} &= \dot{u}_i C_{ijkl} \frac{\partial^2 u_k}{\partial x_j \partial x_l} + C_{ijkl} \frac{\partial \dot{u}_i}{\partial x_j} \frac{\partial u_k}{\partial x_l} \\ &= C_{ijkl} \frac{\partial}{\partial x_j} \left(\dot{u}_i \frac{\partial u_k}{\partial x_l} \right) \end{aligned} \quad (2.15)$$

and since $\underline{\nabla} \cdot \underline{P} = \frac{\partial P_j}{\partial x_j}$ it follows that

$$\begin{aligned} P_j &= C_{ijkl} \frac{\partial u_k}{\partial x_l} \dot{u}_i \\ &= \sigma_{ij} \dot{u}_i \end{aligned} \quad (2.16).$$

This elegant and simple result, also derived by Musgrave (1970), states that the energy flow vector is given by the tensor product of the particle velocity and the stress tensor.

Assuming the same travelling wave solution as before (equation (2.7)) and substituting into equation (2.16) we obtain

$$\begin{aligned} P_j &= C_{ijkl} A_k k_l \sin(\omega t - k_j x_j) A_i \omega \sin(\omega t - k_j x_j) \\ &= C_{ijkl} A_i A_k k_l \omega \sin^2(\omega t - k_j x_j). \end{aligned}$$

The time average over one period ($2\pi/\omega$) of P_j is

$$\bar{P}_j = \frac{1}{2} C_{ijkl} A_i A_k k_l \omega \quad (2.17).$$

As only the direction of \bar{P}_j is of interest, equation (2.17) may be divided on both sides by $\omega |\underline{k}|/2$ so that (2.17) becomes

$$p_j = 2\bar{P}_j \omega^{-1} |\underline{k}|^{-1} = C_{ijkl} A_i A_k n_l \quad (2.18)$$

where n_l are once again the direction cosines of the wave vector \underline{k} and p is now the scaled energy flux vector, whose direction is of interest.

Returning to equation (2.13), and using the wave solution (2.7) the energy density may be written as

$$\xi = \frac{1}{2} \left(\rho \omega^2 |\underline{A}|^2 \sin^2(\omega t - k_j x_j) + C_{ijkl} A_i A_k k_j k_l \sin^2(\omega t - k_j x_j) \right)$$

and using equation (2.8) this becomes

$$\xi = \rho \omega^2 |\underline{A}|^2 \sin^2(\omega t - \underline{k}_j \cdot \underline{x}_j) \quad (2.19).$$

The time average over one period is then

$$\bar{\xi} = \frac{1}{2} \rho \omega^2 |\underline{A}|^2.$$

The vector representing the velocity of the propagation of energy, \underline{s} , will be given by dividing the energy flux vector (\underline{P}) by the energy density, i.e.

$$\begin{aligned} s_j &= P_j \xi^{-1} = \bar{P}_j (\bar{\xi})^{-1} = C_{ijkl} A_i A_k k_l \omega [\rho \omega^2 |\underline{A}|^2]^{-1} \\ &= C_{ijkl} \rho^{-1} \hat{A}_i \hat{A}_k n_l (|\underline{k}| \omega^{-1}) \\ &= C_{ijkl} \rho^{-1} \hat{A}_i \hat{A}_k n_l V^{-1} \quad (2.20) \end{aligned}$$

where $\hat{A}_k = A_k |\underline{A}|^{-1}$ are the components of the normalized polarization vector, and V is the phase velocity. If a normalized polarization vector has been used in the calculation of p_j then \underline{s} is simply given by

$$s_j = p_j (\rho V)^{-1} \quad (2.21).$$

A different approach (Federov 1968) is to view \underline{s} as the group velocity, which is the velocity of the wave packet consisting of a superposition of numerous waves with similar frequencies, and is in general given by $\underline{\nabla}_k \omega$, or

$$s_j = \frac{\partial \omega}{\partial k_j} \quad (2.22).$$

This expression reduces to equation (2.20) as can be seen from the following argument.

Starting from equation (2.8) and multiplying both sides by A_i we

obtain

$$\rho \omega^2 A_i A_i = C_{ijkl} k_j k_l A_k A_i$$

i.e.

$$\omega^2 = \rho^{-1} C_{ijkl} k_j k_l \hat{A}_k \hat{A}_i$$

By taking $\frac{\partial}{\partial k_m}$ of both sides we obtain

$$\begin{aligned} 2 \omega \frac{\partial \omega}{\partial k_m} &= \rho^{-1} C_{ijkl} \hat{A}_k \hat{A}_i \frac{\partial}{\partial k_m} (k_l k_j) \\ &= \rho^{-1} C_{ijkl} \hat{A}_k \hat{A}_i (k_l \delta_{jm} + k_j \delta_{lm}) \\ &= 2 \rho^{-1} C_{imkl} \hat{A}_k \hat{A}_i k_l \end{aligned}$$

or

$$s_j = \frac{\partial \omega}{\partial k_j} = C_{ijkl} n_l \hat{A}_k \hat{A}_i (\rho V)^{-1} \text{ using } V = \omega |\underline{k}|^{-1} \quad (2.23)$$

which is identical to equation (2.20).

A further relationship between phase and group velocities may be obtained by taking the component of \underline{s} along the direction of propagation, i.e.

$$\begin{aligned} s_j n_j &= C_{ijkl} \hat{A}_i \hat{A}_k n_l n_j (\rho V)^{-1} \\ &= (C_{ijkl} n_l n_j A_k) |\underline{A}|^{-1} \hat{A}_i (\rho V)^{-1}. \end{aligned}$$

The expression in brackets may be simplified by dividing both sides of equation (2.8) by $|\underline{k}|^2$ to give

$$\rho V^2 A_i = C_{ijkl} n_j A_k n_l$$

so that

$$\begin{aligned} s_j n_j &= \rho v^2 A_i \hat{A}_i |\underline{A}|^{-1} (\rho v)^{-1} \\ &= v \end{aligned} \quad (2.24).$$

This simple result states that the component of the group velocity in the direction of the wave normal is equal to the wave velocity. It follows, then, that the ray velocity is always greater than or equal to the wave velocity for any given propagation direction. Figure 2.1 shows the relationship between phase and group velocity. In the figure, the wave velocity is proportional to ON which is the normal to the tangent of the wave surface at P. By contrast the ray velocity is proportional to OP. It should be noted, however, that it is unlikely that the wave surface in a real crystal will be a simple ellipsoid of revolution.

The right hand sides of equations (2.8) and (2.18) are similar in form, and thus the matrix \underline{Q} previously defined may be used to write down the components of \underline{p} explicitly. However it must be noted that equation (2.8) is an eigenvalue equation and thus fundamentally different from equation (2.18).

Defining

$$\underline{R} = \begin{bmatrix} A_1^2 \\ A_2^2 \\ A_3^2 \\ 2A_2A_3 \\ 2A_3A_1 \\ 2A_1A_2 \end{bmatrix}$$

and using the Voigt notation as before, the components of the scaled energy flux vector are given by

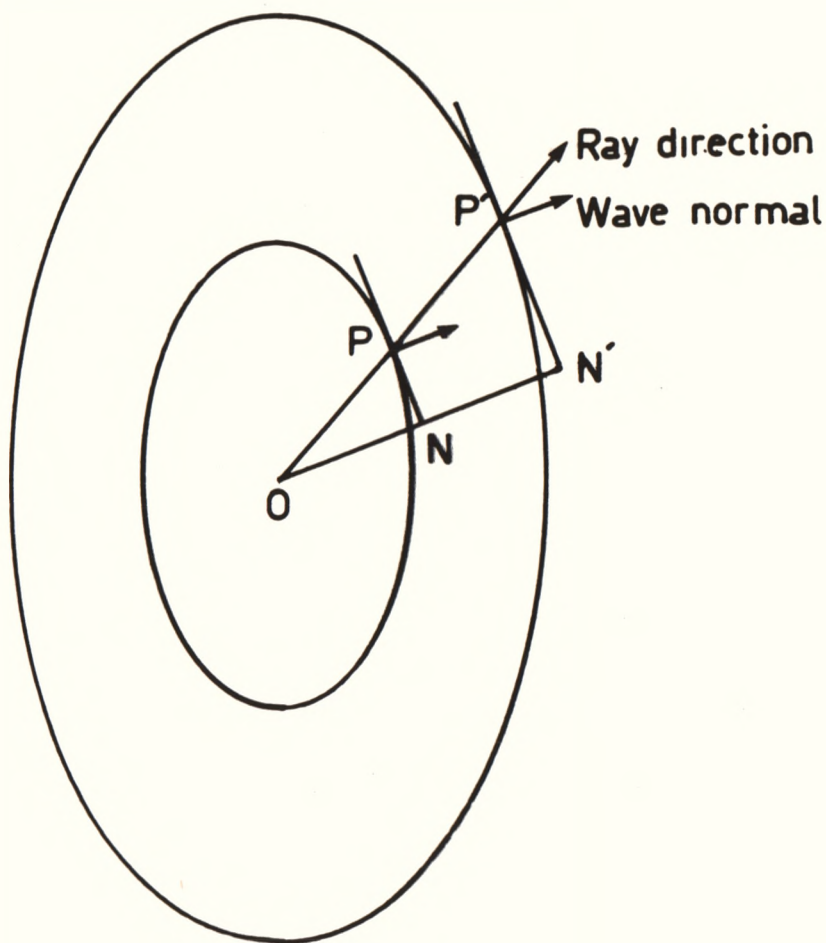


Figure 2.1. Successive portions of a wave surface showing the relationship between the propagation direction (i.e. the wave normal) \underline{n} , and the ray direction \underline{s} . If the fronts are separated in time by Δt , $NN' = V\Delta t$, where V is the phase velocity and $PP' = s\Delta t$ where s is the group or ray velocity. Clearly the projection of the group velocity along the wave normal is equal to the wave velocity (equation 2.24). Note the strong analogy to extraordinary refraction in birefringent crystals.

$$\begin{aligned}
 p_1 &= \ell Q_{1j} R_j + m Q_{6j} R_j + n Q_{5j} R_j \\
 p_2 &= \ell Q_{6j} R_j + m Q_{2j} R_j + n Q_{4j} R_j \\
 p_3 &= \ell Q_{5j} R_j + m Q_{4j} R_j + n Q_{3j} R_j
 \end{aligned} \tag{2.25}$$

where $j = 1$ to 6 .

The matrix \underline{Q} can be formed from the known elastic constants, and the components of $\underline{\lambda}$ calculated for a given propagation direction. The eigenvalue equation (2.10) may then be solved for the velocities and polarization vectors of the three modes propagating in this direction. Once the components of the polarization vectors are known, the components of the column matrix \underline{R} may be calculated and the scaled energy flux vector \underline{p} evaluated. It is then a simple matter to calculate the angle ϕ between the energy flow vector and the propagation direction by using

$$\cos \phi = \frac{\underline{p} \cdot \underline{n}}{|\underline{p}| |\underline{n}|} \tag{2.26}.$$

Provided that the components of \underline{A} have been normalized equation (2.21) may be used to calculate the components of the group velocity by dividing each component of \underline{p} by ρV where V is the phase velocity for that mode. The magnitude of the group velocity is then given by

$$|\underline{s}|^2 = (s_1^2 + s_2^2 + s_3^2) = |\underline{p}|^2 (\rho V)^{-2} \tag{2.27}.$$

The above method of computation, which is simpler than that of Neighbours, (1973) has been successfully used to calculate the deviation of the ray from the wave normal for a number of different crystals which have included representatives of the monoclinic, orthorhombic and tetragonal systems. In particular, calculations for orthorhombic calcium

sulphate are in complete agreement with those of Neighbours (1973).

2.2 DETERMINATION OF THE ELASTIC CONSTANTS OF A MONOCLINIC SYSTEM

In section 2.1 it was shown that if the elastic constant matrix is known, it is possible to calculate the wave and group velocities, polarizations, and ray directions of the three wave modes for any given propagation direction. In this section, a method is presented for determining an unknown elastic constant matrix via measurements of the phase velocity for certain judiciously chosen directions.

2.2.1 Form of the Elastic Constant Matrix for Monoclinic Symmetry

The elastic constant matrix is specified with respect to a Cartesian set of axes xyz , which have a standard orientation with respect to the crystallographic axes a, b, c . For a monoclinic system the convention is (Standards on Piezoelectric Crystals 1949) to set y parallel to the b axis and z parallel to the c axis as shown in Figure 2.2. In order to avoid confusion the normal notation $[a, b, c]$ will refer to directions with respect to the monoclinic axes and the primed notation $[x, y, z]'$ will refer to directions with respect to the Cartesian axes.

The two-fold rotation axis in a monoclinic crystal reduces the number of independent components from 21 (for a triclinic system) to 13 (Nye 1967). With respect to the Cartesian axes the matrix takes the form

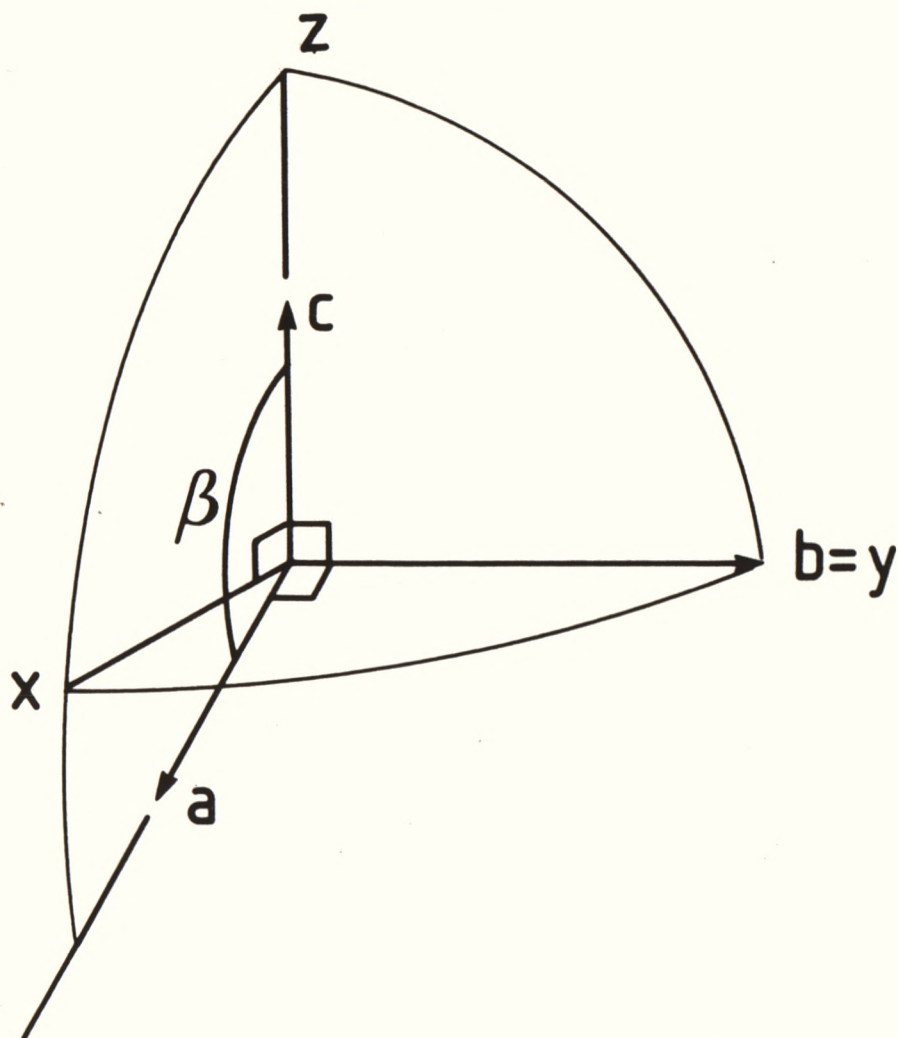


Figure 2.2. Axes of a monoclinic crystal. a and c are perpendicular to b , but not to each other. xyz form the Cartesian axes to which the elastic constants are referred.

$$C_{ij} = \begin{bmatrix} C_{11} & C_{12} & C_{13} & 0 & C_{15} & 0 \\ C_{12} & C_{22} & C_{23} & 0 & C_{25} & 0 \\ C_{13} & C_{23} & C_{33} & 0 & C_{35} & 0 \\ 0 & 0 & 0 & C_{44} & 0 & C_{46} \\ C_{15} & C_{25} & C_{35} & 0 & C_{55} & 0 \\ 0 & 0 & 0 & C_{46} & 0 & C_{66} \end{bmatrix}$$

and thus the matrix \underline{Q} (equation (2.11)) reduces to

$$\underline{Q} = \begin{bmatrix} C_{11} & C_{66} & C_{55} & 0 & C_{15} & 0 \\ C_{66} & C_{22} & C_{44} & 0 & C_{46} & 0 \\ C_{55} & C_{44} & C_{33} & 0 & C_{35} & 0 \\ 0 & 0 & 0 & \frac{1}{2}(C_{44} + C_{23}) & 0 & \frac{1}{2}(C_{46} + C_{25}) \\ C_{15} & C_{46} & C_{35} & 0 & \frac{1}{2}(C_{13} + C_{55}) & 0 \\ C_{16} & C_{26} & C_{45} & \frac{1}{2}(C_{25} + C_{46}) & 0 & \frac{1}{2}(C_{66} + C_{12}) \end{bmatrix}$$

2.2.2 Determination of the Elastic Constant Matrix via Velocity Measurements

Aleksandrov (1958) has shown that it is possible to calculate all 13 elastic constants of a monoclinic system by measuring the velocities of all three modes in six different directions, viz. $[100]'$, $[010]'$, $[001]'$, $[1,0,n]'$, $[110]'$, and $[011]'$. As an example of the calculation consider a wave propagating along $[100]'$. The column matrix \underline{L} (equation (2.11)) reduces to

$$\underline{L} = \begin{bmatrix} 1 \\ 0 \\ 0 \\ 0 \\ 0 \\ 0 \end{bmatrix}$$

and the $\underline{\lambda}$ matrix is given by (equation (2.11))

$$\underline{\lambda} = \begin{bmatrix} C_{11} & 0 & C_{15} \\ 0 & C_{66} & 0 \\ C_{15} & 0 & C_{55} \end{bmatrix} .$$

Using the secular equation (2.12) we obtain the cubic equation

$$\begin{vmatrix} C_{11} - \rho V^2 & 0 & C_{15} \\ 0 & C_{66} - \rho V^2 & 0 \\ C_{15} & 0 & C_{55} - \rho V^2 \end{vmatrix} = 0 \quad (2.28).$$

It is immediately obvious that one solution to (2.28) is given by $C_{66} = \rho V^2$ and the corresponding eigenvector (obtained via equation (2.10)) is $[010]'$, which means that this is a pure transverse mode. The remaining two waves have velocities satisfying

$$\begin{vmatrix} C_{11} - \rho V^2 & C_{15} \\ C_{15} & C_{55} - \rho V^2 \end{vmatrix} = 0$$

and using the properties of the roots of quadratic equations it follows that

$$\rho V_1^2 \rho V_2^2 = C_{11} C_{55} - C_{15}^2$$

and

$$\rho V_1^2 + \rho V_2^2 = C_{11} + C_{55}$$

so that there are two equations relating three unknowns. The eigenvectors for these two waves are semi-pure and are of the form $[\ell, 0, n]'$ and $[-n, 0, \ell]'$ so that the polarization directions lie in the xz plane and are perpendicular to each other. The values of ℓ and n are functions of the elastic constant matrix yet to be determined.

Similar calculations are performed for the remaining five

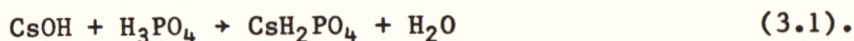
directions. For the off-axis directions the equations are much more complicated because the secular equation does not contain any zero terms. A total of 18 equations relating the 13 unknown elastic constants may be obtained in this way. Some of the relationships are redundant and may be used as cross checks on the data. However, even though there are more equations than unknowns, it was found (see Chapter 5) that the equations did not yield a unique solution for the elastic constant matrix. Physical arguments had to be employed to choose between the possible solutions. The procedure adopted, and a full list of all the necessary relationships is presented together with the velocity measurements in Chapter 5.

CHAPTER 3

MATERIALS PREPARATION

3.1 CRYSTAL PREPARATION

The CsH_2PO_4 (CDP) samples used in this investigation were prepared using the solvent evaporation technique. Equal molar quantities of H_3PO_4 and CsOH^* were added to produce a solution of CsH_2PO_4 (CDP) according to the reaction



In the first attempt to grow crystals, excess ethanol was then added and the precipitated CsH_2PO_4 powder was filtered and dried. The powder was then dissolved in just enough water to provide a saturated solution. The pH of the saturated solution was determined to be 4.4 ± 0.1 using a Corning pH meter. The solution was then placed in crystallizing dishes and held at a constant temperature of $21 \pm 0.5^\circ\text{C}$. After a few days the solutions were seeded with small near perfect crystals of CsH_2PO_4 which were produced by an initial evaporation of a small quantity of the saturated solution, and the crystals left to grow for about 12 weeks. The resulting specimens were parallelepipeds of approximate dimensions $5 \times 13 \times 15 \text{ mm}^3$. The crystals obtained had the orthorhombic (100) platelet type habit reported by Rashkovich et al. (1977). However, the crystals had many visible growth defects which could act as scattering centres for ultrasonic waves. Also, for some off-diagonal measurements crystals larger than those obtained in this first attempt were required, since the orientation and polishing procedure for these off-diagonal measurements left only a small usable

* The starting materials were 99.9% CsOH obtained from Cerac Chemicals and 85% w/w UNIVAR Phosphoric Acid from Ajax Chemicals.

path length between the parallel faces. Small path lengths lead to larger uncertainties in the measured velocity. Therefore, a second attempt at crystal growing was undertaken to produce larger defect-free samples.

In this second attempt, the step of adding the ethanol to produce a powder, which is then dissolved to give a saturated solution, was omitted. Instead, the saturated solution was produced by heating the solution synthesised according to reaction (3.1) to drive off excess water by evaporation. Various crystal growing strategies were adopted in this second attempt, some of which were more successful than others. In general, it was found that slowing the rate of growth, improving the temperature stability, triple filtering the saturated solution and reducing the pH to 2-2.5 by addition of excess H_3PO_4 all led to improved crystal quality. The effect of the pH of the saturated solution on the growth of the crystals is discussed in section 3.3.

The revised procedure was as follows. More CsH_2PO_4 was added to an already saturated solution and the mixture heated whilst being continuously stirred to produce a supersaturated solution. It was found that gentle heating (up to approximately 35°C) gave the best results. The solution was allowed to cool and if any spontaneous crystallization occurred the solution was carefully filtered until no crystallites remained. This often required four or five consecutive filtrations. A great deal of care was taken to prevent dust or other possible nucleation centres from contaminating the solution. The prepared solutions were then covered, with a small opening remaining to allow evaporation, and placed in an air-conditioned environment of $19 \pm 2^\circ\text{C}$.

Three seeding/growing techniques were then employed. In the first, the solution was allowed to stand and any spontaneously formed crystallites were allowed to continue to grow. This technique was

successful on the rare occasions that only one or two nucleation centres appeared. Otherwise no useful crystals could be harvested from the solution.

The second method involved placing a small near-perfect seed into the solution at the bottom of the container after the solution had been left standing undisturbed for a few days. While this proved effective, the resultant crystals showed defects around the seed since the growth was asymmetric and slow, particularly in the vertical direction. Also spontaneous crystallization often ruined the growing crystals by depositing layers of polycrystalline material onto the crystal surface.

The third technique used was to drill a hole in a small seed (more precisely to dissolve a hole using a fine drill moistened with water) and suspend the seed in the middle of the saturated solution on a nylon thread. This proved to be very successful. Growth was rapid and usable crystals were obtained within about four weeks. The crystals obtained had very few visible defects apart from the growth around the seed; hence the need to use as small a seed as possible. Very large crystals of approximate dimensions $4 \times 2 \times 1 \text{ cm}^3$ were obtained in this way. Such crystals could be cut in two to eliminate the defects due to the seed and supporting thread.

The success of all the above methods depended on the degree of supersaturation of the starting solution. If it was too supersaturated spontaneous crystallization ruined any productive crystal growth. If undersaturated, the seed simply dissolved. The best situation was one in which the seed neither grew nor dissolved appreciably in the first few days. This indicated the correct degree of supersaturation which was usually obtained only by trial and error.

Crystal growth times varied between six weeks and six months depending on the rate of evaporation. It was found that the appearance of spontaneous crystallization heralded the end of the useful growth period and when such crystallization occurred any useful crystals were harvested from the solution and the remaining material was redissolved in water and the whole saturating, seeding and growing process restarted. The expertise to grow large defect-free crystals was only developed towards the end of this study after many months of effort. It was therefore necessary to use the crystals that were available at the time when the measurements were taken, even though in retrospect the quality of these crystals was much poorer than that attained subsequently. The best samples from both the first and second crystal growing attempts were used, although these often contained growth defects.

3.2 MATERIALS VERIFICATION

3.2.1 Electron Microprobe

A sample of CsH_2PO_4 powder produced as explained in section 3.1, and a single crystal of CsH_2PO_4 were examined in an electron microprobe (Applied Research Laboratory SEMQ2) in the Department of Earth Sciences, Monash University. X-ray emission lines corresponding to cesium and phosphorous were clearly detected but no other peaks were visible. The probe is not capable of detecting the presence of elements with atomic numbers less than that of sodium. Hence, the oxygen and hydrogen contents were not measurable. It was estimated that impurity levels of elements with atomic numbers greater than that of sodium were less than 0.5%.

3.2.2 Powder X-ray Diffraction

The microprobe results confirmed that no heavy elements other than cesium were present. However, the possibility still existed that the crystals may not have been CsH_2PO_4 but rather some other more complex mixture of hydrogen phosphate salts. To verify that the crystals were indeed CsH_2PO_4 X-ray powder patterns were taken using a standard Philips vertical diffractometer with Cu K_α radiation and a Ni filter at 40 kV. The use of a rotating specimen stage was necessary as no Bragg peaks were detected in the diffractometer scan when the sample was not spun on its axis. In view of the cleavage properties of CsH_2PO_4 the difficulty in producing a random powder is not unexpected.

Two samples for measurement were produced. The first was CsH_2PO_4 powder precipitated by addition of ethanol to the saturated solution. This powder was crushed slightly and packed into the sample holder. The second sample was produced by crushing a single crystal of CsH_2PO_4 that had grown from the saturated solution. The Bragg peak positions of the two samples agreed to within experimental error. The intensities differed slightly for some Bragg peaks. The results are shown in the Table 3.1.

Although there is no entry for CsH_2PO_4 in the powder diffraction file (J.C.P.D.S. 1983, up to and including set 33), the known structure may be used to calculate peak positions and intensities. The calculation was performed on the crystal data of Uesu and Kobayashi (1976) using a computer program kindly provided by Mr G. Tate of Aeronautical Research Laboratories, Melbourne. The experimental results and the predicted diffraction pattern agreed reasonably well except for the (100) peaks which were much more intense than predicted. This is almost certainly due to preferred orientation of (100) platelets which have preferentially formed by cleavage in the pressing and grinding

Table 3.1

Powder Diffraction Peaks of CDP

<u>Computer Prediction</u>			<u>CDP Powder Precipitated From Solution</u>		<u>CDP Ground Crystal</u>	
(h,k,l)	Interplanar Spacing(Å)	Relative Intensity	Interplanar Spacing	Relative Intensity	Interplanar Spacing	Relative Intensity
110	4.861	36.8	4.872(8)	48(2)	4.880(8)	56(3)
200	3.762	88.0	3.772(5)	952	3.773(5)	1078
11 $\bar{1}$	3.745	181	not resolved			
10 $\bar{1}$	3.502	14.3	3.497(4)	42	3.497(4)	53
*20 $\bar{1}$	3.489	27.4				
020	3.185	63.0	3.194(3)	44	3.197(3)	92
111	3.069	100.0	3.076(3)	100	3.078(3)	100
02 $\bar{1}$	2.626	39.0	2.633(2)	27	2.635(2)	51
20 $\bar{1}$	2.565	16.2	2.571(2)	38	2.566(2)	44
*30 $\bar{1}$	2.556	4.6				
220	2.431	58.3	2.438(2)	55	2.438(2)	65
31 $\bar{1}$	2.372	41.4	2.377(2)	60	2.378(2)	70
310	2.334	24.3	2.338(2)	60	2.340(2)	52
002	2.320	23.4	2.322(2)	31	2.321(2)	59
*20 $\bar{2}$	2.315	18.7				
400	1.881	4.4	1.885(1)	76	1.884(1)	94
22 $\bar{2}$	1.534	12.3	1.536(1)	33	1.536(1)	39
*51 $\bar{1}$	1.533	11.2				
*42 $\bar{2}$	1.530	9.6				

The observed peak widths were such that the planes indicated by a * may have also contributed to the observed reflection. The (11 $\bar{1}$) reflection was unresolved from the very large (200) reflection.

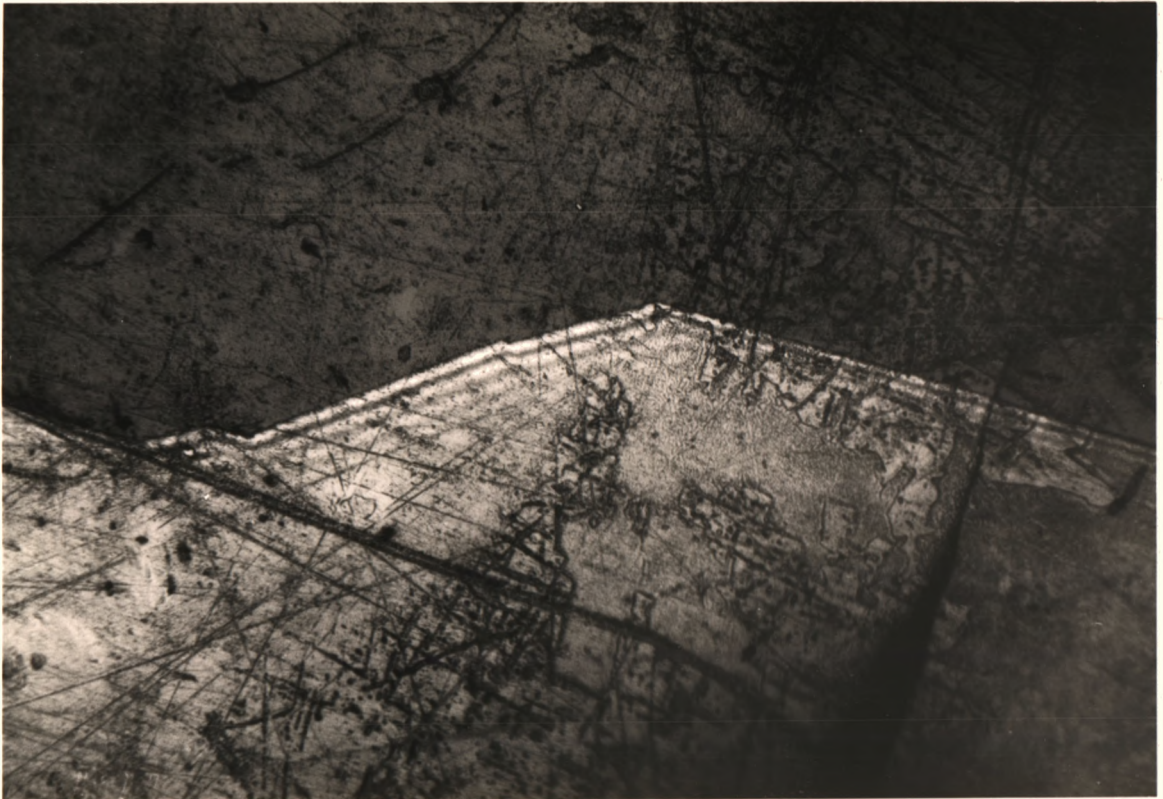
process. This preferred orientation is also observed in the case of the CsH_2PO_4 powder precipitated from solution. Hence, it is likely that the crystal orientations and habits discussed in the following section which favour (100) platelet type formation also occur in microscopic crystal formation resulting from rapid crystallization from solution. The results are summarized for the 13 most intense observed peaks out of a total of 36 in Table 3.1.

These investigations confirmed that the starting material was CsH_2PO_4 and that impurities, if present, were at concentrations less than 0.5%.

3.3 CRYSTAL PROPERTIES

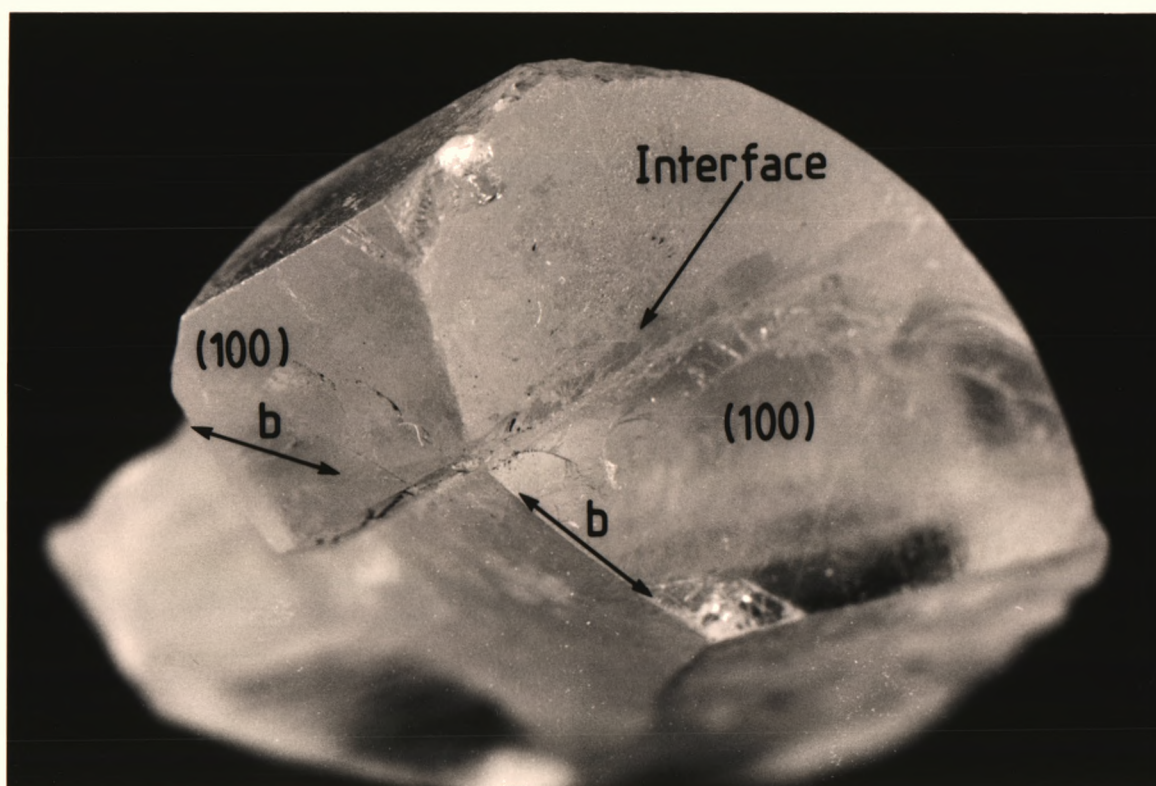
3.3.1 Crystal Habit and Multiple Growth Planes

The techniques outlined in section 3.1 produced some quite large defect-free crystals. However, on closer examination in the polarising microscope these crystals were found to consist of two growth habits. A view through the polarising microscope of one such crystal is given in Figure 3.1. The two growth planes are crystallographically related although a thorough enough investigation was not undertaken to determine if they are twins. Examination of the faces of a number of such crystals did reveal that the (100) cleavage planes of the two respective crystallites make an angle of $75 \pm 1^\circ$ to each other. Optical two-circle goniometric measurements of the large crystal shown in Figure 3.2 showed that it consists of two crystals with the (100) face of one crystal parallel to the $(11\bar{1})$ plane of the second one. It was also determined that the b axes of the two crystals are inclined at an angle of approximately 129° to each other. Unfortunately, the other crystals in this mixed growth habit batch did not have enough visible faces to check these latter observations. However, the angle of $75 \pm 1^\circ$



0.3mm

Figure 3.1. A view of a mixed growth plane sample of CDP seen through crossed polarizers. The dark region is nearly in the extinction position. The light region does not extinguish on rotation of the crystal, indicating that for this path through the crystal at least two different crystallographic orientations are present. Note also the interference fringes at the interface.



3 mm

Figure 3.2. Mixed growth habits of CDP. The two (100) faces of the respective crystallites are shown together with the approximate direction of the b axis in each face. The (100) faces are inclined at $75 \pm 1^\circ$ to each other, whilst the b axes are at an angle of approximately 129° to each other.

between (100) faces of the related crystals was reliably confirmed by repeated measurements on different samples, since this measurement required only two visible (100) cleavage faces.

Although the plane that forms the interface between the two crystals was not indexed it was noticed that this plane lies roughly at right angles to the (100) faces of each crystal. The bonding across this plane is extremely strong. Attempts to separate the two crystals always resulted in the crystal shattering or cleaving along the (100) face rather than separating along the common plane. This type of mixed growth was eliminated entirely by lowering the pH of the saturated solution to 2-2.5 by addition of excess H_3PO_4 . Frazer et al. (1979) have also reported that in order to obtain good crystal growth, it was necessary to add a slight excess of H_3PO_4 to produce a starting solution with a pH of about 2.5. The crystals which then grew had the habit shown in Figure 3.3 of orthorhombic platelets with the largest face being the (100) plane. The angular bisectors of the acute and obtuse angles of the parallelogram formed by the edges of the (100) face are parallel to the b and c axes respectively.

These observations are consistent with those of Rashkovich et al. (1977) who determined the crystal habit as a function of temperature and pH, as shown in Figure 3.4. As the figure shows for conditions of temperature and pH close to the curve, holohedral crystals grow. As the growth continues, however, small changes may occur in the pH of the solution on account of variation in the degree of supersaturation. These changes may be sufficient to change the preferred habit from holohedral to the (100) platelet type. The optical goniometric measurements on the crystal shown in Figure 3.2, whilst not conclusive, did suggest that there was no simple symmetry relationship between the

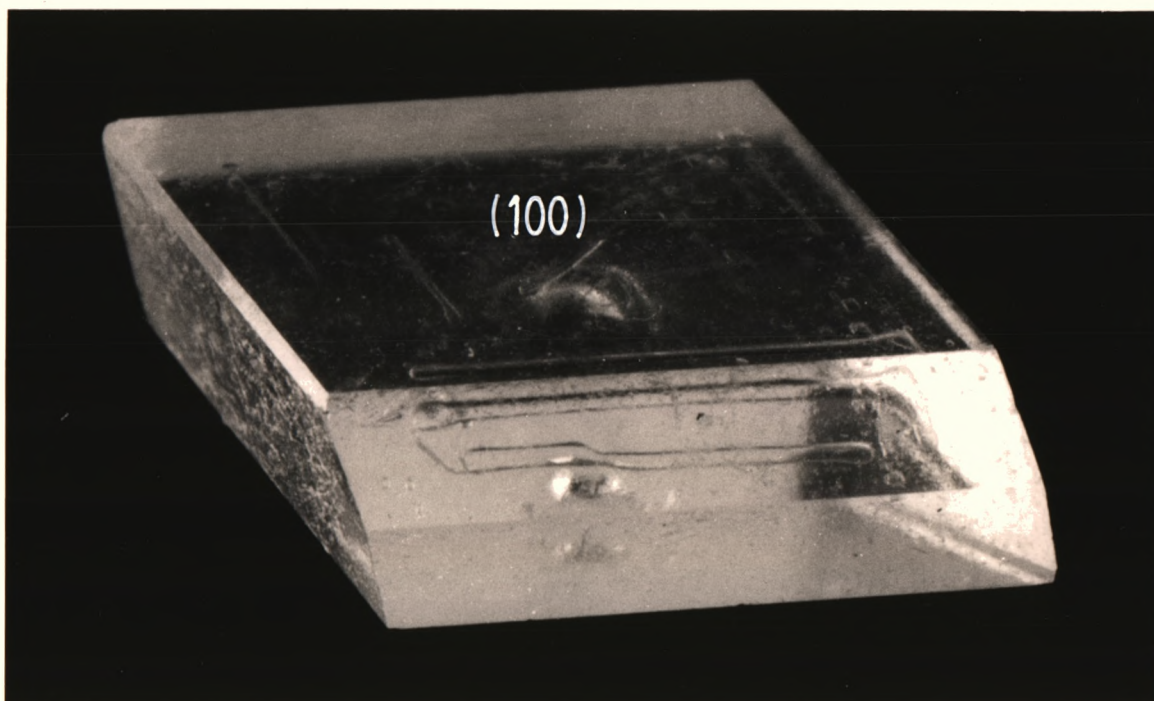


Figure 3.3. A crystal of CDP displaying the orthorhombic platelet habit reported by Rashkovich et al. (1977) (see also Figure 3.4). The angular bisectors of the acute and obtuse angles of the parallelogram formed by the edges of the (100) face are parallel to the *b* and *c* axes respectively.

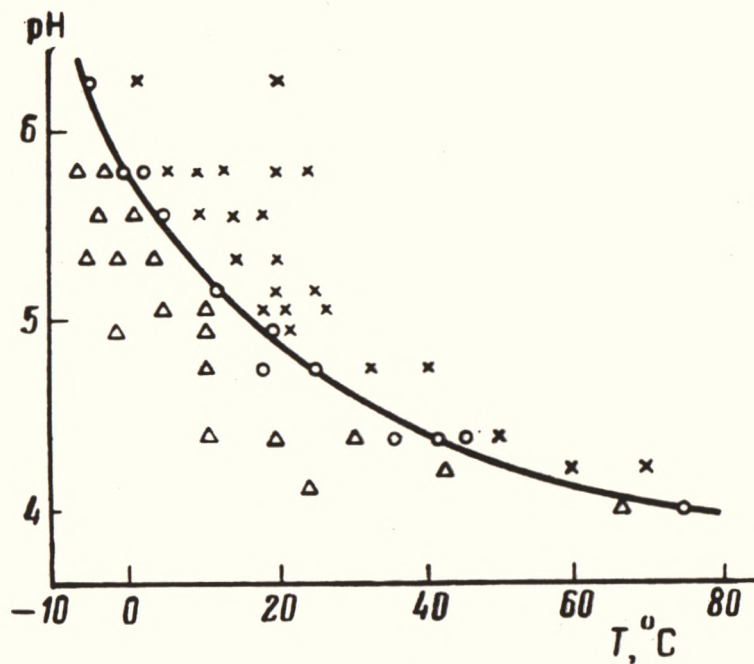
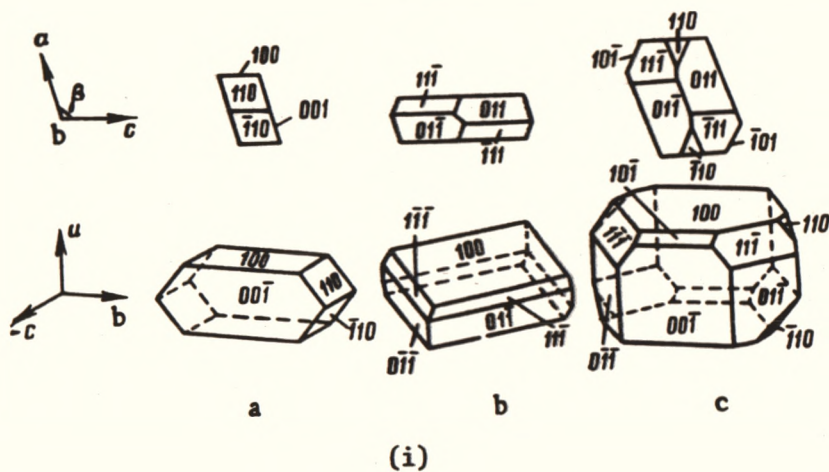


Figure 3.4. (i) Different crystal habits of CDP: (a) prisms, (b) orthorhombic platelets and (c) holohedral type.

(ii) The effect of crystallization conditions on the habit of CDP crystals. Below the curve (Δ) orthorhombic, close to the curve (o) holohedral type, and above the curve (x) prisms (after Rashkovich et al. (1977)).

orientation of the two crystallites†. This left epitaxial growth of one crystal on an exposed face of the other as a possibility. Using the fact that the $(11\bar{1})$ plane of one crystallite is parallel to the (100) face of the other, and that the two b axes make an angle of 129° to each other, it was calculated that the $(11\bar{1})$ face of one crystal would make an angle of only 10° to the $(11\bar{1})$ face of the second crystal. Since $(11\bar{1})$ and $(11\bar{1})$ would be expected to have similar bonding to each other both in and out of the plane, epitaxial growth is a distinct possibility. It should also be pointed out that the interface between the crystals is not a well defined plane, but is rather curved, so that an angle of 10° seems reasonable.

Figure 3.4 predicts that if the starting pH is lowered to 2.5-3.0 at about 20°C , the crystals formed will have the orthorhombic platelet habit. Since this combination of pH and temperature lies well below the curve, the small differences in pH due to varying degrees of supersaturation are not expected to give rise to conditions close to the curve which favour the production of the holohedral habit. Hence the mixed growth habit can be eliminated as was observed.

In practice, whilst this mixed habit crystal growth is interesting especially owing to the very strong bonding across the interface, it renders these crystals useless for ultrasonic measurements unless one crystallite is removed either by polishing or cutting with a thread moistened with water to remove the offending section. In this study, where these types of crystals have been used as source materials in the production of samples suitable for ultrasonic measurements, observations in a polarizing microscope were made to ensure that only one single crystal remained after the cutting or polishing.

† If the two crystallites are related by symmetry, as in twinning, there must be a plane which is common to both crystals. A low index plane for which this was true could not be found hence the comment that a twinned relationship is unlikely.

3.3.2 Other Physical Properties

CsH_2PO_4 possesses a combination of properties that makes grinding and polishing difficult and prevents standard techniques from being used. These properties are:

- (i) CDP is very water soluble (approximately 150 grams of CDP per 100 grams of water) and hence many common solvents such as methanol and acetone contain too much dissolved water to be suitable cleaning or lubricating agents. The samples once prepared must be kept in a desiccator if the surface finish is to be preserved from deterioration from water vapour in the air.
- (ii) CDP is brittle and will shatter if sawed or otherwise mechanically cut. Araldites and other epoxy resins were found to be unsuitable agents for holding the crystal during polishing because the setting of the resin stressed the crystal causing it to shatter.
- (iii) The crystals are heat sensitive and will crack along (100) cleavage planes or along an imperfect (010) cleavage plane if subjected to even moderate thermal shock. Effectively this eliminates the use of waxes as agents for holding the crystal during polishing as the thermal shock of applying and removing the wax cleaves the crystal.

3.4 SAMPLE PREPARATION FOR ULTRASONIC VELOCITY MEASUREMENTS

3.4.1 Requirements

To make ultrasonic velocity measurements on a single crystal sample requires the crystal to be polished to provide two flat parallel surfaces, the planar normal of which is the direction of propagation of the wave under study. The ultimate purpose of sample orientation and polishing is the production of a distortion-free, exponentially decaying echo train. The factors that affect the quality of the echo train and

the accuracy of the velocity and attenuation measurements, such as the degree of parallelism, surface flatness, surface scratches, and misorientation, are discussed in the literature (see for example Truell et al. 1969). However, it was found that in many cases the effort required to polish samples to the tolerances quoted in the literature was not worthwhile because the poor sample quality (i.e. in terms of macroscopic defect concentration) was the limiting factor in the production of high quality echo trains.

The working tolerances adopted for this study in view of sample quality limitations and sample preparation difficulties are now discussed.

(a) Parallelism

In order to achieve an exponentially decaying echo train and to minimise side wall reflections non-parallelism must be kept to a minimum. In general the higher the frequency and the lower the value of attenuation the more severe are the requirements on parallelism (Truell et al. 1969). Truell et al. indicate that polycrystalline steel, for example, measured at 20-30 MHz should have surfaces parallel to about one minute of arc. As a general rule the tolerance is inversely proportional to the frequency and therefore the tolerance for measurements undertaken in this study at 10 MHz should be about 2 minutes of arc. In practice, however, it was found that exponentially decaying echo trains could be obtained provided the surfaces were parallel to better than 10 minutes of arc, a tolerance which was readily achieved by the polishing technique employed. Parallelism was measured using an auto-collimator.

(b) Flatness

Surface flatness is important in the production of a thin bond between the transducer and specimen as well as in attaining the required

degree of parallelism. Flatness was measured by placing an optical flat on the prepared surface and counting the number of interference fringes per centimeter across the surface. Sensible readings of parallelism may be obtained if each surface is flat to within 10 fringes per centimetre.

(c) Surface scratches

Commonly the bond between the transducer and specimen is of the order of a few microns thick and therefore surface scratches should be less than 1 micron deep. In practice, a compromise must be reached between flatness which is achieved by polishing with metal plates and removal of surface scratches using a cloth lap (which often degrades the flatness). It was found that the effort required to reduce surface scratches to less than 1 micron deep was not worthwhile in terms of the quality of the resultant echo train as bonding the transducer to the specimen caused surface defects much deeper than one micron. A criterion of requiring scratches to be less than 10 microns deep proved to be satisfactory.

(d) Orientation

In the computation of elastic constants from the velocity data, the direction of propagation must be accurately known. Fractional velocity changes as a function of misorientation will depend on the elastic constants. In CDP such changes will be crucially dependent on the elastic anisotropy close to the direction of interest. For example, for a 1° misorientation $\frac{\delta V}{V}$ may vary between 0.9% and less than 0.03% depending on the direction of propagation and the direction of the 1° misalignment. Obviously, it is desirable to orient the samples as closely as possible to the required direction. Since the minimum errors in velocity measurements are of the order of 0.4% it seemed reasonable to align the samples to better than $\pm 0.5^\circ$ and to obtain an estimate of the misorientation.

In summary samples used in this study were polished and oriented to provide two parallel surfaces to within the following tolerances:

- (i) The misorientation is less than $\pm 0.5^\circ$.
- (ii) Non parallelism of the surface is less than 10 minutes of arc.
- (iii) Surface scratches are less than 10 microns deep.
- (iv) Surfaces are flat to better than 10 interference fringes per centimetre.

3.4.2 Polishing Technique

The requirements listed in the previous section would normally pose no problems for metallic samples but standard polishing and cutting techniques proved unsatisfactory for CDP in view of the properties listed in section 3.3.2. The following method developed over a long period of trial and error has proved successful not only for CDP but also for other molecular crystals such as CsD_2PO_4 , CsSCN , KSCN , K_2SeO_4 and KH_2PO_4 .

The crystal was mounted onto a brass plate using 'Tarzan's Grip' glue. This glue was suitable because it did not stress the crystal during the drying process and because it was easily removed using n-butyl acetate as a solvent which appeared to have no ill effect on the crystal. The mounted crystal was then placed on a goniometer and oriented with the aid of X-ray Laue photographs such that the required crystallographic plane was perpendicular to the X-ray beam (see next section). The goniometer was then removed from the X-ray machine and mounted in the grinding rig shown in Figure 3.5. In the first stage of the preparation of a face perpendicular to the required crystallographic direction 1200 "wet and dry" grinding paper lubricated with "Engis Hyprez type OS" fluid was found to be suitable. Coarser papers tended

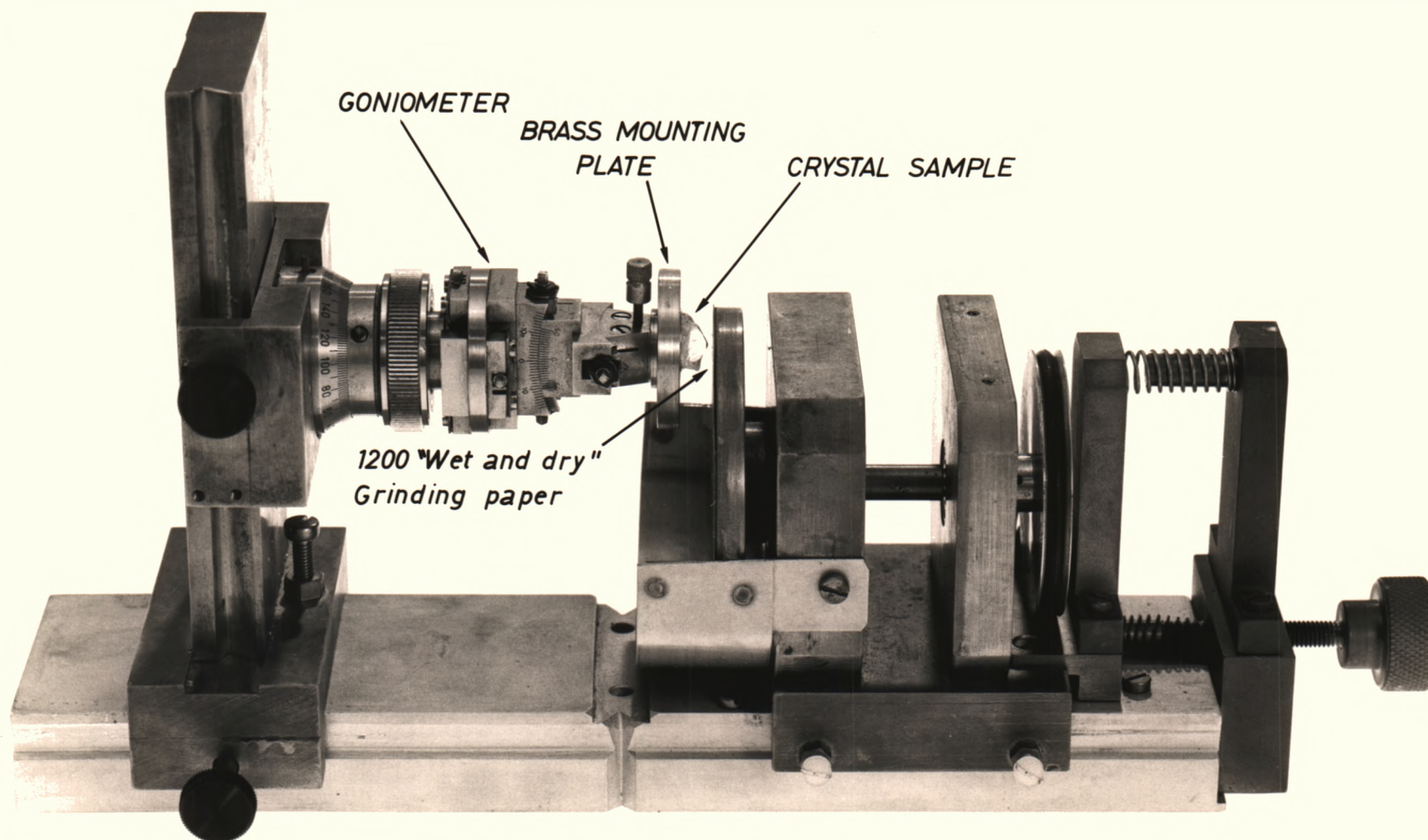


Figure 3.5. Crystal grinding rig.

to produce a pitted surface. Large misoriented or defected sections of crystal were removed using a thread saw with water as the etchant prior to the grinding.

After the rough preparation of the first oriented face the crystal was removed from the brass plate, turned over, remounted and the second oriented face was prepared.

The surface obtained by cutting and grinding was not flat and had scratches in it of the order of 25-50 microns deep. These were removed by polishing on a Kent automatic polishing machine with a "Siro Lap" tin plate†, using 1 micron diamond paste and "Hyprez type OS" lubricating fluid. Other standard commercial plates tended to pit the surface and gave an unsatisfactory finish.

The even pressure provided by a plunger chase arrangement (see Figure 3.6) ensured flatness and a surface parallel to the brass mounting plate. Once the required surface finish had been obtained (which usually required 10 to 15 minutes polishing) the crystal was again removed, turned over, and remounted to polish the second face. By this method surfaces parallel to within 4 minutes of arc and flat to about 5 fringes per centimetre over the surface have been obtained. With careful attention to cleanliness, surface scratches can be kept down to less than 5 microns in depth. Often, after polishing on the Siro Lap plate, one or two large scratches remained on the surface which were probably due to small pieces of crystal which had broken away and run across the lap. For a better surface finish, finer diamond pastes could be used or, alternatively, a final polish could be obtained using

† The "Siro Lap" tin plate (Engis Australia Pty. Ltd.) consists of a tin lap surface bonded onto an aluminium base plate. The lap is machined and a spiral V shaped groove is cut into the lapping surface. This enables the waste material to collect in the groove preventing it from passing between the lap and the material being machined. The surface of the lap is treated by a glass bead blasting process.

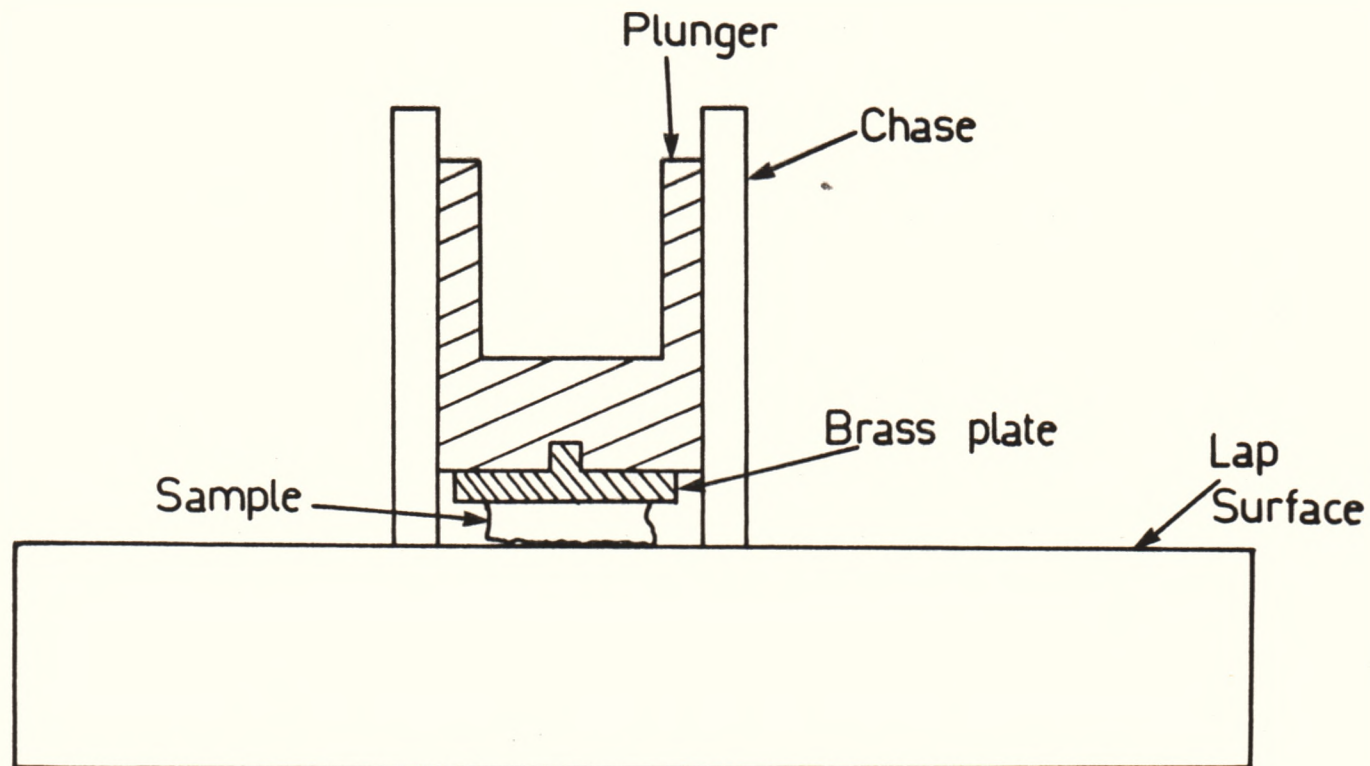


Figure 3.6. Lapping arrangement to provide uniform plunger pressure during polishing to ensure flatness.

a cloth lap, although cloth tended to round the edges of the specimen. However, as previously mentioned, the effort and time required to prepare the samples to these tolerances was not justified in terms of improved echo train quality and the polishing requirements were relaxed to those given in section 3.4.1.

3.4.3 Orientation

The task of orienting a monoclinic crystal with the aid of Laue photographs is difficult and time consuming especially if low-symmetry directions are of interest. An invaluable aid to the orientation procedure was a computer simulation program (Cornelius 1981) that allowed rapid identification of crystal orientation even for these low-symmetry directions.

(a) The Laue simulation program.

The program requires as input the X-ray tube voltage, specimen to film separation, maximum spot to centre distance, lattice parameters for the unit cell, the required scan range for each Miller index, the crystal orientation for which a simulation is required, and the atomic number and position of all atoms in the unit cell. The program then calculates the predicted position and intensity of each possible Laue spot that will lie on the film. If the intensity is greater than a minimum intensity discriminator, the spot will be plotted on the simulation. The final result is a predicted Laue pattern for that orientation.

Using a catalogue of such predictions, the one closest to the actual crystal orientation was used to index at least three Laue spots. The Miller indices and film co-ordinates of these spots were fed back into the program which calculated the most likely specimen to film separation and the direction anti-parallel to the X-ray beam in terms of

both real and reciprocal lattice vectors. An estimate of the error in the determined orientation was also obtained.

(b) The procedure and an example.

The orientation of a single crystal of monoclinic CsH_2PO_4 along $[110]'$ where the primed direction is with respect to a Cartesian set of axes xyz (see Figure 2.2) is used here as an example. The corresponding crystallographic direction is $[2.053, 2.426, 1.000]$. The sample was mounted on a goniometer and a Laue photograph taken. Comparison to a catalogue of Laue patterns generated by the simulation program indicated that the x axis was parallel to the incident X-ray beam and allowed the c axis in the plane of the photograph to be identified. The crystal was then rotated through 45° about the c axis and another Laue photograph taken. This photograph was compared to the simulation for the $[2.053, 2.426, 1.000]$ crystallographic direction (Figure 3.7(i)) and it was found using a Greniger chart that a further 1° rotation correction was needed in order to align the Laue photograph with the simulation. A further Laue photograph was taken following this rotation and this is shown in Figure 3.7(ii). Using the simulation, six spots were indexed and their x - y film coordinates measured. The agreement between the spot positions on the photograph and on the simulation is excellent. The indexed spots and co-ordinates were input to the program and the real space direction anti-parallel to the X-ray beam was determined to be $[1.994 \pm 0.014, 2.391 \pm 0.025, 1.000 \pm 0.034]$. This implies that the direction cosines with respect to the xyz orthogonal axes are $\alpha = .704 \pm .005$, $\beta = .713 \pm .005$ and $\gamma = .003 \pm .007$. Therefore the crystal has been successfully aligned along the $[110]'$ direction with a tolerance of $\pm 0.4^\circ$. The information provided by the program could be used to refine the orientation further. Accuracies of $\pm 0.2^\circ$ were possible.

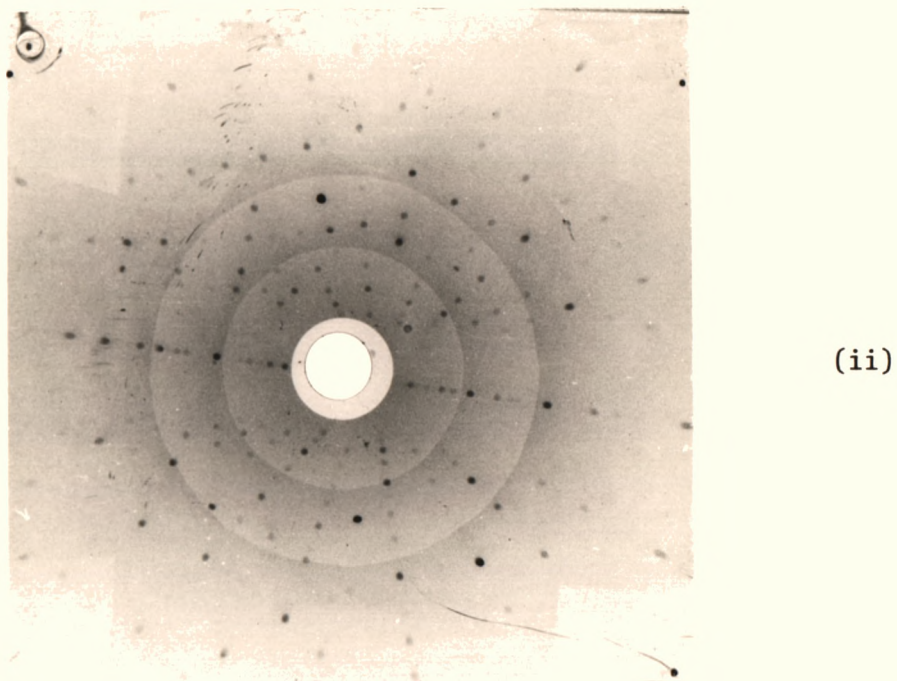
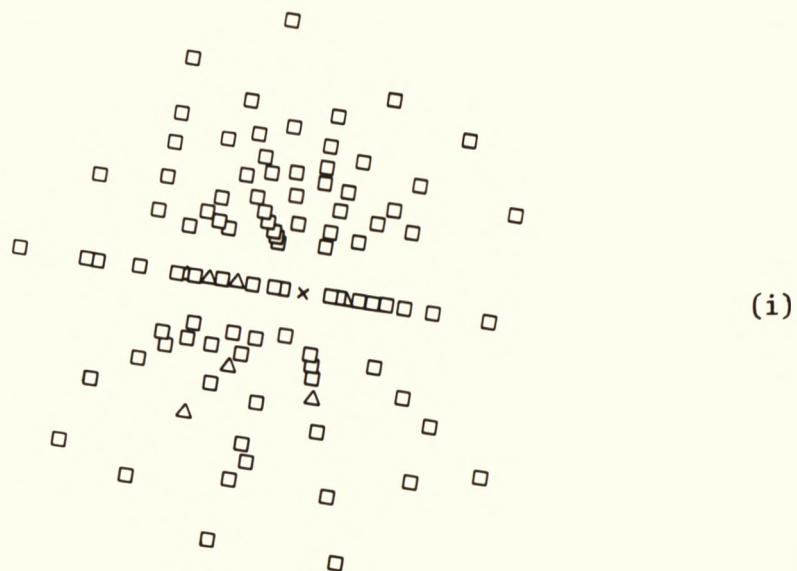
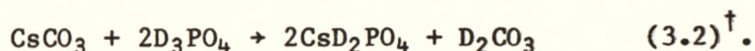


Figure 3.7. (i) Laue simulation for the $[2.053, 2.426, 1.000]$ crystallographic direction anti-parallel to the X-ray beam in CDP.

(ii) Contact print of the Laue reflection photograph of CDP aligned parallel to the above direction.

3.5 PREPARATION OF DEUTERATED SAMPLES

The CsD_2PO_4 (CDDP) samples used in this study were prepared by the solvent evaporation technique. The saturated solution was synthesized according to the reaction



The production of crystals followed the method outlined in section 3.1 except that at all times the solution was kept out of contact with water vapour in the air which can exchange with the D_2O in solution thus reducing the level of deuteration. In practice, this required growing the crystals in a desiccator over silica gel. Despite attempts to employ the same growing and seeding techniques that had proved so successful in the case of CsH_2PO_4 , the CsD_2PO_4 crystal quality was poorer than for comparable crystals of CDP. The mixed growth habit phenomenon was not observed and lowering the pH by addition of excess D_3PO_4 did not seem to have much effect on crystal growth. These differences between CDP and CDDP growth may be due to the difference in evaporation rates (since the CDDP must be grown in a desiccator) or to the presence of dissolved deuterated carbonic acid which is a by-product of the synthesis.

An alternative synthesis technique, which may avoid the latter problem, would be to produce CDDP by successive recrystallizations from D_2O of CsH_2PO_4 . Frazer et al. (1979) have reported producing crystals of 'good quality' with a deuterium content of 94% by this method. Unfortunately, limitations on time and the expense and unavailability of the relatively large quantities of D_2O required, prevented this from being attempted.

† Starting materials were 99.9% CsCO_3 obtained from Cerac Chemicals and 85% w/w D_3PO_4 in D_2O from Aldrich Chemicals. The D_2O was provided by the Australian Atomic Energy Commission, Lucas Heights, Sydney.

The CDDP samples were oriented and polished to the same tolerances and by the same techniques as for CDP. An unsuccessful attempt was made to measure the level of deuteration using infrared spectroscopy (Rumble 1983). A sample of CDDP was finely ground, mixed with a cesium bromide matrix and pressed into a disc. However, the resultant spectra were identical to those obtained from CDP and failed to show any peaks attributable to deuterium. This was probably due to exchange of water for D₂O in the fine grinding or pressing process. Unfortunately, other facilities for measuring the deuterium content, such as a single crystal infrared spectrometer, or neutron diffraction facilities, were not available.

Dielectric measurements (see Chapter 6) yielded a ferroelectric transition at a temperature of 246 ± 1 K which is well below the value of 267.5 K reported for the fully deuterated crystal (Levstik et al. 1975). In contrast to the dielectric measurements, the Raman spectra of CDDP samples synthesized in a similar manner but polished differently from the above, showed a transition temperature of 263 ± 1 K (Rumble 1983). Therefore, it is likely that despite the precautions taken, hydrogen contamination occurred either during the production of the crystals or during the subsequent grinding and polishing.

CHAPTER 4

EXPERIMENTAL DETAILS

4.1 THE MEASUREMENT OF ULTRASONIC PHASE VELOCITY

4.1.1 Introduction

The ultrasonic velocity has already been defined in Chapter 2 by the solution to the wave equation given by

$$u_i = A_i \sin(\omega t - k_j x_j) \quad (2.7)$$

where $V = \omega |k|^{-1}$.

In principle the experimental arrangement for measuring this velocity was straightforward (Figure 4.1). A 10 MHz quartz transducer was bonded to one end of the specimen and excited by a short (1.5-5.0 microsecond) burst of radio frequency (r.f.) waves. The echoes were detected by either the exciting transducer or by a second transducer bonded to the opposite face. The signal from the detecting transducer was amplified and displayed on an oscilloscope (see Figure 4.2). The round trip travel time, τ , is measured by the time delay T between successive echoes (the relationship between τ and T is discussed in section 4.1.2) and, if the length between the opposite faces of the specimen is L , the ultrasonic velocity is given by

$$V = 2L/\tau \quad (4.1).$$

The measurement of phase velocity, then, depends on accurately measuring the delay time between echoes.

There were two distinct objectives associated with the velocity measurement. On the one hand, for the determination of the elastic constants of CDP, absolute accuracy was required. Because the relationships between the elastic constants and the measured velocities are, in general, very complex (see Chapter 5), relatively small errors

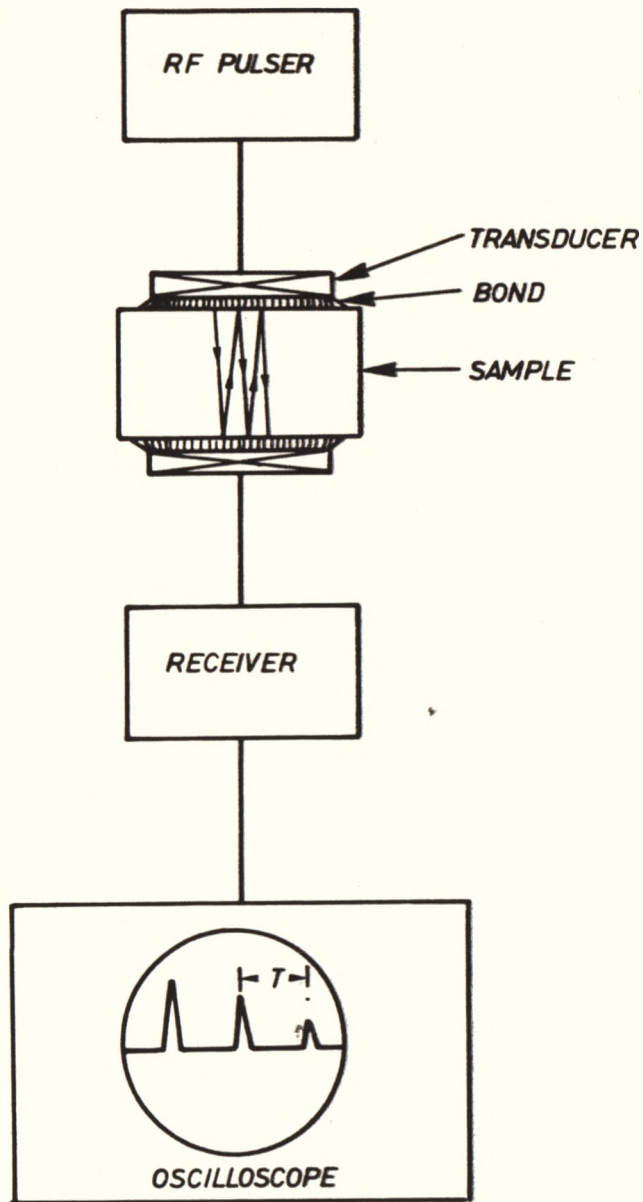
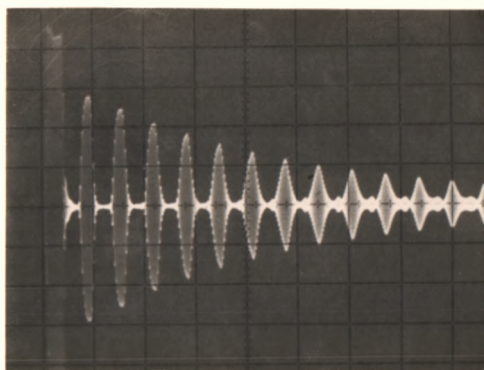
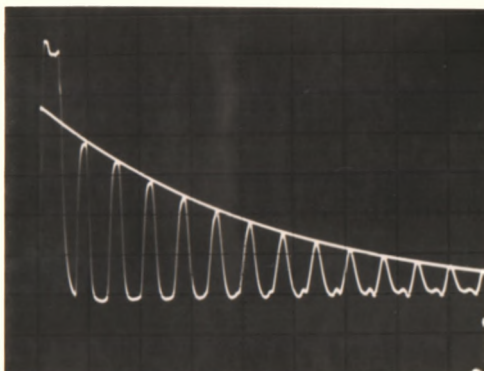


Figure 4.1. The Essential Features of a Pulsed System for the Determination of the Phase Velocity. T is a measure of the round trip delay time in the specimen, and hence the phase velocity is given by $2L/T$, where L is the path length between the opposite faces of the specimen.

(a)



(b)



(c)

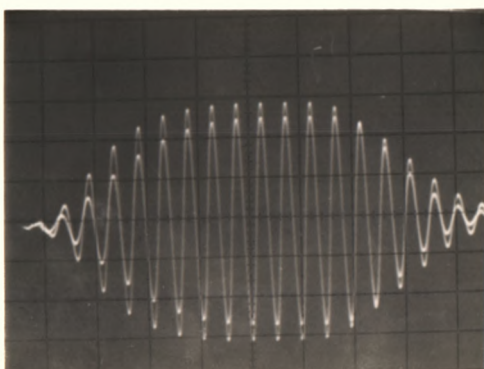


Figure 4.2. A Typical Echo Train for Longitudinal Propagation in CDP.

(a) The amplified echo train showing the r.f. cycles in each echo. The distorted pulse on the left of the trace is due to receiver saturation following receipt of the incident high power pulse.

Horizontal scale: 5 μ s/division, Vertical scale: 5 V/division.

(b) The detected and filtered echo train together with a superimposed exponential decay curve (see section 4.2.2(a)).

Horizontal scale: 5 μ s/division, Vertical scale: 1 V/division.

(c) Overlapped echoes showing the correct r.f. cycle-for-cycle match.

Horizontal scale: 0.2 μ s/division, Vertical scale: 5 V/division.

in the velocity measurement lead to large errors in the determined elastic constants.

In practice it was found that the calculation of the elastic constant matrix could proceed successfully if the velocities were measured to an accuracy of about 1%. However, even this small error in velocity measurement led to errors of the order of 50% in some of the off-diagonal constants. Thus it was important to measure the velocities as accurately as possible. Absolute accuracies of 0.2% were obtained for some modes, whereas in the worst case the errors amounted to 1.3%.

On the other hand, the examination of the ferroelectric transition required very small changes in the velocity ($< 1\%$) to be measured as a function of temperature. For these velocity measurements, the sensitivity of the technique was much more important than the absolute accuracy. In order to monitor the velocity dependence close to T_c , precision in the measurement of better than 0.05% was required.

The delay time, T , may be crudely measured from the time base of the oscilloscope to a precision of 2% at best. Even using pulses from a time mark generator the maximum precision achievable is 0.1%. Therefore, these methods were unsuitable for the requirements of this study, particularly for the temperature dependence measurements.

Various methods have been described for accurate and precise determination of delay times (Papadakis 1973, 1976). Of these, the Pulse Echo Overlap (P.E.O.) method used in this study is reported to be capable of achieving precision of 0.025% or better and accuracies of 0.4% in the determination of a delay time of 4 microseconds at 10 MHz (Papadakis 1976).

4.1.2 The Pulse Echo Overlap Method

(a) Principle of operation

The principle of measurement of delay times using the Pulse Echo Overlap (P.E.O.) method is to arrange the two signals of interest (usually individual r.f. cycles of the echoes under study) so that they overlap on the oscilloscope by triggering the time base with a signal, the period of which is equal to the delay time between the echoes. In this way the measurement of T was accomplished to within a small fraction of the period of one r.f. cycle. Although the determination of the correct position for overlap was somewhat operator dependent, precision of 1/100 of the period of the ultrasonic frequency was attainable. This represented a precision of 1 nsec for 10 MHz waves, or, typically, an error of 250 ppm for a 4 microsecond delay time. An example of cyclic overlap is shown in Figure 4.2(c).

(b) Implementation and circuitry

The essential elements of the P.E.O. system employed are shown in Figures 4.3 and 4.4. The continuous sine wave (csw) generator phase synchronized all the elements of the system and allowed for jitter-free overlap. The output from this generator was divided by an integer (20,50,200,500,2000,5000) to provide a square wave trigger (output B in Figures 4.3 and 4.4) for the pulsed r.f. oscillator. The integer divisor was chosen to be large enough to ensure that all echoes from one pulse died out before the next pulse was applied. The pulsed oscillator produced a burst of r.f. that maintained a constant phase relationship with the trigger pulse. This property was essential for jitter-free operation. (By comparison, a gated amplifier with a csw source was found to be unsatisfactory because the constant phase relationship was not maintained.) Before being applied to the exciting transducer, the r.f.

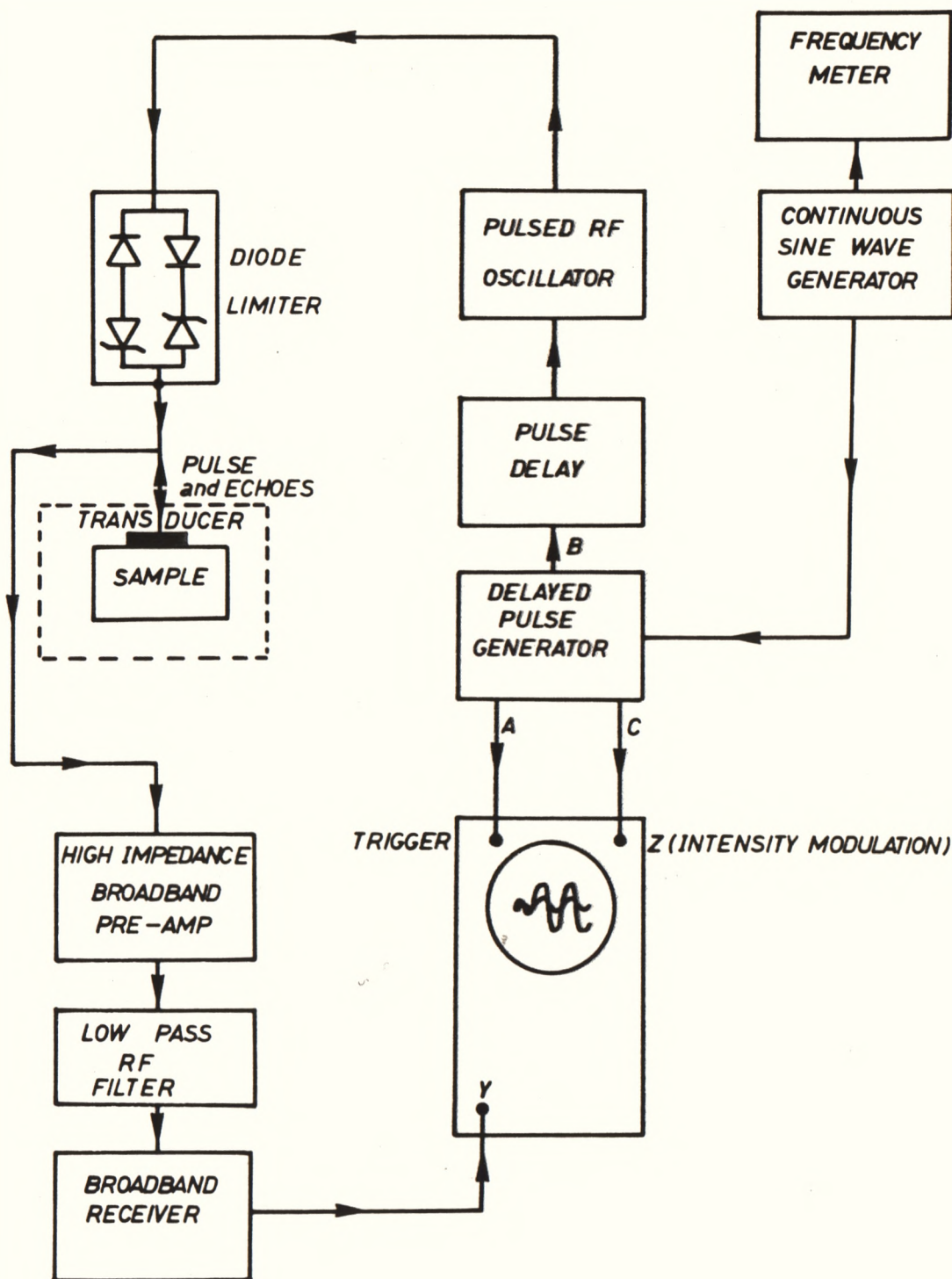


Figure 4.3. Block Diagram for the P.E.O. Method of Velocity Measurement. The sample assembly (shown enclosed by a broken line) may be situated in a cryostat, furnace, or room temperature rig. The outputs A, B, and C from the delayed pulse generator are detailed in Figure 4.4.

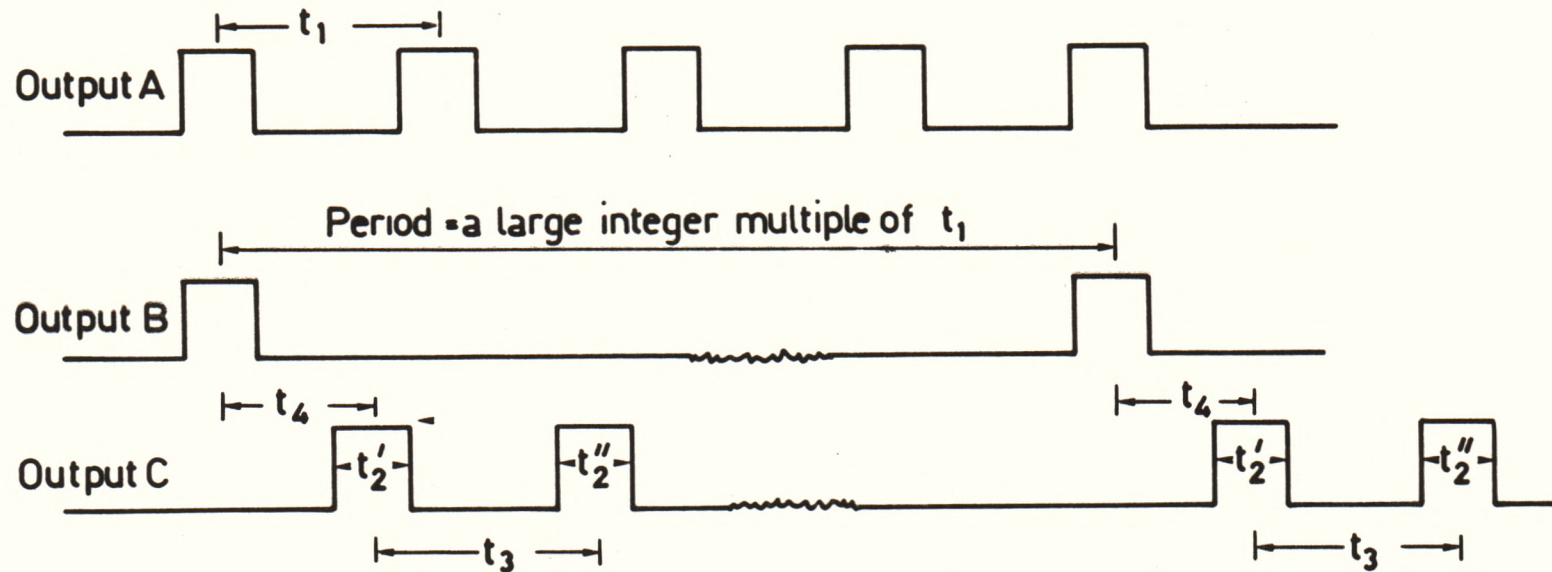


Figure 4.4. The Relationship between the Outputs A, B and C from the Delayed Pulse Generator shown in Figure 4.3. Outputs A, B, and C are synchronized by the continuous sine wave generator. Output C serves to intensity modulate the oscilloscope. t_2' , t_2'' , t_3 , and t_4 are all continuously variable to enable any echo to be chosen for study. Output B triggers the pulsed r.f. oscillator and output A is used to trigger the oscilloscope to produce the cycle-for-cycle overlap.

pulse passed through a diode limiter that allowed the large incident pulse through, but blocked the echoes from feeding back into the pulsed oscillator. The pulses used were 10 MHz, 50-100 volts peak to peak, and 1-5 microseconds in duration.

In order to eliminate the problem of receiver saturation and dead time following the large pulse, other authors (see Papadakis 1976) have found it necessary to use pulse limiters that prevented the large incident pulse, but not the echoes, from reaching the amplifier. Unfortunately, due to cost, such devices were not available for use in this study. An alternative option was to use a separate receiving transducer, bonded to the second parallel face of the specimen. This eliminated the recovery problem, but, in most cases, it was found that the disadvantages of the introduction of a second bond/transducer interface to the system (see below section (e) and Chapter 6) outweighed the problems due to receiver recovery following saturation by the incident pulse. The receiver network, which consisted of a high impedance broadband preamplifier, r.f. filter, and broadband receiver, generally had a fast enough recovery time (1-2 microseconds) to allow the echoes to be observed.

The broadband receiver was capable of displaying either the detected echoes or the individual r.f. cycles on the oscilloscope.

Corresponding to each trigger pulse to the pulsed r.f. oscillator, the delayed pulse generator provided two pulses (output C in Figures 4.3 and 4.4) that were used to intensity modulate the two echoes chosen for study. The lengths of these two pulses, their delay times with respect to each other and with respect to the trigger pulse to the pulsed r.f. oscillator were continuously variable so that any two echoes in the trace could be selected for study. The delayed pulse generator also provided a square wave of 1/10 the frequency of the csw input (output A

in Figures 4.3 and 4.4). This signal was used to trigger the oscilloscope to produce the overlap pattern.

(c) Procedure

To use the P.E.O. method, the echo train was first displayed on the oscilloscope. The frequency of the csw source was adjusted so that the period of the trigger pulse (output A in Figures 4.3 and 4.4) was approximately equal to the delay time between the echoes of interest. Any integer dividend of this period could be used, up to the maximum frequency range of the csw oscillator and pulse delay box. The intensity modulation was then adjusted so that the intensity of the two echoes of interest was increased. The overall intensity was then decreased so that only two echoes remained visible on the trace. The oscilloscope was switched to trigger from output A (Figures 4.3 and 4.4). Thus, the oscilloscope triggered for the first echo of interest and again for the corresponding following echo under study, which resulted in an overlap of the two echoes in oscilloscope time. In this mode the oscilloscope triggered many times between echo trains but the overlap pattern was undisturbed by the other echoes since the trace of an echo only appeared on the oscilloscope if its intensity had been modulated.

The csw frequency was adjusted until the two echoes overlapped r.f. cycle for r.f. cycle. The reciprocal of this frequency, multiplied by the appropriate integer scaling factors, was the delay time between the echoes of interest.

In many instances the overlap pattern was not centred on the oscilloscope screen. In such cases an additional pulse delay (shown in Figure 4.3) was used to alter the delay time between the trigger pulse to the oscilloscope and the emission of the r.f. pulse. This extra adjustment was sufficient to enable examination of any section of the

overlap pattern.

(d) Correct overlap condition

The P.E.O. technique does not produce one unique overlap condition but several, displaced from one another by an integral number of r.f. cycles. Incorrect matching of the r.f. cycles can lead to substantial errors, because the measured delay time between echoes, T , is related to the true round trip travel time, τ , by the equation (McSkimin 1961)

$$T = p\tau - p\gamma/360f + n/f \quad (4.2)$$

where p is the number of round trips between the echoes chosen for study, γ is the phase shift in degrees of the r.f. pulse on reflection from the specimen-bond-transducer interface, f is the radio frequency and n is the number of cycles of mismatch. For example, for 10 MHz waves a mismatch of one r.f. cycle would lead to an error of 0.1 microseconds, or 2.5% for a typical round trip travel time of 4 microseconds. Mismatch was the predominant factor which determined the accuracy of the P.E.O. method. The correction due to the bond (corresponding to the second term on the right hand side of equation (4.2)) and diffraction corrections were much smaller than the mismatch error. The precision of the P.E.O. method is not affected by cyclic mismatch, provided that the same overlap condition is maintained throughout a series of measurements.

McSkimin and Andreatch (1962) and later Papadakis (1967) have developed a criterion for determining the correct cycle-for-cycle match (i.e. $n=0$) and hence eliminating this major source of error. A brief summary of the method is presented below but for further details the reader is referred to the review article by Papadakis (1976).

It can be shown that the shift in the phase of the r.f. pulse introduced on reflection at the interface between the sample and bond is given by γ where

$$\tan \gamma = \frac{-2 Z_e Z_s}{(Z_s^2 - Z_e^2)} \quad (4.3)$$

and where Z_s is the acoustic impedance (density x velocity) of the sample, and Z_e is given by

$$Z_e = \frac{Z_1 [(Z_1/Z_2) \tan B_1 L_1 + \tan B_2 L_2]}{[(Z_1/Z_2) - \tan B_1 L_1 \tan B_2 L_2]} \quad (4.4)$$

where the subscripts 1 and 2 refer to the bond and transducer respectively, L is the thickness, and $B = 2\pi f/V$ is the propagation constant.

For the resonant frequency, f_R , of the transducer, L_2 is equal to one half a wavelength, and $B_2 L_2 = \pi$ rad. If the acoustic impedance of the bond, sample, and transducer are known, the only remaining variable is the bond thickness. Thus the phase shift, γ , may be calculated and plotted versus $B_1 L_1$ for various frequencies and various values of sample impedance. For example, Figure 4.5 shows a calculation of γ versus equivalent thickness of the bonding layer expressed in terms of degrees of phase ($B_1 L_1$) for a bond of Dow Corning 276-V9 resin. The calculation was also made for materials of different acoustic impedance (Z_s) at the resonant frequency of the X-cut quartz transducer and at a frequency 10% lower.

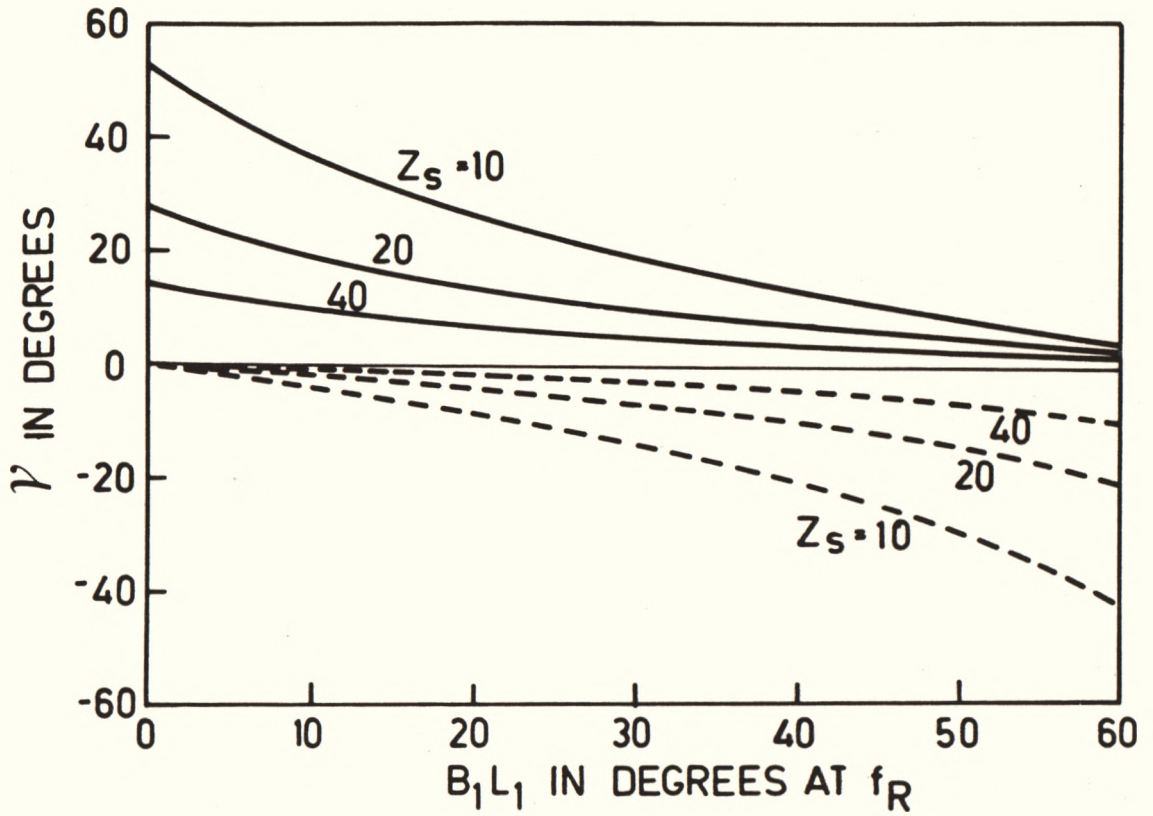


Figure 4.5. Phase Shift as a function of $B_1 L_1$. The calculations have been made for a X-cut quartz transducer ($Z_2 = 15.3 \times 10^5 \text{ g cm}^{-2} \text{ s}^{-1}$) and a bond of Dow Corning 276-V9 resin ($Z_1 = 2.25 \times 10^5 \text{ g cm}^{-2} \text{ s}^{-1}$). The sample impedances (Z_s) are in units of $10^5 \text{ g cm}^{-2} \text{ s}^{-1}$. The broken lines refer to operation at the resonant frequency of the transducer, whilst the solid lines refer to operation at a frequency 10% lower.

If T is measured at the resonant frequency, T_R , and at a frequency 10% lower, T_L , then from equation (4.2), the difference between these two measured travel times is given by,

$$\Delta T = T_L - T_R = \frac{1}{f_L} (n - p\gamma_L/360) - \frac{1}{f_R} (n - p\gamma_R/360) \quad (4.5).$$

ΔT values may be calculated as a function of B_1L_1 using equations (4.3)-(4.5). Typically, longitudinal wave velocities in CDP are of the order of $3 \times 10^3 \text{ m s}^{-1}$, and the density is known to be 3.22 g cm^{-3} (section 5.1.2), so that the impedance of CDP is about $10 \times 10^5 \text{ g cm}^{-2} \text{ s}^{-1}$ for longitudinal waves. Figure 4.6 shows a plot of ΔT versus B_1L_1 for various overlap conditions (including the correct one at $n=0$) for this value of sample impedance.

Equation (4.5) provided the basis for determining the correct overlap condition. The procedure was first to produce a plausible overlap condition on the oscilloscope screen (with each cycle of the second echo smaller than the first due to attenuation) and to measure the delay time, T_R , with the transducer being excited at the resonant frequency. The frequency was then reduced to 90% of the resonant value. The csw oscillator frequency was readjusted so as to realign the cycles in order to measure the delay time, T_L , and calculate ΔT . The whole procedure was repeated for several possible adjacent overlaps. The value of ΔT for each overlap was compared to the theoretical values calculated using equation (4.5). Although the actual bond thickness was unknown, thin film thicknesses typically lie in the range 3-25 microns. The wavelength of sound in the bond was of the order of 200 microns so that the bond thickness, expressed in terms of B_1L_1 , lay in the range 5° - 45° . Thus, as can be seen from Figure 4.6, the usual range for ΔT for the correct cyclic match (i.e. $n=0$) lies in the range $-0.014 < \Delta T < -0.0095$ microseconds. The overlap condition for which the measured ΔT value lay

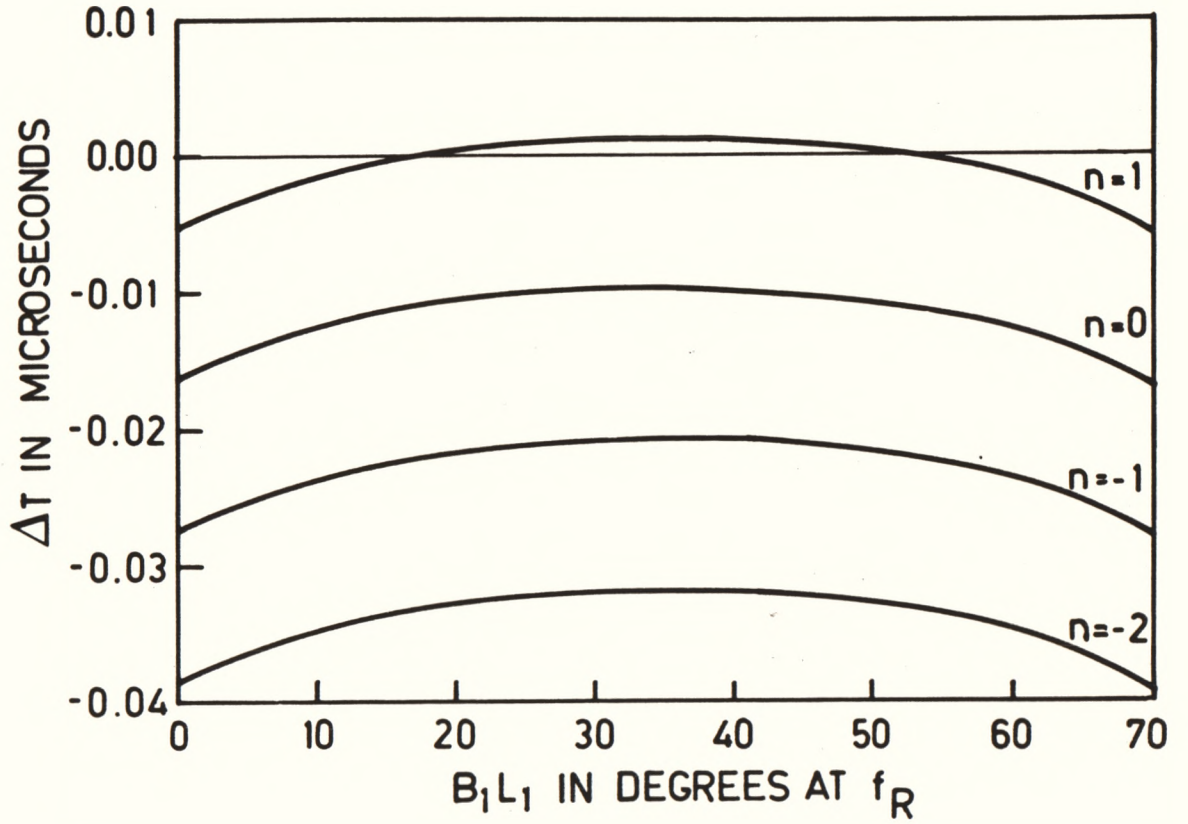
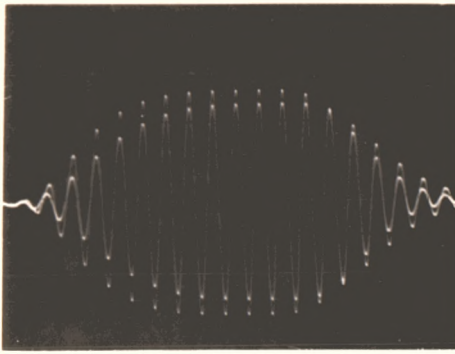


Figure 4.6. The Difference, ΔT , in the Delay Times Measured at 10 MHz and 9 MHz as a Function of $B_1 L_1$. The transducer and bond details are as in Figure 4.5. The calculation has been performed for a sample impedance of $10 \times 10^5 \text{ g cm}^{-2} \text{ s}^{-1}$, which is a typical value for CDP.

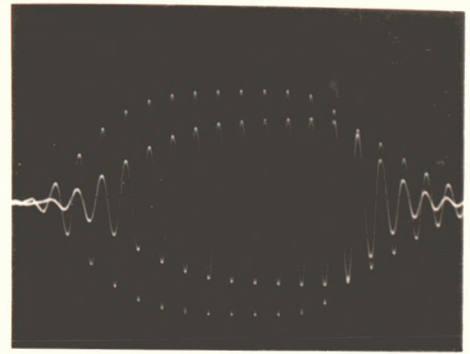
in this range was therefore taken as the correct cycle-for-cycle match. Ignoring the very small corrections due to the bond and to the diffraction of the beam, the true round trip travel time is given by $\tau = T_0/p$ where T_0 is the delay time for the $n=0$ condition.

It is important to note that the correct overlap condition (i.e. the cyclic match for which ΔT lies in the correct range as explained above) does not correspond to an alignment of the leading edges of the echoes (see Figure 4.7). The phase advance on reflection due to the bond shifts the centre of gravity of the echoes towards later arrival times. It is for this reason that the McSkimin ΔT technique is necessary to determine the correct cyclic overlap condition. Aligning the leading edges would have been an incorrect procedure for P.E.O. as it would have been equivalent to choosing $\Delta T=0$ instead of $n=0$ in equation (4.5). The error which would have resulted from aligning the leading edges, instead of using the correct procedure of examining the ΔT values, could have amounted to many cycles of overlap, because CDP has a small value of acoustic impedance leading to quite large phase shifts on reflection at the bond.

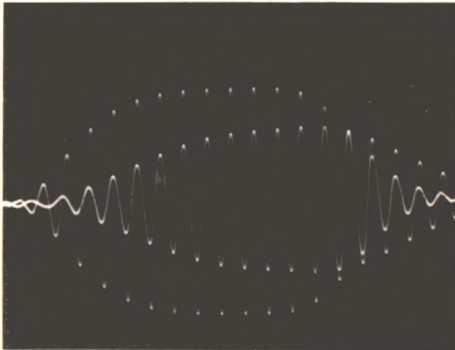
The application of the McSkimin technique to measurements on CDP was only partially successful in achieving the correct cyclic matching condition. Whereas the authors of the technique applied it to homogeneous samples such as fused silica, which gave excellent echo trains, not only did the CDP samples contain defects which resulted in poor echo train quality, but the inherent monoclinic symmetry of the system also gave rise to mixed modes which produced an echo train composed of a superposition of separate modes, each with a different velocity. In these cases the determination of the correct overlap condition was difficult and an ambiguity of one r.f. cycle could not be avoided. The true round trip travel time was then taken to be the



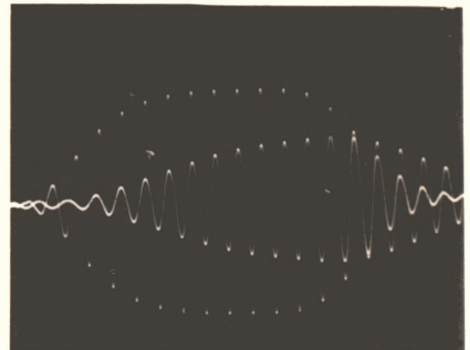
1 and 2



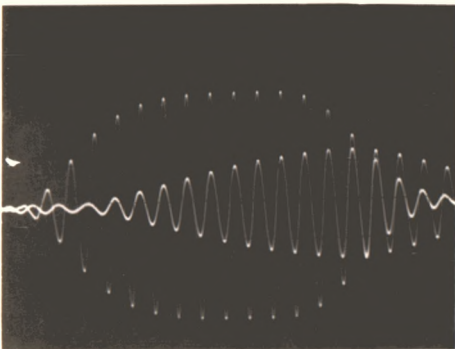
1 and 3



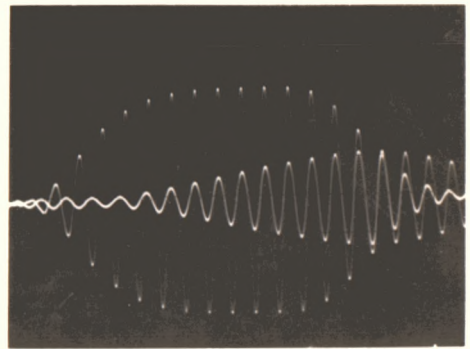
1 and 4



1 and 5



1 and 6



1 and 7

Figure 4.7. Oscilloscope Traces Showing the Proper Overlap Condition for Different Pairs of Echoes. The centre of gravity of the echoes shifts towards later arrival times due to the phase shift on reflection at the sample-bond-transducer interface. Note that aligning the leading edges would have resulted in a large error of many cycles of mismatch in the measurement of the delay time.

average of the delay times measured by the two possible overlap conditions. The resultant error was of the order of 1%. However, even in these cases the McSkimin technique was valuable because it reduced the number of possible overlap conditions from 3 or 4 to only 2, thus reducing the error from 3 or 4% to 1%.

(e) Bonding considerations

For the room temperature measurements Dow Corning 276-V9 resin (a thick, very viscous alpha methyl styrene fluid) was a satisfactory bonding agent, which provided sufficient acoustic coupling for both longitudinal and transverse waves. Less viscous bonding agents, such as silicon greases, whilst satisfactory for longitudinal waves, lacked sufficient acoustic coupling for the transverse waves. The 276-V9 resin has the important advantage over solid bonds (such as salol) that the crystal may be rotated in situ with respect to the transverse transducer to allow the excitation of each of the two transverse modes separately. This is essential in the case of a monoclinic system, because for some propagation directions, the polarization of the transverse mode, with respect to the crystal axes, is a function of the elastic constants which are yet to be determined.

The echo train quality, and hence the ability to determine the correct echo for overlap, was also very dependent on bond quality. In general, the thinner the bond the better the quality of the echo train. Other authors (e.g. McSkimin and Andreatch 1962) have reported that a thin bond may be produced by heating the bonding material to about 60°C and allowing it to set under slight pressure so as to squeeze out excess material. Unfortunately, in the case of CDP the heating process cleaved or otherwise damaged the crystal. The procedure adopted was to warm the resin slightly, up to about 35°C, in order to allow it to flow more

freely before applying it to the transducer. The sample-bond-transducer system was then subjected to moderate spring pressure. The echo train quality improved dramatically as a function of time and the best quality was achieved after 6-24 hours. Apparently, the application of pressure for relatively long periods of time replaced heating the resin as a means of squeezing out excess material and producing a thin bond.

The introduction of a second receiving transducer bonded to the opposite face degraded the echo train quality, increased the attenuation and made the determination of the correct echo for overlap less certain because it was not possible to ensure the same thickness for both bonds. However, in some special cases, for excellent defect-free samples which gave very good quality echo trains with one transducer, it was possible to observe a doubling of the measured value of ΔT for the correct overlap when a second transducer was bonded to the opposite face. The introduction of two, instead of one, phase advances on reflection resulted in a doubling of ΔT only for the correct overlap condition because for all other (mismatched) overlaps ΔT is also a function of n/f (see equation (4.5)). This result, whilst confined to some special cases, confirmed that the McSkimin criterion was effective in determining the correct echo for overlap and hence avoiding (or at least minimizing) mismatch error. To the best of the author's knowledge, this observation has not been previously reported.

The bonding requirements for velocity measurements as a function of temperature are quite different from those discussed above, and their discussion is left until Chapter 6.

4.1.3 Sample Limitations On Accuracy

In some instances, especially for off-diagonal measurements, the available samples had short path lengths (3-4mm), which reduced the

accuracy in two ways. Firstly, with a shorter path length, the travel time is shorter and hence the error in the determined velocity is larger. Secondly, the small delay time required a reduction in the incident pulse length in order to avoid the echoes interfering with one another. In this case fewer r.f cycles were available in each echo to form the overlap pattern on the oscilloscope. For example, for a mode with a velocity of $3 \times 10^3 \text{ m s}^{-1}$, the round trip travel time in a 3.0 mm sample is 2.0 microseconds. Since some broadening of the pulse always occurs as the echoes travel back and forth through the specimen, the longest pulse that can be used without the echoes interfering with one another is about 1.5 microseconds. For 10 MHz waves, this pulse contains 15 r.f. cycles, but since the rise and fall times are both a minimum of 3 cycles, only 9 cycles at best are available for overlap. However, in the correct overlap condition the leading edges are not aligned, so that even fewer cycles can be overlapped. Whilst this small number of cycles was often just sufficient for overlap at the resonant frequency, the extra distortion introduced when the frequency was reduced to 90% of the resonant frequency of the transducer made the determination of ΔT difficult.

The macroscopic growth defects, as well as degrading echo train quality, also introduced differences in the measured velocity between specimens and even between different portions of the same sample. For optical quality fused quartz the variability due to inhomogeneity has been reported (Papadakis 1967) to be as high as 0.036% for path lengths of about 2.5 cms. This error would be 0.18% for the typical path lengths of 5 mm of CDP samples used in this study. Thus, for those modes for which it is possible to determine the correct echo for overlap, it is unlikely that the absolute accuracy of the measurement is better than 0.2%. This error may be reduced by averaging over a large number of

samples, but in view of the other factors affecting the accuracy, and in view of the difficulty of sample preparation, this was not considered feasible.

Finally, it is worth noting that despite the bonding problems, small path lengths, growth defects, mixed modes due to monoclinic symmetry, and small values of acoustic impedance, the McSkimin technique is surprisingly successful in at least reducing the ambiguity in the overlap to one r.f. cycle.

4.2 ATTENUATION MEASUREMENTS

4.2.1 Introduction

Attenuation measurements provide information about the absorption and scattering processes occurring in the specimen. For a plane wave and an exponentially decaying echo train, the attenuation coefficient is given by (Truell et al. 1969)

$$\alpha = \frac{20 \log_{10}(A_1/A_2)}{(x_2 - x_1)} \quad (4.6).$$

in dB per unit length for amplitudes A_1 and A_2 sensed at positions x_1 and x_2 . If absolute accuracy is required, corrections due to beam spreading, non-parallelism of the opposite faces, and losses in the bond must be applied to equation (4.6) (Truell et al. 1969, Papadakis 1973). However, in this study, the attenuation was measured mainly as a function of temperature in the region of T_c , and hence sensitivity, rather than absolute accuracy, was required.

Three schemes, which are described below, were used to find the amplitude of the echoes, and hence determine the attenuation coefficient.

4.2.2 Methods Of Measurement

(a) Exponential delay generator

In this scheme (Chick et al. 1960) an electronically generated exponential decay curve was displayed together with the echo train on the oscilloscope trace (see Figure 4.2(b)). The exponential wave form was generated by rapidly charging a capacitor with the gating pulse of the r.f. burst which is synchronous with the trigger pulse to the pulsed oscillator (output B in Figure 4.3). The time constant was varied by adjusting R of the RC circuit. The resolution of this technique (1-2 dB)

was poor compared to the direct reading method described below, but it had the important advantage that any deviations of the echo train from exponential decay were immediately obvious. Thus the method allowed a visual indication of parallelism of the faces, sample homogeneity and especially bond quality, all of which can cause such deviations (Truell et al. 1969).

(b) Pulse comparator method

In this scheme (Roderick and Truell 1952) a pulse of the same frequency as that of the r.f. burst applied to the sample was fed into a calibrated attenuation box before being passed into the receiver and detector circuit. The comparator pulse was attenuated until its height matched the echo of interest on the oscilloscope screen. In order to avoid the comparator pulse interfering with the echoes a switching circuit was used which alternately triggered the pulsed r.f. oscillator and the pulse comparator, and thus the echoes and the comparison pulse were displayed on alternate sweeps of the oscilloscope. In this way a direct reading in decibels of the amplitude of each echo was obtained. Because both the echoes and comparator pulse were passed through the receiver system, errors due to non-linearity of the receiver-detector system were eliminated. However, measurements using this method were slow, and the precision of the measurement was limited to the smallest division of the calibrated attenuation box (1dB). Another disadvantage was that the method required committing a second pulsed oscillator to the measurement system.

(c) Direct reading

If the electronic components amplify and display the signals in a linear way, the heights of the echoes on the oscilloscope trace may be

measured and equation (4.6) applied directly to determine the attenuation. The Matec 625 receiver used in this study is claimed by the manufacturer to be linear to better than 0.2 dB for detector output levels from 4 volts to 100 millivolts (i.e. a 32 dB range). If this specification is true, the sensitivity of the measurement will only depend on the precision to which the height of a given echo can be measured on the oscilloscope screen. Using the graticule of the C.R.O. the best precision that could be obtained in the measurement of the echo amplitude was about 2%, which typically gave the attenuation to 1 dB. This was not sensitive enough to monitor some of the attenuation anomalies in the region of T_c and hence it was necessary to employ the following technique to improve the sensitivity of the measurement.

A square wave of period much longer than the time for the entire echo train to decay was input to the second channel of the C.R.O. and the oscilloscope switched so that the two inputs were added. This resulted in a "copy" of the original echo train being displayed on the trace, together with the "original" but displaced from it in the vertical direction by an amount proportional to the amplitude of the square wave. An example of the resultant pattern is shown in Figure 4.8. The amplitude of the square wave, which was monitored by a digital AC voltmeter, was varied until the top and bottom of the echo being measured just touch on the trace (see Figure 4.8), in which case the voltage read from the AC voltmeter was taken to be the amplitude of the echo. Precision of better than 0.1 dB has been obtained using this method for the measurement of the attenuation α between any two echoes.

It was found in all cases that the value of α determined by the pulse comparator method was consistent with the direct reading method to within the precision of the former. This confirmed that the receiver does indeed meet the manufacturer's specifications with regard to

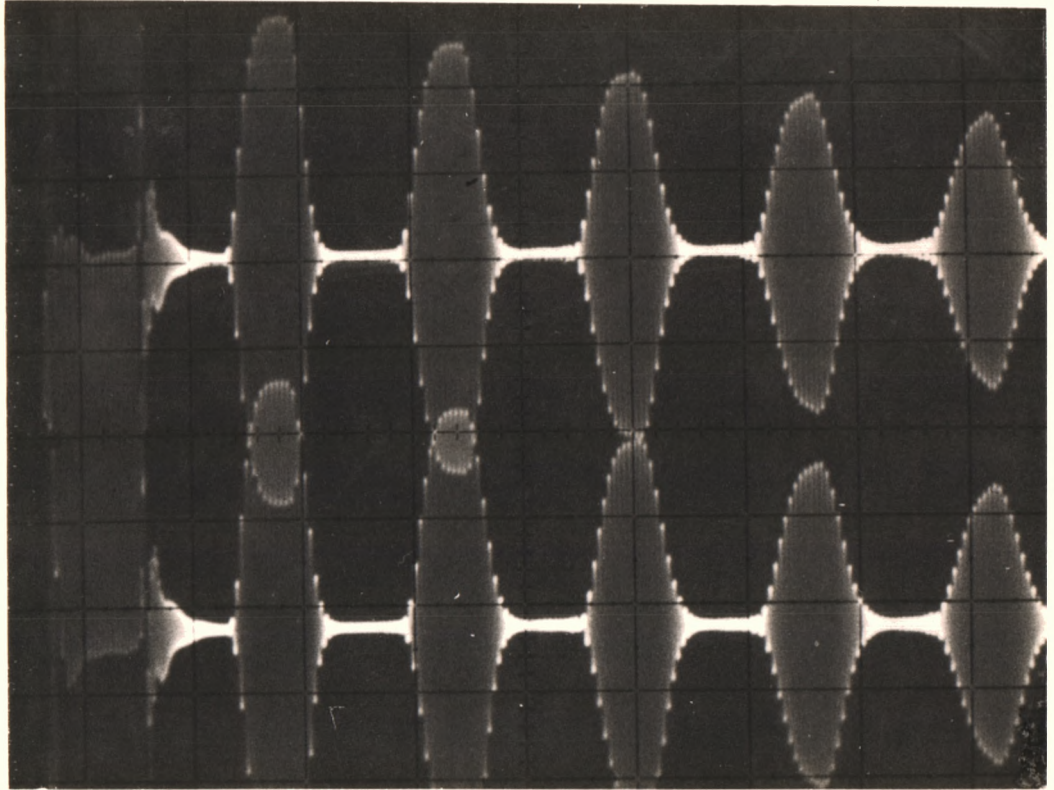


Figure 4.8. Oscilloscope Trace Showing the Direct Reading Method of Attenuation Measurement. The amplitude of the square wave has been adjusted until the top and bottom of the third echo from the right just touch. The amplitude of the square wave is then equal to the amplitude of this echo.

linearity. Since the direct reading method was found to be both more sensitive and faster than the pulse comparator method, the former was adopted for the measurement of attenuation as a function of temperature.

Since α was measured to a precision of 0.1 dB it was possible to detect small deviations of the echo train from exponential decay by repeating the measurement for different pairs of echoes. Even for echo trains that appeared to closely fit the electronically generated exponential decay curve (section (a) above) differences of up to 0.5 dB in the attenuation between different pairs of echoes were measured by the direct reading technique. In practice, especially for temperature dependent measurements, in which the quality of the bond was often a problem (see Chapter 6) and the echo train was not exponential, the procedure adopted was to monitor α for the same pair of echoes over the whole temperature range.

It was also observed that the amplitudes of the first few echoes were smaller than expected for exponential decay. This was associated with the dead time of the receiver following the large incident pulse. It was therefore desirable to avoid choosing the first few echoes to monitor α as a function of temperature. Unfortunately, due to the high attenuation at T_c this was not always possible and in these cases care had to be taken to optimize the circuit in order to minimize the recovery time.

4.3 EQUIPMENT

4.3.1 Overview

The circuitry necessary for velocity and attenuation measurements has been described above. The experimental layout is shown in Figure 4.9. The delayed pulse generator, exponential decay generator, thermometer power supply and temperature controller were all built in the Electronics Workshop of the Department of Physics at Monash University.

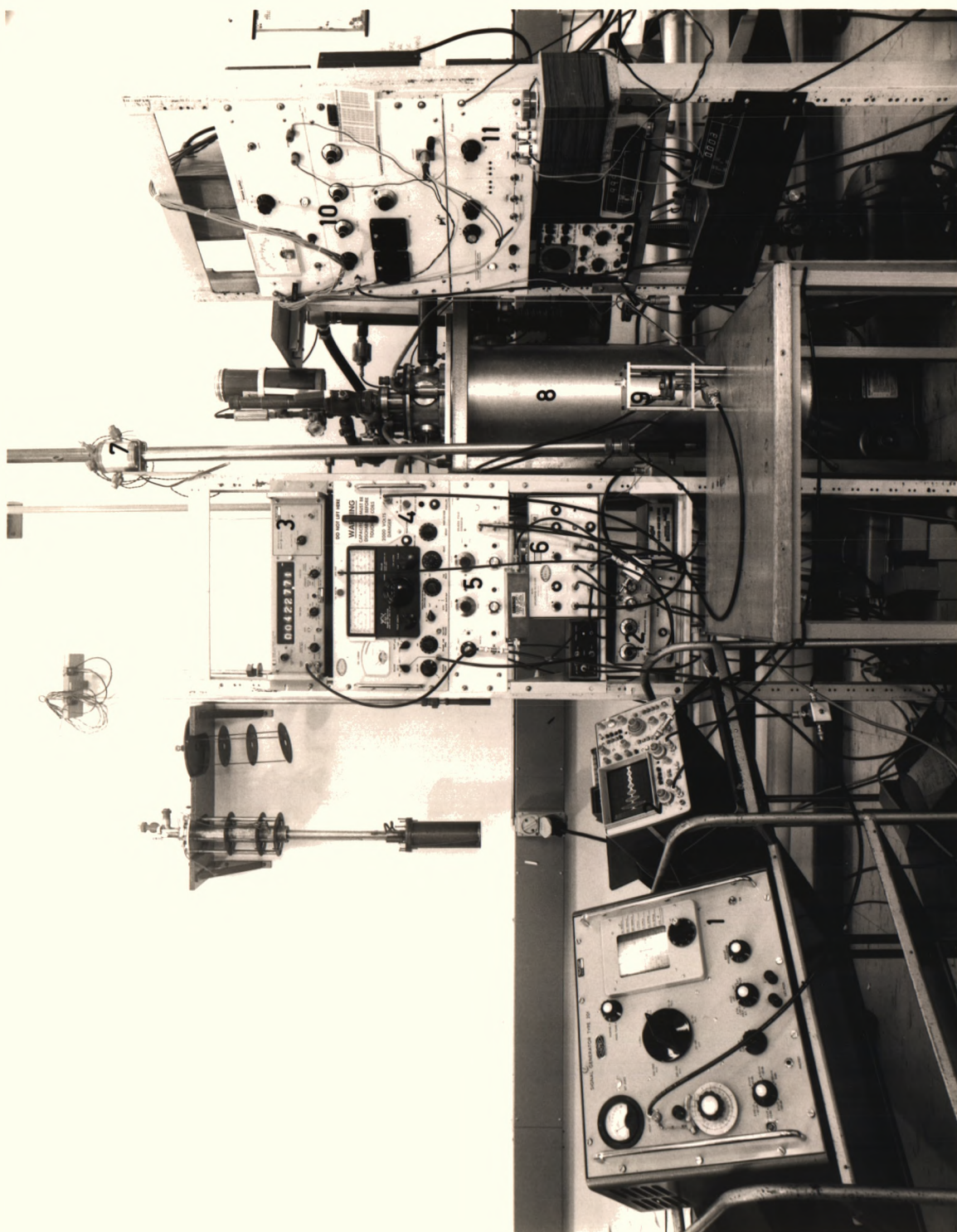
In the early part of this study a Tektronix 585A oscilloscope was used but this was later replaced by the Hewlett-Packard 100 MHz oscilloscope shown in Figure 4.9. The oscilloscope must have very stable external triggering in order to achieve jitter-free overlap in the P.E.O. technique. In this regard the Hewlett-Packard oscilloscope was found to be superior to comparable 100 MHz oscilloscopes manufactured by Tektronix and Philips.

4.3.2 Transducers

The transducers used to introduce the plane wave into the sample were fine ground discs of quartz 3.175mm (0.125") in diameter, with a nominal resonant frequency of 10 MHz, supplied by Valpey-Fisher Corporation, Hopkinton, Massachusetts. X-cut transducers were used to generate longitudinal waves, whilst Y-cut were used for transverse waves. The latter had a small portion of the edge removed which indicated the polarization direction.

For electrically conducting samples, the sample itself serves as the ground electrode for the transducer and it is only necessary to evaporate a gold electrode onto one side of the transducer. However for non-conducting samples, such as CDP, co-axially gold plated electrodes are necessary. In order to make firm electrical contact with both

Figure 4.9. Overview of Equipment used to Measure Ultrasonic Velocity and Attenuation. (1) Airmec type 201 continuous sine wave generator, (2) Hewlett-Packard 1746A oscilloscope (100 MHz), (3) Hewlett-Packard 5245L electronic counter, (4) Arulab PG-650C pulsed r.f. oscillator, (5) Delayed pulse generator, (6) Matec 625 broadband receiver, (7) Probe for low temperature ultrasonic measurements, (8) Cryostat, (9) Rig for room temperature ultrasonic measurements, (10) Temperature controller, (11) Thermometer power supply, (12) Pulse delay box and exponential decay generator.



electrodes of the transducer, the transducers were glued into the transducer holders shown in Figure 4.10 with a silver-loaded, two-part epoxy resin. These holders were then screwed into either the room temperature rig or low temperature probe (see below). In this way the sample could be rotated with respect to the fixed transducer, which was particularly useful when (a) a search was made for the most defect free path in the specimen to produce the best echo train, and (b) when rotating the specimen with respect to the Y-cut transducer in order to excite each one of the two possible transverse modes separately. The holders also protected the fragile transducers from breakage during handling and bonding to the specimen.

4.3.3 Room Temperature Measurements

The apparatus used to measure velocity at room temperature is shown in Figure 4.11. The transducer holder was screwed into the bottom plate (which formed the earth electrode) whilst the wire carrying the r.f. pulse was soldered to the central contact of the transducer holder. Pressure was applied to the bond via the weight of the top plate and the springs. A second transducer could be screwed into the top plate if two transducer measurements were required.

Unfortunately the laboratory in which this work was carried out was not air-conditioned and measurements were taken over an ambient temperature range of 16-26°C, although most of the measurements were performed in the range 18-24°C. The temperature dependence of the ultrasonic velocity in CDP at room temperature has been measured to be as large as $0.04\% \text{ K}^{-1}$ for some modes (see Chapter 6), so that an error of up to 0.4% in the velocity due to temperature fluctuations was possible. Because of the limitations on accuracy discussed in section 4.1, the size of the error due to fluctuations in the ambient

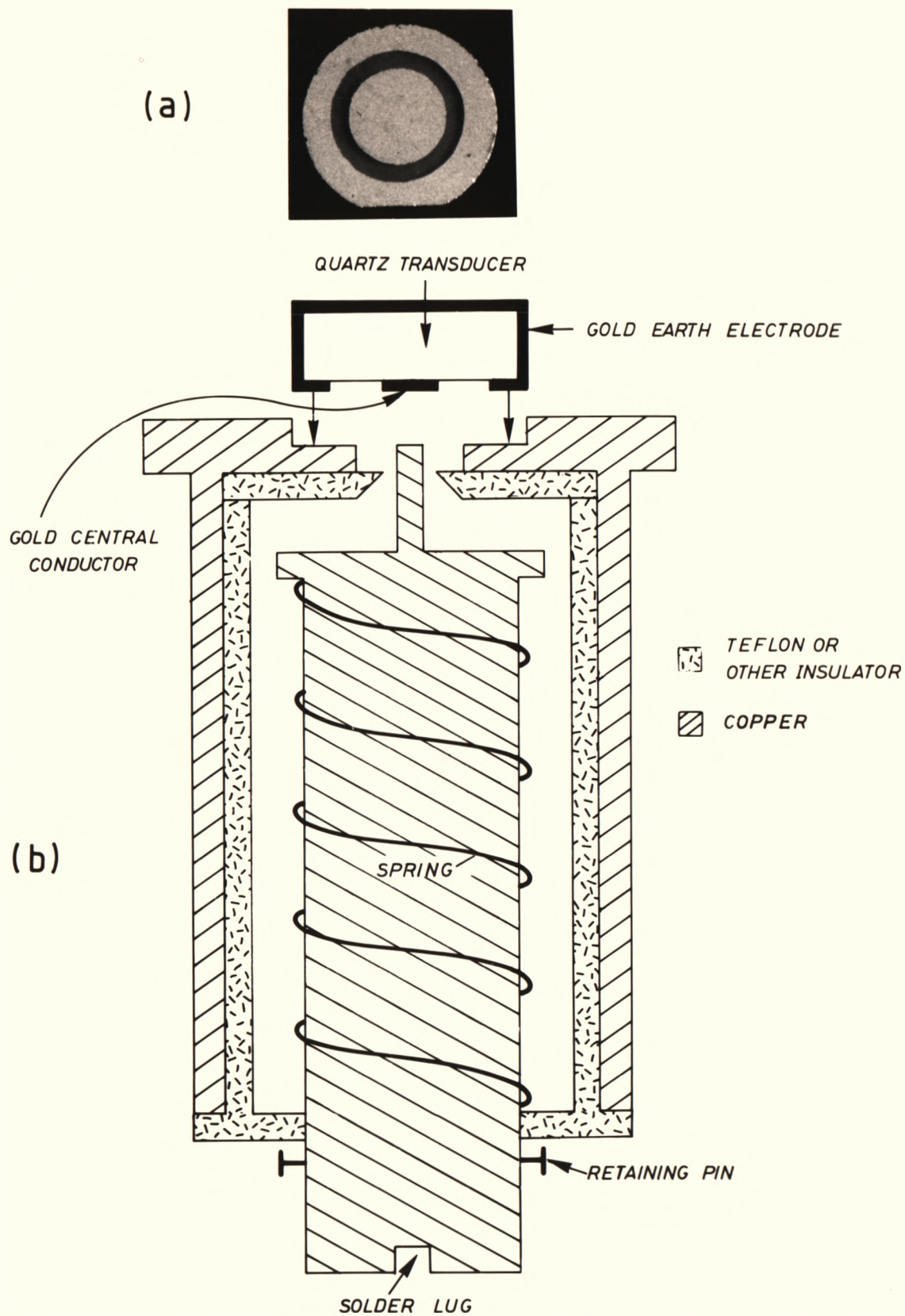
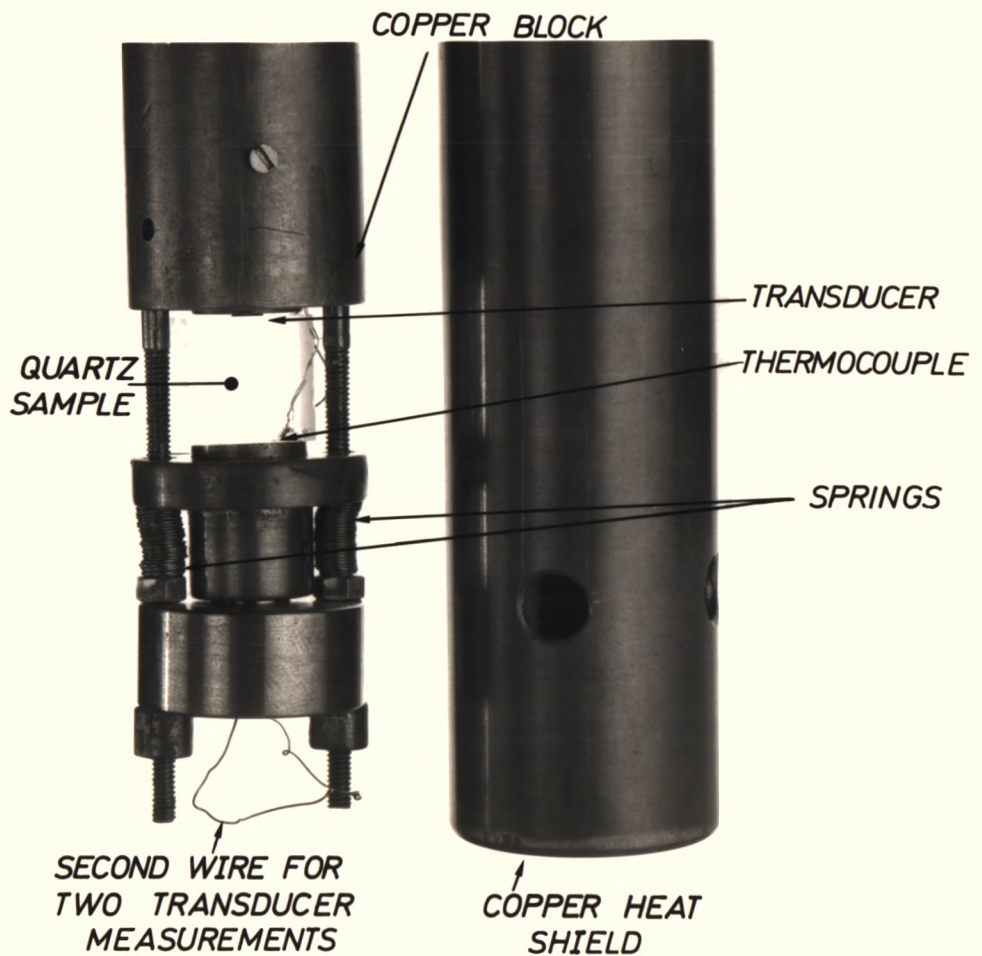
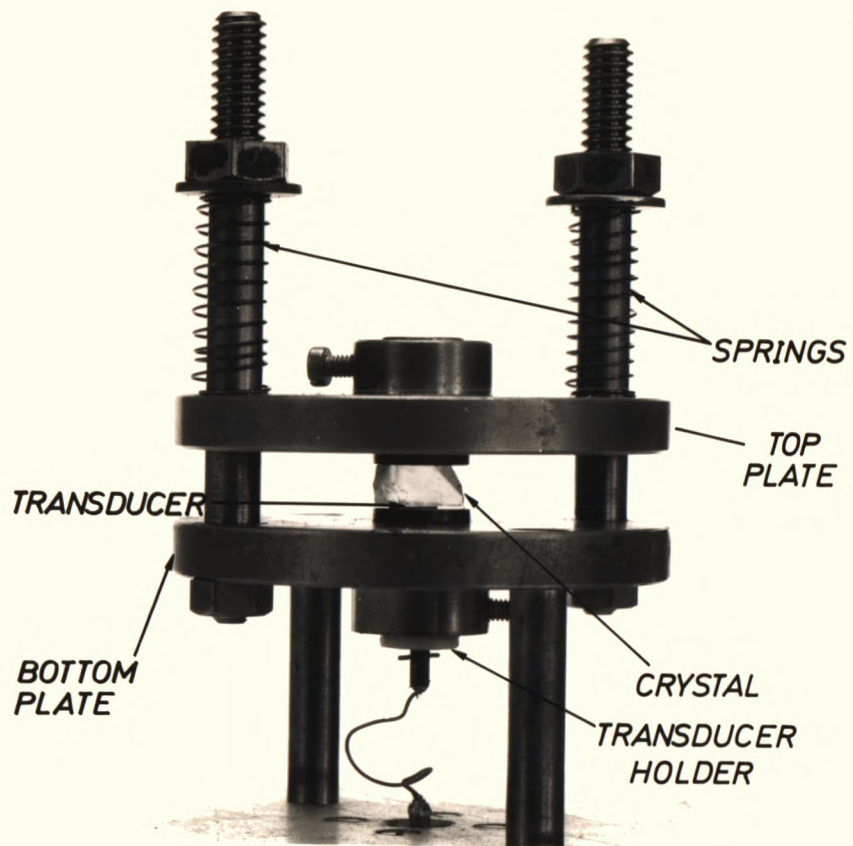


Figure 4.10. (a) Plan View of a Transverse (Y-cut) Co-axial Quartz Transducer. The polarization direction is orthogonal to the flat portion of the edge of the transducer. The diameter is 3.175 mm.

(b) Schematic Diagram of the Transducer Holder Designed to Make Firm Electrical Contact with the Electrodes of the Transducer.

**Figure 4.11. Apparatus for Room Temperature
Ultrasonic Velocity Measurements.**

**Figure 4.12. Sample Holding Assembly for Low
Temperature Ultrasonic Measurements.**



temperature did not justify the additional complexity involved in controlling the temperature of the sample. Temperature control of the laboratory environment to ± 1 °C could reduce this error to 0.08%, but if better accuracy than this is required an accurately temperature-controlled environment for the sample would be necessary.

4.3.4 Low Temperature Measurements

(a) Low Temperature Probe

The sample holding assembly of the low temperature probe is illustrated in Figure 4.12 together with the copper heat shield used to reduce temperature gradients in the sample. The transducer holder was screwed into the bottom of the copper block which also contained the thermometers and heater. If two transducer measurements were required the second transducer could be screwed into the bottom plate. The springs kept the bond under pressure. Transmission lines consisting of two co-axial stainless steel tubes 9mm and 2mm in diameter were used to carry the r.f. pulse from the BNC connectors at the top of the probe to the sample assembly, and to carry the echoes back to the receiver. A schematic of the probe is shown in Figure 4.13.

(b) Temperature control

The probe was inserted into a double-walled, vacuum-jacketed cryostat, using liquid nitrogen as the refrigerant. A schematic of the cryostat is shown in Figure 4.14. The sample space was filled with about 1 Torr of helium exchange gas. However, it was found that this pressure rose to about 10 Torr over the period of a run, presumably due to out-gassing of the material used to bond the transducer to the specimen. The cooling rate was slowed by maintaining a vacuum between the sample space and liquid nitrogen bath. In order to minimize temperature

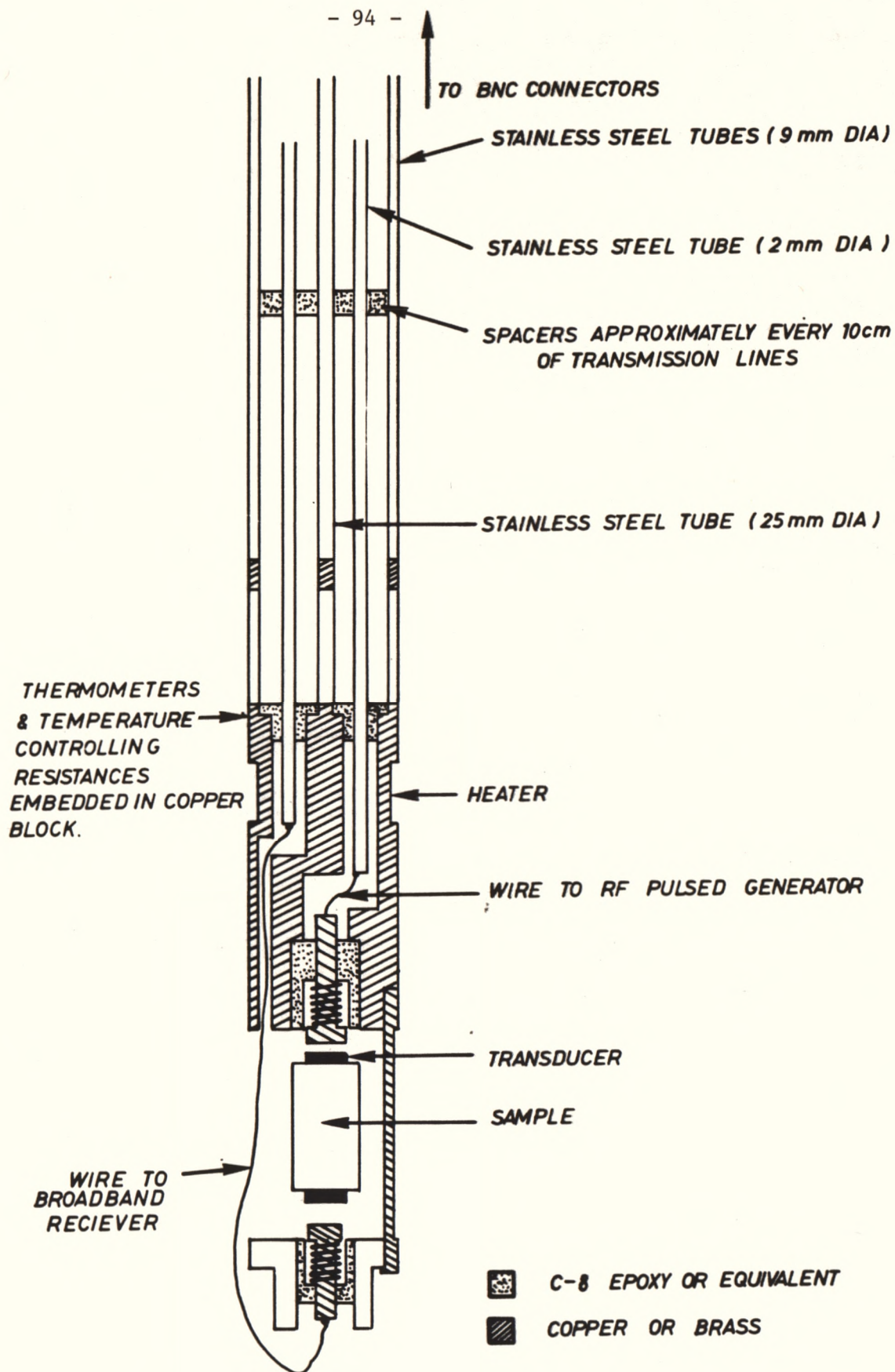


Figure 4.13. Schematic Diagram of Probe Used for Low Temperature Ultrasonic Measurements.

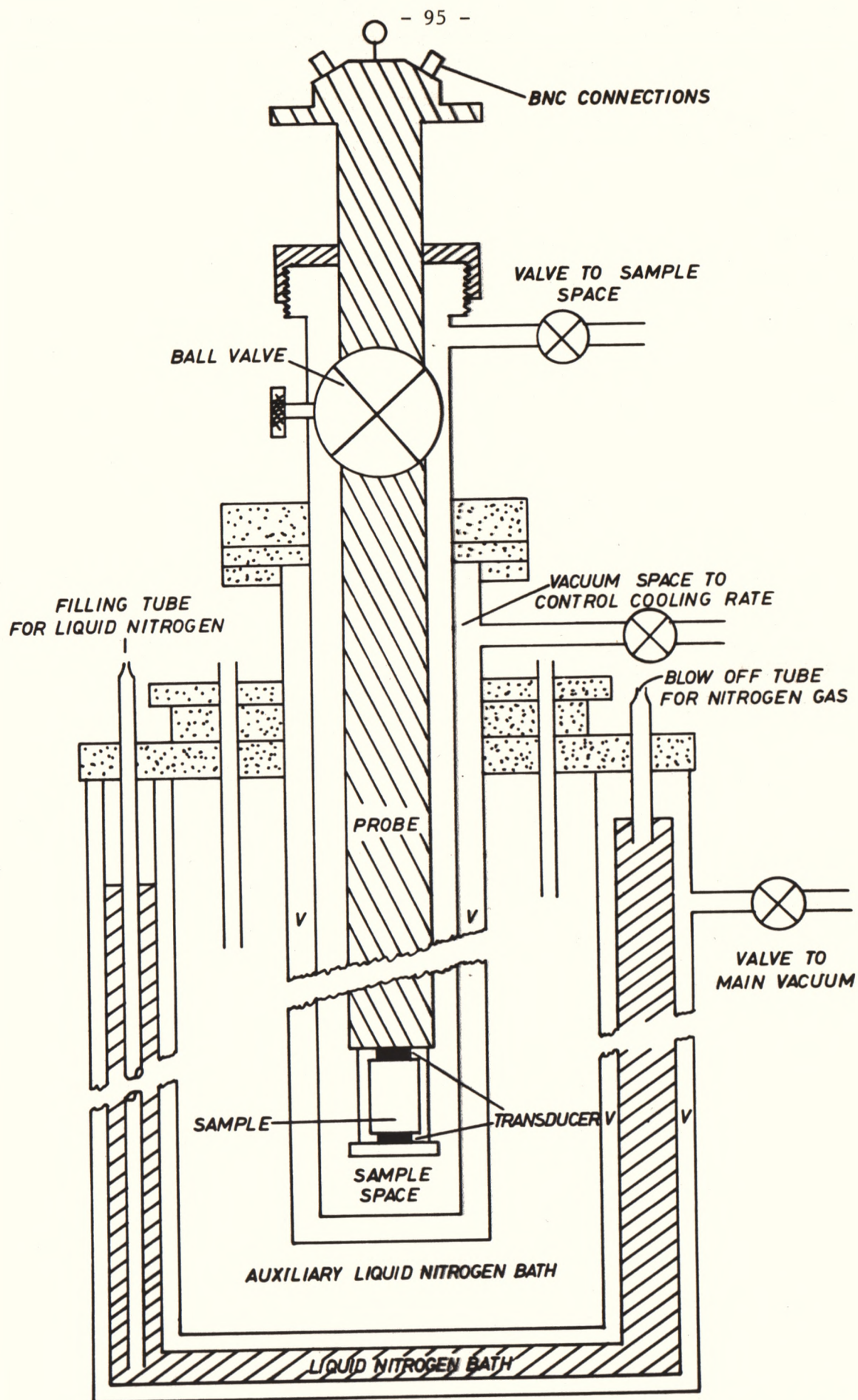


Figure 4.14. Schematic diagram of Cryostat used for Low Temperature Ultrasonic Measurements.

gradients along the length of the sample, a copper heat shield (shown in Figure 4.12) was used to enclose the sample holding arrangement.

The current to a 150 ohm heating wire wound around the copper block was controlled by a temperature controller designed by Pickup and Kemp (1969), using a platinum resistor embedded in the copper block as the temperature sensor. The set-point temperature could be increased in steps as small as 10-20 mK, and the temperature stability once the system had come to equilibrium was 5-10 mK.

(c) Thermometry

The temperature of the copper block was measured by a four terminal Rosemount platinum resistance thermometer, calibrated using a Z-function of the type described by Yet-Chong and Forrest (1968). A Au-0.07%Fe versus chromel thermocouple with reference to the ice point was used to measure the temperature of the bottom of the sample in order to check for temperature gradients and to monitor temperature stability. A two-point calibration procedure described by Cornelius (1982) was used.

In order to check the thermocouple calibration, measurements were taken with the thermocouple embedded in the copper block next to the platinum thermometer over the temperature range 90-300 K. Differences of up to 0.5 K were noted between the two temperature measuring devices. The discrepancy is probably caused by an inadequacy of the calibration procedure to take into account variation in the composition of commercially supplied Au-0.07%Fe thermocouple wire. As the Z-function calibration is accurate to within 0.1 K (Yet-Chong and Forrest 1968) the absolute accuracy of the thermocouple may be assumed to be 0.5 K.

The anomalies in velocity and attenuation at T_c are very sharp (see Chapter 6) and since it was desired to attempt to fit an analytical

function to these dependences it was necessary to measure temperature as precisely as possible. For the thermocouple, a 1 microvolt change in voltage (which was the typical limit of resolution of the Hewlett-Packard D.V.M. used in this study) corresponded to a 0.05 K change in temperature at about 120 K. In order to improve the resolution a variable voltage from a mercury battery was used to offset most of the thermocouple voltage and the remaining microvolts were amplified using a Keithley 140 Precision Nanovolt DC Amplifier and displayed on a chart recorder. Resolution of 0.2 microvolts (corresponding to 0.01 K) was then possible. This was particularly useful in ascertaining when the sample had come to thermal equilibrium following a small change in the set-point temperature close to T_c . A similar technique was applied to the platinum thermometer voltage output and resolution of the order of 1 mK was obtained.

The temperature gradient across the sample was monitored by the difference in the temperature reading between the thermocouple (attached to the bottom of the sample) and the platinum resistance thermometer (embedded in the copper block near the top of the sample). Temperature gradients of up to 0.9 K were recorded, although by carefully adjusting the exchange gas pressure and the cooling rate this could be reduced to 0.1 K. The measured difference proved to be remarkably constant over a wide temperature range, and hence the chief value in continuously monitoring the gradient was as an indication of the achievement of thermal equilibrium following a change in the set-point temperature.

(d) Experimental difficulties

Long thermal time constants:

Thirty to fifty minutes were required to achieve thermal equilibrium following a change in the set-point temperature. Hence many

weeks were required to complete a temperature run. The time consuming nature of the data collection severely limited the number of runs which could be attempted during the course of this study. As an illustration of the limitations that this long thermal time constant imposes, consider the measurement of the temperature dependence of all thirteen elastic constants of CDP. At least eighteen separate temperature runs must be performed (see Chapter 5) and if the current apparatus is employed this will require approximately two years of data collection! This unsatisfactory situation could be alleviated by either redesigning the sample holding assembly to reach thermal equilibrium much more rapidly, or by automating the measurement system to continuously monitor the velocity and attenuation.

Ambient temperature fluctuations:

Difficulties were encountered in ascertaining whether observed drifts in the monitored thermocouple and platinum thermometer voltages were due to genuine drifts in the sample temperature or to fluctuations in the ambient temperature of the laboratory environment. Fortunately, the resistance of platinum increases with increasing temperature whereas the thermocouple voltage decreases. Hence genuine sample temperature drift was characterized by the platinum thermometer and thermocouple voltages drifting in opposite directions. By contrast, drifts in the offset voltage of the mercury battery (which could be monitored independently using an appropriate DVM) caused drifts in the platinum thermometer and thermocouple voltages in the same direction. However, ambient temperature fluctuations also caused drifts in the constant current supply to the platinum thermometer, and, to a lesser extent, in the DC amplifiers. The effect of these drifts on the monitored platinum thermometer and thermocouple voltages was much more difficult to trace

than the effect of the drifting offset voltage. Therefore, on days of high ambient temperature fluctuations in the laboratory it was difficult to monitor temperature equilibrium. It is clear that an air-conditioned laboratory environment is necessary if future work is to be carried out on velocity and attenuation measurements close to T_c .

CHAPTER 5

THE ROOM TEMPERATURE ELASTIC BEHAVIOUR OF CDP

5.1 DETERMINATION OF THE ELASTIC CONSTANT MATRIX

The measurements of the ultrasonic phase velocities leading to a determination of the elastic constant matrix are presented in this chapter. As previously pointed out the elastic constants fully describe the elastic behaviour of a material so that once the matrix is determined it is possible to calculate a wide range of elastic properties such as the linear compressibility, Young's modulus, and the bulk modulus as well as constant phase and group velocity surfaces. It was found that these elastic properties reflect the chain and layer-like structure of CDP.

5.1.1 Velocity Measurements

The measured velocities are shown in Table 5.1. The wave displacement directions are approximate only, as in most instances the waves are not pure and their true displacement vectors can only be determined by calculation from the determined elastic constants. Nevertheless, experience has shown that most waves are predominantly either longitudinal or transverse in character and hence one may assume that the polarization of the exciting transducer (which is the basis for the approximate wave displacement directions given in Table 5.1) is a reasonable first approximation to the actual eigenvector.

The measurement of the velocity was repeated at least twice for each mode using different specimens. An exception to this was for propagation along $[011]'$ for which the measurement was repeated by repolishing the sample to reduce its path length and examining a

Table 5.1

Ultrasonic Sound Velocities in CsH_2PO_4

No.	Direction of Wave Propagation with respect to xyz axes	Approximate Wave Displacement Direction	Velocity (10^3 m s^{-1})	Type
V_1	100	100	$3.047 \pm .005$	Semi-Pure Longitudinal
V_2	100	010	$1.688 \pm .02$	Pure Transverse
V_3	100	001	$1.133 \pm .01$	Semi-Pure Transverse
V_4	010	010	$2.878 \pm .02$	Pure Longitudinal
V_5	010	100	$1.788 \pm .02$	Pure Transverse
V_6	010	001	$1.416 \pm .002$	Pure Transverse
V_7	001	001	$4.540 \pm .01$	Semi-Pure Longitudinal
V_8	001	010	$1.586 \pm .015$	Pure Transverse
V_9	001	100	$1.153 \pm .003$	Semi-Pure Transverse
V_{10}	0.520, 0, -0.854	0.520, 0, -0.854	$3.847 \pm .006$	Semi-Pure Longitudinal
V_{11}	0.520, 0, -0.854	010	$1.796 \pm .004$	Pure Transverse
V_{12}	0.520, 0, -0.854	0.854, 0, 0.520	$0.7605 \pm .006$	Semi-Pure Transverse
V_{13}	110	110	$2.982 \pm .006$	Quasi-Longitudinal
V_{14}	110	001	$1.683 \pm .003$	Quasi-Transverse
V_{15}	110	$\bar{1}10$	$1.307 \pm .013$	Quasi-Transverse
V_{16}	011	011	$3.622 \pm .08$	Quasi-Longitudinal
V_{17}	011	$0\bar{1}1$	$1.980 \pm .008$	Quasi-Transverse
V_{18}	011	100	$1.409 \pm .007$	Quasi-Transverse
V_{19}	0.252, 0.588, -0.769	0.252, 0.588, -0.769	$3.686 \pm .08$	Quasi-Longitudinal
V_{20}	0.252, 0.588, -0.769	Trans 1	$2.014 \pm .01$	Quasi-Transverse
V_{21}	0.252, 0.588, -0.769	Trans 2	$1.219 \pm .009$	Quasi-Transverse
V_{22}	0.698, 0, -0.716	0.698, 0, -0.716	$3.217 \pm .13$	Semi-Pure Longitudinal
V_{23}	0.698, 0, -0.716	010	$1.796 \pm .004$	Pure Transverse
V_{24}	0.698, 0, -0.716	0.716, 0, 0.698	unknown	Semi-Pure Transverse
V_{25}	0.925, 0, 0.395	0.925, 0, 0.395	$3.151 \pm .004$	Semi-Pure Longitudinal
V_{26}	0.925, 0, 0.395	010	$1.520 \pm .004$	Pure Transverse
V_{27}	0.925, 0, 0.395	0.395, 0, -0.925	$0.83 \pm .03$	Semi-Pure Transverse

The quoted errors in Table 5.1 reflect variations between measurements of the same mode on different specimens.

different section of the crystal. In general the consistency in the velocity between the different measurements was within ± 1 r.f. cycle ($\sim 1-2\%$). However, in some cases, particularly for semi-pure modes, the velocity data from different measurements of the same mode were consistent to between 0.2-0.6%. INSERT

5.1.2 Density Determination

The density used in the calculations was obtained by hydrostatic weighing in chloroform at 20°C and found to be $\rho = 3.22 \pm 0.04 \text{ g cm}^{-3}$ which corresponds well to the value given by Rashkovich et al. (1977) of $3.24 \pm 0.01 \text{ g cm}^{-3}$. The X-ray density, computed from the unit cell data given by Uesu and Kobayashi (1976) is 3.27 g cm^{-3} which also agrees well with the value of 3.22 g cm^{-3} .

5.1.3 Method of Calculation

(a) Pure modes

Direct, simple relationships between measured velocities and elastic constants are only possible for C_{22} , C_{66} and C_{44} . These constants are related to the velocities of the pure modes propagating along each of the Cartesian axes by the equations,

$$C_{22} = \rho V_4^2 = 26.67 \pm 0.37 \text{ GPa} \quad (5.1)$$

$$C_{66} = \rho V_2^2 = 9.17 \pm 0.22 \text{ GPa} \quad (5.2)$$

$$C_{44} = \rho V_8^2 = 8.10 \pm 0.15 \text{ GPa} \quad (5.3).$$

The quoted uncertainties include the errors in the velocity determination, but not the error in the density. This is because all the calculations could be performed in terms of C_{ij}/ρ , so that the density is, computationally speaking, merely a scaling factor for the elastic constant matrix.

For waves propagating along a direction in the xz plane, say $[l, o, n]'$, one mode is pure transverse. Its velocity is related to C_{46} by

$$C_{46} = \frac{\rho V_{11}^2 - l^2 C_{66} - n^2 C_{44}}{2nl} = -2.25 \pm 0.31 \text{ GPa} \quad (5.4).$$

The two pure transverse waves propagating along the b axis provide cross checks on the elastic constants thus far determined. The relationships are:

$$\rho V_5^2 + \rho V_6^2 = C_{44} + C_{66} \quad (5.5)$$

$$\text{and} \quad C_{46}^2 = C_{44} C_{66} - \rho V_5^2 \rho V_6^2 \quad (5.6).$$

On substituting the numerical values the left and right hand sides of (5.5) agree to within 3%, which is well within experimental error. The numerical agreement of the left and right hand sides of (5.6) is 24%, which, although much larger than for that (5.5), is still within experimental error. The latter error is large because the small value of C_{46} corresponds to subtracting nearly equal terms on the right hand side of (5.6).

(b) Semi-pure modes

The semi-pure modes propagating along the $[100]'$ and $[001]'$ directions provide four equations relating the five unknown constants C_{11} , C_{55} , C_{33} , C_{15} and C_{35} . For the $[100]'$ direction the equations are:

$$C_{11} + C_{55} = \rho(V_1^2 + V_2^2) = 34.03 \pm 0.19 \text{ GPa} \quad (5.7)$$

$$\text{and} \quad C_{11} C_{55} - C_{15}^2 = \rho V_1^2 \rho V_2^2 = 123.6 \pm 2.7 (\text{GPa})^2 \quad (5.8)$$

and for the $[001]'$ direction:

$$C_{33} + C_{55} = \rho(V_7^2 + V_9^2) = 70.65 \pm 0.29 \text{ GPa} \quad (5.9)$$

$$\text{and} \quad C_{33} C_{55} - C_{35}^2 = \rho V_7^2 \rho V_9^2 = 284.1 \pm 2.8 (\text{GPa})^2 \quad (5.10).$$

The semi-pure modes for propagation along $[\ell, o, n]'$ provide the necessary fifth equation given by

$$\begin{aligned} \ell^2 C_{11} + C_{55} + n^2 C_{33} + 2\ell n(C_{15} + C_{35}) &= \rho V_{10}^2 + \rho V_{12}^2 \\ &= 49.51 \pm 0.18 \text{ GPa} \end{aligned} \quad (5.11)$$

where $\ell^2 + n^2 = 1$.

Whilst it is possible (but tedious) to solve (5.7)-(5.11) analytically, it is more convenient to solve these equations numerically using a generalized Newton-Raphson algorithm (Carnahan et al. 1969). The system was found to converge to two separate solutions, depending on the starting values of the variables. One solution has been rejected as unphysical, as, on substituting this set of elastic constants back into the eigenvalue equation $\underline{\lambda}A = \rho V^2 \underline{A}$ it was found that the eigenvector corresponding to the fastest mode (i.e. the quasi-longitudinal wave) is polarized close to 90° to the propagation direction.

The errors in C_{11} , C_{55} , C_{33} , C_{15} and C_{35} were calculated by varying the right hand side of (5.7)-(5.11) by plus or minus the quoted error for all possible permutations and noting the maximum and minimum values of the constants which emerge when the equations are solved. This is considered to be a more realistic estimate of the error than would be obtained by solving (5.7)-(5.11) analytically and summing all possible maximum errors. In the latter case the errors calculated are unreasonably large, as no account is taken of the self-consistency requirements which do not allow worst case errors to occur independently of one another.

The value of C_{13} may be calculated from the constants calculated above and the velocities of the semi-pure modes propagating along $[\ell, o, n]'$ by the equation

$$\begin{aligned}
 & [\ell^2 C_{15} + n^2 C_{35} + \ell n(C_{13} + C_{55})]^2 \\
 & - [\ell^2 C_{11} + n^2 C_{55} + 2\ell n C_{15}][\ell^2 C_{55} + n^2 C_{33} + 2\ell n C_{35}] \\
 & - \rho V_{10}^2 - \rho V_{12}^2 = 88.75 \pm 0.84 \text{ (GPa)}^2
 \end{aligned} \tag{5.12}$$

There will be two solutions for C_{13} depending on whether the positive or negative square root is taken in (5.12). Once again one solution has been rejected as unphysical on the criterion that the quasi-longitudinal wave travels faster than the quasi-transverse wave and is polarized closer to the propagation direction.

(c) Non-pure modes

To obtain C_{12} , C_{25} and C_{23} , the velocities in the $[110]'$ and $[011]'$ directions were measured. None of the waves in these directions are pure. The solution to the secular equation (2.12) requires, for the $[110]'$ direction:

$$\begin{vmatrix}
 C_{11} + C_{66} - 2\rho V^2 & C_{12} + C_{66} & C_{15} + C_{46} \\
 C_{12} + C_{66} & C_{22} + C_{66} - 2\rho V^2 & C_{25} + C_{46} \\
 C_{15} + C_{46} & C_{25} + C_{46} & C_{55} + C_{44} - 2\rho V^2
 \end{vmatrix} = 0 \tag{5.13}$$

and for the $[011]'$ direction:

$$\begin{vmatrix}
 C_{66} + C_{55} - 2\rho V^2 & C_{46} + C_{25} & C_{46} + C_{35} \\
 C_{46} + C_{25} & C_{22} + C_{44} - 2\rho V^2 & C_{44} + C_{23} \\
 C_{46} + C_{35} & C_{44} + C_{23} & C_{44} + C_{33} - 2\rho V^2
 \end{vmatrix} = 0 \tag{5.14}$$

The properties of the roots (Spiegel 1968) of the cubic equations (5.13) and (5.14) respectively provide relations that may be used as internal consistency checks. These relations are for the $[110]'$ direction

$$2\rho(V_{13}^2 + V_{14}^2 + V_{15}^2) = C_{11} + C_{22} + 2C_{66} + C_{55} + C_{44} \quad (5.15)$$

and for the [011]' direction

$$2\rho(V_{16}^2 + V_{17}^2 + V_{18}^2) = C_{66} + C_{55} + 2C_{44} + C_{22} + C_{33} \quad (5.16).$$

On substituting the values of the constants so far determined the left hand side and right hand side of (5.15) and (5.16) agree to within 0.7% and 0.2% respectively which is well within experimental error. The properties of the roots of the cubic equations (5.13) and (5.14) provide four equations relating the three remaining unknowns $(C_{12}+C_{66})$, $(C_{25}+C_{46})$ and $(C_{23}+C_{44})$. The equations are for the [110]' direction

$$\begin{aligned} & (C_{12}+C_{66})^2 + (C_{25}+C_{46})^2 \\ &= (C_{11}+C_{66})(C_{22}+C_{66}) + (C_{11}+C_{66})(C_{55}+C_{44}) + (C_{22}+C_{66})(C_{55}+C_{44}) \\ & - (C_{15}+C_{46})^2 - (2\rho)^2 (V_{13}^2 V_{14}^2 + V_{14}^2 V_{15}^2 + V_{13}^2 V_{15}^2) \end{aligned} \quad (5.17)$$

and

$$\begin{aligned} & (C_{55}+C_{44})(C_{12}+C_{66})^2 + (C_{11}+C_{66})(C_{25}+C_{46})^2 \\ & - 2(C_{12}+C_{66})(C_{15}+C_{46})(C_{25}+C_{46}) \\ &= (C_{11}+C_{66})(C_{22}+C_{66})(C_{55}+C_{44}) - (2\rho V_{13}^2)(2\rho V_{14}^2)(2\rho V_{15}^2) \\ & - (C_{22}+C_{66})(C_{15}+C_{46})^2 \end{aligned} \quad (5.18).$$

For the [011]' direction the corresponding relationships are

$$\begin{aligned} & (C_{23}+C_{44})^2 + (C_{25}+C_{46})^2 \\ &= (C_{66}+C_{55})(C_{22}+C_{44}) + (C_{66}+C_{55})(C_{44}+C_{33}) + (C_{22}+C_{44})(C_{44}+C_{33}) \\ & - (C_{46}+C_{35})^2 - (2\rho)^2 (V_{16}^2 V_{17}^2 + V_{17}^2 V_{18}^2 + V_{16}^2 V_{18}^2) \end{aligned} \quad (5.19)$$

and

$$\begin{aligned} & (C_{66}+C_{55})(C_{23}+C_{44})^2 + (C_{44}+C_{33})(C_{46}+C_{25})^2 \\ & - 2(C_{46}+C_{25})(C_{46}+C_{35})(C_{44}+C_{23}) \\ &= (C_{66}+C_{55})(C_{22}+C_{44})(C_{44}+C_{33}) - (2\rho V_{16}^2)(2\rho V_{17}^2)(2\rho V_{18}^2) \\ & - (C_{22}+C_{44})(C_{35}+C_{46})^2 \end{aligned} \quad (5.20).$$

The right hand sides of (5.17)-(5.20) are functions of the elastic constants already determined, so that it is possible to plot $(C_{12}+C_{66})$ versus $(C_{25}+C_{46})$ using equations (5.17) and (5.18) and $(C_{23}+C_{44})$ versus $(C_{25}+C_{46})$ using equations (5.19) and (5.20). The plots, shown in Figure 5.1, indicate that there are two sets of distinct solutions for the unknowns for each pair of equations. The variable $(C_{25}+C_{46})$ is common to all four equations and appears on the y axis of both graphs in Figure 5.1. Figure 5.2 shows a region of intersection of the curves in more detail, and from this plot the solutions were estimated to be

Equations (5.17) and (5.18)		Equations (5.19) and (5.20)	
Set 1	Set 2	Set 1	Set 2
(GPa)	(GPa)	(GPa)	(GPa)
$C_{12} + C_{66} = \pm 20.5$	± 21.4		
$C_{25} + C_{46} = \pm 6.2$	∓ 1.3	± 5.8	∓ 1.7
$C_{23} + C_{44} =$		± 22.7	± 23.4

The graphic mode of solution has two drawbacks. Firstly it was impractical to estimate the uncertainties in C_{12} , C_{25} and C_{23} by using the permutation technique of the errors that had proved successful previously for equations (5.7)-(5.11), and secondly only two equations at a time could be considered so that a different value for $(C_{25}+C_{46})$ emerged depending on which pair of equations was used.

These drawbacks were avoided by solving equations (5.17), (5.18) and (5.19) simultaneously by a Newton-Raphson algorithm. As expected the system converged to two sets of solutions depending on the starting values of the variables. The solutions were checked by substitution into equation (5.20) which yielded consistency of right and left hand sides of better than 0.7%. The two pairs of solutions were

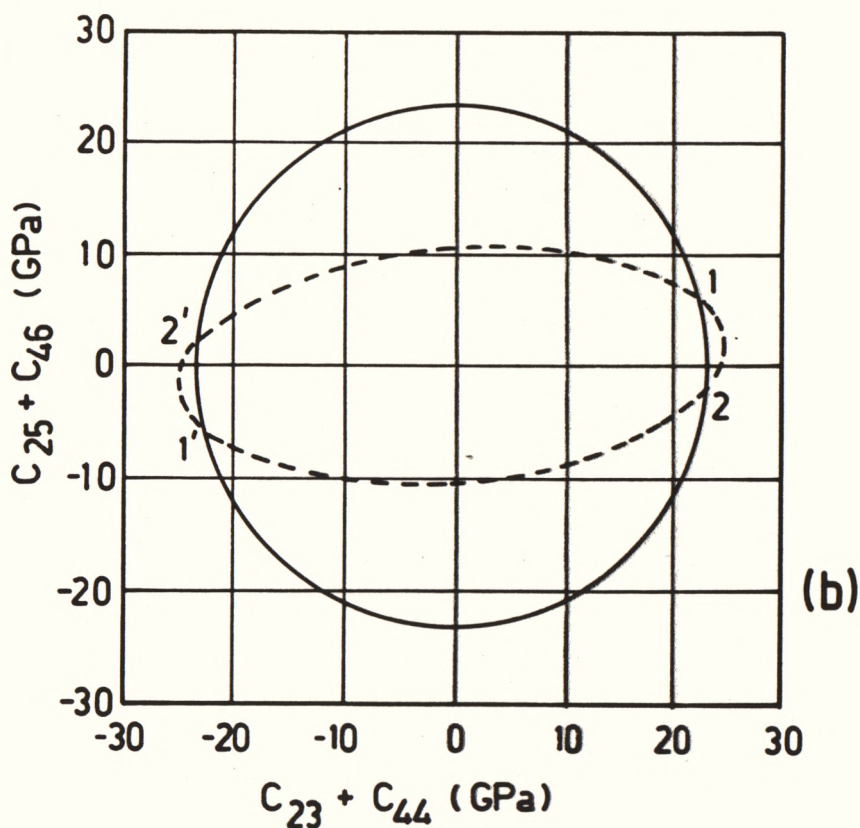
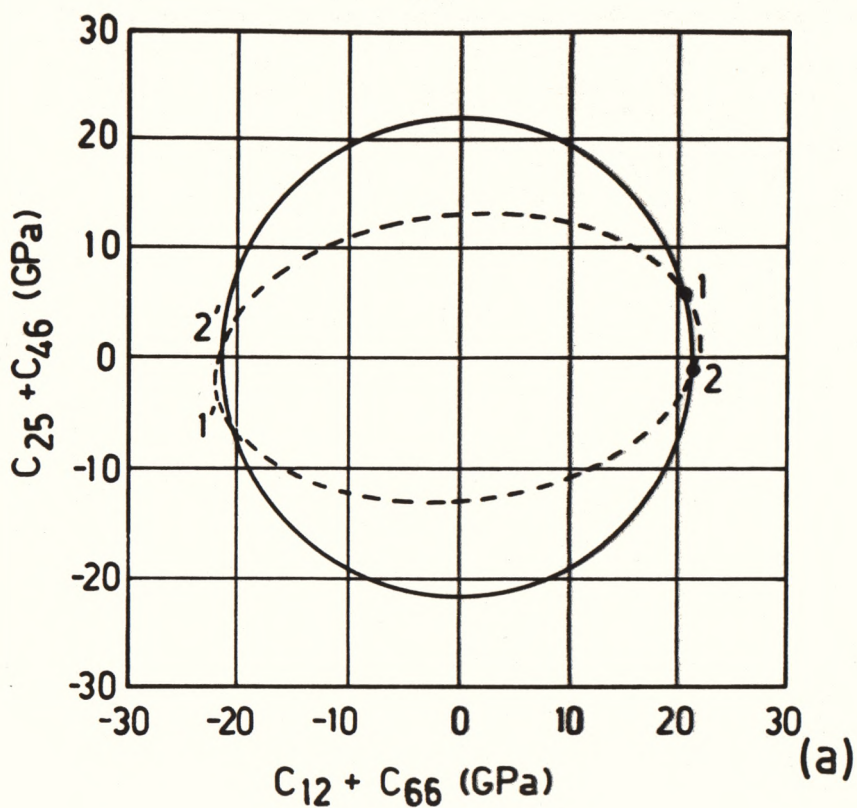


Figure 5.1. (a) Plot of $(C_{25} + C_{46})$ versus $(C_{12} + C_{66})$ according to equations (5.17) (solid line) and (5.18) (broken line).

(b) Plot of $(C_{25} + C_{46})$ versus $(C_{23} + C_{44})$ according to equations (5.19) (solid line) and (5.20) (broken line)

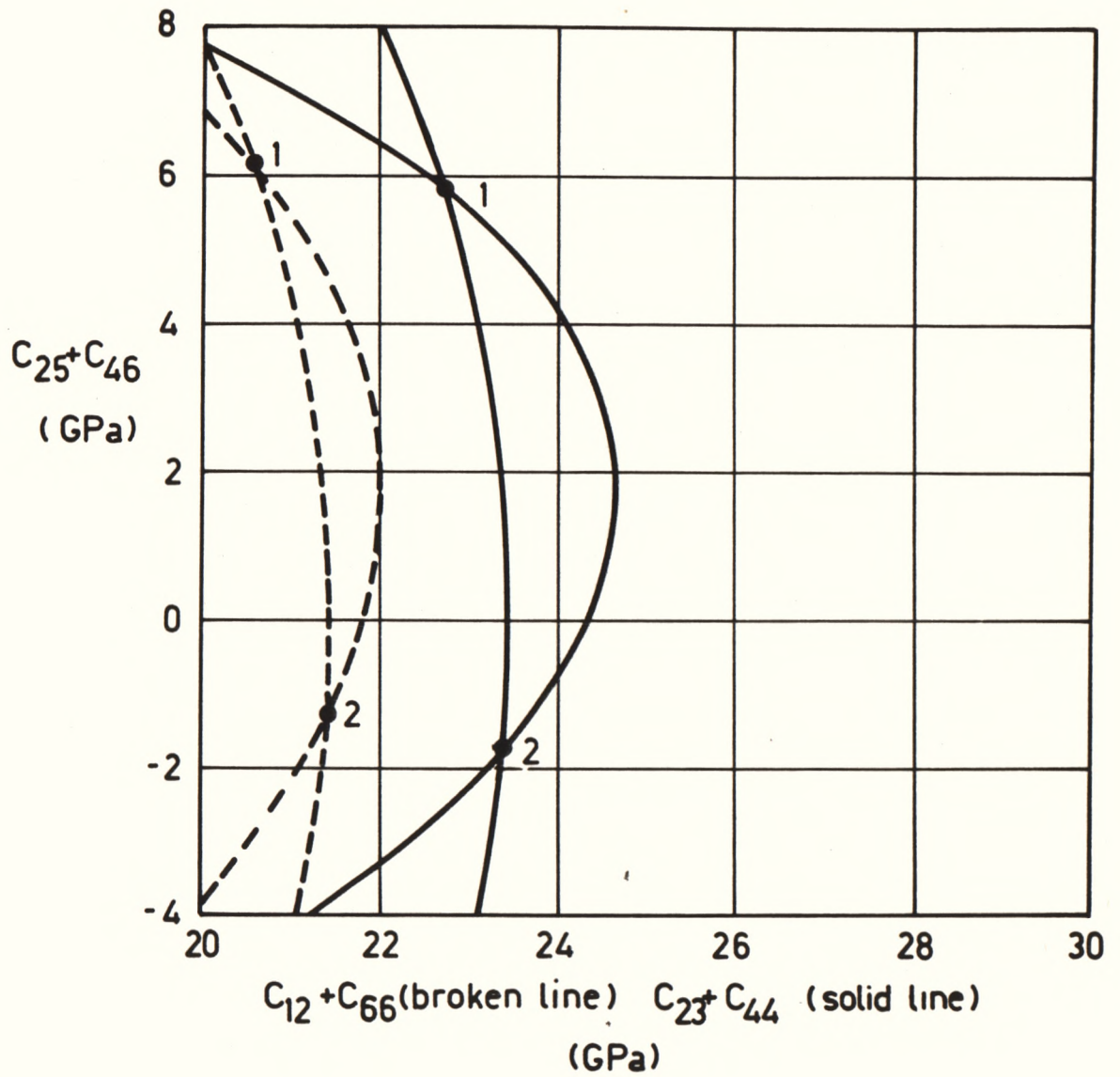


Figure 5.2. The Intersection Region of Figure 5.1 Shown in More Detail.

	Set 1	Set 2
	(GPa)	(GPa)
$C_{12} + C_{66}$	± 20.6	± 21.4
$C_{25} + C_{46}$	± 6.1	± 1.3
$C_{23} + C_{44}$	± 22.6	± 23.4

which are in good agreement with the graphical results.

An attempt to calculate the errors in C_{12} , C_{25} and C_{23} by solving the equations for all the possible permutations of plus or minus the quoted errors in C_{11} , C_{22} , C_{33} , C_{44} , C_{55} , C_{66} , C_{13} , C_{15} , C_{35} , C_{46} and the measured velocities $V_{13} \dots V_{18}$ was unsuccessful. For most permutations of the errors the system of equations (5.17)-(5.20) no longer converged, as the internal consistency requirements of (5.15) and (5.16) were no longer satisfied. The uncertainties in C_{12} , C_{25} and C_{23} quoted above were calculated by restricting the errors in the velocities so that the left and right hand sides of (5.15) and (5.16) agreed to within 1% for all permutations of the errors in the velocities. In this case the system of equations (5.17)-(5.20) converged for most error permutations except those extreme cases for which all the errors were either added or subtracted. After substituting the previously determined constants C_{66} , C_{46} and C_{44} the results were

	Set 1	Set 2
	(GPa)	(GPa)
$C_{12} =$	$\pm 11.4 \pm 3.6$	$\pm 12.2 \pm 2.9$
$C_{25} =$	$\pm 8.4 \pm 4.3$	$\pm 0.95 \pm 4.2$
$C_{23} =$	$\pm 14.5 \pm 4.4$	$\pm 15.3 \pm 4.0.$

Two of the above solutions (the negative of each pair) may be rejected as unphysical by a consideration of the eigenvectors as described above. This still leaves two distinct solutions, and although the eigenvectors corresponding to each solution are different, both are

physically quite reasonable. Clearly, the choice of solution has little effect on the value of C_{12} and C_{23} , but the value of C_{25} is radically changed. In order to differentiate between these solutions the velocity in a further general direction $[0.252, 0.588, -0.769]'$ was measured.

The criterion

$$R_{19-21} = \sum_{i=19}^{21} \frac{(v_{\text{calc}_i} - v_i)^2}{v_i^2}$$

where v_{calc_i} are the velocities calculated for the $[0.252, 0.588, -0.769]'$ direction from the elastic constants, was used as a measure of the goodness of fit of the data. The first solution gives an R value three times smaller than for the second solution and has therefore been adopted. The criterion

$$R_{1-18} = \sum_{i=1}^{18} \frac{(v_{\text{calc}_i} - v_i)^2}{v_i^2}$$

has been calculated and a value of 1.8×10^{-3} obtained. This compares very favourably with the value of R obtained by Krupnyi et al. (1972) in their calculations for some monoclinic organic crystals. However, they found it necessary to employ a least squares error function to refine the elastic constants in order to reduce their value of R to less than 10^{-2} . This procedure resulted in their final value for C_{22} being lower than the directly measured value. No physical justification was offered by them for modifying a directly measured quantity as a result of numerical calculation.

The complete elastic constant matrix C_{ij} is given in Table 5.2. The inverse of the elastic constant matrix was calculated to give the elastic compliance matrix S_{ij} which is also listed in Table 5.2. Quantities discussed in the following section, such as bulk modulus and linear compressibility, are calculated in terms of these S_{ij} .

Table 5.2
Elastic Constants of CsH_2PO_4 at $21 \pm 5^\circ\text{C}$

ij	C_{ij} (GPa)	S_{ij} (GPa) ⁻¹
11	28.83 ± 0.43	1.82
22	26.67 ± 0.37	0.103
33	65.45 ± 0.48	0.772
44	8.10 ± 0.15	0.133
55	5.20 ± 0.24	0.450
66	9.17 ± 0.22	0.117
12	11.4 ± 3.6	-0.219
13	42.87 ± 1.58	-1.17
15	5.13 ± 0.67	0.249
23	14.5 ± 4.4	0.138
25	8.4 ± 4.3	-0.150
35	7.50 ± 0.81	-0.181
46	-2.25 ± 0.31	0.033

The C_{ij} were calculated using a density of 3.22 g cm^{-3} at 20°C .

5.2 CALCULATION OF THE ELASTIC PROPERTIES

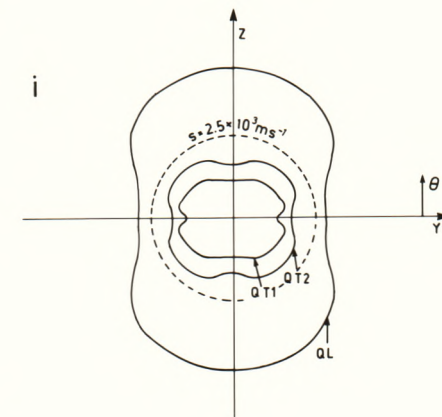
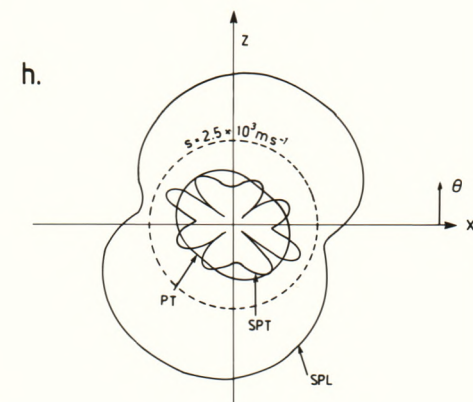
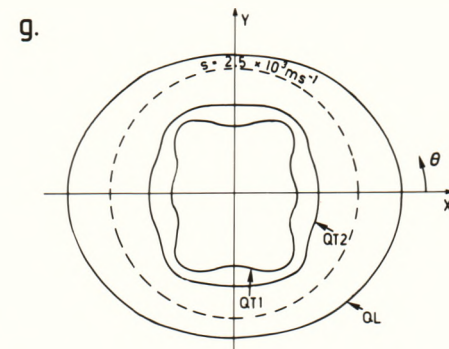
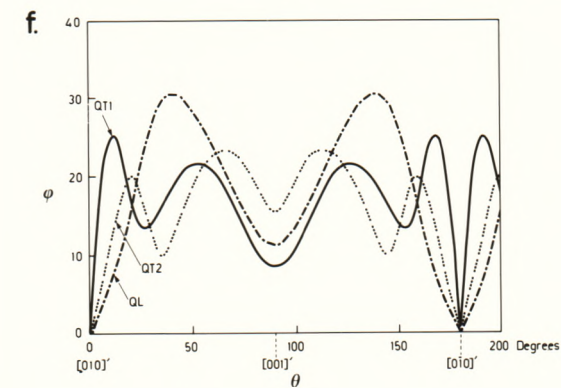
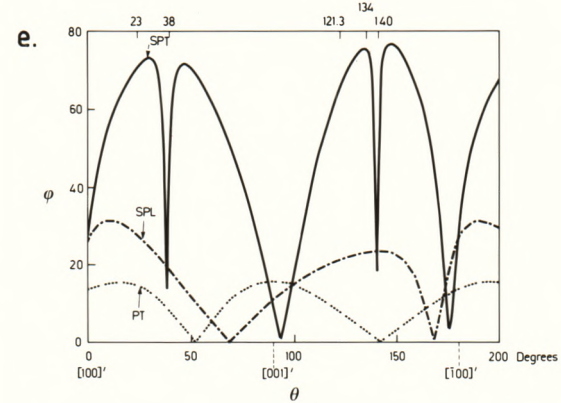
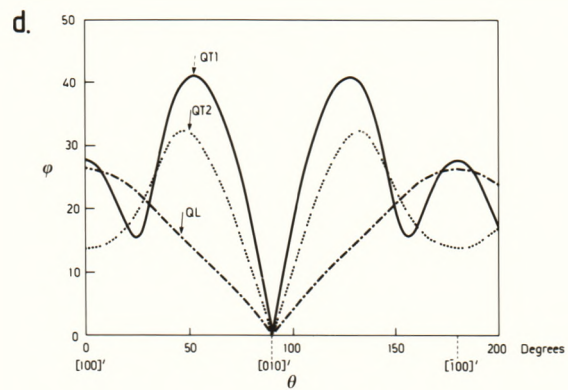
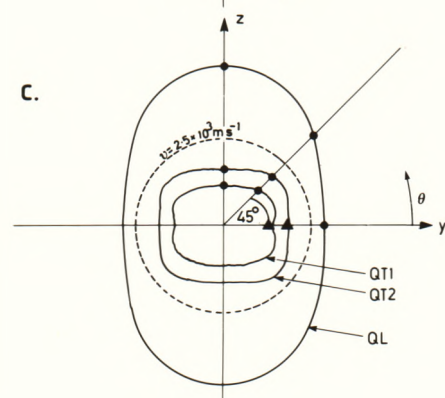
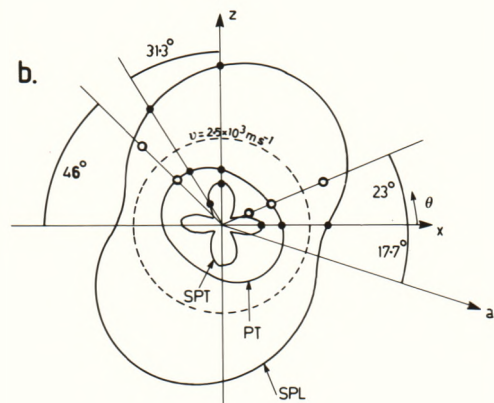
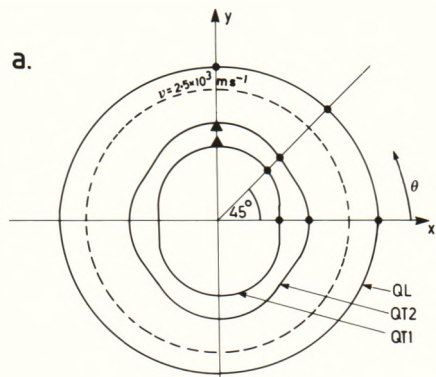
5.2.1 Wave Velocity Surfaces

Using the values of the C_{ij} matrix in Table 5.2, the wave velocity for any propagation direction can be calculated using equations (2.10) and (2.11). Figures 5.3(a), (b) and (c) are polar plots of velocity versus propagation direction for propagation vectors in the xy, xz, and yz planes.

It is immediately obvious that, for propagation directions in the xy and yz planes, the wave velocity is quite isotropic. This stands in very marked contrast to the plot for the xz plane (Figure 5.3(b)), which displays very marked anisotropy, particularly for the semi-pure transverse (SPT) mode with the smallest velocity. The calculations predict a minimum in the velocity of this mode of $0.290 \times 10^3 \text{ m s}^{-1}$ for propagation directions making angles of 38° and 140° to the x axis. This is a remarkably low value. For comparison, Sil'vestrova et al. (1975) have reported a value of $0.347 \times 10^3 \text{ m s}^{-1}$ for the velocity of a transverse wave propagating in the yz plane in Calomel, which they claimed to be the "lowest value" measured for crystals at that time. It should be pointed out, however, that Sil'vestrova et al. actually determined this value experimentally whilst the value of $0.290 \times 10^3 \text{ m s}^{-1}$ is calculated from the determined elastic constants.

In an effort to check the unusual predictions arrived at from the calculations, an attempt was made measure the velocity of each of the three modes for other propagation directions in the xz plane. For all propagation directions in this plane, one mode is pure transverse (PT), having a polarization vector parallel to $[010]'$. The other two modes are semi-pure, having polarization vectors of the form $[n \ 0 \ -l]'$ and $[l \ 0 \ n]'$. For propagation at 134° to the x axis the measured pure

Figure 5.3. Polar Plots of the Calculated Phase Velocity for the (a) xy, (b) xz and (c) yz Planes, together with the Absolute Value ϕ of the Deviation Angle between the Ray and Propagation Vectors (d)-(f), (where θ is measured in the same sense given in the corresponding polar plot), and the Corresponding Polar Plots of the Ray Velocity (g)-(i). The solid circles show the measured velocities actually used in the calculations. The triangles represent the measured velocities for the two pure transverse (PT) waves propagating parallel to the b axis and are used as a cross check. The open circles show other measured velocities in the xz plane.



transverse velocity agrees very well with the predicted value. The semi-pure transverse mode (SPT), with a predicted velocity of $0.363 \times 10^3 \text{ m s}^{-1}$, could not be generated at all. It was found on rotating the crystal with respect to the transverse exciting transducer that the pure mode decreased in amplitude as expected, but that no other mode could be detected. Similar difficulties were encountered for the measurements of V_{12} (Table 5.1), although in that case a weak mode could be detected. It was also noted that this semi-pure transverse mode could be generated by a longitudinal transducer.

The failure to observe the very low velocity mode is not unexpected as such a mode would be expected to be heavily damped compared to the faster modes. However, as can be seen from Figure 5.3(b), the measured velocity of the semi-pure longitudinal mode (SPL), which is strongly propagated, is significantly smaller than the predicted value in this direction. Similar results were obtained for propagation at 23° to the x axis, in that the measured pure mode velocity is very close to the predicted value and the semi-pure longitudinal wave velocity is significantly less than the predicted value. In this case, the semi-pure transverse wave could be detected, but it was very weakly propagated and only a rough estimate of its velocity could be obtained ($V = 0.83 \times 10^3 \text{ m s}^{-1}$).

The discrepancy between the measured and calculated values of this semi-pure longitudinal mode suggests that the severe damping of the semi-pure transverse mode influences the longitudinal mode as well. The formulation of the equation of motion assumes an infinite lossless medium and therefore does not include any damping term. Normally, the introduction of such a term should have little or no influence on the velocities. However, if the damping is sufficiently severe so as to almost stop one mode from propagating at all, the nature of the

eigenvalue equation can be expected to change, since the dimensionality of the problem would effectively be reduced from 3 to 2. There is a need for further investigation of the effect that a severe damping term for one mode will have on the other measured velocities.

5.2.2 Ray Directions

For each direction of propagation there are three associated wave modes, each with a different velocity, polarization and ray energy propagation direction. Figures 5.3(d), (e) and (f), show plots of the magnitude of the absolute angle between the ray direction and the propagation direction, calculated using equation (2.25), for the xy, xz and yz planes.

Deviation angles of up to 70° are not unusual (see for example Neighbours 1973). The plots for the xy and yz planes show that there are no accidental pure modes of propagation, since the deviation angle only goes to zero for propagation along the b axis, which is demanded by symmetry. Once again the plot for the xz plane is very peculiar. The deviation angle for the semi-pure transverse mode increases rapidly for propagation off the x axis, reaching a value of 73° at 30° from the x axis. With further displacement, the deviation angle decreases abruptly to a value of 14° at 38° from the x axis and then abruptly increases. Similar behaviour occurs for propagation directions about 140° to the x axis†. Note that the minima in the calculated velocities of this mode occur for the same propagation directions. The sharpness of the dip is striking. In the region of the anomalies the deviation angle changes by about 38° for a 1° change in propagation direction. Calomel (Sil'vestrova et al. 1975) displays similar behaviour for the

† The eigenvectors in the xz plane are well behaved and do not deviate from pure mode behaviour by more than 17° .

transverse mode, the velocity of which has a minimum value of $0.347 \times 10^3 \text{ m s}^{-1}$ for propagation at 45° to the x axis in the xy plane.

The deviation angles for the measured velocities ($V_{22} - V_{27}$) in the xz plane can be read from Figure 5.3(e). It can be seen that the mode propagating at 134° to the x axis has a deviation angle of 76° . It is therefore not unexpected that this ray was unobserved since it must reflect off the sides of the crystal many times during its round trip. The mode at 23° has a smaller deviation angle, viz., 69° and was weakly observed. The mode at 121.3° (V_{12}) has a deviation angle of 64° and was clearly observed.†

In order to test these conclusions, measurements of the velocity for propagation at the angles in the xz plane at which the minima in velocity and deviation angle occur (viz. 38° and 140°) would be desirable. However, such measurements would require the crystal to be aligned very precisely as even small errors in alignment will lead to large changes in the deviation angle. The crystal would also have to be of excellent quality as a mosaic spread of even 1° will lead to a gross divergence of the beam. Finally, even if the beam were propagated without a large divergence, the very low value of velocity for this mode will probably be accompanied by a high value of attenuation, making the mode difficult or impossible to observe experimentally.

Using equation (2.20), the group (or ray) velocity may be calculated as a function of propagation direction. Polar plots of the ray velocity versus propagation direction for propagation vectors in the xy, xz and yz planes are shown in Figure 5.3(g), (h), (i). The plots may also be deduced by dividing the phase velocity for a given

† It should be recalled that the number of reflections off the side walls of the crystal will depend on the tangent of the deviation angle. Thus a deviation angle of 76° ($\tan 76^\circ = 4.01$) will result in about twice as many side wall reflections as a deviation of 64° ($\tan 64^\circ = 2.05$).

propagation direction (Figure 5.3(a), (b), (c)) by the cosine of the deviation angle for that direction (Figure 5.3(d), (e), (f)). (see equation (2.24)) As expected the ray velocity is greater than or equal to the wave velocity for any propagation direction. The plot for the xz plane once again displays marked anisotropy. The minimum in the ray velocity of $0.299 \times 10^3 \text{ m s}^{-1}$ occurs, not surprisingly, for propagation at 38° to the x axis in the xz plane. Thus for this propagation direction energy associated with the SPT mode travels very slowly through the crystal. The slow energy transfer would tend to be associated with large values of absorption. This is consistent with previous comments as to why this mode is not easily observed experimentally.

5.2.3 Bulk Modulus, Linear Compressibility and Young's Modulus

The bulk modulus of CsH_2PO_4 was calculated using the relationship $B = (S_{11} + S_{22} + S_{33} + 2(S_{12} + S_{23} + S_{13}))^{-1}$ (Nye 1967). A value of 5.28 GPa was obtained using the S_{ij} matrix calculated by taking the inverse of the C_{ij} matrix in Table 5.2. An attempt was made to calculate the error in the bulk modulus by adding all possible permutations of the errors to the values of C_{ij} before inverting the matrix. However, for most permutations of the errors, especially those involving extreme cases where all the errors were either added or subtracted, the C_{ij} matrix ceased to be positive definite. Positive definiteness is the mathematical consequence of demanding a positive strain energy for lattice stability. Thus a C_{ij} matrix which is not positive definite cannot describe the elastic properties of any real material. Hence those error permutations for which the C_{ij} matrix is not positive definite may be rejected as unphysical.

When the calculation was performed using only those error combinations for which the C_{ij} matrix was positive definite, the bulk modulus was found to lie in the range 0.9 - 16.5 GPa. This large uncertainty is due to ignoring the fact that constants are coupled in such complicated ways that the quoted errors cannot occur independently. A more sophisticated error calculation system is required - possibly a Monte-Carlo method of assigning the value of C_{ij} to be used as a normally distributed variable with mean and standard deviation equal respectively to the values and errors given in Table 5.2.

The value of B is remarkably small. For comparison, the bulk moduli for some other materials are shown in Table 5.3. These values have been calculated using the elastic constants given in the listed references. Note that Calomel, whilst displaying some similar anisotropic features to CDP in the behaviour of the velocity and ray directions, nevertheless has a value of bulk modulus comparable to the other crystals listed.

Since CDP displays a chain-like structure it is of interest to calculate the linear compressibility K_{lmn} , which is the strain response of the crystal along a given direction $[l,m,n]'$, to the application of hydrostatic pressure. For a monoclinic system the expression is (Nye 1967)

$$K_{lmn} = (S_{11} + S_{12} + S_{13})l^2 + (S_{12} + S_{22} + S_{23})m^2 + (S_{13} + S_{23} + S_{33})n^2 + (S_{15} + S_{25} + S_{35})ln.$$

A plot of linear compressibility versus direction in the xy, xz and yz planes is given in Figure 5.4. Note how the compressibility along the x axis is twenty times larger than that along the y axis, and that the compressibility along the z axis is negative. Thus when hydrostatic pressure is applied to CsH_2PO_4 the crystal responds by contracting along the x axis and expanding along the z axis. By

Table 5.3

Bulk moduli for selected crystals

<u>Crystal</u>	<u>Class</u>	<u>Bulk Modulus</u> (GPa)	<u>Reference</u>
CsH ₂ PO ₄	Monoclinic	5.28	This paper
KH ₂ PO ₄	Tetragonal	27.3	Fritz (1976)
Potassium Tartrate	Monoclinic	16.8	Aleksandrov (1958)
NH ₄ H ₂ PO ₄	Tetragonal	20.1	Fritz (1976)
CsSCN	Orthorhombic	13.2	Irving <u>et al.</u> (1983)
Calomel	Tetragonal	18.0	Sil'vestrova <u>et al.</u> (1975)

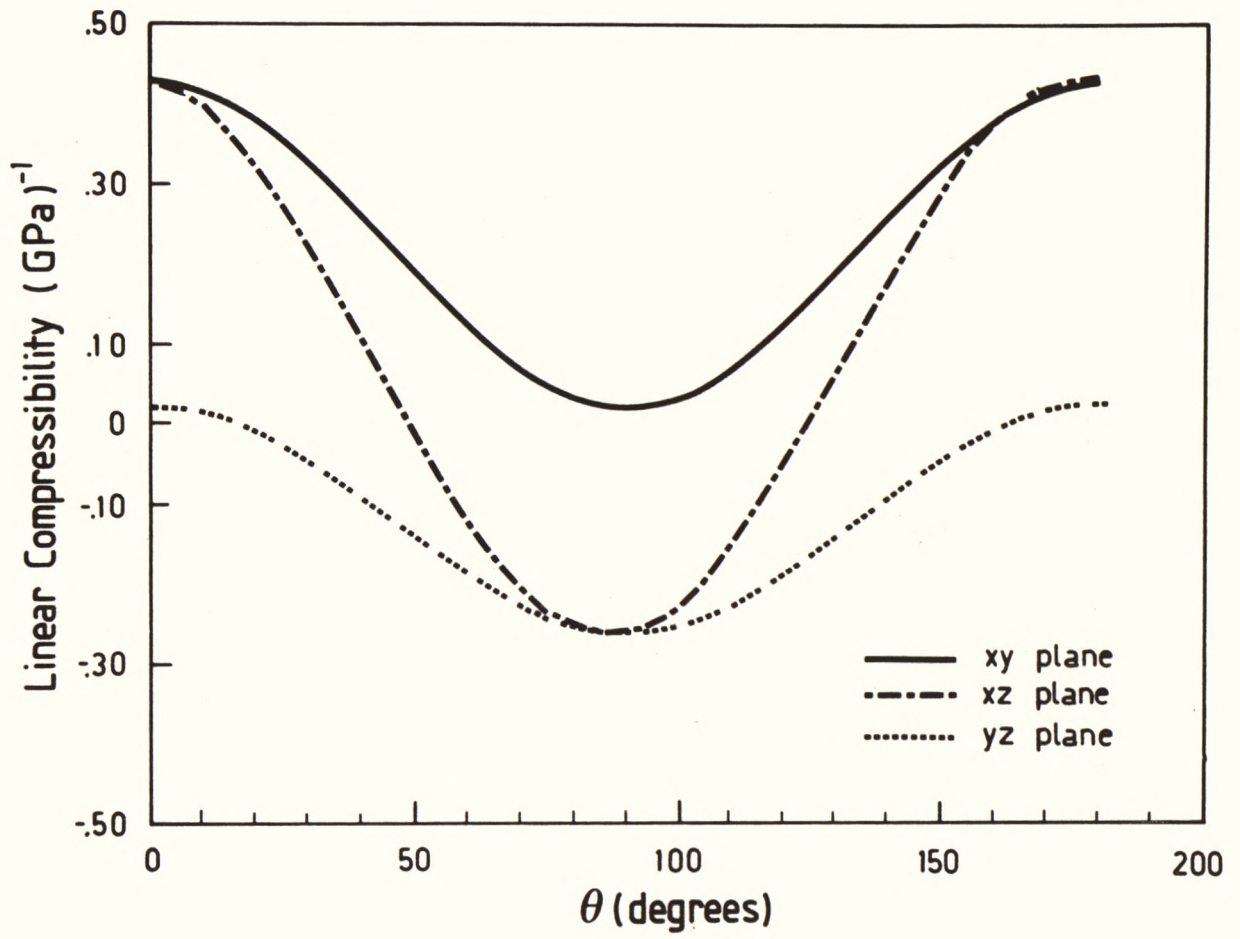


Figure 5.4. Linear Compressibility for Directions in the xy, xz, and yz planes, with θ measured as in Figure 5.3.

comparison the length change along the y axis is small. This further demonstrates the marked elastic anisotropy of CDP.

Finally, the central sections of the Young's modulus surface on the xy, xz and yz planes were calculated and are shown in Figures 5.5(a), (b) and (c). In Figure 5.5 the radius vector is proportional to the value of Young's modulus for that direction. The curves were calculated from the expression (Nye 1967)

$$\begin{aligned} \frac{1}{Y} = & \ell^4 S_{11} + 2\ell^2 m^2 S_{12} + 2\ell^2 n^2 S_{13} + 2\ell^3 n S_{15} \\ & + m^4 S_{22} + 2m^2 n^2 S_{23} + 2\ell m^2 n S_{25} \\ & + n^4 S_{33} + 2\ell n^3 S_{35} + m^2 n^2 S_{44} + 2\ell m^2 n S_{46} \\ & + \ell^2 n^2 S_{55} + \ell^2 m^2 S_{66} . \end{aligned}$$

Young's modulus gives a measure of the 'stiffness' of the crystal to a uniaxial stress applied along the direction of interest. Once again the elastic behaviour is clearly very anisotropic.

5.2.4 Debye Temperature

The Debye temperature was estimated using the elastic constants of Table 5.2 to be 134.5 K for Avogadro's number of ions. The calculation was kindly carried out by Dr J.G. Collins of National Measurement Laboratory, C.S.I.R.O. Division of Applied Physics. The value is consistent with an estimate given by Spörl et al. (1984) of (140±10) K from thermal conductivity data.

5.3 RELATIONSHIP TO CRYSTAL STRUCTURE

Much of the elastic anisotropy in CDP originates from the extremely low velocity predicted for the semi-pure transverse mode for propagation in the xz plane at 38° and 140° to the x axis. This anomaly results in the sharp dip for the deviation angle between ray and wave normals for these propagation directions. It also results in the very

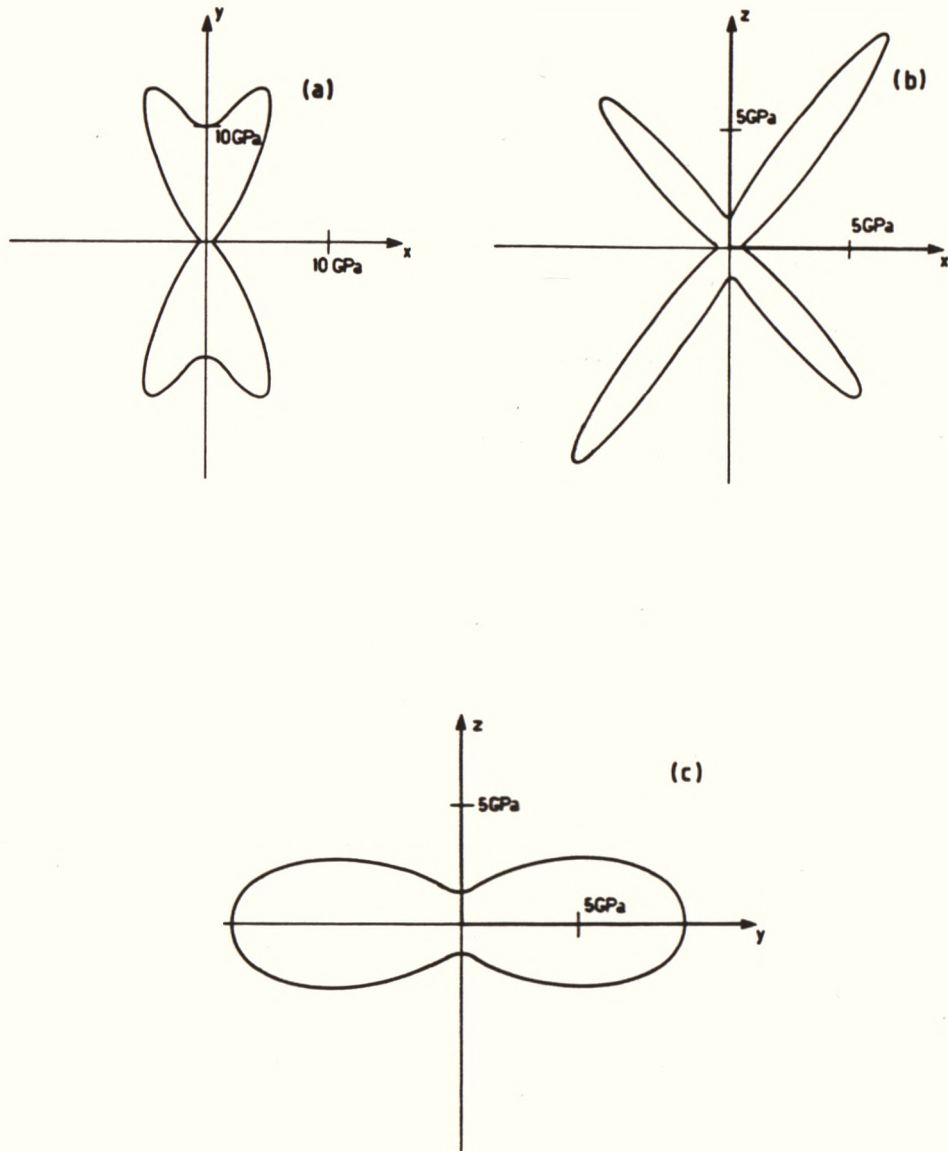


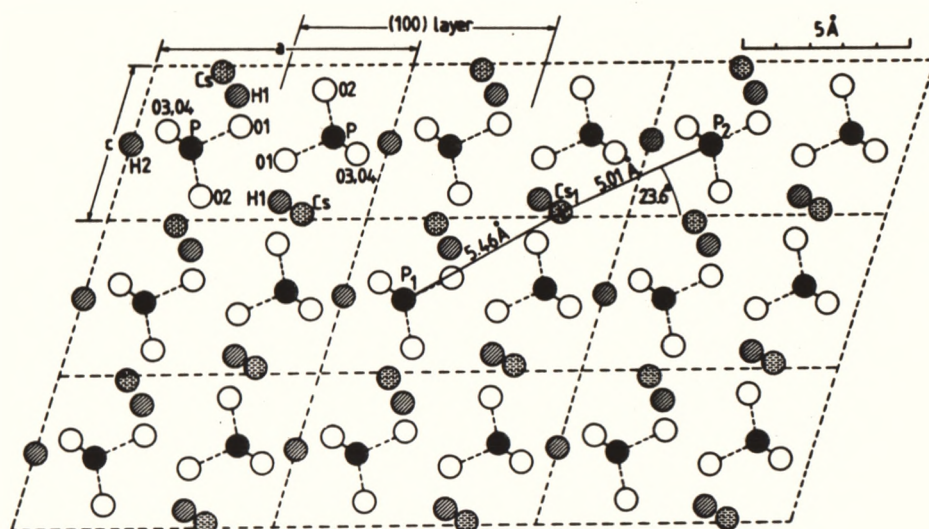
Figure 5.5. Central Sections of the Young's Modulus Surface for the (a) xy , (b) xz , and (c) yz planes in CDP. The magnitude of the radius vector is proportional to the value of Young's modulus.

low value for the bulk modulus, and the large anisotropies in Young's modulus and the linear compressibility. The following qualitative explanation is suggested, in terms of the known crystal structure of CDP, as to why this mode should behave anomalously.

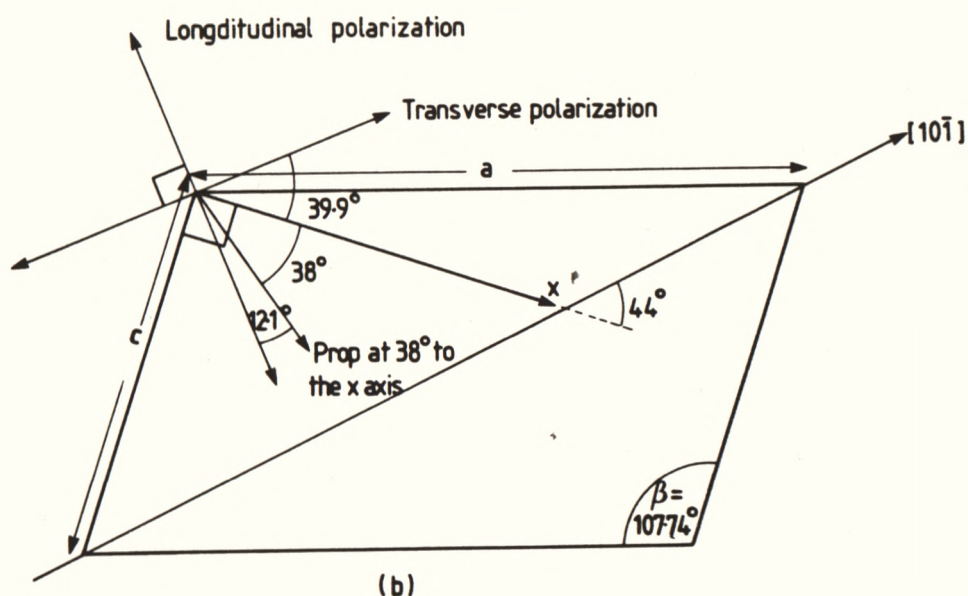
As previously noted, CDP consists of (100) layers of hydrogen bonded PO_4 groups, the layers being held together by electrostatic attraction to the Cs^+ ions. A projection of the structure onto the (010) plane is given in Figure 5.6(a) based on the atomic positions given by Uesu and Kobayashi (1976) and Matsunaga *et al.* (1980). The H2 hydrogen links 03-03 and 04-04 groups to form the PO_4 chains along the b axis. The H1 hydrogen cross links the chains to form the (100) layers.

Uesu and Kobayashi (1976) point out that nearly linear chains of Cs and P ions are formed along the $[10\bar{1}]$ direction with an interatomic distance of 4.03Å. However, it is evident from Figure 5.6(a) that this is an error and that the chains with close to this interatomic distance lie along the [101] direction. It is also seen in Figure 5.6(a) that there are nearly linear chains of P-01, Cs^+ , P-01 groups along the $[10\bar{1}]$ direction where the Cs_1 - P_1 separation is 5.46Å (with an oxygen intervening) and the Cs_1 - P_2 separation is 5.01Å (with no intervening atoms). Uesu and Kobayashi (1976) point out that these distances are considerably longer than the K-P distance of 3.49Å in KDP.

If we consider a wave propagating in the xz plane at 38° to the x axis, the eigenvectors for this direction can be calculated by solving the eigenvalue equation (2.10). The eigenvectors lie in the xz plane and make angles of 39.9° (semi-pure transverse) and 50.1° (semi-pure longitudinal) to the x axis as shown in Figure 5.6(b). The third mode is pure transverse and has polarization parallel to [010]. The semi-pure transverse polarization is approximately parallel to the



(a)



(b)

Figure 5.6. (a) Projection of the Structure of CDP onto the ac Plane. The disordered hydrogen H2 forms the chains of PO_4 tetrahedra up the b axis, whilst the ordered H1 cross-links the chains. The nearly linear chains of Cs and P atoms can be seen along the $[10\bar{1}]$ and $[101]$ directions. (b) Direction of Transverse and Longitudinal Polarization for a Mode Propagating at 38° to the x axis in the ac Plane.

$[10\bar{1}]$ direction and makes an angle of only 1.4° with the direction joining Cs_1 and P_2 .

Since there are no intervening atoms between Cs_1 and P_2 and since the eigenvectors are constrained to lie in the xz plane, the force constants associated with this mode may be expected to be small due to the comparatively very large nearest neighbour separation. It is also noteworthy that the particle vibration direction shown in Figure 5.6(b) is roughly (to within 5°) parallel to the projection of the 03-H2-03 hydrogen bond onto the xz plane. This bond is expected to be quite compliant as this hydrogen is disordered in the room temperature phase. As a consequence of both these factors the velocity may be expected to be correspondingly small for this mode.

Irrespective of the above explanation, the correspondence of the transverse polarization for the mode propagating at 38° to the x axis to the linear Cs-P arrays and the 03-H2-03 hydrogen bond direction seems unlikely to be coincidental. It is unfortunate that this mode is not more easily observed experimentally, for the response of the velocity of this mode to temperature through the ferroelectric ordering would be very interesting.

It has also been observed by Uesu and Kobayashi (1976) that nearly linear arrays of Cs and P atoms also occur along the $[0, \pm 1, 1]$ directions with a comparatively large Cs-P separation. However, in this study, it was observed that in the yz plane the velocity of all modes is very isotropic, showing none of the peculiar effects of the xz plane. This difference may be accounted for by recalling that, for propagation in the xz plane, the eigenvectors are constrained by symmetry to lie in that plane, whereas for propagation in the yz plane no such restriction applies and, in fact, the eigenvectors lie considerably out of the plane. Thus the force constants for this mode will not necessarily be

determined by the comparatively large Cs-P interatomic distance within the yz plane.

The anisotropy of the linear compressibility and of Young's modulus is related to the layer and chain structure of CDP. The maximum in the value of the linear compressibility and the corresponding minimum in the value of Young's modulus for the x axis direction correspond to the weak bonding between the (100) layers. Under hydrostatic pressure these layers are forced closer together. The corresponding expansion along the c axis may be explained by a small rotation of the PO_4 tetrahedron, (possibly caused by repulsion between the 01 and 02 atoms of adjacent layers) which results in an elongation of the hydrogen bonded c axis chain. Selenium and Tellurium are examples of other chain-like materials which have negative linear compressibility parallel to the chain axis (Munn 1972). Under uniaxial stress, however, the bonding in the c axis chain is only about as strong as the interlayer bonding (Figure 5.5(b)).

It is surprising that the b axis bonding is so much stronger than that for the c axis (Figure 5.5(c)), especially in view of the disordered state of the hydrogen bonds linking this chain. This may be explained by noting that these hydrogen bonds lie nearly parallel to the a axis, so that compression of the b axis chain would involve a bending of the bond, rather than a compression of the double well potential along its axis. The strength of the b axis bonding is consistent with the findings of Frazer et al. (1979) that the correlation length along the b axis is much longer than those along the a and c axes.

The very strong anisotropy for Young's modulus in the xz plane (Figure 5.5(b)) is correlated to the anomalous semi-pure transverse mode discussed above. The maxima in Young's modulus (at 54° and 131° to the x axis) occur for directions which are almost parallel to the semi-pure

longitudinal polarization for wave propagation directions for which the semi-pure transverse mode has its minimum velocity. Thus the crystal is stiffest at right angles to the $[10\bar{1}]$ Cs-P chains (see Figure 5.6).

Finally, as mentioned in the introduction, most of the studies on CDP to date have focussed on the comparison between the transition mechanism in pseudo-one-dimensional CDP, and the more familiar 3-dimensional KH_2PO_4 . The plots of Young's modulus for KH_2PO_4 (calculated from the elastic constants quoted by Fritz (1976)) for the xy and yz (\equiv xz) planes (Figure 5.7) indicate clearly that the very anisotropic elastic behaviour in CDP is absent in the case of KH_2PO_4 . In particular it is obvious that the elastic behaviour for the ferroelectric z axis in KH_2PO_4 is not very different from that for the other axes, in contrast to CDP for which the ferroelectric b axis is much stiffer than the a and c axes.

5.4 SUMMARY

The elastic constant matrix of CsH_2PO_4 has been determined via ultrasonic velocity measurements. Significant anisotropy in the elastic constants was found. In particular, calculations using the determined matrix predict a very low velocity of sound ($0.290 \times 10^3 \text{ m s}^{-1}$) for the semi-pure transverse mode propagating in the xz plane at 38° to the x axis. This could not be confirmed experimentally due to the failure to propagate the mode. As the polarization direction for this mode is almost parallel to the linear Cs-P chains with a large (5.01\AA) nearest neighbour separation and to the direction of the disordered hydrogen bond, its low velocity is attributed to the relatively weak forces acting in this direction.

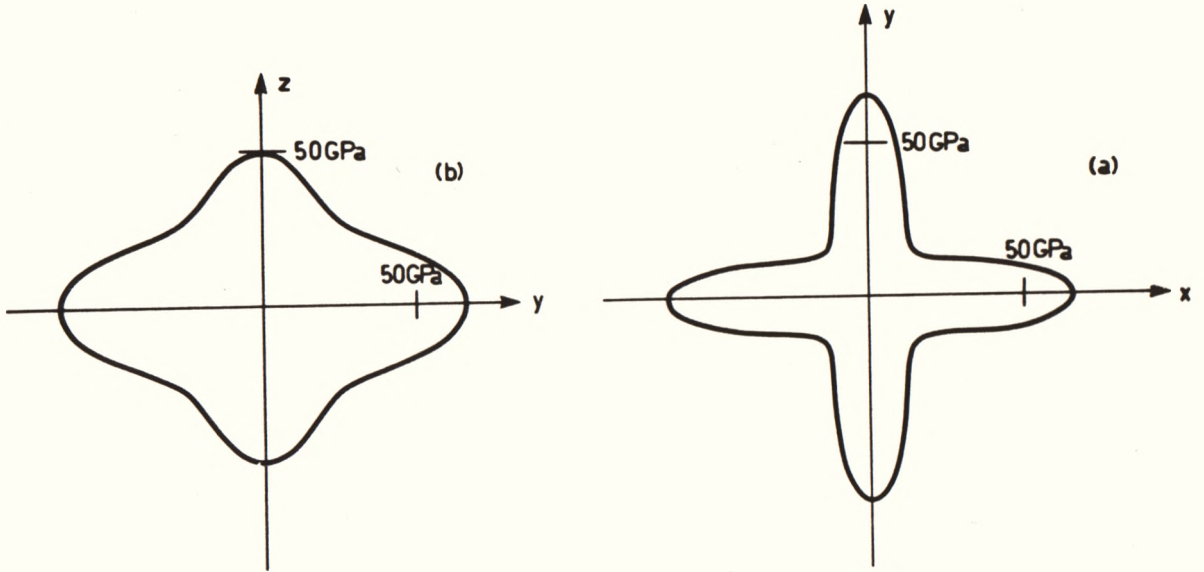


Figure 5.7. Central Sections of the Young's Modulus surfaces for the (a) xy and (b) yz planes in KH_2PO_4 . The magnitude of the radius vector is proportional to the value of Young's modulus.

The significant anisotropy found in Young's modulus and the linear compressibility reflect the weak forces between the (100) layers and show clearly that even in the paraelectric state the bonding along the b axis chain is different from that along the c axis. Hence, the one-dimensional chain-like structure of CDP reveals itself, not only in the critical phenomena, but also in the static elastic behaviour at room temperature.

CHAPTER 6

INVESTIGATION OF THE FERROELECTRIC TRANSITION

6.1 INTRODUCTION

This chapter reports investigations into the temperature dependences of the ultrasonic velocity and attenuation, thermal expansion coefficient and the dielectric constant near the ferroelectric phase transition.

Ultrasonic studies in the critical region can provide valuable information regarding the nature and mechanism of the phase transition (see for example Lüthi and Rehwald, 1981 and Garland, 1970). In particular, the nature of the dominant interactions in the system may be deduced from the functional form of temperature dependences of the ultrasonic velocity and attenuation anomalies. In this regard two papers appeared during the course of this study which both reported studies of the transition in CDP using ultrasonic measurements, but with conflicting conclusions. Yakushkin et al. (1981) (hereinafter cited as Y81) found that the ultrasonic velocity and attenuation anomalies for the ferroelectric b axis could be described by $(T-T_c)^{-\theta}$ type dependences for which the critical indices were found to be unusually large. They also found that the velocity anomalies along the x and z axes could be represented by the usual critical exponent of 0.5 but that the transition region extended over a much broader temperature range than they expected for normal ferroelectrics. On the basis of their analysis they concluded that the normal long-range, 3-D, dipole-dipole interaction is absent in CDP and that the behaviour of the system is similar to one in which short-range interaction forces are dominant.

By contrast, Kanda et al. (1983) (hereinafter cited as K83) found that the critical anomalies are described by a $\log(T-T_0)$ type dependence (where T_0 was determined from a Curie-Weiss fit to the

simultaneously measured dielectric constant). On the basis of their measurements they concluded that the usual dipole-dipole interaction is dominant. In this chapter, the results of this work are compared to the findings of the above-mentioned papers, and suggestions are made to account for the differences in the observed behaviour. Although the quality of the data collected was not sufficient to allow a complete analysis to be carried out, there is evidence to suggest that as $T \rightarrow T_c$ there is a cross-over between regions dominated by different types of interaction forces.

Dielectric measurements, undertaken as an adjunct to the ultrasonic measurements on CDDP, convincingly showed such a cross-over between a region close to T_c dominated by 3-D dipole-dipole interactions and a region further away from T_c dominated by 1-D type interactions.

The thermal expansion measurements also helped to elucidate the transition mechanism via a calculation of the Grüneisen parameters. It was found that close to T_c , CDP behaves as a "uniaxial" crystal whose thermodynamic properties are dominated by the b axis Grüneisen parameter. This is consistent with the known 1-D nature of the ordering in CDP.

6.2 VELOCITY AND ATTENUATION MEASUREMENTS AS A FUNCTION OF TEMPERATURE

6.2.1 Introduction

Small changes in velocity and attenuation as a function of temperature were monitored using the pulse-echo-overlap technique described in Chapter 4. The absolute velocities at room temperature extracted from the plots in this chapter may differ by one r.f. cycle of overlap from the values given in Table 5.1. The discrepancy is due to the fact that the accurate room temperature determination of velocity for a particular mode was not always completed before the temperature

dependent measurements were undertaken. However, since relative precision, rather than absolute accuracy, was required for the latter, the determination of the correct cycle for cycle match was not important, provided that the same overlap condition was maintained throughout a series of measurements.

Since corrections due to losses in the bond have not been applied to the measured value of attenuation, the attenuation coefficient has been plotted as dB/echo rather than dB/cm, so as to indicate clearly that no comparison of absolute values of attenuation is possible between different specimens. However, since only changes in attenuation are important in the context of the critical phenomena, this will not affect the analysis.

The measured quantity for the velocity measurements was the delay time in the specimen, which was converted to a velocity using equation (4.1). The length used in the calculation was measured at room temperature. Corrections to take into account the change in the length due to thermal expansion were found to be negligible in the context of the investigation of the ultrasonic behaviour close to the transition.

6.2.2 Experimental Details

A description of the apparatus used to perform measurements of velocity and attenuation as a function of temperature has been given in section 4.3.4. The problems encountered in making these measurements on CDP are now discussed.

6.2.2.1 Bonding considerations

The most important single factor governing the relative precision to which velocity and attenuation changes as a function of temperature could be monitored, was the quality of the bond between the quartz transducer and the specimen. The reason for this is that if the bond

(and as a result the echo train quality) was poor, the error in the determination of the overlap position was much larger than the figure of 1/100 of one r.f. period mentioned in section 4.1.2(a).

Changes in the bonding properties as a function of temperature often caused difficulty in ascertaining which changes in the velocity and attenuation were due to the bond and which were genuine crystal properties. The attenuation was found to be particularly sensitive to these bond changes because the measured value of attenuation depended not only on the attenuation loss in the crystal, but also on the acoustic coupling in the bond. By comparison, the effect of bond changes on the velocity was small, and was due to the increased attenuation changing the shape of the echo envelope and thus subtly changing the overlap position. However, in some cases, in which the background attenuation due to a poor bond was high, the increased absorption in CDP close to T_c resulted in the echo train being so attenuated that it was impossible to achieve a sensible overlap condition. Thus, for ultrasonic measurements as a function of temperature, it was most important to use a bond which maintained good acoustic coupling between the transducer and the sample over the temperature range of interest.

Finding a suitable bonding material proved to be a very time-consuming task. Initial, unsuccessful attempts were made using a variety of bonding agents commonly employed for ultrasonics at low temperatures such as Dow Corning series 200 fluids (of viscosities ranging from 1000-50000 centistokes), Apiezon grease, Nonaq stopcock grease (Fisher Scientific Company), and Dow Corning 276-V9 resin, as well as solid bonds such as salol, benzophenone, Tarzan's Grip glue, and a range of araldites. All failed on cooling at temperatures between 180 and 240 K. The echo train obtained using the solid bonds deteriorated sharply on cooling as the bond broke. For the bonds which are liquid at

room temperature the usual pattern was that the echo train would begin to deteriorate at temperatures below 200-240 K, and continue to deteriorate on cooling until no echo train at all was detectable below about 180K.

Two of the bonding agents listed above, viz. Apiezon grease and DC 200 fluid (1200 centistokes), were used in measurements on a quartz block and gave excellent echo trains over the range 90-300 K. The DC 200 fluid has been used successfully at liquid helium temperatures (J.A. Rayne 1981, private communication) during measurements on V_3Si . Hence, the deterioration of the echo train cannot be attributed solely to the intrinsic properties of the bond. In view of the large anomalous and anisotropic expansion behaviour in CDP (see section 6.3), it was likely that differential thermal expansion between the quartz transducer and the CDP sample gave rise to a stress on the bond, which, upon further cooling, exceeded the yield stress of the bond, causing it to crack.

During measurements on KDP, Garland and Novotny (1969) also found DC 200 fluids and Nonaq stopcock grease to be unsuitable bonding agents which failed on cooling at 190 K. However, they found that n-propyl alcohol was a suitable bonding agent for shear waves in KDP below 146 K (the freezing point of the alcohol). The use of alcohols was found to be unsuitable for measurements on CDP because the slow cooling rate required to prevent the crystal shattering or cleaving allowed the alcohol to evaporate before it froze. Also, the alcohols did not seem to provide sufficient acoustic coupling to produce good echo trains while still in the liquid state.

Some success was finally obtained using ethylene glycol (1,2-ethane diol, $HOCH_2CH_2OH$), which is a clear viscous liquid with a freezing point of 261 K, and which gave good echo trains at room temperature. The echo train still deteriorated on cooling, but the bond

did not break entirely so that it was possible, although difficult, to monitor attenuation and velocity changes in the vicinity of T_c .

Much better results were obtained using a 50/50 mixture (by volume) of ethylene glycol and methanol. A detailed study of this mixture was not performed, but it is reasonable to assume, by comparison with the properties of aqueous solutions of ethylene glycol (Miller 1969), that the methanol depresses the freezing point of the ethylene glycol considerably, and that the mixture does not form a solid crystalline structure on freezing but rather a glassy layer which is capable of accommodating the thermal stresses discussed above.

Nevertheless, on some temperature runs, this bond also broke. Adjusting the sample holding assembly (Figure 4.12) to provide more even central pressure on the sample resulted in improved echo trains at low temperatures. Hence the bond failure may be due in part to stresses induced on the bond by uneven expansion of the copper sample-holding assembly.

Since 30-50 minutes were required to reach thermal equilibrium following a change in the set-point temperature (see section 4.3.4(d)), temperature runs took many weeks. In general, it was found that if the temperature was kept constant overnight the velocity drift was usually negligible, even close to T_c where the velocity changes sharply as a function of temperature. However, the attenuation drift was often significant. This was assumed to be due to an ageing effect in the bond, the acoustic properties of which change with time due to either the continued stress on the bond, or, possibly, the constant bombardment with the ultrasonic pulses. This effect was displayed as discontinuous jumps in the attenuation versus temperature curves after an overnight break in data collection. Fortunately, however, changes in attenuation in CDP close to T_c are so sharp that in general there was no confusion

between these genuine crystal-dependent effects and the discontinuous jumps in attenuation due to long term ageing effects in the bond properties. Nevertheless, in order to obtain a smooth set of data suitable for fitting to an analytical function, it was desirable to scan as much of the transition region as possible without an overnight break. These considerations strongly indicate the need to automate the measurement system.

6.2.3 Results

6.2.3.1 CDP

The temperature dependence of the velocity and attenuation of longitudinal waves propagating along the y, x, and z axes in CDP are shown in Figures 6.1 - 6.4. The results are presented in the order in which they were taken and hence reflect improvements that were made in the data collection technique during the course of this study. A different specimen was used for each measurement. Part (a) of each figure shows the measurements over the whole temperature range, whilst part (b) shows the transition region in more detail. The z axis measurements (Figure 6.3) showed a very peculiar double anomaly and so the measurements were repeated on a second specimen (Figure 6.4). The data in Figure 6.1 were taken on a cooling run, whilst the data in Figures 6.2, 6.3, and 6.4 were taken on heating runs.

(a) Y axis propagation

The longitudinal mode propagating along the y axis is pure and its velocity is related directly to C_{22} by equation (5.1).

The measurements in Figure 6.1 represent one of the earliest successful attempts of this study to measure the velocity and attenuation close to T_c . The bonding material used was pure ethylene

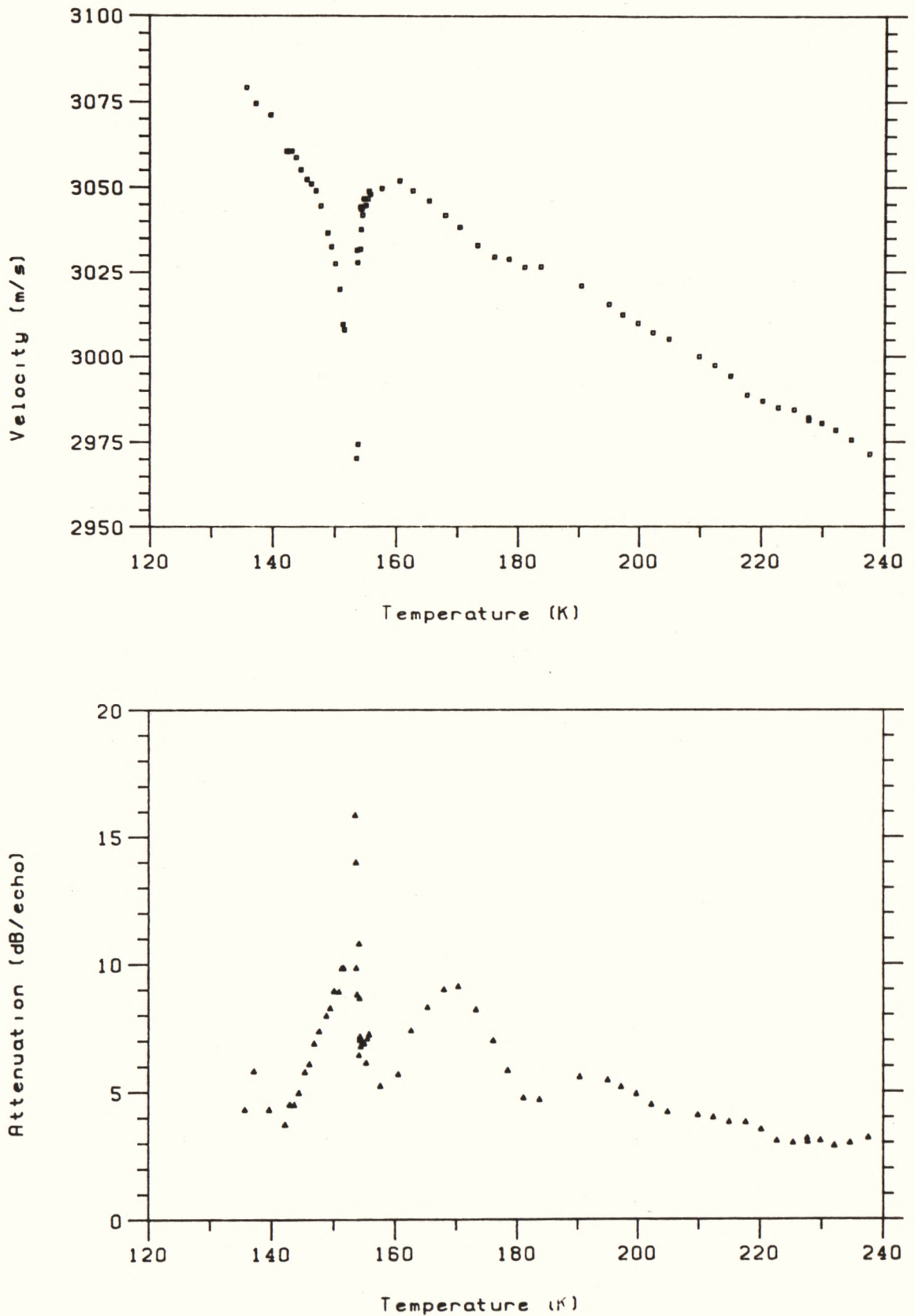


Figure 6.1(a). Temperature Dependences of the Velocity and Attenuation of Longitudinal Waves Propagating along the Ferroelectric y axis in CDP.

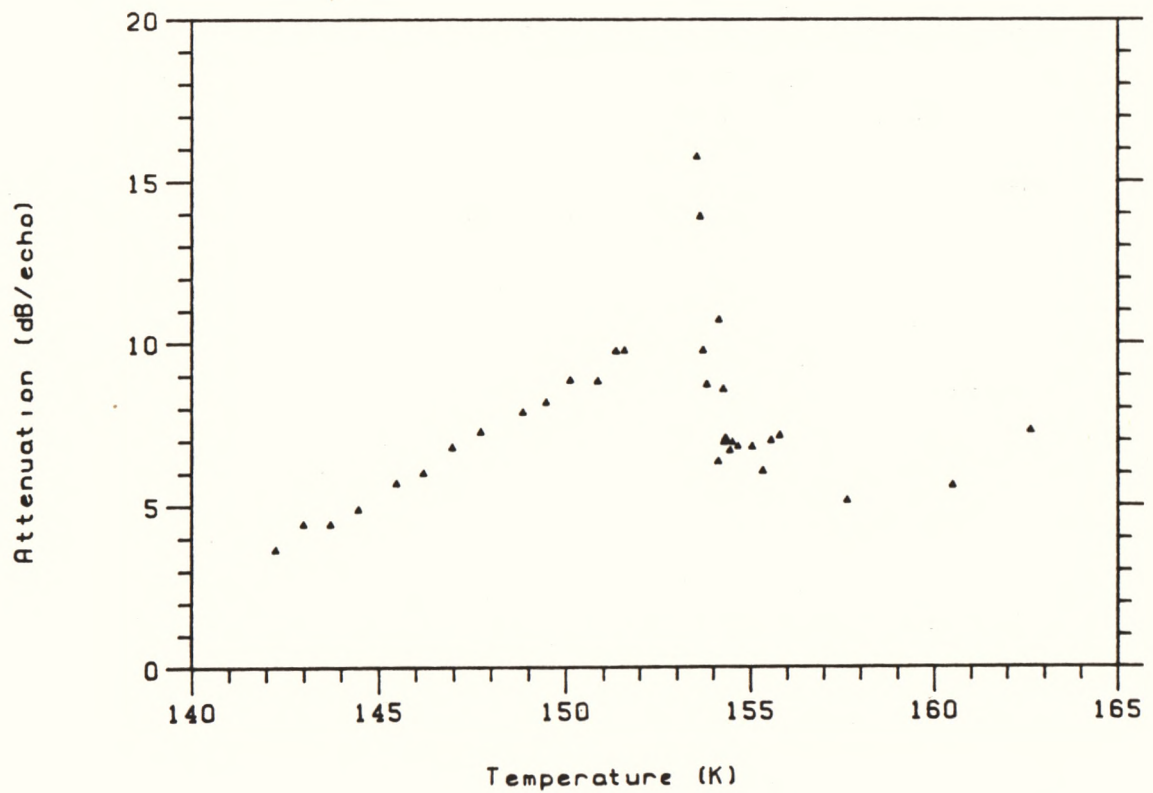
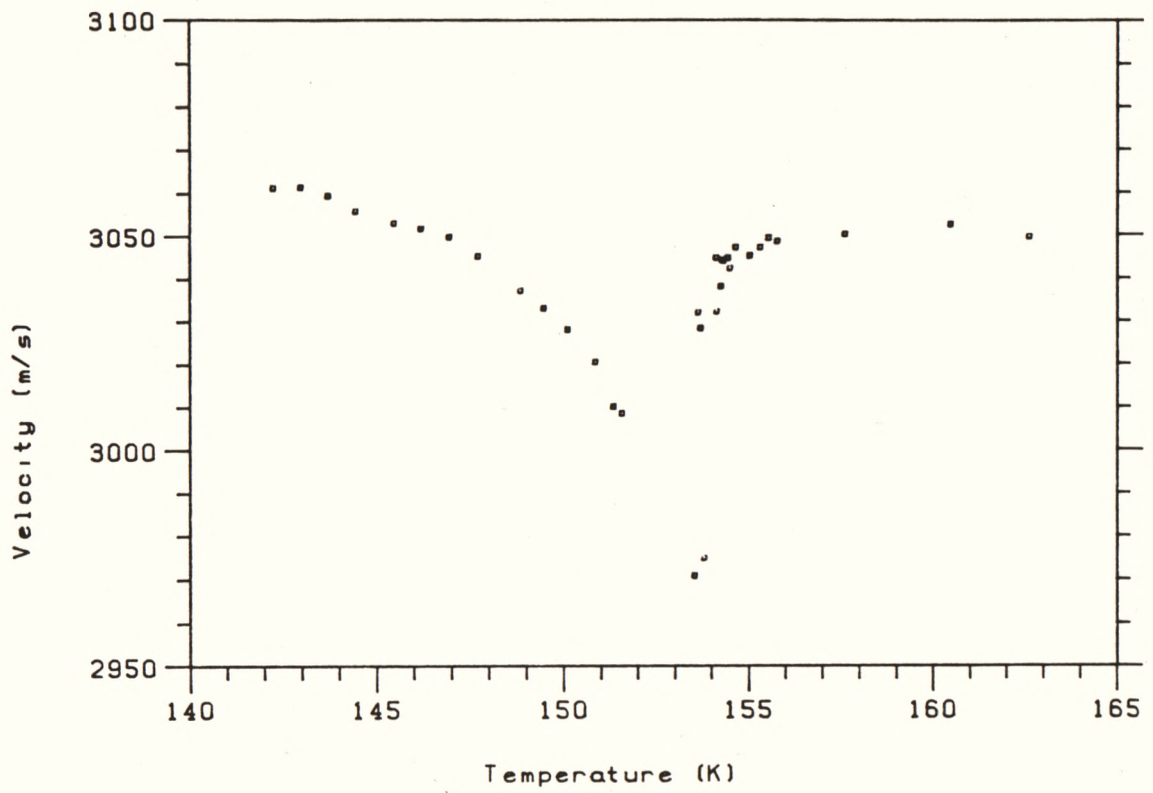


Figure 6.1(b). The Transition Region of Figure 6.1(a) Shown in Greater Detail.

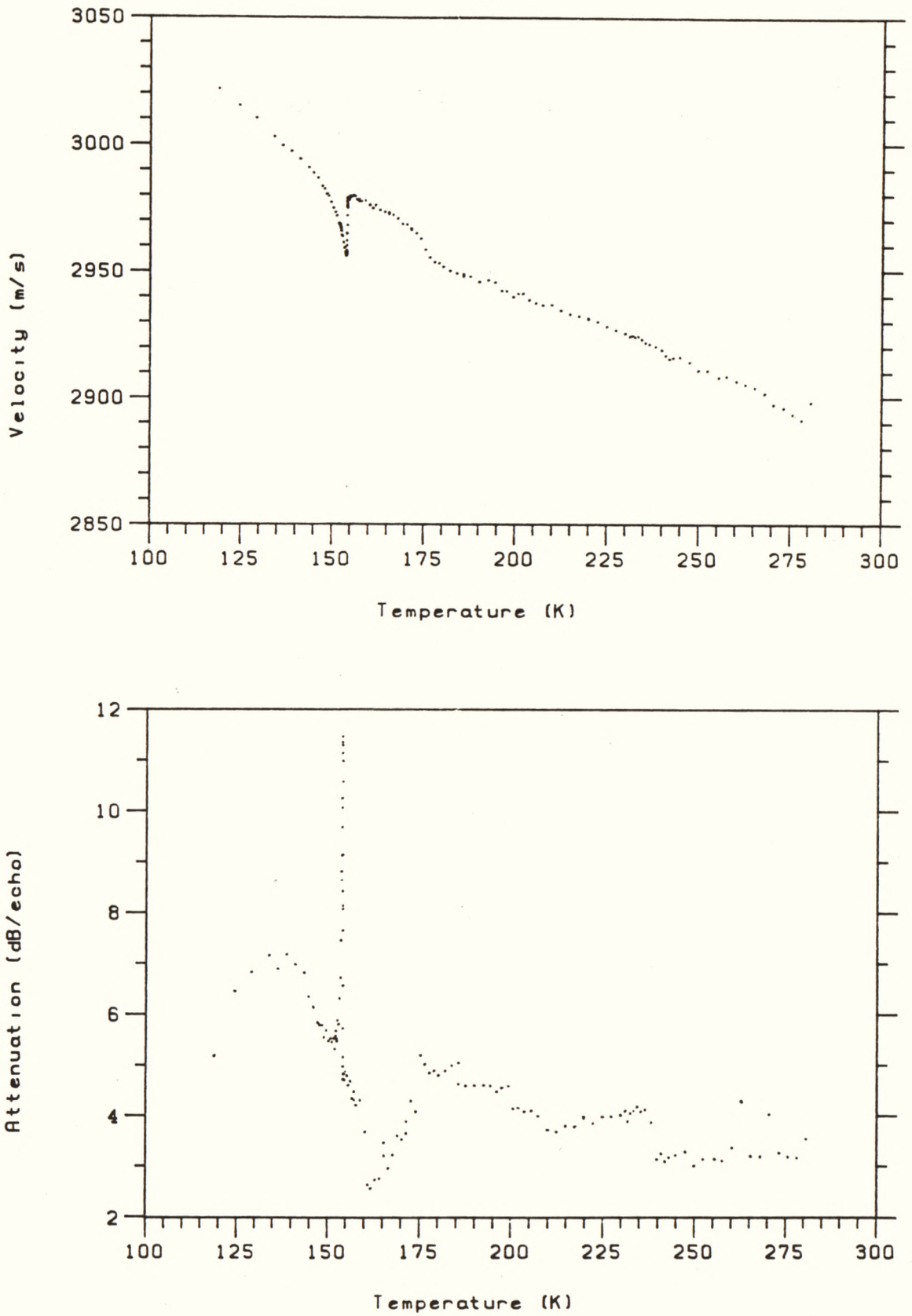


Figure 6.2(a). Temperature Dependences of the Velocity and Attenuation of Longitudinal Waves Propagating along the x axis in CDP.

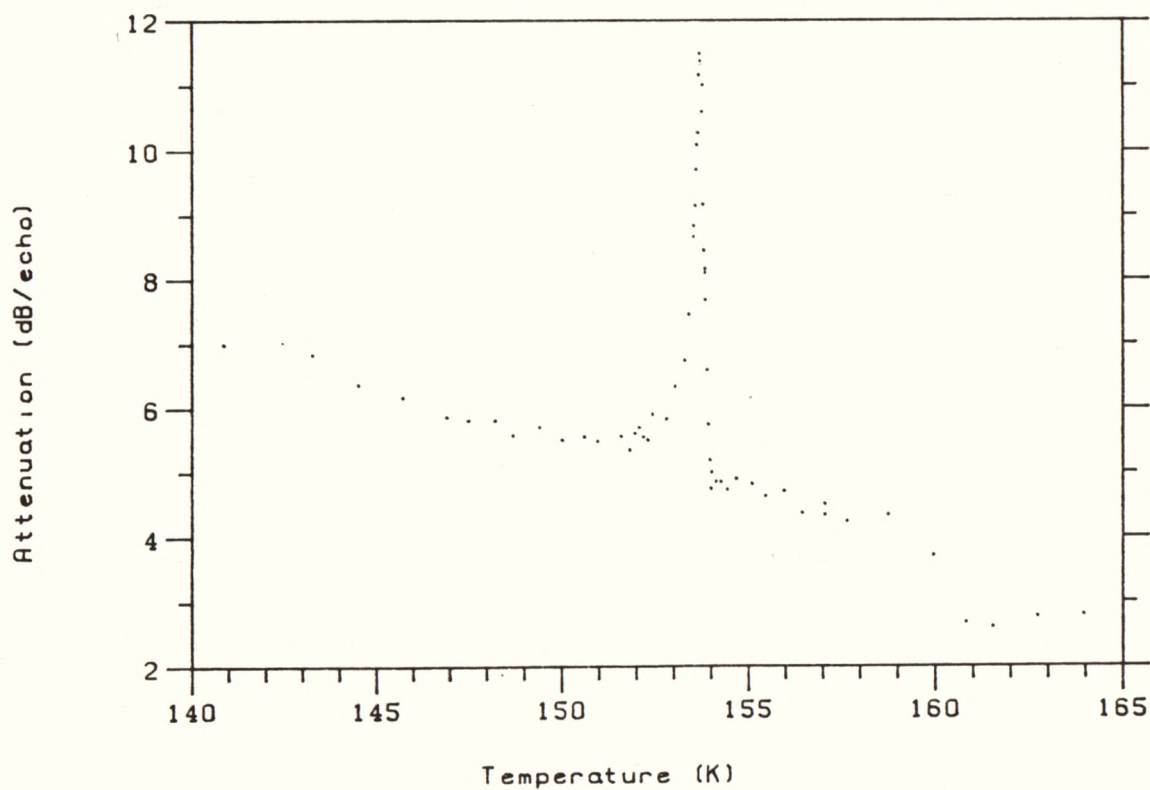
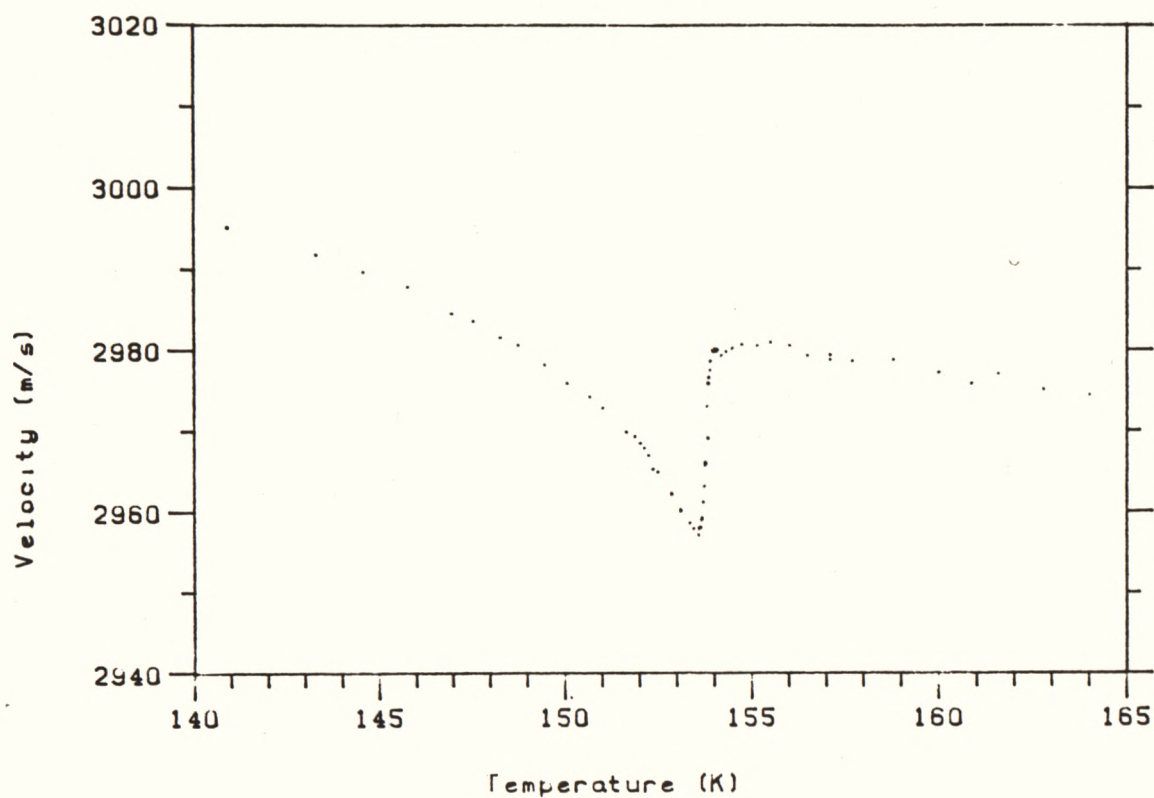


Figure 6.2(b). The Transition Region of Figure 6.2(a) Shown in Greater Detail.

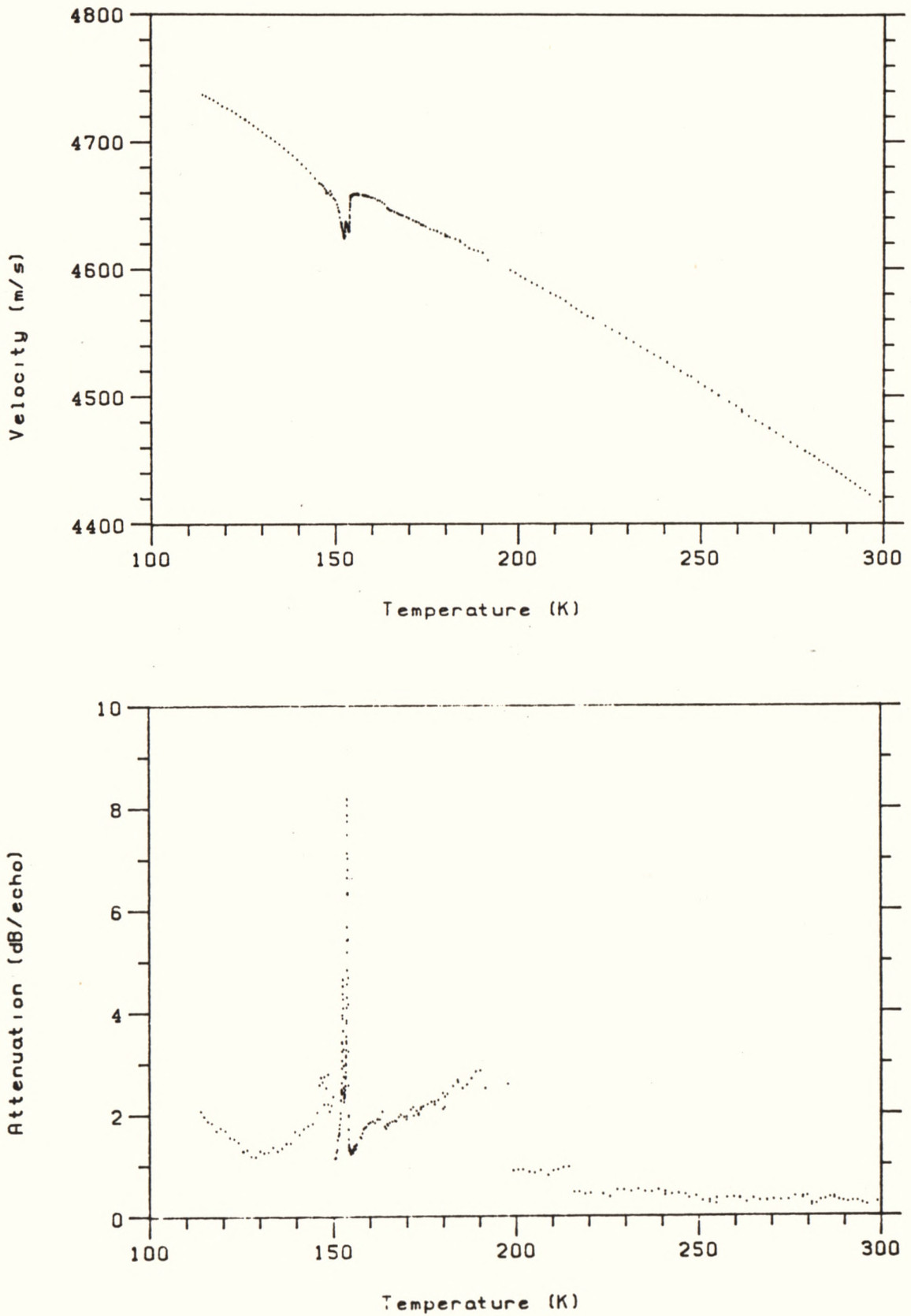


Figure 6.3(a). Temperature Dependences of the Velocity and Attenuation of Longitudinal Waves Propagating along the z axis in CDP.

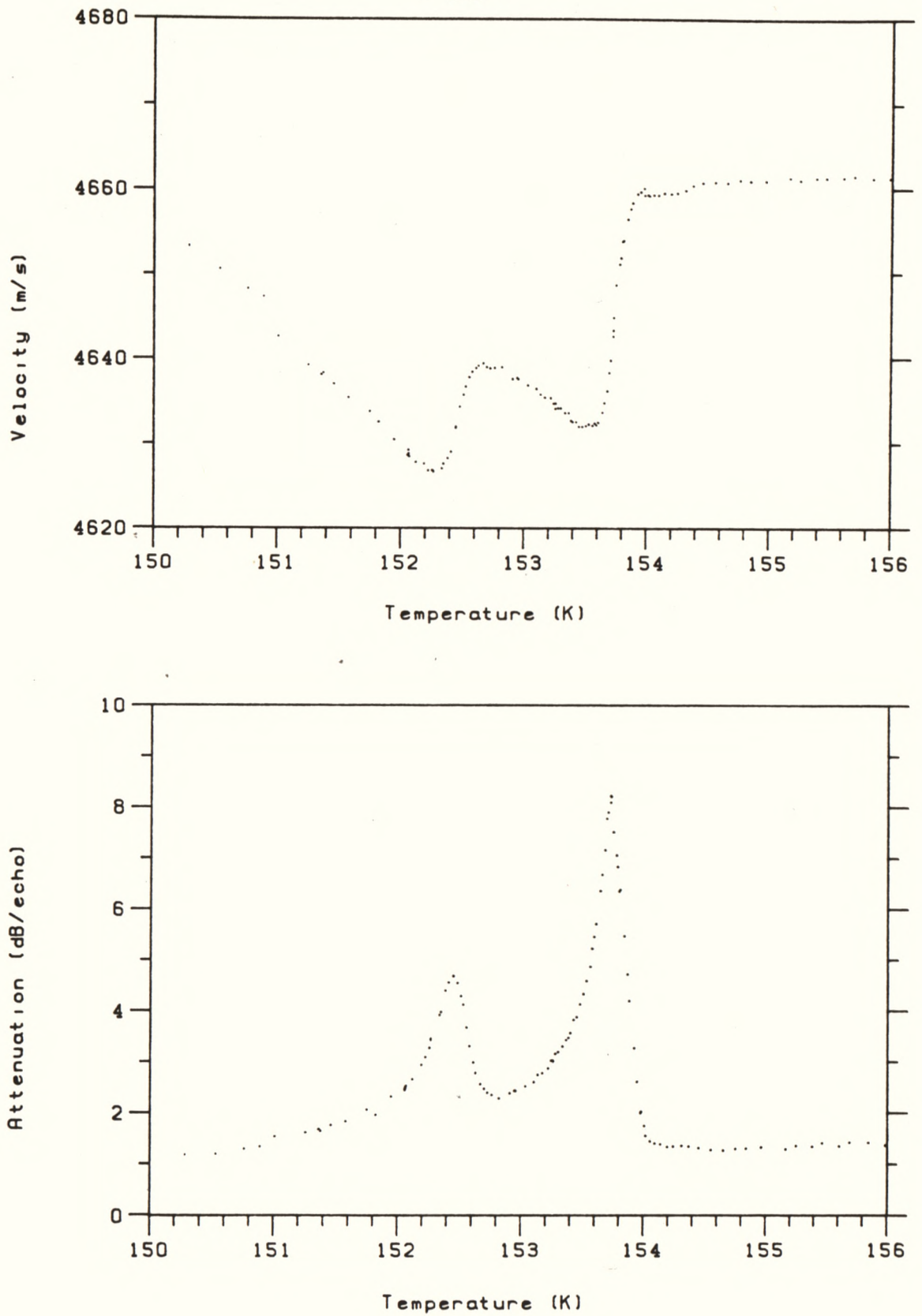


Figure 6.3(b). The Transition Region of Figure 6.3(a) Shown in Greater Detail. Note the second anomaly occurring 1.3° below T_c .

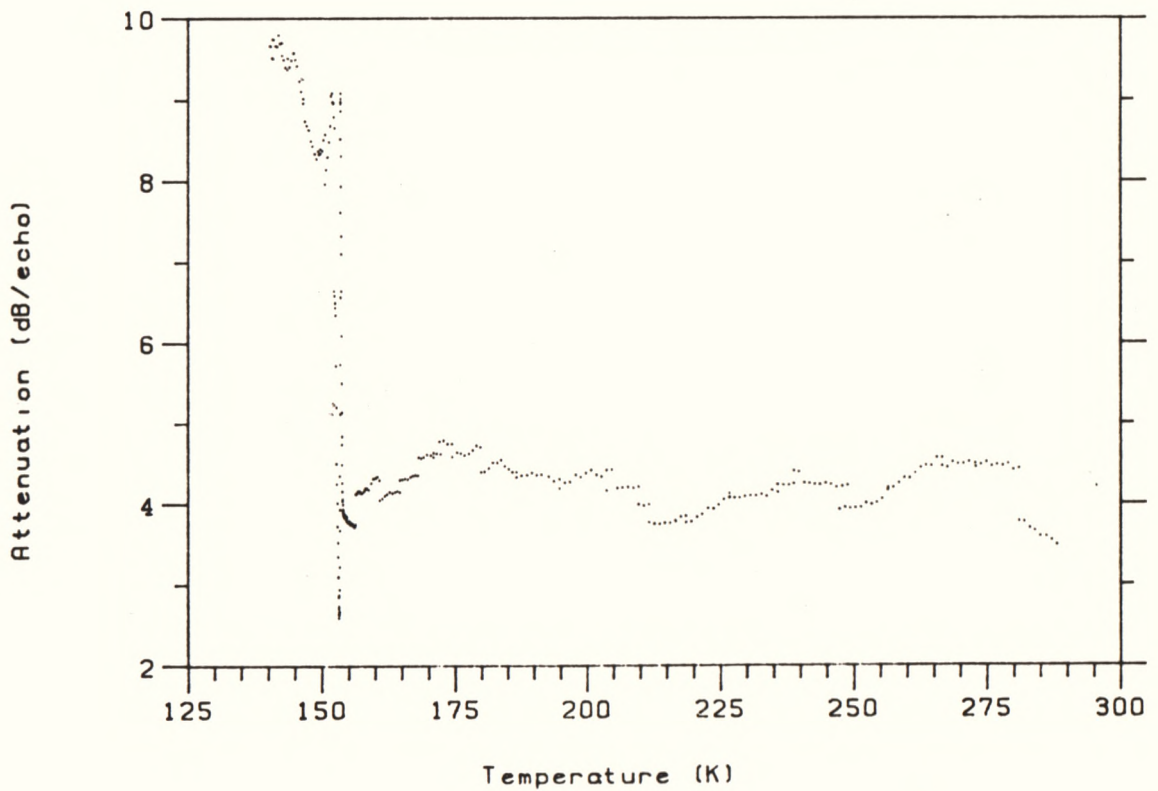
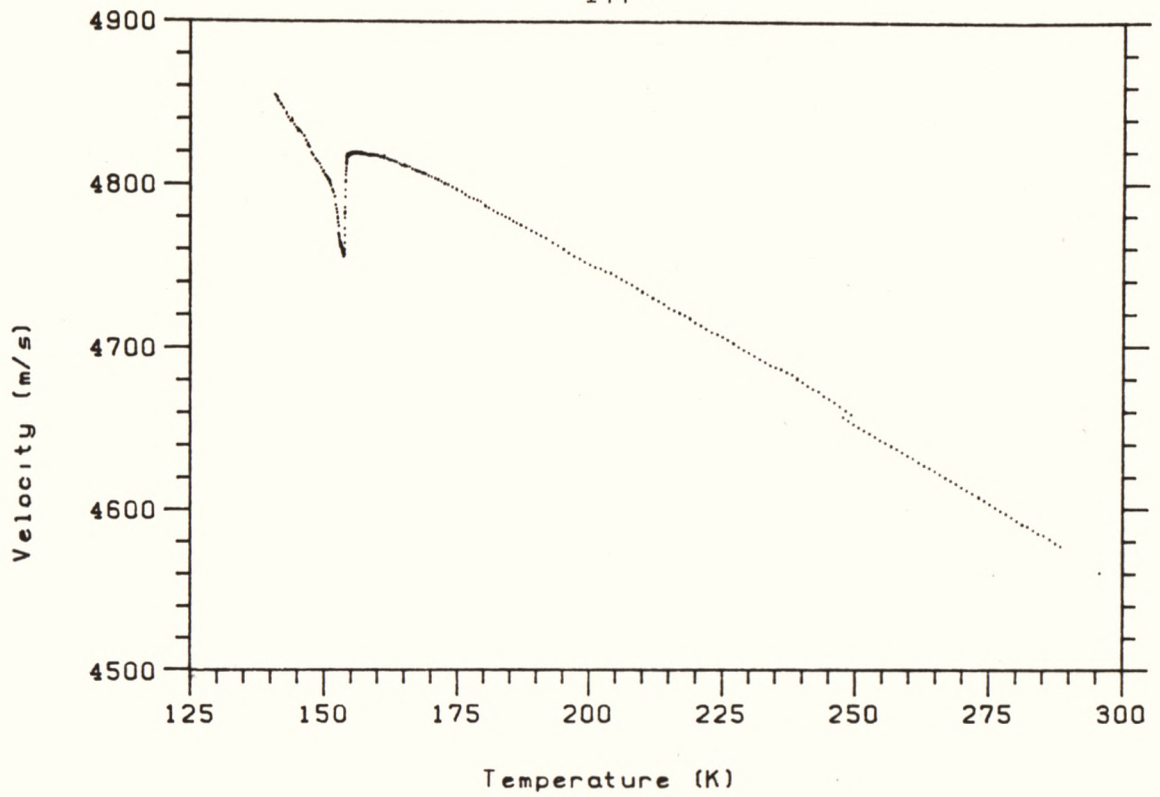


Figure 6.4(a). Temperature Dependences of the Velocity and Attenuation of Longitudinal Waves Propagating along the z axis in CDP.

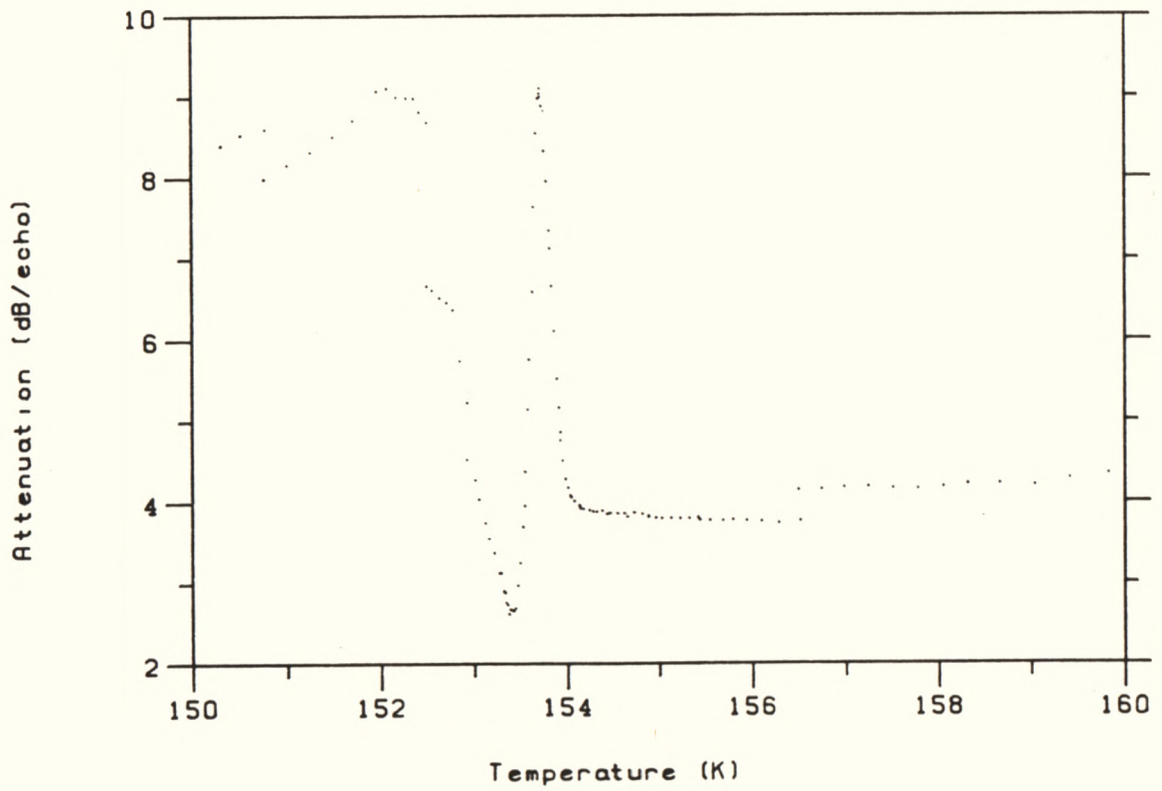
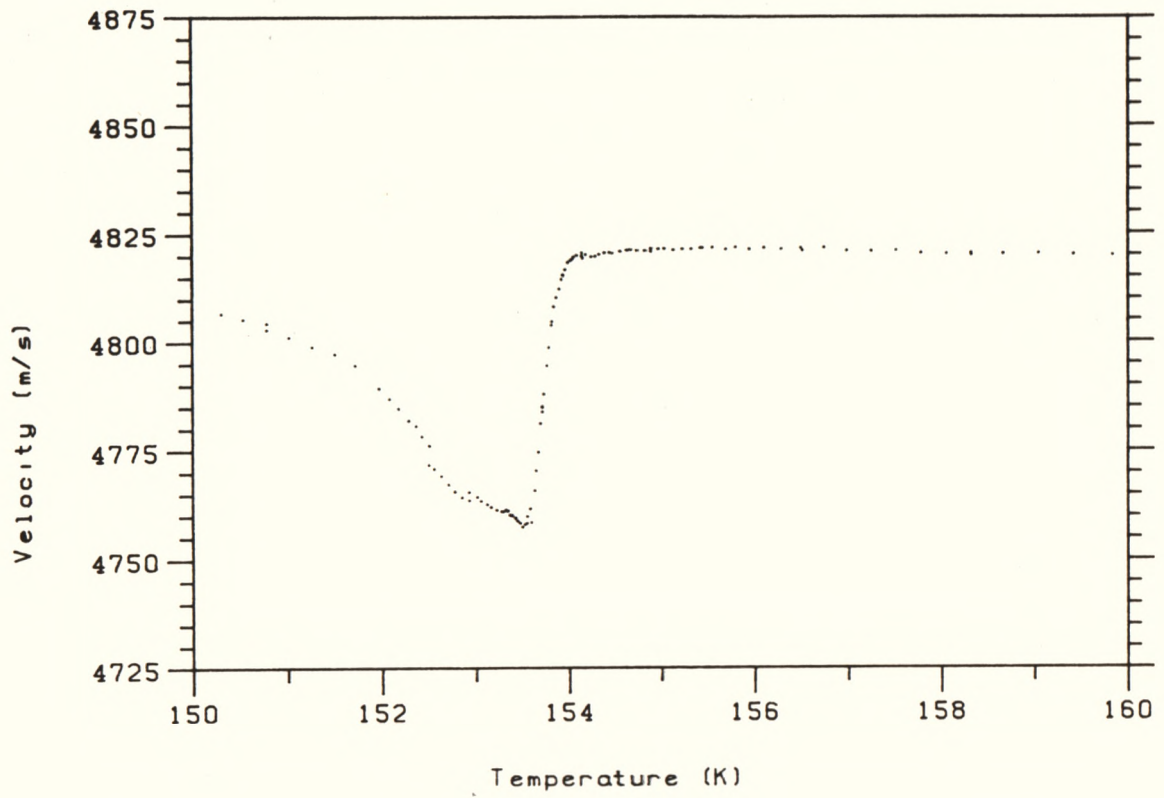


Figure 6.4(b). The Transition Region of Figure 6.4(a) Shown in Greater Detail.

Also, due to bonding problems, the data corresponding to the Y axis heating run (not shown in the thesis) were not of sufficient quality to ascertain if any hysteresis effects were present.

glycol which gave poor echo trains compared those achieved with the ethylene glycol-methanol mixture used in later runs for propagation along the x and z axes. Also, at this early stage of the work, the temperature controlling and measurement systems had not yet been developed to the extent that it was possible to monitor the velocity and attenuation close to T_c . Because of these limitations it was not possible to perform a critical point analysis on this data. INSERT

Nevertheless, it is clear that the velocity deviates from a reasonably linear background at about 160 K and decreases sharply at 155 K, reaching a minimum at 153.5 ± 0.5 K. The corresponding attenuation anomaly is sharper than this, with the attenuation rising from a background of about 6.5 dB/echo at 154.5 K to a maximum of 16 db/echo at 153.5 ± 0.5 K (Figure 6.1(b)).

At about 180 K there is a noticeable change of slope in the velocity dependence, and an associated change in attenuation. This corresponded to a weakening of the bond which was observed as a deterioration of the echo train as the sample was cooled below 180 K.

The anomaly for $T < T_c$ is much broader than that for $T > T_c$. It appears that the velocity slowly "recovers" its linear temperature dependence following the transition. Since this velocity is directly related to C_{22} , this implies that the elastic behaviour of the ferroelectric state well below T_c is not very different from the behaviour of the paraelectric state reported in Chapter 5.

(b) X axis propagation

The temperature dependence of velocity and attenuation for x axis propagation (Figure 6.2) displays the same general features as for the y axis. The data of Figure 6.2 show less scatter than those in Figure 6.1 because the ethylene glycol-methanol bond gave better echo trains over

Unfortunately, the data corresponding to the cooling run for this mode (not shown in thesis) were not of sufficient quality to ascertain if any hysteresis effects were present.

the whole temperature range than were obtained for the y axis measurements. Also, in this run it was possible to monitor velocity and attenuation changes much closer to T_c . However, the discontinuities in attenuation discussed above in section 6.2.2.1 are clearly visible in Figure 6.2(a).

The velocity decreases sharply at 154 K, reaching a minimum at 153.54 ± 0.05 K. The attenuation anomaly is very sharp, with a maximum at 153.71 ± 0.05 K. The background to the attenuation anomaly is reasonably described by a linear function of temperature in the range 145-160 K. The decreasing attenuation in this region as the sample was warmed was due to an improvement in the properties of the bond as evidenced by an observed improvement in the echo train quality. INSERT

As in Figure 6.1, there is a change of slope in the temperature dependence of the velocity in Figure 6.2 at about 180 K, associated with changes in the bond properties as evidenced by observed changes in the echo train quality. However, unlike the y axis measurements, Figure 6.2(a) shows a decrease, rather than an increase in attenuation below 180 K. Unfortunately, the change of slope in the velocity caused difficulties in fitting a linear temperature dependent background to the velocity anomaly at 154 K. This change of slope at 180 K for x and y axis propagation may be due to changes in the z axis thermal expansion coefficient. This possibility is discussed further in section 6.3.

(c) Z axis propagation

Figure 6.3 shows the temperature dependence of the velocity and attenuation for the semi-pure mode propagating along the z axis. The bond of ethylene glycol-methanol gave very good echo trains over the temperature range of interest and hence the small degree of scatter in the data compared to Figures 6.1 and 6.2. As in Figure 6.2, there are

Similarly, to within the experimental precision of 0.1K, no hysteresis was observed in the temperature at which the velocity reaches its minimum value.

discontinuous jumps in the attenuation.

The velocity is once again reasonably described by a linear function of temperature in the region 180-250 K. The velocity deviates from the linear background at about 180 K, and, as for the y and x axis measurements, shows a sharp decrease at 154 K, reaching a minimum at 153.5 ± 0.1 K. However, as is clear from Figure 6.3(b), there is an unexpected second anomaly in the velocity with a minimum at 152.28 ± 0.08 K. Also unexpectedly, there are two peaks in the attenuation at 153.73 ± 0.03 K and 152.45 ± 0.03 K. This "double" anomaly was observed on both heating and cooling the specimen, and within the experimental precision of 30 mK, no hysteresis in the peak positions of the attenuation anomalies was observed. INSERT

Because of the unexpected nature of the double anomaly, it was necessary to repeat the measurements on a different sample (Figure 6.4). The second sample showed only one anomaly, with the maximum in attenuation occurring at 153.71 ± 0.03 K and the minimum in the velocity at 153.5 ± 0.1 K. The sharp decrease in attenuation at 152.5 K was accompanied by a sudden change in the echo train quality after leaving the sample overnight at the same set-point temperature. The small discontinuity in the velocity just below 250 K was due to an electrical mishap which allowed the specimen to warm up to room temperature before measurements were resumed after recooling the specimen to 247 K.

Since the measured temperature gradient across the sample was less than 0.2 K, the second anomaly 1.28 K below T_c cannot be attributed to temperature inhomogeneities in the specimen. The "double" anomaly effect, whilst clearly not found in both specimens investigated, is worthy of further investigation because the sample which gave the "double" anomaly gave reasonably sharp extinction between crossed polarizers, indicating good single crystallinity, and the room

temperature value of velocity in the specimen agreed within experimental error (i.e. one r.f. cycle of overlap) to the one quoted in Table 5.2 for the same mode. Hence, there was nothing to suggest that the sample should not have been used for ultrasonic measurements.

It is possible that this second anomaly is connected with the structural reconstruction of the domain walls in CDP as reported by Kamysheva et al. (1981). They found that (i) CDP has a very "soft" domain structure (i.e. a domain structure very sensitive to external influences such as radiation), (ii) the domain walls have very high mobility, as evidenced by very high dielectric loss in the ferroelectric state, (iii) the coercive field is close to zero at temperatures 3-5 K below the transition, and (iv) for samples that had been irradiated (so as to introduce defects) there were large fluctuations in the pyroelectric coefficient in the region between T_c and T_f , where T_f is the "freezing" point of the domain structure. These observations all suggest that it is not difficult (from the energetic point of view) to rearrange the domains in the ferroelectric state of CDP. The second anomaly may then be attributed to a rearrangement of the domain structure leading to changes in the macroscopic surface charge, which may either occur spontaneously on cooling the system, or may be induced by the stress wave used for the measurement.

The work of Kamysheva et al. (1981) also suggests that the behaviour of the domains is very dependent on the defect concentration, and, therefore, it is reasonable to assume that defects introduced randomly into the specimens during the growing or polishing processes may account for the appearance of the second anomaly in only one of the specimens studied. This hypothesis could be tested by annealing the specimen and remeasuring the temperature dependence of the velocity and attenuation. However, before attempting this, it would be very

interesting to measure the temperature dependence of the dielectric behaviour of this specimen to see if there is evidence of the soft domain structure similar to that reported by Kamysheva et al. (1981).

Finally, it would be very interesting to measure the velocity of waves propagating along the x and y axes in the specimen which displayed the "double" anomaly (although the specimen used is probably too small to carry out both these measurements). The absence of a double anomaly for the x and y directions would show that there is considerable texture associated with the domain formation. The investigation could be extended by attempting to deliberately produce "double" anomaly specimens by introducing defects using γ -ray irradiation in a manner similar to that described by Kamysheva et al. (1981).

6.2.3.2 CDDP

Limitations on time did not permit the measurement of all three longitudinal waves in CDDP. Measurements for propagation along the x axis were chosen because the specimen could be easily and quickly prepared using the (100) cleavage faces.

The room temperature value of the velocity of the semi-pure longitudinal wave propagating along the x axis was measured to be $3.049 \pm 0.006 \times 10^3 \text{ m s}^{-1}$, which is in excellent agreement with the velocity of this mode in CDP. This is not surprising, since CDP and CDDP are isomorphic and are expected to be described by the same elastic constants.

Figure 6.5 shows the temperature dependence of the velocity and attenuation of this mode. As expected, the anomaly occurs at a much higher temperature than for CDP. If it is assumed that a linear relationship exists between the transition temperature for the deuterated crystal, T_c^d , and the degree of deuteration, then the

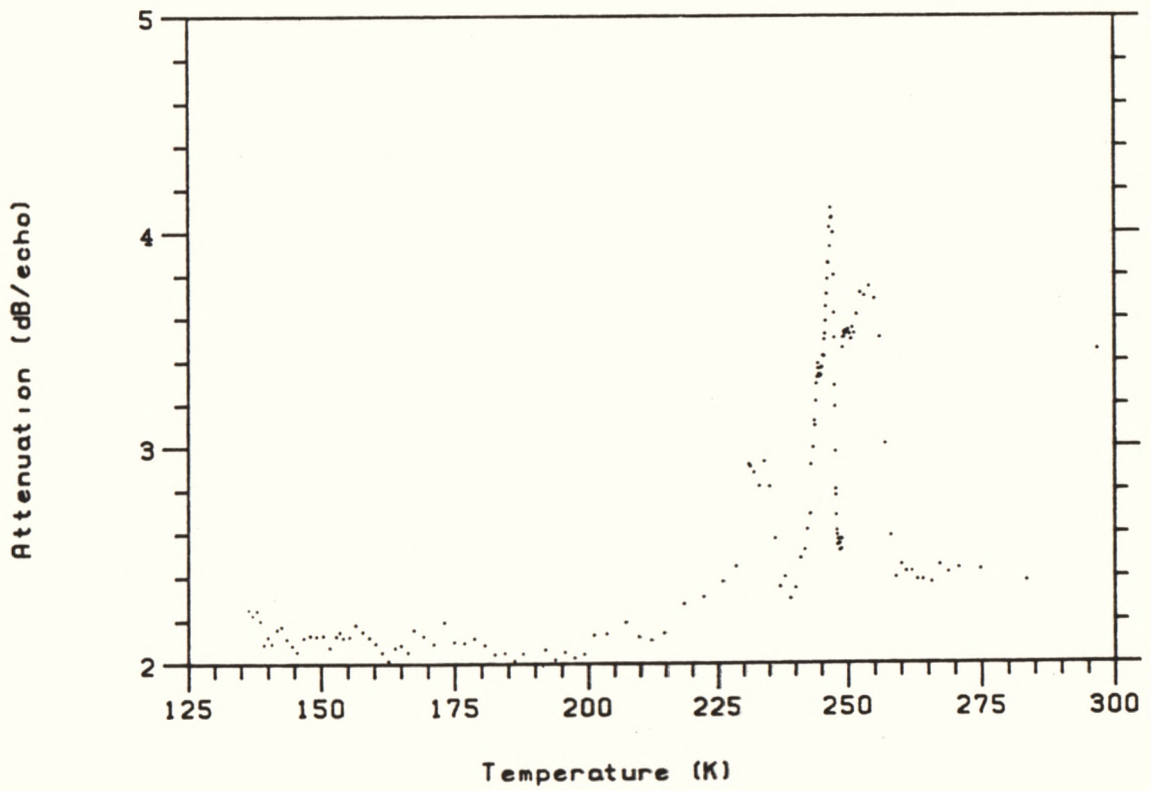
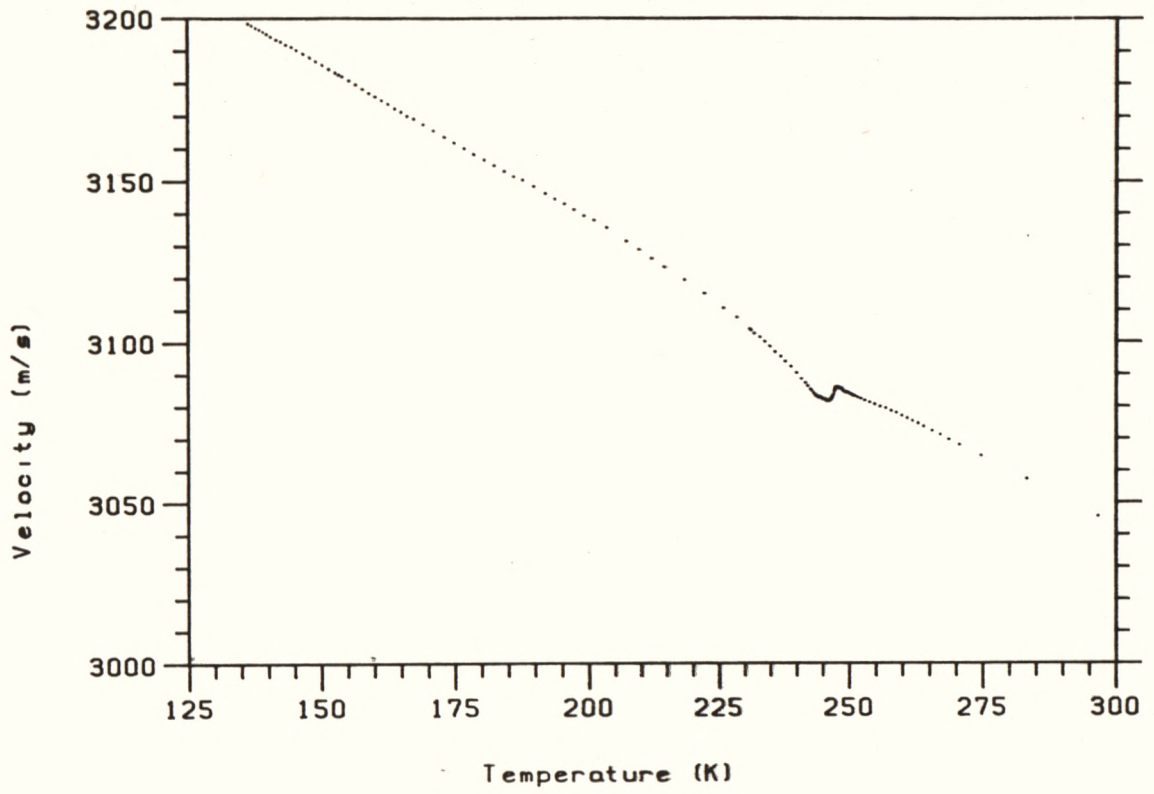


Figure 6.5(a). Temperature Dependences of the Velocity and Attenuation of Longitudinal Waves Propagating along the x axis in CDDP.

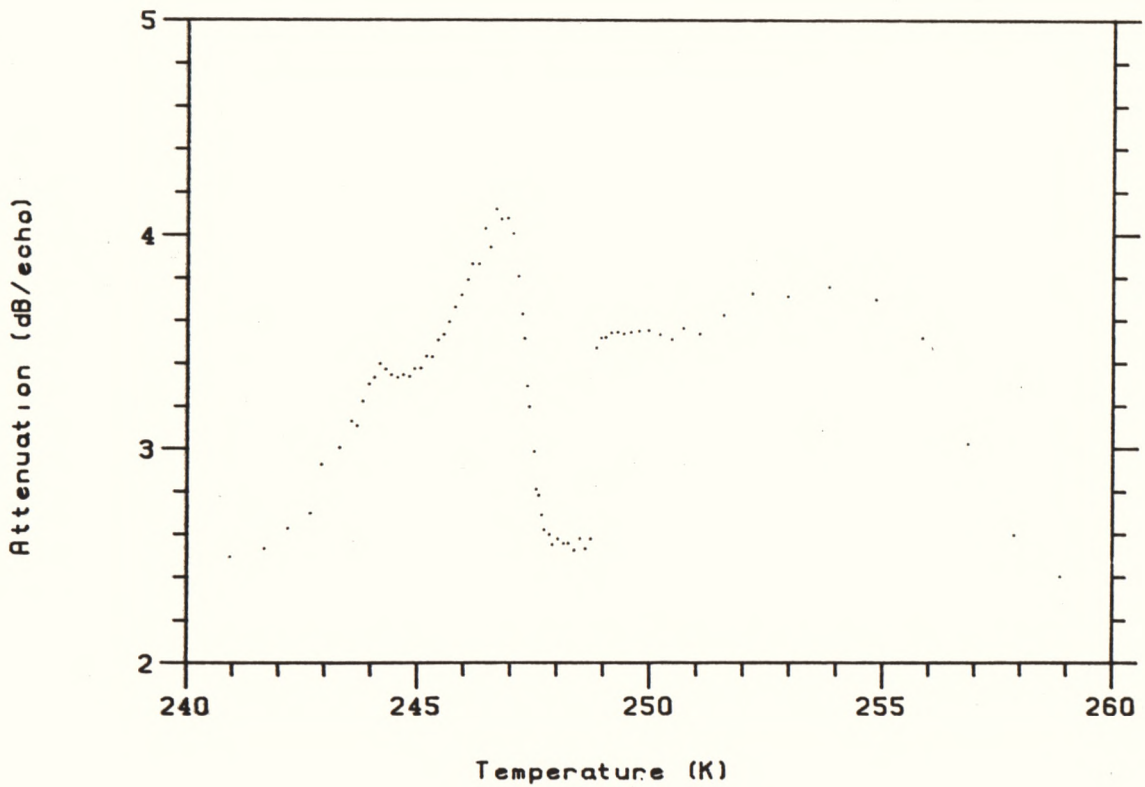
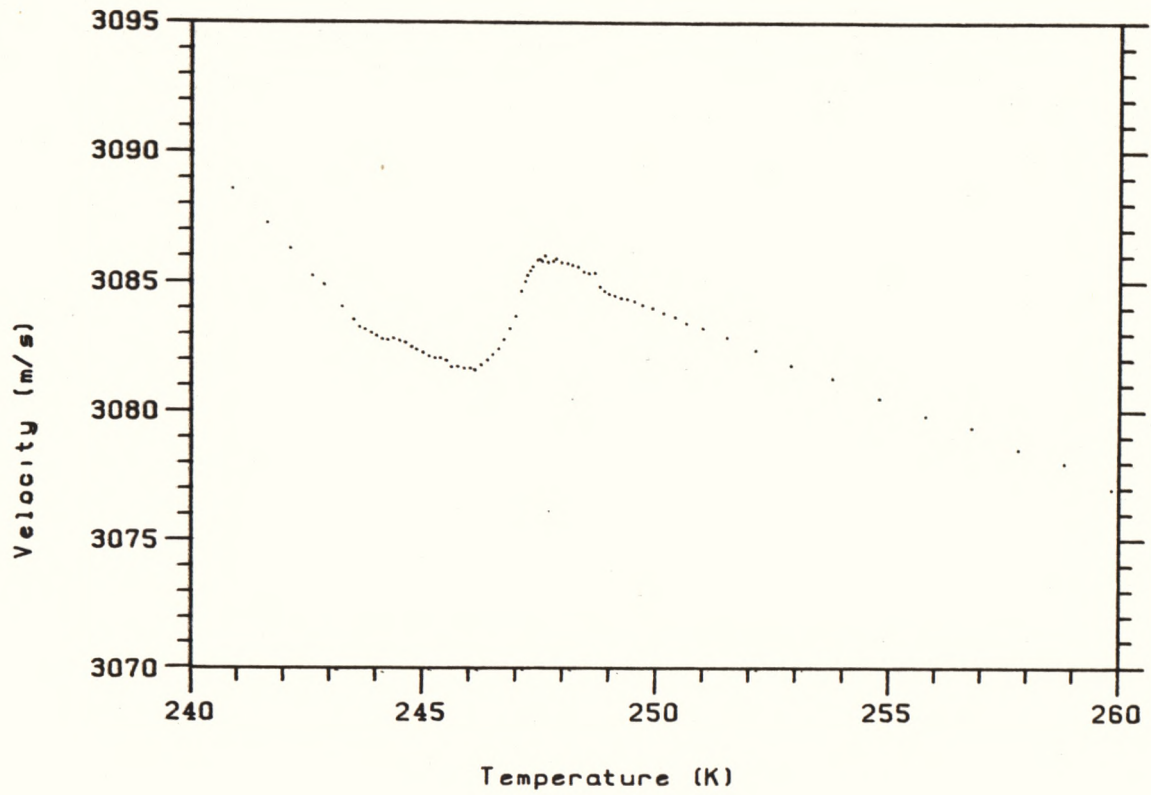


Figure 6.5(b). The Transition Region of Figure 6.5(a) Shown in Greater Detail.

approximate transition temperature of 247 K implies a deuterium concentration of about 80%. However, Baranov et al. (1980) report that $T_c^d = 240$ K for a deuterium concentration of 57%, although the authors do not explain how they determined the deuterium concentration. In any case it is clear that considerable hydrogen contamination has occurred either during the growing process or during the subsequent cutting and polishing (see section 3.5).

The anomaly is much smaller and broader than the comparable anomaly in CDP (see Figure 6.2). The maximum in the attenuation occurs at 246.8 ± 0.2 K, and the minimum in the velocity at 246.1 ± 0.4 K. However, the measured transition temperature differed by up to 3 K between different runs on this sample. In particular, measurements taken on cooling displayed attenuation peaks of about twice the width of that shown in Figure 6.5, which is from a heating run. It is not clear why the attenuation peak should be sharper on heating runs than on cooling runs, and why these effects should be observed in CDDP and not in CDP. However, in view of the very long-term relaxation effects discussed in section 6.4, it is possible that these irregularities are in some way connected with the very soft domain structure of CDDP (see also Baranov et al. 1983).

The discontinuity in the attenuation at 249 K (Figure 6.5(b)) was associated with a large change in the bond properties after a break in data collection over the 48 hour period of the weekend. The shoulder in the attenuation at 244 K was not associated with any bond changes. However it must be regarded as spurious because it was not reproducible on cooling the sample and because there was no accompanying velocity change.

Finally, the smooth temperature dependences of velocity and attenuation in the region 130-200 K in Figure 6.5 confirm that the

anomalies in Figures 6.1-6.4 are due to changes in the properties of the CDP crystal, rather than any intrinsic changes in the ethylene glycol-methanol bond. However, it must be stressed that this does not imply that every observed anomaly is automatically attributable to changes in the elastic properties of the sample, because, as seen above, changes in the acoustic properties of the bond caused by the expansion behaviour of the specimen will also appear as anomalies in the velocity and attenuation. For example, the change in slope in the velocity at about 180 K in Figures 6.1 and 6.2 is accompanied by a change in the quality of the observed echo train, indicating a change in the properties of the bond. This change in the bond quality has been correlated to a decrease in the z axis expansion coefficient at this temperature (see section 6.3).

6.2.4 Discussion

6.2.4.1 General features of the critical region

The major parameters relating to the transition region shown in Figures 6.1-6.5 are summarized in Table 6.1. From the table it is clear that T_c , as measured by the peak in the attenuation anomaly, is 153.72 ± 0.03 K. The attenuation peak width in the table refers to the approximate temperature range of anomalous behaviour for $T > T_c$, because in most cases the wing of the attenuation peak is not well defined for $T < T_c$. With regard to the velocity anomaly in CDP, the quoted width in the table refers to the region of the very sharp dip in the velocity from about 154 K to the temperature at which the velocity reaches its minimum value, and not to the broad region in which the velocity slowly deviates from its linear background. Because the temperature control and measurement systems had not been perfected at the time of the y axis measurements to the extent that it was possible to measure the velocity

Table 6.1

Parameters Relating to the Transition Region.

PROPAGATION DIRECTION	ATTENUATION ANOMALY			VELOCITY ANOMALY		
	PEAK POSITION (K)	PEAK WIDTH T>T ^c (K) ^c	PEAK HEIGHT %	POSITION OF VELOCITY MINIMUM (K)	WIDTH OF ANOMALY (K)	SIZE OF ANOMALY %
<u>CDP</u>						
Y	153.5 ±0.5	~1	146	153.5 ±0.5	~1.5	2.7
X	153.71±0.05	0.3	139	153.54±0.05	0.5	0.8
Z						
Sample 1:						
Anomaly 1:	153.73±0.03	0.4	530	153.5 ±0.1	0.5	0.6
Anomaly 2:	152.45±0.03	0.35	104	152.28±0.08	0.4	0.3
Sample 2:	153.71±0.03	0.5	139	153.5 ±0.1	0.6	1.3
<u>CDDP</u>						
X	246.8 ±0.2	1.2	64	246.1 ±0.4	1.8	0.13

and attenuation close to T_c (see section 6.2.3.1(a)), the widths of the anomalies in Table 6.1 for this propagation direction are only rough estimates, and are probably considerably greater than the true widths of the anomalies.

(a) Size of anomalies and corresponding atomic displacements

If the z axis specimen displaying the "double" anomaly is disregarded for purposes of comparison, Table 6.1 indicates that the major difference in the ultrasonic measurements for propagation along the different axes in CDP is the size of the velocity anomaly, with the largest anomaly occurring for the ferroelectric y axis. This result may be correlated to the results of Iwata et al. (1980) who measured the atomic displacements occurring during the transition. As mentioned in Chapter 1, they found that, apart from the ordering of the hydrogens at T_c and a 3° rotation of the PO_4 tetrahedra, the transition is accompanied by a 0.06 Å displacement of the P atom along the y axis and a 0.04 Å displacement of the Cs atom along the z axis. In view of the long wavelengths of the ultrasonic waves, it seems reasonable to assume that the velocity and attenuation will be much more sensitive to microscopic translations of the atoms than to the ordering of the hydrogens. Hence, one might expect the largest anomaly for propagation along the y axis (corresponding to the P atom displacement), with the second largest anomaly occurring for z axis propagation (corresponding to the Cs atom displacement). The last column of Table 6.1 shows that this is actually the case. The ratio of the size of the y axis anomaly to that for the z axis is about 2. Considering the non-rigorous nature of this line of reasoning, this seems to be in reasonable agreement with the ratio of the size of the P atom displacement to that of the Cs atom of $0.06/0.04 = 1.5$. The smallest anomaly occurs along the x axis, and in

the present context this is understood to be due to the small displacements of the atoms in this direction which are associated with the 3° rotation of the PO_4 tetrahedra.

(b) Comparison of the anomalies in CDDP and CDP

It is clear from the table that the anomaly in CDDP is much broader and shallower than that for the corresponding mode in CDP. Such a broad, shallow anomaly has also been reported by Kasahara and Tatsuzaki (1982) for a CDDP crystal with $T_c^d = 260$ K. Also, their results show, as does Figure 6.5, that in contrast to the velocity measurements on CDP, there is no broad temperature region in which the velocity slowly deviates from a linear background. Whilst it is reasonable to expect that, due to its greater mass, the deuterium in CDDP will order at a higher temperature than the hydrogen in CDP, it is not clear why deuteration should "wash out" the anomaly. The basic question here, which is still unresolved in the literature, is whether or not the essential nature of the transition mechanism is changed by partial or complete deuteration. As an example of the conflicting evidence appearing in the literature, the dielectric measurements of Deguchi et al. (1982(a),1982(b)) on CDP and CDDP suggest that there is no essential change in the transition mechanism, although they do point out (Deguchi et al. 1982(b)) that the one-dimensional Ising model used to describe the transition in CDP needs modification if it is to account completely for the effects of deuteration on the behaviour of the dielectric constant. By contrast, Baranov et al. (1980) found that the shape of the temperature dependence of the dielectric constant changes significantly with deuteration. They suggest that increasing the deuterium concentration results in an enhancement of the interchain coupling.

The analysis of the critical region of the ultrasonic measurements in CDP and CDDP has the potential to shed light on this question of the possible effects of deuteration on the transition mechanism. If the ultrasonic anomalies for CDP and CDDP are found to share a common functional form, it would be very reasonable to conclude that the two salts share essentially the same transition mechanism. The converse is also true, although any differences in the measured critical exponents would have to be interpreted cautiously. Unfortunately, due to the lack of data of sufficient quality, the critical point analysis of this study (see following section) failed to determine conclusively the functional form of the anomalies in CDP and CDDP for x axis propagation. There is a need to extend the measurements to other propagation directions and to samples of different degrees of deuteration.

If, in fact, the transition mechanisms in CDP and CDDP are the same, and, as suggested above, the size of the anomaly is related to the size of the atomic displacements occurring during the transition, then one may expect that the displacements of the P and Cs atoms will be much smaller in CDDP than in CDP. Unfortunately, this hypothesis cannot at present be compared to experiment, as, to the best of the author's knowledge, work similar to that of Iwata et al. (1980) in determining the atomic displacements in CDP at T_c has not been reported for CDDP.

(c) Relationship between velocity and attenuation anomalies

It is clear from Figures 6.1-6.5 and Table 6.1 that the attenuation peak occurs at a higher temperature than the minimum in the velocity. This observation prompted a closer look at the transition region, which revealed that the attenuation appears to be proportional to the temperature derivative of the velocity in the region of the very sharp anomaly of the latter from 153.5-154.2 K. As an illustration,

Figure 6.6 shows this region for the z axis specimen of Figure 6.4. A similar relationship exists for the other propagation directions, although the poor temperature resolution of the y axis measurements (Figure 6.1) obscures the effect. In fact this view of the attenuation as being proportional to the slope of the very sharp velocity anomaly, seems even to extend to each of the two anomalies of Figure 6.3, and also to the CDDP specimen (Figure 6.5).

This relationship between velocity and attenuation is not surprising if they are viewed as being measures of the real and imaginary parts respectively of a generalized complex elastic constant. Thus viewed, any softening of the elastic behaviour must be accompanied by both velocity and attenuation anomalies. This linkage of the elastic response function (i.e. the velocity) to the loss mechanism (i.e. the attenuation) may be analogous to the well-known Kramers-Kronig relationships which link the real and imaginary part of the complex dielectric constant (see for example Kittel 1976), although it must be pointed out that the Kramers-Kronig relationships usually describe the response of the system as a function of frequency rather than temperature.

K83 measured the ultrasonic velocity and attenuation for both monodomain and polydomain specimens of CDP. The monodomain state was achieved at each temperature by applying an electric field to the specimen along the b axis, and then reducing it to zero before taking the elastic or dielectric measurement. They assumed that if such a field is not applied, the specimen is in a polydomain state. (According to K83, then, the present study was carried out using polydomain specimens.) They observed that, for the polydomain specimen, the peak in the attenuation occurred at a higher temperature than the minimum in the velocity and at a lower temperature than the maximum in the

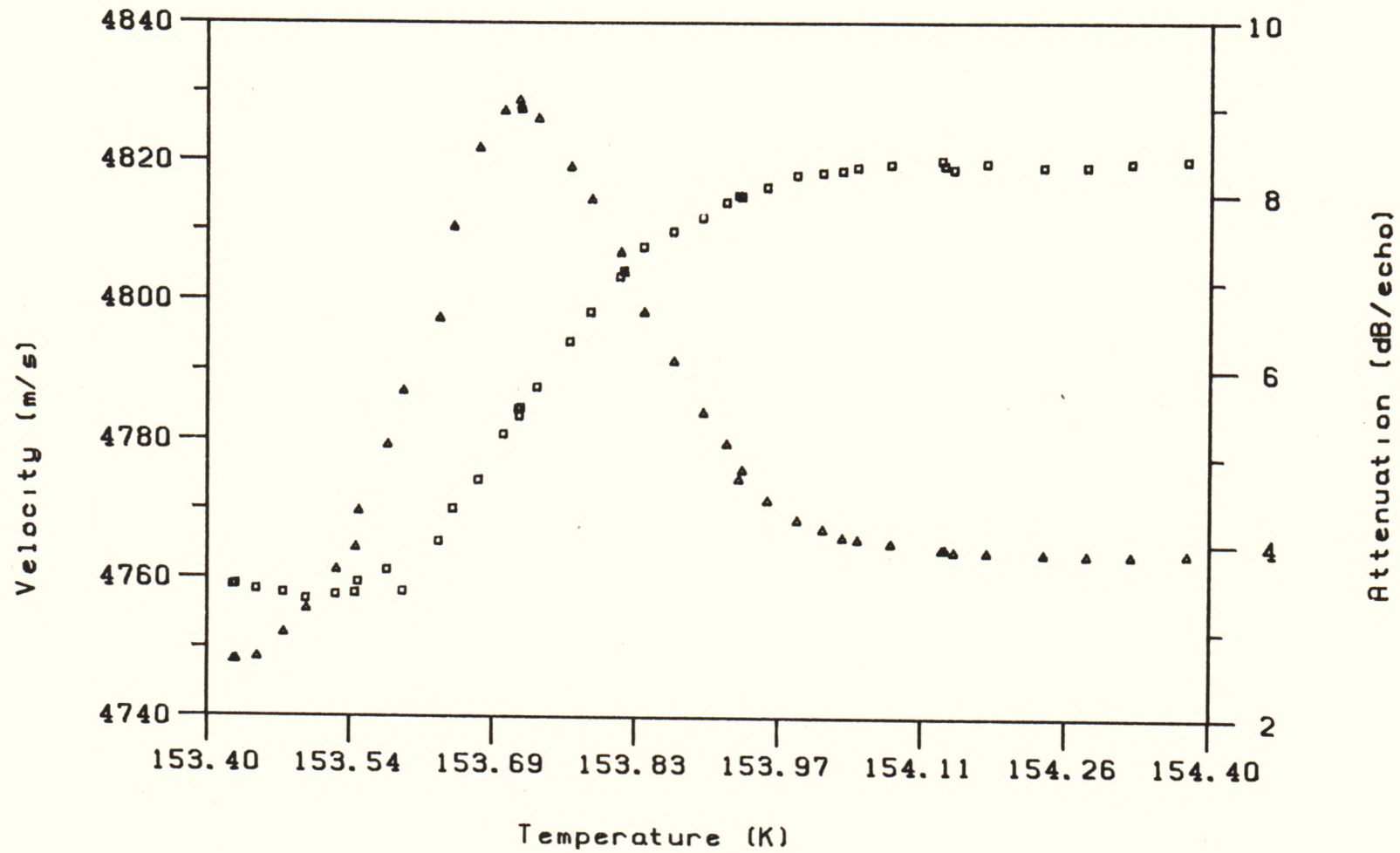


Figure 6.6. The Temperature Dependences of the Velocity (□) and Attenuation (Δ) Close to T_c for z axis Propagation in CDP. The plot suggests that the attenuation is proportional to the temperature derivative of the velocity.

simultaneously measured dielectric constant. By contrast, for the monodomain specimen, the peak in the attenuation and the dielectric constant and the minimum in the velocity all occurred at the same temperature. The anomalies for the monodomain specimen were found by them to be considerably smaller than those for the polydomain specimen, and also of a considerably different shape.

These observations may be understood in terms of the "soft" domain structure of CDP. In the polydomain state, since the peak in the attenuation occurs below the ferroelectric transition (as measured by the peak in the dielectric constant), it is reasonable to assume that the energy of the ultrasonic wave is being absorbed by the crystal in domain formation, growth, reconstruction or alignment. Normally one might not expect there to be enough energy in the ultrasonic wave to effect such changes in the domain structure but, as pointed out above, the coercive field is known to be close to zero near T_c (Kamysheva et al. 1981). For the monodomain state, the field applied to produce the monodomain state presumably supplies most of the energy to effect these changes in the domain structure. Hence, the ultrasonic anomalies for the monodomain specimen are smaller than those for the polydomain specimen and, in the absence of domain effects, the peak in the attenuation coincides with the maximum in the dielectric constant and the minimum in the velocity.

Hence, in summary, it may be said that the non-coincidence of the maximum in the dielectric constant with the minimum in the velocity is evidence of a domain wall effect in the ferroelectric state. This lends further support to the hypothesis (section 6.2.3.1(c)) that the second anomaly for z axis propagation (Figure 6.3) is indeed due to a reconstruction of the domain walls.

Finally, it is interesting to note that K83 could not stabilize

the monodomain state after reducing the field to zero. This seems to be consistent with the very "soft" domain structure mentioned above, and furthermore is consistent with the observed non-stability of the dielectric constant close to T_c^d in CDDP due to a very long-term relaxation effect (see below section 6.4).

6.2.4.2 Critical point analysis

(a) The present study

The anomalous part of the velocity, ΔV , in the critical region was defined to be the difference between the measured velocity and the linear background extrapolated from a region far above the transition (185-250 K for CDP). Figure 6.7 shows $\log \Delta V$ and ΔV plotted as functions of $\log (T-T_c)$ for the critical region of Figure 6.4 (z axis). In the absence of simultaneously measured dielectric data, T_c was taken to be the temperature of the maximum in the attenuation. It is clear from the figure that ΔV does not obey the power law $(T-T_c)^{-\theta}$, nor does it satisfy a $\log (T-T_c)$ type dependence over the whole temperature range. There is a clear change in the functional dependence at $\Delta T = T-T_c \approx 0.40$ K, which corresponds to the temperature at which the abrupt change in the temperature dependence of the velocity anomaly occurs (at about 154 K for CDP). However, there is a $\log \Delta T$ type dependence in the range $0.40 < \Delta T < 15$ K (Figure 6.7(b)). Figure 6.7(a) does suggest that in the range $0.08 < \Delta T < 0.40$ K, the data may be described by a $\Delta T^{-\theta}$ dependence where $\theta = 0.5 \pm 0.1$, although it must be pointed out that this dependence should be considered unconfirmed, since the linear portion of the fit in Figure 6.7(a) only extends over half a decade.

The anomalous part of the attenuation, $\Delta \alpha$, was defined (in a manner similar to that for ΔV) to be the difference between the measured attenuation and the (nearly constant) background extrapolated into the

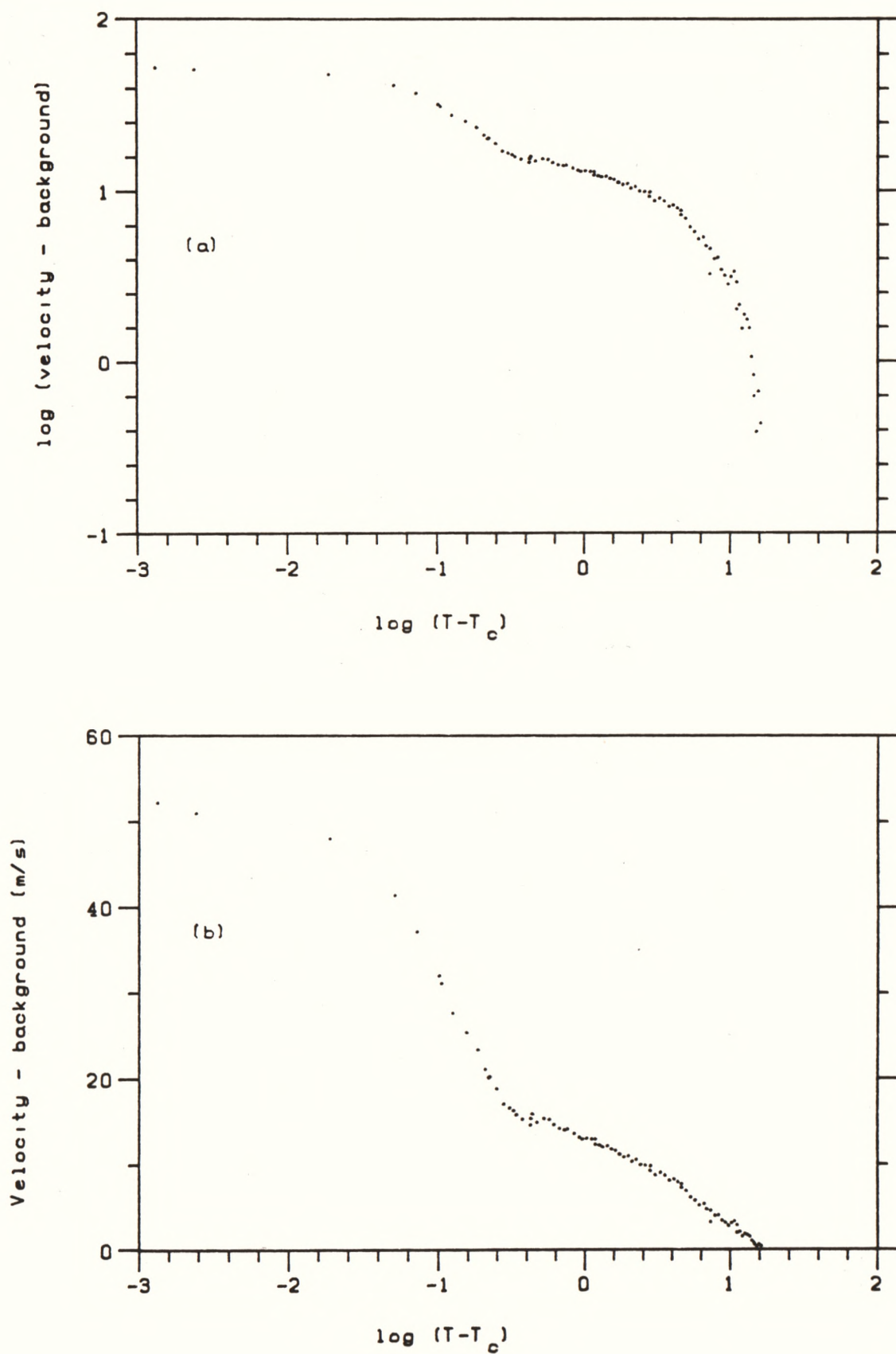


Figure 6.7. Log-log (a) and Linear-log (b) Plots of the Anomalous Part of the Velocity in the Critical Region for the z axis Data of Figure 6.4.

critical region. Figure 6.8 shows a plot of $\log \Delta\alpha$ versus $\log \Delta T$ and $\Delta\alpha^{1/2}$ versus $\log \Delta T$ for the attenuation data of Figure 6.4. (K83 found that the latter relationship well described their anomalous attenuation data.) It is clear from Figure 6.8(b) that $\Delta\alpha$ is not well described by a $\log^2 \Delta T$ type dependence. Figure 6.8(a) suggests that a $\Delta T^{-\phi}$ type dependence is a possibility for the range $0.19 < \Delta T < 0.47$ K where $\phi = 3.3 \pm 0.5$. This is a very large value for a critical exponent. As for the velocity measurements, it should again be noted that the linear region in Figure 6.4(a) only extends over about half a decade and hence the power law dependence must be considered unconfirmed. However, in this case, the narrowness of the linear region and the large value of the critical exponent are to be expected in view of the very sharp and narrow nature of the attenuation anomaly, which only begins to deviate from the background at 0.4 K above T_c . Some rounding of the attenuation peak is inevitable due to sample defects and inhomogeneities. It is possible that with improved precision in temperature control and measurement the linear region of the fit may extend closer to T_c , but it is likely that the limitations imposed by sample quality will prevent the observation of the power law dependence for ΔT less than about 10 mK.

Very similar results were obtained for the analysis of the anomaly occurring at the higher temperature in Figure 6.3. For the velocity anomaly the results were $\Delta V \sim \Delta T^{-\theta}$, $\theta = 0.35 \pm 0.1$ in the range $0.05 < \Delta T < 0.40$ K and $\Delta V \sim \log \Delta T$ in the range $0.40 < \Delta T < 10$ K, and, for the attenuation anomaly, $\Delta\alpha \sim \Delta T^{-\phi}$, $\phi = 4.3 \pm 0.5$ in the range $0.20 \Delta T < 0.50$ K. Once again the power law dependences must be considered to be unconfirmed since they only extend over half a decade. Nevertheless, the consistency between the two measurements on different samples lends some support to justify accepting the regions of power law

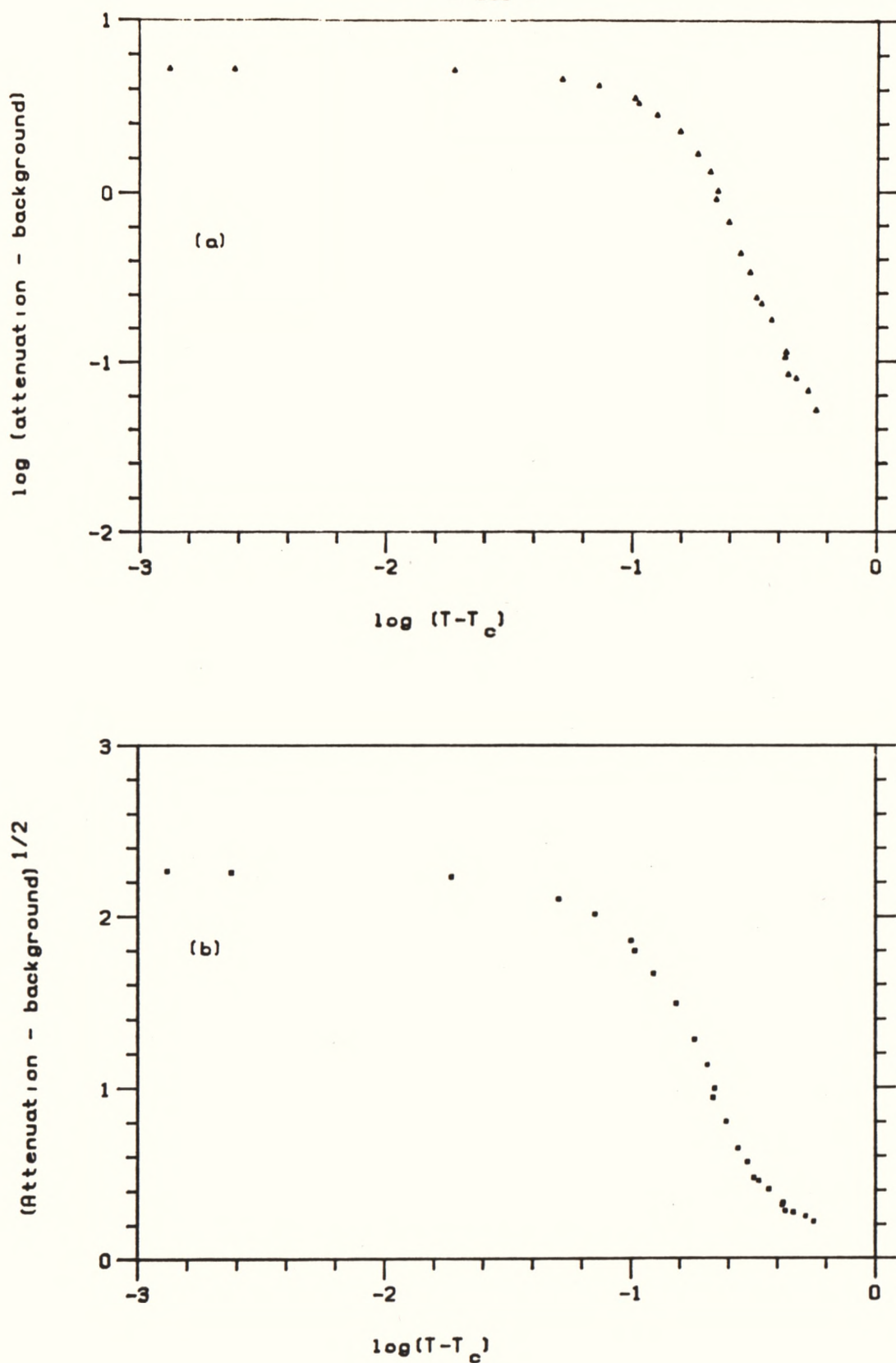


Figure 6.8. The Anomalous Part of the Attenuation $\Delta\alpha$ in the Critical Region for the x axis Data of Figure 6.2 plotted as (a) $\log(\Delta\alpha)$ versus $\log(T-T_c)$ and (b) $\Delta\alpha^{1/2}$ versus $\log(T-T_c)$.

The critical point analyses were repeated using a range of values for T_c . It was found that the derived functional forms were not sensitive to the choice of T_c . However the exact value of the derived critical exponents did vary with T_c . This variation is included in the above quoted errors for the critical exponents.

dependences as genuine. INSERT

Although bonding problems obscure the true behaviour of the attenuation over a wide temperature range in Figures 6.3 and 6.4, it appears that the slow deviation of the velocity from its linear background (described by the $\log \Delta T$ type dependence) is unaccompanied by any genuine attenuation anomaly. (The measurements of K83 and Y81 confirm this observation.)

In summary, then, and keeping in mind the reservations expressed above as to the narrowness of the regions of apparent power law dependences, it may be said that the measurements along the z axis display two distinct regions in which the functional forms of the anomalies are quite different. In the region further away from T_c , ΔV is described by a $\log \Delta T$ dependence and is unaccompanied by any significant attenuation anomaly. In the region closer to T_c , ΔV seems to be described by a power law with the critical exponent having the classical value of 0.5, accompanied by a very sharp attenuation anomaly described by an unusually large value of the critical exponent. These observations suggest that different interaction forces are dominant in each of the two regions of the velocity anomaly.

A similar analysis was attempted for the x axis data of Figure 6.2, and is shown in Figure 6.9 and 6.10. It is clear from the plots that the data were not of sufficient quality for the analysis to be meaningful. The major difficulty encountered here, apart from the obvious poor temperature resolution compared to that obtained for the z axis measurements of Figures 6.3 and 6.4, was the change of slope in the velocity at 180 K which made it impossible to carry out the analysis of the region in which there is a slow deviation of the velocity from its linear background. The best that can be said of the analysis is that if a $\Delta T^{-\phi}$ dependence does exist for the attenuation anomaly (and this is

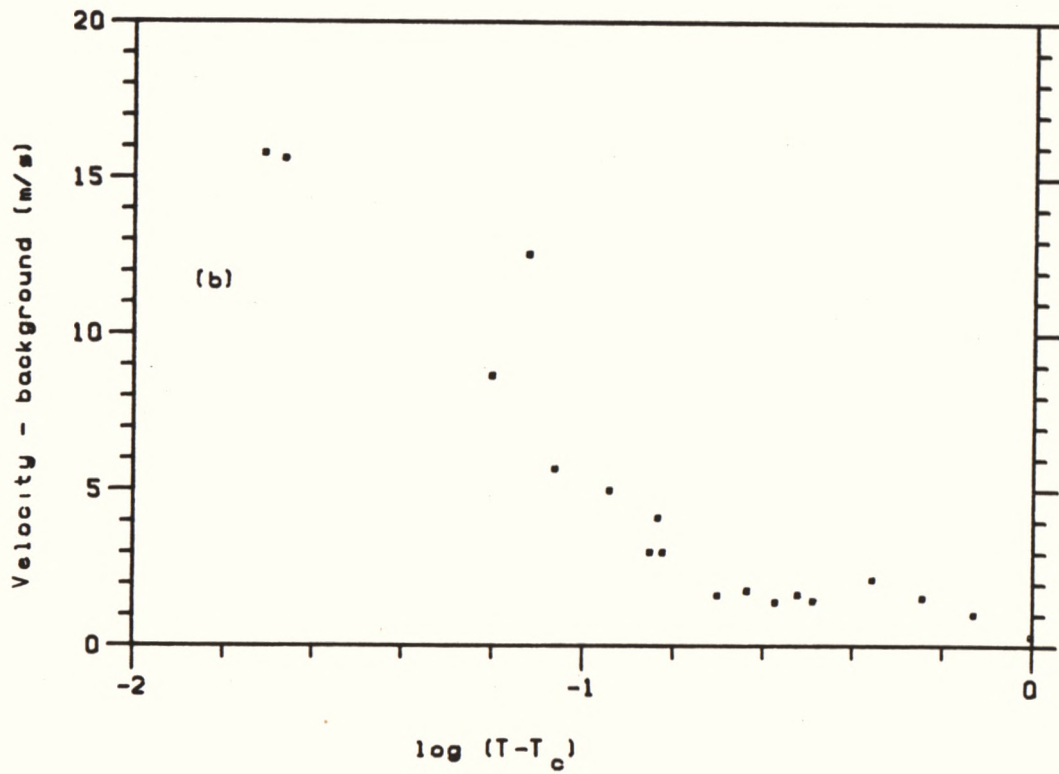
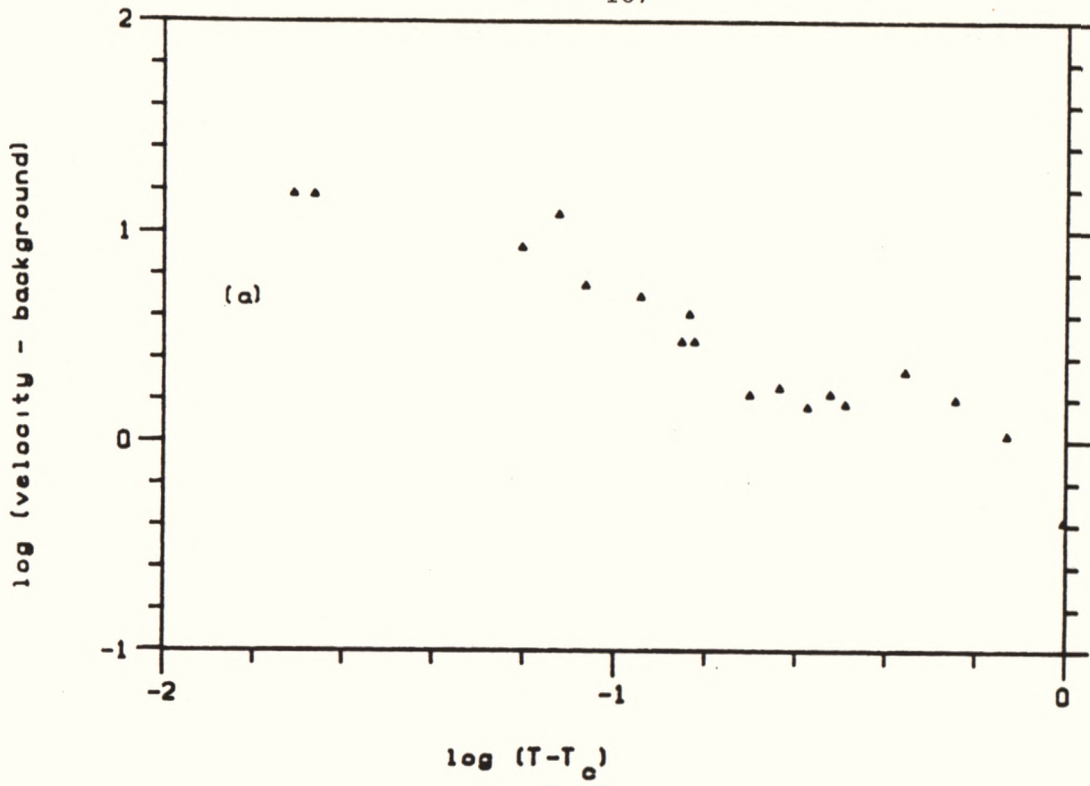


Figure 6.9. Log-log (a) and Linear-log (b) Plots of the Anomalous Part of the Velocity in the Critical Region for the x axis Data of Figure 6.2.

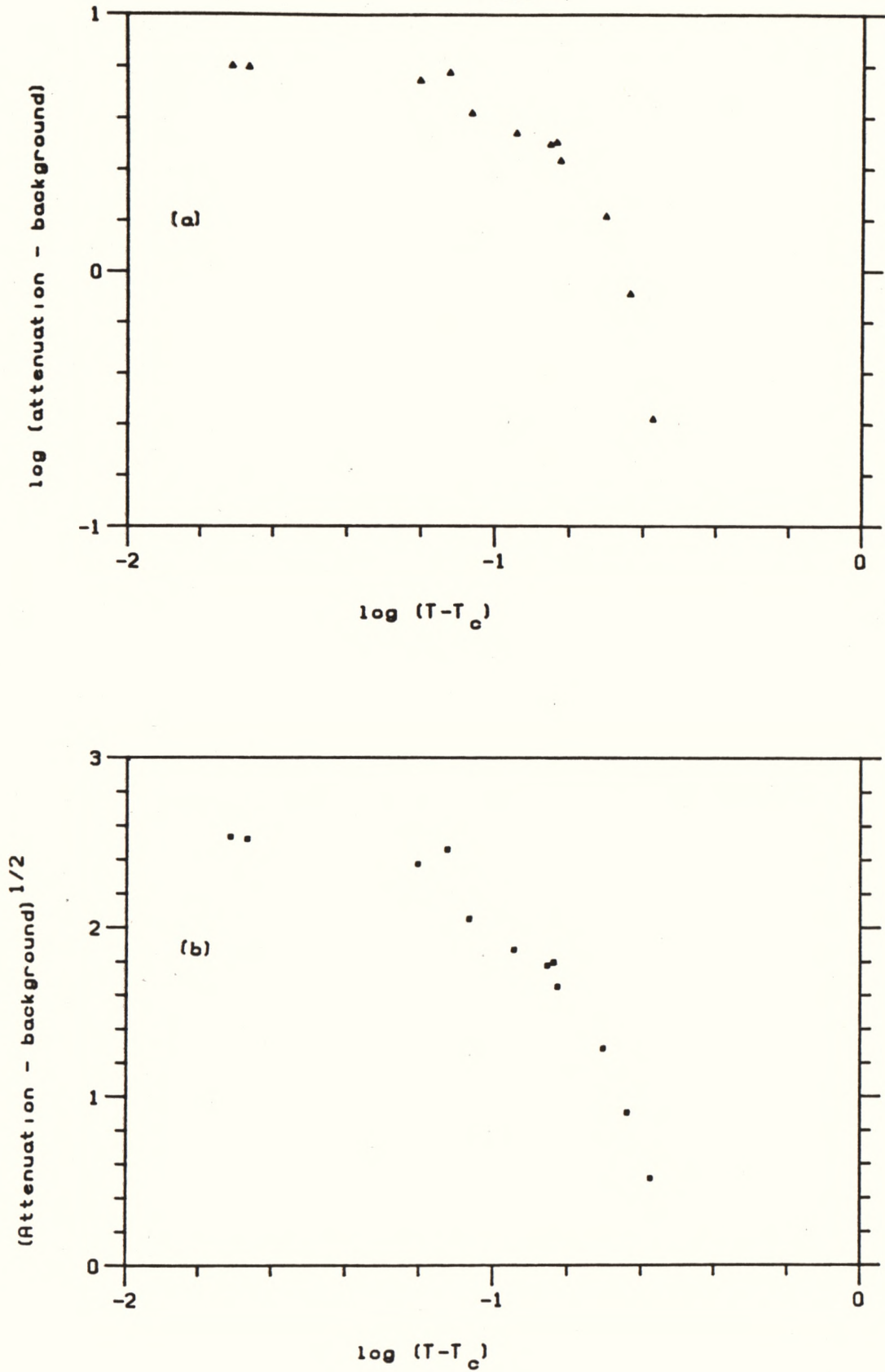


Figure 6.10. The Anomalous Part of the Attenuation $\Delta\alpha$ in the Critical Region for the x axis Data of Figure 6.2 plotted as (a) $\log (\Delta\alpha)$ versus $\log (T-T_c)$ and (b) $\Delta\alpha^{1/2}$ versus $\log (T-T_c)$.

far from clear in Figure 6.10) then the exponent must be of the order of 3 ± 1 , which would be consistent with the large value of the exponent obtained for the z axis measurements.

The critical point analysis for the CDDP sample (Figure 6.5) was also inconclusive. Unlike CDP, there is no broad region in which the velocity slowly deviates from a linear background, and not enough data were collected in the critical region for the analysis to be meaningful. This was unfortunate, since in retrospect the measurements could have been taken using smaller temperature increments, although a limiting factor is that because the anomaly is so small ($\sim 0.13\%$), the changes in velocity and attenuation associated with temperature increments of less than about 50 mK would be difficult to observe since they would be of about the same magnitude as the precision of the ultrasonic measurement. The other factor preventing a successful critical point analysis was the rounding of the attenuation peak which was much greater than that for CDP.

(b) Comparison of the ultrasonic work of other authors to each other and to this work

Table 6.2 shows a comparison of the critical point analysis carried out by K83, Y81, and the present study. Y81 used a partially deuterated sample with $T_c \approx 175$ K and hence it was necessary to make the comparison in terms of the "normalized" quantity $\eta = (T - T_c)/T_c$. In the table some functional relationships have been labelled as "no plot provided". In these cases the authors have stated the functional form in the text of their papers, but have not plotted their data to support their claim. This is particularly disturbing in the case of the paper by Y81, because they claim a much broader range of validity for a power law dependence of ΔV along the x and z axes (for which they do not plot

Table 6.2
Comparison of the Analysis of the
Critical Region by Different Authors. $\Delta T = T - T_c$.

		$\log \eta = \log [(T - T_c)/T_c]$				Comments
		-4	-3	-2	-1	
This study $T_c = 153.72 \text{ K}$						
z axis	ΔV		$ \Delta T^{-\theta} $	$ \log \Delta T $		$\theta = 0.43 \pm 0.1$ $\phi = 3.8 \pm 0.5$ The values of θ and ϕ are averages of two z axis measurements
	$\Delta \alpha$		$ \Delta T^{-\phi} $			
y axis				Analysis unsuccessful		
x axis						
Kanda et al. (1983) $T_c = 154.3 \text{ K}$						
z axis	ΔV		$ \log \Delta T $			No plot provided
	$\Delta \alpha$		$ \log^2 \Delta T $			
y axis	ΔV		$ \log \Delta T $			
	$\Delta \alpha$		$ \log^2 \Delta T $			
x axis	ΔV		$ \log \Delta T $			No plot provided
	$\Delta \alpha$		$ \log^2 \Delta T $			
Yakushkin et al. (1981) $T_c = 175 \text{ K}$						
z axis	ΔV		$ \Delta T^{-\theta} $			$\theta = 0.50 \pm 0.05$ no plot provided
	$\Delta \alpha$		not given			
y axis	ΔV		$ \Delta T^{-\theta} $			$\theta = 1.0 \pm 0.05$ $\phi = 2.3 \pm 0.05$
	$\Delta \alpha$		$ \Delta T^{-\phi} $			
x axis	ΔV		$ \Delta T^{-\theta} $			$\theta = 0.50 \pm 0.05$ no plot provided
	$\Delta \alpha$		not given			

their data) than they found for ΔV along the y axis for which they do plot their data.

It is clear that results of K83 and Y81 are in disagreement as to the functional form of the anomalies for the same critical region. The results of this study for z axis propagation share a $\log \Delta T$ dependence in common with K83 for $\eta > -2.6$, but Figure 6.8(b) would seem to rule out a $\log^2 \Delta T$ dependence for the attenuation anomaly. As pointed out in section 6.1, using their respective analyses, K83 and Y81 are led to conflicting conclusions as to the nature of the dominant forces in CDP close to T_c . The arguments of K83 and Y81 are summarized and evaluated below, and suggestions are made as to how the findings of this study might be interpreted. Finally, some possible causes for the discrepancies between the observations of Y81 and K83 are given below in section (c).

K83 point out that the anomaly in the specific heat in CDP has also been found to be logarithmic (Kanda et al. 1982(b)). The combination of logarithmic singularities in both the ultrasonic and specific heat anomalies has also been observed in other uniaxial ferroelectrics, such as TGSe and TGS, which are not piezoelectric above T_c (Todo 1975), and has in these cases been attributed to the dominance of a strong dipole-dipole interaction (see also Nattermann 1978). TGSe, TGS and CDP all undergo a phase transition from the space group $P2_1/m$ in the paraelectric phase to $P2_1$ in the ferroelectric phase, and all have a unique polar axis parallel to the y direction. Hence, by analogy with TGS and TGSe, K83 attribute the logarithmic singularities in CDP to the dipole-dipole interaction. Their conclusion is supported by the dielectric measurements of Deguchi et al. (1982(b)) who found that in the framework of the 1-D Ising model, 3-D dipole-dipole interactions are dominant in the region $0 < \Delta T < 20$ K. (However, Blinc et al. (1979)

found that this region only extends to $0 < \Delta T < 3 \text{ K}$ (see also section 6.4).) Perhaps the most striking difficulty with the interpretation of K83 is that within the framework of 3-D, dipole-dipole interactions, the anomaly along the ferroelectric y axis is expected to be suppressed by what has been termed the "depolarization effect" (Yagi et al. 1976). In fact, in TGSe and TGS, the y axis anomaly is very much smaller than those for the x and z axes. This is in marked contrast with the findings of this study, as well as the studies of Y81 and K83, that the largest anomaly of all occurs for propagation along the the y axis.

Y81 use the fact that the velocity anomaly is largest for the y axis, together with their observations of power law dependences with large critical exponents, to support their conclusion that the 3-D, dipole-dipole interaction is absent. They argue that the critical region in systems with dipole-dipole interactions is very small ($\eta \sim 10^{-4}$) and that the large values of the critical exponent and the validity of the power law dependences over a wide temperature range are evidence of a system dominated by 1-D interactions. To support this claim they used a dynamical scaling relationship between the critical exponents for the y axis (Schwabl 1973), viz.

$$\Phi - \theta = \kappa$$

where θ and Φ have been defined in Table 6.2 and κ is the critical exponent for the dielectric constant (see section 6.4). Then, according to the results of Y81 shown in Table 6.2, κ should be 1.3. In fact Y81 point out that just this value of κ was found by Blinc et al. (1979) in a wide temperature range in which 1-D interactions are dominant. However, the difficulty with this line of reasoning is that Blinc et al. (1979) found this value of κ only in the range $3 < \Delta T < 90 \text{ K}$ (i.e. $-1.7 < \log \eta < -0.23$) whereas they found that κ has the classical value

of unity in the range $0 < \Delta T < 3$ K. Hence in the region of the power law dependences of Y81 (Table 6.2), $\kappa = 1$, not 1.3. It is therefore difficult to see how the measurements of Blinc et al. (1979) support the conclusions of Y81 as to the 1-D nature of the transition, unless it is assumed that some theoretical basis exists (and has been used by Y81) to scale the critical region by a factor dependent on the physical quantity being measured, so that the region dominated by 1-D interactions found by Blinc et al. (1979) would coincide with the power law dependences found by Y81.

Despite the strength of the short-range, 1-D, intrachain interactions, the long-range, 3-D, dipole-dipole interaction must grow larger as $T \rightarrow T_c$ and eventually dominate the behaviour of the crystal. In this context, the disagreement between Y81 and K83 lies in ascertaining how close to T_c this occurs. Y81 believe that this region occurs much too close to T_c ($\log \eta < -4$) to be observed in the ultrasonic measurement, whereas K83 conclude that 3-D correlations are dominant in the whole region of the ultrasonic measurements with the cross-over to 1-D behaviour presumably at $\Delta T > 20$ K (as suggested by the results of Deguchi et al. 1982(b)).

However, there seems to be no reason to preclude the possibility that the ultrasonic measurements, like the dielectric measurements (see section 6.4), may show a cross-over between regions dominated by 1-D and 3-D interactions. The results of this study (Figure 6.7), whilst admittedly incomplete, do present preliminary evidence of such a cross-over. A possible interpretation is as follows.

Far away from T_c , 1-D type forces dominate the ultrasonic behaviour. In this region the order of the hydrogen ions is gradually increasing as $T \rightarrow T_c$. This is reflected by a gradual change in the force constants between the atoms which is displayed as a softening of the

elastic behaviour and hence a gradual change in the velocity. In this region the attenuation is not expected to show anomalous behaviour because the frequency of the ultrasonic wave is very much smaller than the tunnelling frequency of the hydrogen between its two possible sites in the double potential well. Hence the hydrogens cannot absorb much energy from the ultrasonic wave. Close to T_c , however, 3-D, long-range forces, including those which give rise to the microscopic translations of the Cs and P atoms, dominate the behaviour. This region (as explained in section 6.2.4.1(a)) is characterized by very sharp changes in the velocity and attenuation.

In order to be consistent with the underlying theoretical bases of the work of Y81 and K83, the region close to T_c in Figure 6.7 would have to be described by a log type dependence (3-D interactions) and the region further away from T_c by a power law dependence (1-D, short range interactions). In fact, as is clear in Figure 6.7, the reverse is the case, and hence the results of this study are not only different from those of Y81 and K83 in that a cross-over region was observed, but also the interpretation presented is inconsistent with their theoretical assumptions. At present, these inconsistencies remain unresolved.

(c) Possible causes for the discrepancies in the observed behaviour between different studies

Table 6.3 lists some of the factors which may account for the discrepancies in the reported ultrasonic behaviour between this study, Y81 and K83. It will be noted that none of the three studies have used exactly the same experimental arrangement or analysis technique.

Table 6.3

Possible Origins of the Discrepancies in the Observed
Ultrasonic Behaviour between Different Studies.

Experimental or Analytical Details	This Study	Y81	K83
Bias Field	No bias field applied and there- fore the samples used were in the polydomain state	As for this study	Bias field applied along the b axis and reduced to zero prior to taking measure- ments in order to produce monodomain specimens
Crystal Used	CsH_2PO_4 $T_c \approx 154 \text{ K}$	$\text{Cs}(\text{H}_{1-x}\text{D}_x)_2\text{PO}_4$ with $x \approx 0.1$ and $T_c \approx 175 \text{ K}$	CsH_2PO_4 $T_c \approx 154 \text{ K}$
Analysis	Used T_c where T_c is the temperature of the peak in the attenuation	As for this study	Used T_0 where T_0 was determined from the Curie-Weiss fit $C/(T-T_0)$ to the dielectric constant

Although one gains the impression from their paper that the data analysed to give logarithmic dependences were for a monodomain specimen, K83 do not state this explicitly. Figure 2 of K83 shows that the anomaly for the monodomain specimen is a more slowly varying function of temperature than that for the polydomain specimen, so that it is perhaps not surprising that the analysis for the monodomain specimen shows a logarithmic type dependence which is a more slowly varying function of temperature than a power law dependence. One cannot help conjecture that the analysis of K83 may well have not shown a log dependence if the polydomain specimen had been used, and may even have shown evidence of the cross-over region found in the present study. In any case, in view of the importance of domain effects in CDP, there is a need to compare the functional form of the anomalies for the polydomain and monodomain specimens.

Y81 do not state why they have used a partially (~10%) deuterated sample, but perhaps the motivation was to increase T_c so as to make it more convenient to measure the velocity and attenuation. The work described in section 6.2.4.1(b) shows that deuteration significantly "washes out" the anomaly, although the question of whether or not the deuteration changes the functional form remains unresolved. It is possible, then, that the discrepancy between the power law dependence of Y81 and the logarithmic dependence of K83 reflects a genuine change in the nature of the transition with deuteration. In any case, the underlying assumption of Y81 that the dynamics of CDP may be inferred from measurements on a 10% deuterated sample is questionable.

K83 do not explain their choice of T_0 (which was determined from the $C/(T-T_0)$ fit of the simultaneously measured dielectric constant) rather than T_c (i.e. the maximum in the dielectric constant) to analyse their data, but they claim that this may be one reason for the

differences between their data and those of Y81. However, K83 found that the maximum difference between T_c and T_0 was 0.10 K, and in the analysis of this study it was found that varying T_c by this amount had no effect on the derived functional form. Hence, it is difficult to see how the choice of T_0 or T_c could account for the different functional forms found by Y81 and K83.

The measurements of this study are in agreement with those of K83 for temperatures which are sufficiently high so that domain effects will not be important. Closer to T_c , where domain effects are expected to be important, the results of this study are closer to those of Y81. Deuteration may have the effect of "washing out" the precursor effect to the transition of the log type dependence, so that Y81 observe a power law dependence over the whole temperature range. Hence, the findings of this study may be viewed as possessing elements of the features reported by both Y81 and K83. This is perhaps not surprising in view of the significant differences between the conditions for the three sets of measurements.

6.3 THERMAL EXPANSION MEASUREMENTS ON CDP

6.3.1 Introduction

Thermal expansion measurements on CDP revealed significant anomalies in the expansion coefficients at T_c , as well as very anisotropic behaviour including a negative expansion coefficient along the z axis. By making use of an approximation, it was possible to calculate the linear Grüneisen parameters, and using the elastic constants, determine the role of the cross-compliances in the production of a negative expansion coefficient for the z axis. The investigation also provided some insight into the one-dimensional nature of the transition in CDP.

The thermal expansion measurements were also used to (a) ascertain whether the failure of the bond between the transducer and the specimen in the ultrasonic measurements could be attributed to stresses set up in the bond due to differential thermal expansion and (b) to determine the changes in the length of the specimen due to thermal expansion and to decide whether these changes were large enough to warrant the inclusion of a correction term to the length used in equation (4.1) to calculate the ultrasonic velocity. In particular, it was important to check if there were any discontinuities in the length of the specimen at the transition which might have accounted for the anomalies in the measured delay times at T_c .

6.3.2 Theory

The coefficient of linear expansion is defined as the temperature derivative of the strain at constant pressure, i.e.

$$\alpha_j = \left(\frac{\partial \epsilon_j}{\partial T} \right)_P \quad (6.1)$$

where the Voigt notation has been used and $j=1$ to 6 (Barron et al. 1980). The thermal expansion conforms to the crystal symmetry and in the case of a monoclinic system there are four independent components of the expansion tensor (Nye 1967). With respect to the Cartesian axes of Figure 2.2, and using the Voigt notation, these components are α_1 , α_2 , α_3 , and α_5 .

Directional Grüneisen parameters may be defined by the strain derivatives of the entropy S , i.e.

$$\gamma_j = \frac{1}{C_\epsilon} \left(\frac{\partial S}{\partial \epsilon_j} \right)_P \quad (6.2)$$

where C_ϵ is the heat capacity at constant strain and $j=1$ to 6 . The Grüneisen parameters are related to the expansion coefficients by (Barron et al. 1980)

$$\alpha_j = \left(\frac{C_\sigma}{V_{\text{mol}}} \right) S_{ij} \gamma_j \quad (6.3)$$

where C_σ is the heat capacity at constant stress, V_{mol} is the molar volume and the compliances S_{ij} are understood to be adiabatic. Equation (6.3) may be inverted to give

$$\gamma_j = \left(\frac{V_{\text{mol}}}{C_\sigma} \right) C_{ij} \alpha_j \quad (6.4).$$

Equation (6.3) suggests that the thermal expansion in solids is a combination of two effects. A "thermal pressure", produced by the strain dependent entropy (as measured by the Grüneisen parameters), coupled with the elastic behaviour of the crystal (as measured by the S_{ij} matrix) determines the actual strain response of the crystal (Munn 1972, Grüneisen and Goens 1924).

6.3.3 Experimental Details

The thermal expansion was measured using a three-terminal capacitance dilatometer identical in design to the one described by White and Collins (1972). Further details of the cell and experimental arrangement may be found elsewhere (Gibbs 1983, Simpson 1979). The cell was designed with very low temperature measurements in mind, and hence was not particularly suited for measurements in the range 100-300 K. In particular, it took up to two hours for the cell to come to thermal equilibrium between measurements which made the task of measuring the expansion coefficient in this range very time-consuming. Some improvement in the speed of attaining thermal equilibrium was achieved by amplifying the heater current output from the available temperature controller (which was the one used in the thermal expansion measurements of Gibbs (1983)).

6.3.4 Results

The thermal expansion coefficients along the x and z axes are shown in Figures 6.11 and 6.12 respectively. The solid line in each case represents a satisfactory fit to the data using a knotted, least-squares cubic spline function (I.M.S.L. routine ICSCCU). On account of the problems with thermal equilibrium of the cell, it was impractical to take measurements at intervals of less than 0.5 K. Figure 6.11 shows a minimum in the x axis expansion (hereinafter referred to as α_x) at 151 ± 2 K, corresponding to the ferroelectric transition. There is, however, a second, smaller anomaly at 235 ± 3 K, which was reproducible on both heating and cooling the specimen. At first it was thought that this anomaly might be associated with the freezing of pockets of supersaturated solution caught in the CDP crystal. However, preliminary

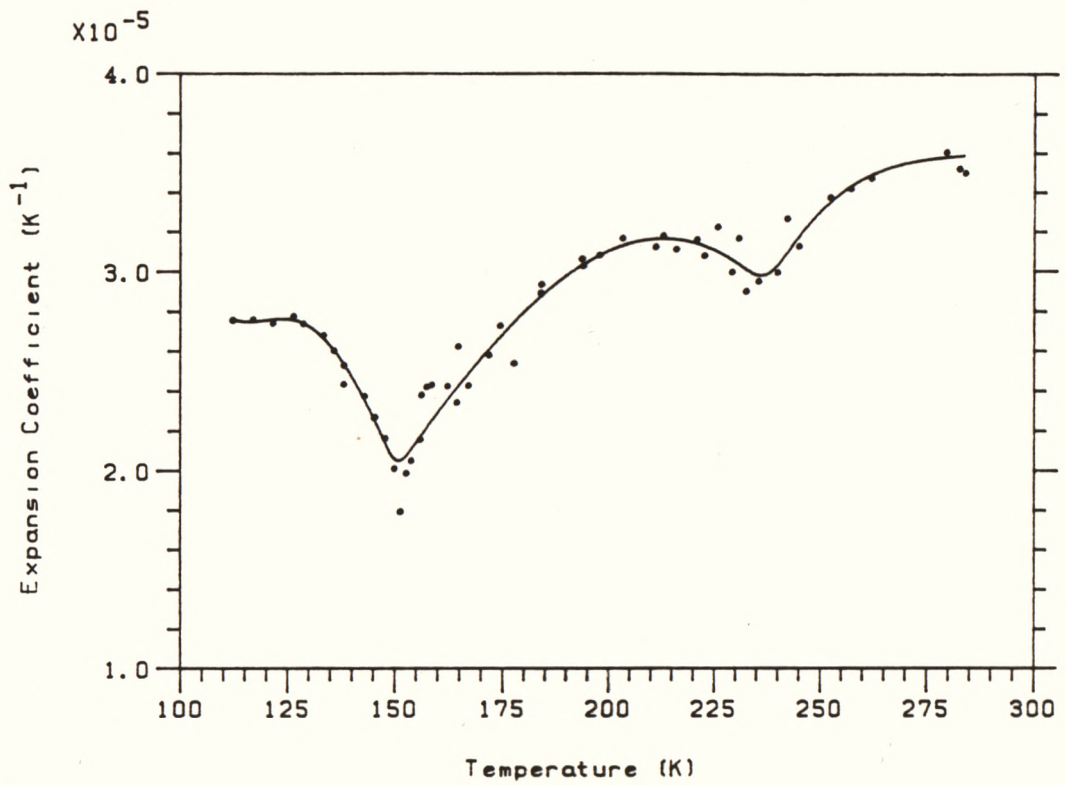


Figure 6.11. Temperature Dependence of the x axis Linear Thermal Expansion Coefficient (α_x) of CDP.

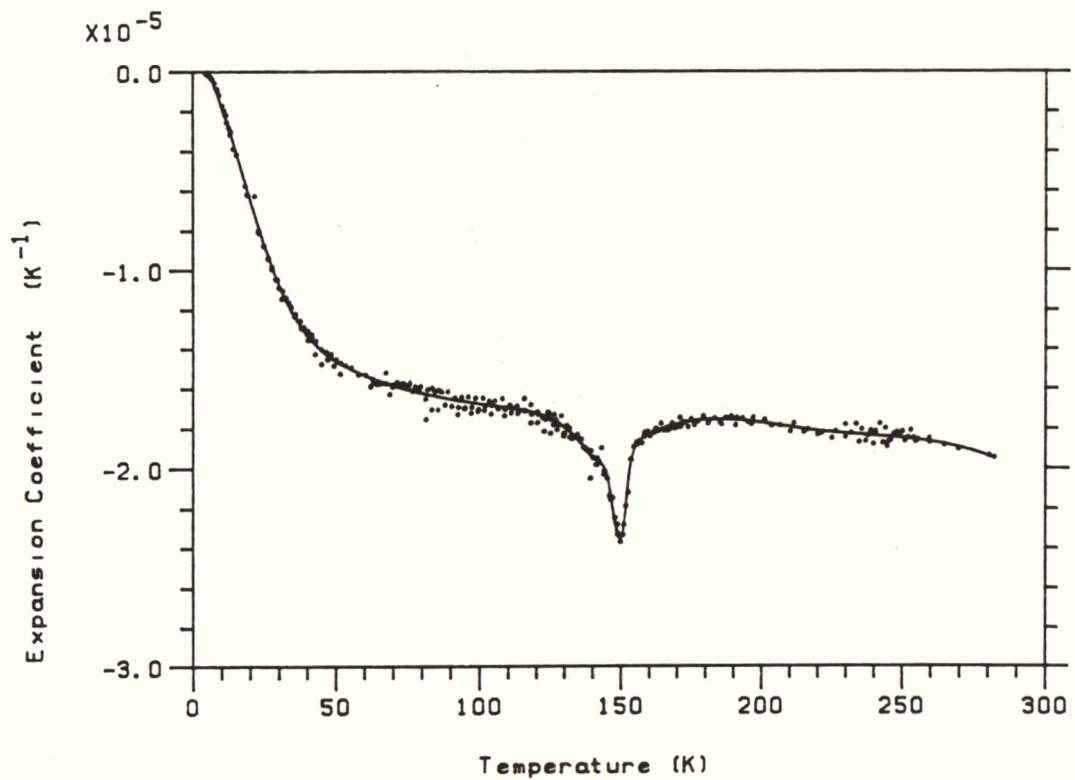


Figure 6.12. Temperature Dependence of the z axis Linear Thermal Expansion Coefficient (α_z) of CDP.

DTA measurements (W. Flagge, private communication) showed that the freezing temperature of a saturated solution of CDP was 264 ± 1 K, and no anomaly was detected near 235 K. Unfortunately, time was not available to repeat the thermal expansion measurement on a different specimen.

As Figure 6.12 shows, the z axis expansion (hereinafter referred to as α_z) is negative even at very low temperatures. There is a dip in the expansion coefficient at 150 ± 2 K, but apart from this α_z is remarkably constant over quite a broad temperature range. The plot also demonstrates that the scatter in the data is greater at higher temperatures, due to the increased difficulty of attaining good thermal equilibrium.

It is of interest to note that at T_c , α_x and α_z are equal in magnitude, but opposite in sign. The significance of this observation will be discussed below in section 6.3.6.

Time was not available to measure the expansion along the y axis (hereinafter referred to as α_y). However this expansion has been measured by Deguchi et al. (1981). Figure 6.13 is a plot of α_y which was digitized from Figure 2 in the above reference. The data have been fitted in a manner similar to that for the x and z axes using a knotted least-squares cubic spline function.

6.3.5 Calculation of the Grüneisen parameters

Since data are only available for the x and z axes (from this study) and for the y axis (from the work of Deguchi et al. 1981), α_5 remains unknown, and therefore the Grüneisen parameters of the monoclinic system (γ_1 , γ_2 , γ_3 , and γ_5) could not be calculated.

In an attempt to proceed with the calculation, the simplification had to be made that CDP could be adequately described by the elastic,

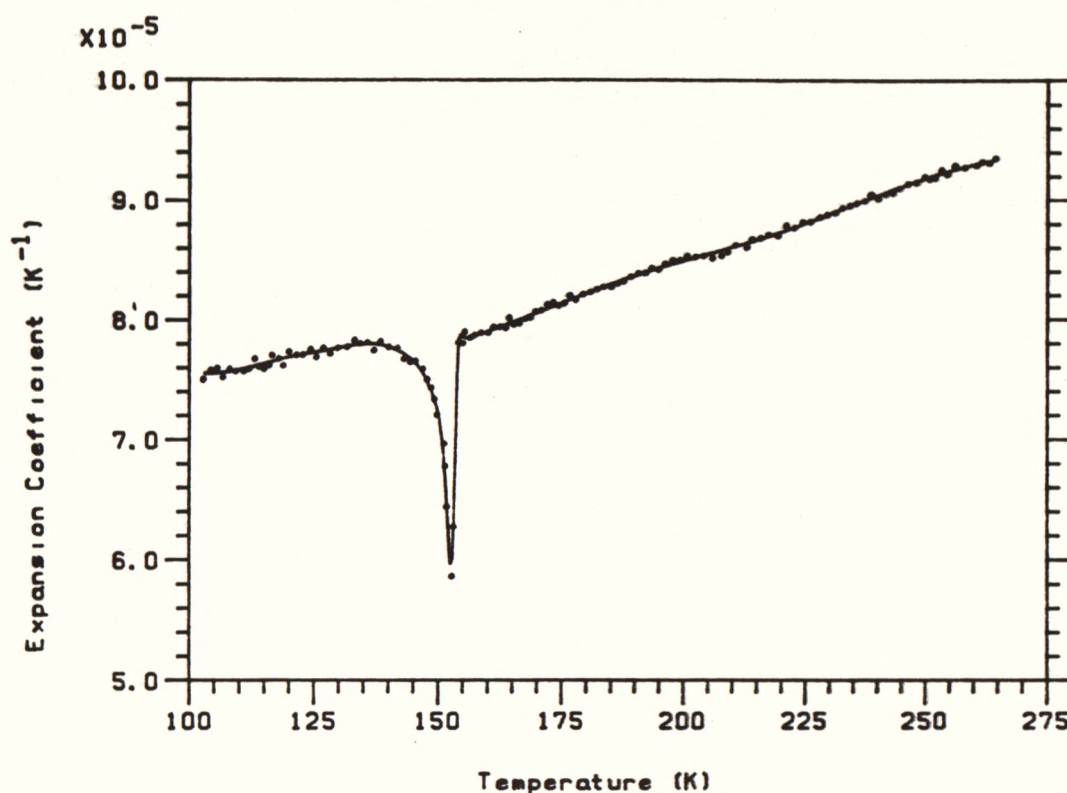


Figure 6.13. Temperature Dependence of the y axis Linear Thermal Expansion Coefficient (α_y) of CDP. The data have been taken from Deguchi et al. (1981).

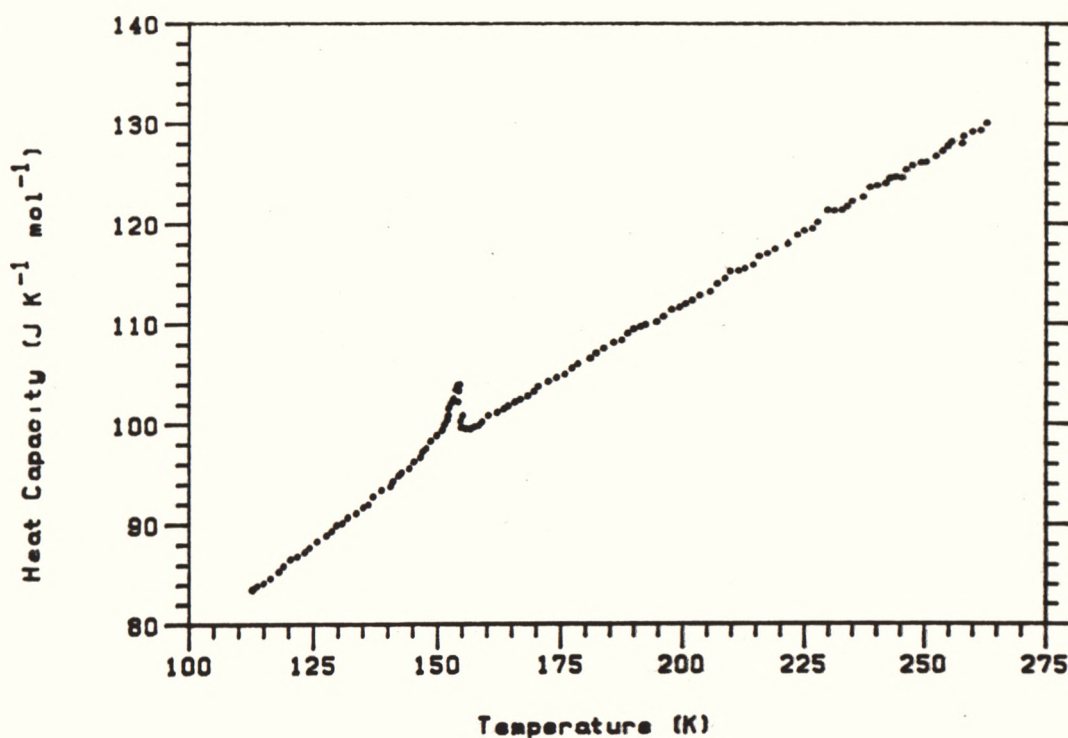


Figure 6.14. Temperature Dependence of the Heat Capacity of CDP. The data have been taken from Kanda et al. (1982(b))

thermal, and Grüneisen parameters appropriate to orthorhombic symmetry. This was equivalent to setting $C_{15} = C_{25} = C_{35} = C_{46} = 0$ in the elastic constant matrix of Table 5.2, so that the "orthorhombic" elastic constant matrix, $(C_{ij})^0$ is given by

$$(C_{ij})^0 = \begin{bmatrix} 28.83 & 11.4 & 42.87 & 0 & 0 & 0 \\ 11.4 & 26.67 & 14.5 & 0 & 0 & 0 \\ 42.87 & 14.5 & 65.45 & 0 & 0 & 0 \\ 0 & 0 & 0 & 8.10 & 0 & 0 \\ 0 & 0 & 0 & 0 & 5.20 & 0 \\ 0 & 0 & 0 & 0 & 0 & 9.17 \end{bmatrix} \text{ GPa}$$

The Grüneisen parameters can then be calculated by (Barron et al. 1980)

$$\begin{bmatrix} \gamma_x \\ \gamma_y \\ \gamma_z \end{bmatrix} = \begin{bmatrix} 28.83 & 11.4 & 42.87 \\ 11.4 & 26.67 & 14.5 \\ 42.87 & 14.5 & 65.45 \end{bmatrix} \begin{bmatrix} \alpha_x \\ \alpha_y \\ \alpha_z \end{bmatrix} \frac{V_{\text{mol}}}{C_\sigma} \quad (6.5)$$

It is reasonable to make this "orthorhombic" approximation for two reasons. Firstly, the three pairs of velocities, V_3 and V_9 , V_5 and V_2 , V_6 and V_8 , in Table 5.1, which would be required by symmetry to be equal for a crystal of the orthorhombic class, differ, in the case of CDP, by 2, 6, and 12% respectively, so that, in terms of the velocity measurements, CDP does not behave very differently from an orthorhombic system. Secondly, and more convincingly, the calculations of the elastic properties such as velocity surfaces, bulk modulus, and linear compressibilities using $(C_{ij})^0$ in place of C_{ij} of Table 5.2 showed that, despite the assumption of orthorhombic symmetry, all the important features discussed in Chapter 5 remained basically unchanged. Table 6.4 presents a comparison between the calculations using C_{ij} and $(C_{ij})^0$. In particular, the results using the $(C_{ij})^0$ matrix still show a very anomalous semi-pure transverse (SPT) mode propagating in the xz plane and reasonably isotropic behaviour for propagation in the xy and yz

planes. The bulk modulus is very small, and the compressibilities indicate that under hydrostatic pressure there is a contraction in length along the x axis, an expansion along the z axis and that by comparison the length change along the y axis is small.

Table 6.4
Comparison of some calculated
Elastic Properties for C_{ij} and $(C_{ij})^o$

	Calculations using C_{ij}	Calculations using $(C_{ij})^o$
Minimum in velocity of SPT mode in xz plane (see Figure 5.3)	$0.290 \times 10^3 \text{ m s}^{-1}$ for propagation at 38° to the x axis	$0.291 \times 10^3 \text{ m s}^{-1}$ for propagation at 39° to the x axis
Bulk modulus (GPa)	5.28	5.73
Linear compressibilities (GPa) ⁻¹	X: 0.428 Y: 0.022 Z: -0.260	0.473 -0.005 -0.293

The heat capacity data, shown in Figure 6.14, were digitized from Figure 1 of Kanda et al. (1982(b)). The molar volume, V_{mol} , was calculated to be 71.40 cm^3 , taking the density as 3.22 g cm^{-3} as in

section 5.1.2.

At every temperature at which a specific heat point is plotted in Figure 6.14, the expansion coefficients were interpolated using the knotted least-squares cubic spline fits, and the Grüneisen parameters were calculated using equation (6.5). The results are shown in Figure 6.15.

The coefficient of volume expansion β is given by

$$\beta = \alpha_x + \alpha_y + \alpha_z$$

and the volume Grüneisen parameter is given by

$$\gamma_{vol} = \frac{\beta V_{mol} B_s}{C_\sigma}$$

where B_s is the adiabatic bulk modulus. The temperature dependence of γ_{vol} is also shown in Figure 6.15, where B_s has been calculated using the $(C_{ij})^0$ matrix.

From the figure it is clear that $\gamma_x < \gamma_z < \gamma_y$ over the whole temperature range and that as $T \rightarrow T_c$, $\gamma_x \rightarrow \gamma_z$. By comparison with the directional Grüneisen parameters, γ_{vol} is reasonably constant over the whole temperature range. In order to check that these features were not artifacts of the fitting procedure for the expansion data, the calculations were repeated using fewer knots which significantly reduced the quality of the fits to the expansion data, particularly close to T_c . Despite this, all the general trends in the temperature dependence of the Grüneisen parameters discussed above were still observed. This confirmed that these trends are not sensitive to the details of the fitting procedure.

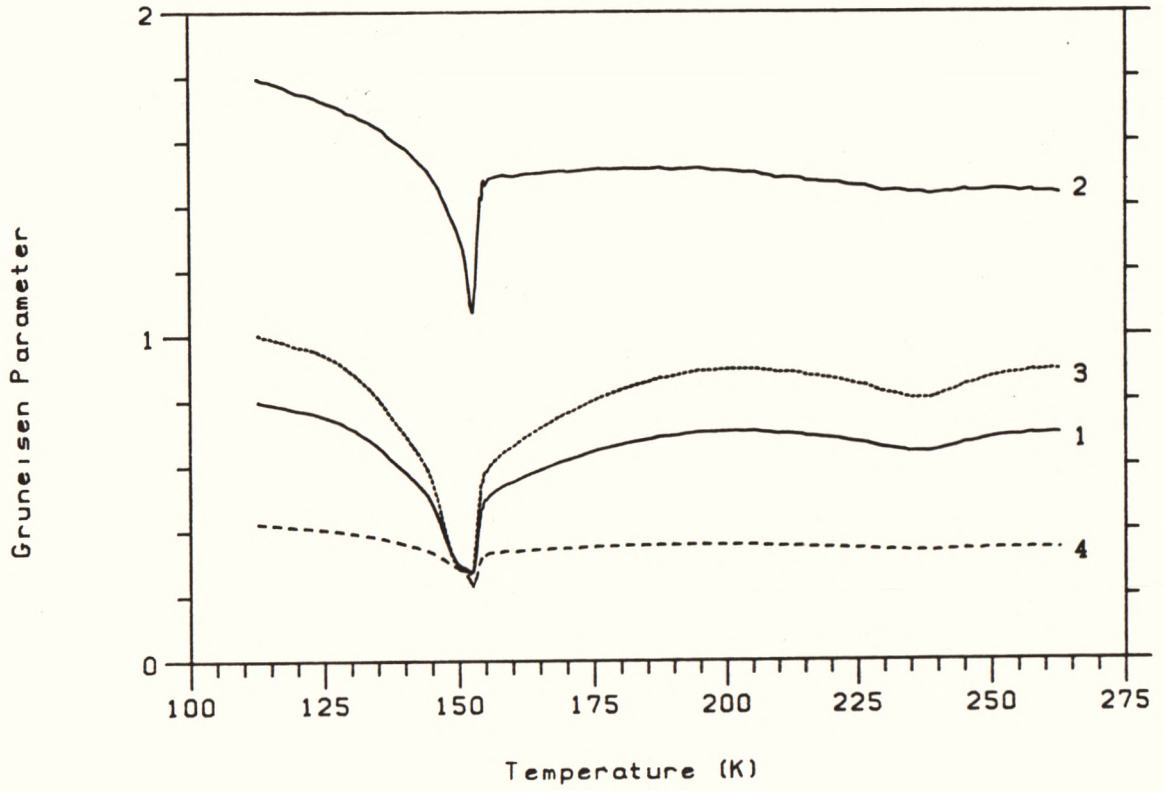


Figure 6.15. Temperature Dependences of the Directional Grüneisen Parameters of CDP. (1) γ_x , (2) γ_y , (3) γ_z , (4) γ_{vol} . Note that $\gamma_x \approx \gamma_z$ close to T_c .

6.3.6 Discussion

(a) Grüneisen parameters

Munn (1972) has attempted to explain the expansion behaviour of axial solids (such as arsenic, graphite, selenium, tellurium, and indium) by a consideration of the interplay between the Grüneisen functions and the elastic properties. In Munn's analysis, the expansion is written as the sum of a quasi-cubic term and a cross-linking term. The analysis can be extended to symmetries lower than axial, although the identification of the dominant terms becomes more difficult.

Following Munn, the expansion coefficients in the orthorhombic system are

$$\alpha_x = \frac{C_\sigma}{V_{mol}} [\chi_x \gamma_x + (S_{12})^0 (\gamma_y - \gamma_x) + (S_{13})^0 (\gamma_z - \gamma_x)]$$

$$\alpha_y = \frac{C_\sigma}{V_{mol}} [\chi_y \gamma_y - (S_{12})^0 (\gamma_y - \gamma_x) + (S_{23})^0 (\gamma_z - \gamma_y)]$$

$$\text{and } \alpha_z = \frac{C_\sigma}{V_{mol}} [\chi_z \gamma_z - (S_{23})^0 (\gamma_z - \gamma_y) - (S_{13})^0 (\gamma_z - \gamma_x)]$$

where χ_x , χ_y , χ_z are the linear compressibilities along the x, y and z axes respectively, and the $(S_{ij})^0$ are the elastic compliances in the orthorhombic system.

Table 6.5 shows the individual contributions to the expansion coefficients at different temperatures. The values of the elastic compliances $(S_{12})^0$, $(S_{13})^0$, $(S_{23})^0$, and the linear compressibilities have been calculated from the $(C_{ij})^0$ matrix.

Table 6.5

Contributions to the Expansion Behaviour

T (K)	Heat Capacity (J K ⁻¹ mol ⁻¹)	γ_x	γ_y	γ_z	α_x	α_y	α_z
		(calculated)			(measured)		
					(10 ⁻⁴ K ⁻¹)		
264.0	130.23	0.697	1.44	0.893	0.351	0.933	-0.188
160.6	100.70	0.558	1.50	0.670	0.231	0.791	-0.182
152.3	101.78	0.270	1.10	0.271	0.206	0.602	-0.212

$$\begin{aligned}
 \chi_x &= 0.473 \text{ (GPa)}^{-1} & (S_{12})^0 &= -0.136 \text{ (GPa)}^{-1} \\
 \chi_y &= -0.005 \text{ (GPa)}^{-1} & (S_{13})^0 &= -1.07 \text{ (GPa)}^{-1} \\
 \chi_z &= -0.293 \text{ (GPa)}^{-1} & (S_{23})^0 &= 0.077 \text{ (GPa)}^{-1}
 \end{aligned}$$

T (K)	$\chi_x \gamma_x$	$\chi_y \gamma_y$	$\chi_z \gamma_z$	$(S_{12})^0 (\gamma_y - \gamma_x)$	$(S_{13})^0 (\gamma_z - \gamma_x)$	$(S_{23})^0 (\gamma_z - \gamma_y)$
	(GPa) ⁻¹					
264.0	0.33	-0.007	-0.26	-0.10	-0.21	-0.042
160.6	0.26	-0.008	-0.20	-0.13	-0.12	-0.064
152.3	0.13	-0.006	-0.08	-0.11	-0.001	-0.064

It is immediately clear that the negative sign of α_z is attributable to the large negative value of χ_z . At room temperature the cross-linking term $(S_{13})^0 (\gamma_z - \gamma_x)$ adds a positive contribution to what would otherwise be a very large negative coefficient. From the table, and from Figure 6.15, it is clear that as $T \rightarrow T_c$, $(\gamma_z - \gamma_x) \rightarrow 0$. Hence it is the near-vanishing of the cross-linking term $(S_{13})^0 (\gamma_z - \gamma_x)$ which is responsible for the decrease in the z axis expansion. Thus, increasing isotropy of the Grüneisen parameters in the xz plane governs the anomaly of α_z at T_c .

It might be expected that the sharp decrease in γ_y is directly responsible for the sharp anomaly in α_y at T_c . In fact this is not the case because χ_y is so small that the y axis expansion is dominated by the cross-linking terms rather than the quasi-cubic term, and it is the decrease in $(\gamma_y - \gamma_x)$ which causes the decrease in α_y at T_c . Thus, once again, it is the relative anisotropy of the Grüneisen parameters rather than their absolute values which dominates the expansion behaviour.

However, in the case of the x axis expansion, the quasi-cubic and cross-linking terms are of comparable magnitude and it is not possible to identify a dominant contribution to the broad anomaly for this direction.

As has been pointed out previously, close to T_c , $\alpha_z \approx -\alpha_x$. Hence thermally induced strains along the x and z axes will be nearly equal in magnitude but opposite in direction. Equation (6.2) defined the directional Grüneisen parameters as the strain derivatives of the entropy, and since $\gamma_x \approx \gamma_z$ in this temperature region, it follows that the changes in entropy due to strains along the x and z directions will tend to cancel each other. This leaves the y axis expansion and Grüneisen parameter as the dominant factor governing changes in disorder (\equiv entropy) in the system close to T_c . Hence, close to T_c , CDP behaves

as a "uniaxial" system from the thermodynamic point of view. This is consistent with the known one-dimensional nature of the ordering of the hydrogen ions at the transition.

Finally, it is worthwhile to note that despite the quite strong temperature dependences of the directional Grüneisen parameters, γ_{vol} is nearly temperature independent except for a small decrease at T_c . This further supports the conclusion that anisotropy in CDP, rather than any instability of the crystal as a whole, is responsible for the expansion behaviour.

(b) Bond failure in the ultrasonic measurements

Typical expansions of copper ($0.16 \times 10^{-4} \text{ K}^{-1}$ at 298 K) and of X-cut quartz ($0.14 \times 10^{-4} \text{ K}^{-1}$ at room temperature) are considerably smaller than the expansion coefficients of CDP along the x and y axes. Also, since α_z is negative, a decrease in temperature results in an expansion, rather than a contraction, along the z axis. These two factors both contribute to cause a differential thermal expansion between the sample and the quartz transducer, which gives rise to a stress in the bond.

Small changes in the slope of the velocity versus temperature curves occur at about 180 K for propagation along the x and y axes (see Figures 6.1 and 6.2), but appear to be absent for propagation along the z axis (Figures 6.3 and 6.4). This may simply reflect the improvement in the data collection techniques in the course of this study. However, it is interesting to note that α_z begins to decrease at about 175 K, reaching a minimum at 150 K. Since α_z is negative, this decrease will serve to increase the differential thermal expansion between the sample and transducer. For measurements of waves propagating along the x and y axes, this increase will appear as an increase in the shear strain in

the bond. By contrast, for ultrasonic measurements along the z axis, the decrease in α_z would appear as an increased compressional stress in the bond. The latter is unlikely to affect the echo train adversely, as the effective result is an increased pressure of the transducer on the specimen. Hence small anomalies caused by bond changes may be expected to occur for propagation along the x and y axes, but not along the z axis.

In order to confirm the above conclusion, it will be necessary to repeat the ultrasonic measurements along the x and y axes with the same echo train quality, temperature resolution, and thermal equilibrium, that were attained for the measurements along the z axis. Nevertheless, it is clear that differential thermal expansion is a plausible explanation for the failure of a wide variety of bonding agents to maintain good acoustic coupling over the temperature range of interest.

(c) Thermal expansion corrections to the ultrasonic velocities

A close examination of the length changes associated with the expansion behaviour along the x and the z axes showed that there was no discontinuous length change at the transition. Figure 2 of Deguchi et al. (1981) shows that, despite the sharp dip in α_y at T_c , the length changes are continuous. Therefore the changes in the measured delay time in the specimen close to T_c are certainly not due to thermal expansion effects. (The absence of any discontinuous length change also suggests that the transition is not first-order.)

Corrections to the velocities shown in Figures (6.1)-(6.4) due to thermal expansion could be applied by multiplying the velocity at every temperature T by a correction term

$$1 - \int_{T_i}^T \alpha_i dT$$

where T_i is the temperature at which the length of the specimen was measured, and α_i is the expansion coefficient for the propagation direction for that velocity measurement. The largest correction will apply for the y axis since α_y is the largest of the three measured coefficients, but even in this case the correction will only amount to 0.008% / K. Since the velocity changes close to T_c are of the order of 2%, thermal expansion corrections are negligible.

However, if the absolute slopes of the velocity versus temperature curves well above T_c are of interest, thermal expansion corrections should be applied. The effect of the correction will be to decrease the magnitude of the slope for the x and y axes, but to increase the magnitude of the slope for the z axis. These corrections are unnecessary in the context of the present study because the linear temperature region well above T_c is only used to determine a suitable background term for the ultrasonic anomaly, and hence the correction term will have no effect on the analysis of the critical region.

Note in Proof: Very recently Nakamura et al. (1984) have applied a quasi-one-dimensional Ising model to the y axis expansion data of Deguchi et al. (1981). They found reasonable agreement between the experimental values and those calculated from the model. Their interpretation is consistent with the findings of this study.

6.4 DIELECTRIC MEASUREMENTS ON CDDP

6.4.1 Introduction

Measurements of the temperature dependence of the dielectric behaviour of CDDP were originally undertaken in an attempt (a) to confirm that the small, broad ultrasonic anomaly in CDDP (Figure 6.5) was indeed associated with the ferroelectric transition, as evidenced by a peak in the dielectric constant, and (b) to measure the transition temperature T_c^d accurately for fitting the ultrasonic data to a $(T-T_c^d)^{-\theta}$ type dependence.

Whilst the results confirmed that the ferroelectric transition takes place at about 247 K, very peculiar relaxation effects prevented an accurate determination of T_c^d . However, somewhat unexpectedly, the results provided very significant information that helped to elucidate the mechanism of the transition itself. Evidence was collected which convincingly shows the presence of both one-dimensional, short-range interactions, and the more usual three-dimensional, long-range, dipole-dipole interactions. It was also shown, contrary to previous reports, that, despite the one-dimensional nature of the transition, a significant anomaly exists in the dielectric behavior orthogonal to the ferroelectric y axis. It is suggested that the long term relaxation effects are related to peculiarities in the domain structure below T_c^d .

6.4.2 Experimental Method

The measurements were performed using a General Radio capacitance bridge (GR 1621) operating at 1kHz. The maximum measuring field was 2 V cm^{-1} . Electrodes of gold approximately 800 Å thick were evaporated onto opposite parallel faces of the specimen. The same cell was used for these dielectric measurements as for the thermal expansion measurements. Only a small modification was required in order to monitor the

capacitance across the sample instead of across the air gap as in the thermal expansion measurements.

The temperature was stabilized for every reading, unlike the work of other authors (e.g. Uesu and Kobayashi (1976), Kamysheva et al. (1981), Yasuda et al. (1979)) who measured the dielectric behaviour using slow (0.01-0.25 K/min), but continuous, heating or cooling runs. Up to an hour was required for the probe to come to thermal equilibrium between measurements so that the runs took many days. Because of the inability to collect data over the whole temperature range without overnight interruptions, the very long term relaxation effects (see below) could not be thoroughly investigated.

6.4.3 Results

(a) Dielectric constant along the ferroelectric y axis

The temperature dependences of the capacitance and conductance measured along the ferroelectric y axis, taken on a heating run, are shown in Figure 6.16. The sample used was the same one that had been used for the ultrasonic measurements (Figure 6.5).

The capacitance is directly proportional to the dielectric constant, whilst the conductance is a direct measure of the loss factor (i.e. the imaginary part of the complex permittivity). Since the sample was not of a regular rectangular-prism shape, it was not possible to calculate the dielectric constant accurately from the capacitance. However, using the sample thickness of 0.966 cm and the approximate area of the parallel faces of 0.51 cm^2 , and assuming the formula for a parallel plate capacitor, an estimate of the dielectric constant may be obtained by multiplying the capacitance (in pF) in Figure 6.16 by a factor of 21.4.

Outside the range 215-245 K, following a change in the set-point

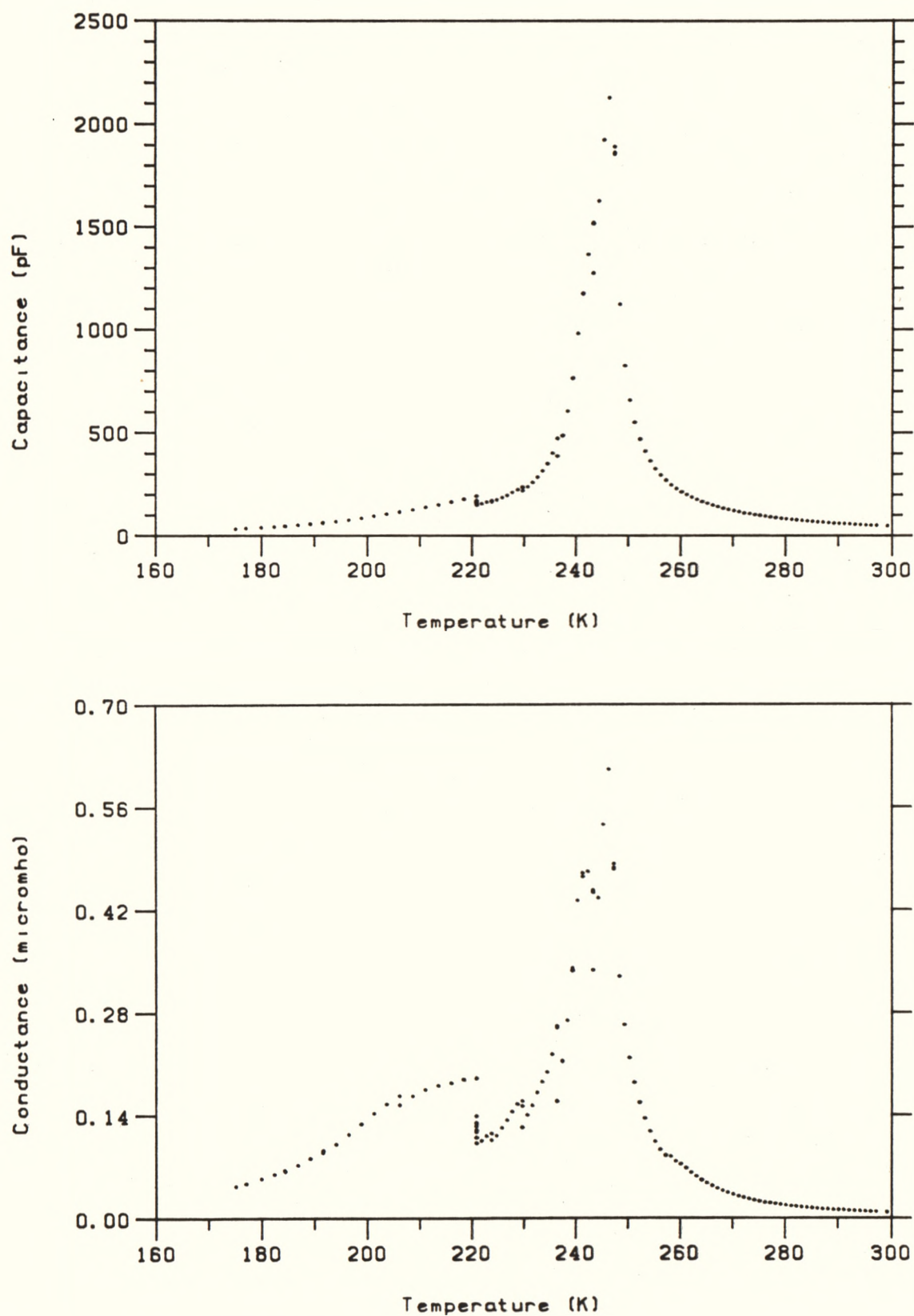


Figure 6.16. Temperature Dependences of the Capacitance and Conductance of CDDP Measured along the Ferroelectric y axis.

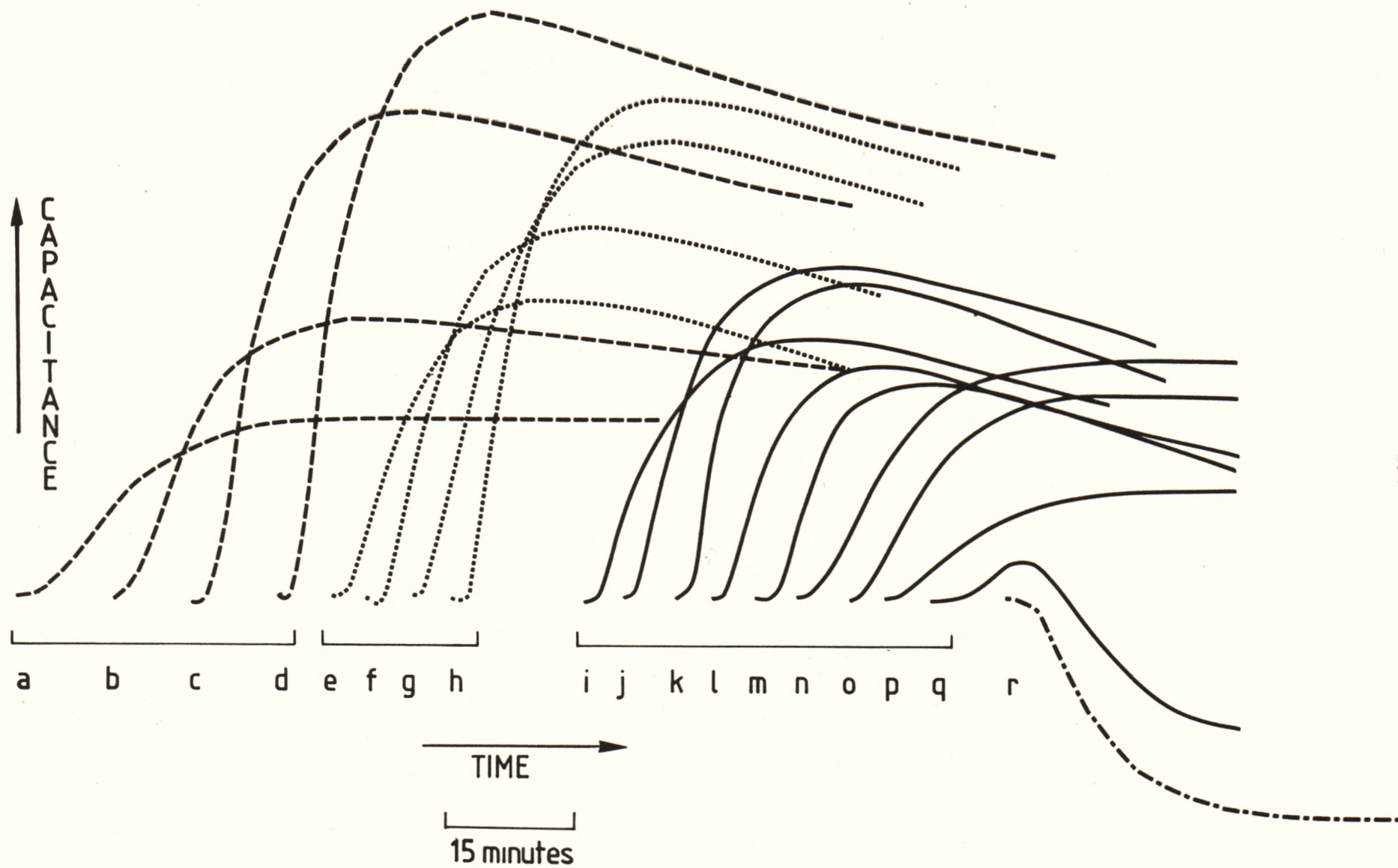
temperature, it took 20-30 minutes for the cell to reach the new temperature (as judged by the cell thermometer), and a further 20-30 minutes for the sample to reach thermal equilibrium (as judged by the stabilization of the sample capacitance and conductance). Typical examples of the normal behaviour of the capacitance following a change in the set-point temperature are shown in Figure 6.17 by curves (a) and (r). As can be seen from these curves, an increase in temperature well below T_c^d resulted in an increase in capacitance (curve (a)), whilst above T_c^d an increase in temperature resulted in a decrease in the capacitance. In both cases the capacitance had levelled off and adopted steady values after about one hour, indicating that this interval of time is sufficient for the cell and sample to come to thermal equilibrium.

However, in the range 215-245 K this pattern changed. Following a rise in the set-point temperature, the capacitance and conductance rose during the 20-30 minutes that the probe was warming up, but then, instead of levelling out to steady values, the capacitance and conductance relaxed back to lower values. The variation of this relaxation effect as $T \rightarrow T_c^d$ is shown schematically in Figure 6.17 (curves (b)-(o)). At 221 K, the rate of relaxation of the capacitance immediately following the stabilization of the cell was about 3.6 pF/hour (or about 2% of the total capacitance per hour). In an attempt to monitor this effect further, the temperature was kept steady at 221 K for the next six days. In the first 15 hours the capacitance relaxed back to the value it held at about 211 K, so that the magnitude of these effects is very large indeed. By the end of this time the rate of relaxation had slowed to about 0.8 pF/hour. A further six days were required before the rate dropped to 0.4 pF/hour. The time constant for the relaxation effect was estimated to be about 26 hours.

Figure 6.17. Schematic Diagram Showing the Variation of Capacitance Following a Change in the Set-point Temperature.

Curve	Temperature prior to increase in the set-point temperature (K)	Increase in the set-point temperature (K)	Gain setting (dB)
a	206.0	2.5	60
b	218.5	2.5	60
c	232.6	1.0	60
d	233.6	1.0	60
e	234.5	1.0	50
f	235.5	1.0	50
g	236.5	1.0	50
h	237.5	1.0	50
i	238.5	1.0	40
j	239.5	1.0	40
k	240.4	1.0	40
l	241.4	1.0	40
m	242.4	1.0	40
n	243.4	1.0	40
o	244.4	1.0	40
p	245.3	1.0	40
q	246.3	1.0	40
r	248.3	0.5	30

Note that since the changes in capacitance were much larger closer to the transition, it was necessary to decrease the gain settings as $T \rightarrow T_c^d$ so that the curves in the figure are plotted using different vertical scales as listed above. The peak in curve (q) corresponds to the maximum in the capacitance at T_c^d .



The rate of relaxation to lower values increased as $T \rightarrow T_c^d$, reaching a maximum of about 3 pF/min (or about 18% of the total capacitance per hour) at 241 K. At this temperature the time constant was estimated to be about 3-4 hours. The rate decreased until, at about 243 K, the capacitance and conductance adopted fairly steady values following changes in the set-point temperature (see Figure 6.17). The relaxation effects made it difficult to monitor the dielectric behaviour in the temperature region close to the transition, so that it was not possible to determine the transition temperature as accurately as was originally desired. An estimate of T_c^d (as measured by the peak in the capacitance) was 246.8 ± 0.7 K, which coincides with the temperature of the peak of the attenuation for the longitudinal wave propagating along the x axis (see Figure 6.5).

Because of the length of the time-dependence of the values of capacitance and conductance resulting from the relaxation phenomenon, it was necessary to adopt a fixed time interval between the change of the set-point temperature and taking a reading. As the measurements in the absence of the relaxation phenomenon (i.e. outside the range 215-245 K) indicated a period of one hour to reach thermal equilibrium, this time interval was adopted for all measurements. Overnight breaks in data collection appear as large discontinuous jumps in the values of capacitance and conductance plotted in Figure 6.16, particularly visible in the range 220-245 K.

A similar relaxation effect was observed below 245 K whilst cooling the specimen. The relaxation effect appeared suddenly as the specimen was cooled into the transition region. The rate of relaxation was a maximum of 8.5 pF/min just below T_c^d . (The capacitance was about 3000 pF at this temperature.) T_c^d for the cooling run was estimated to be 245 ± 1 K. The rate decreased steadily as the temperature was lowered

until, at about 210 K, relaxation, if present at all, was too small to be observed.

In summary, then, it may be said that in the sample studied there is a very long term (hours-days) relaxation of the dielectric constant to lower values in the range 215-243 K. These relaxation effects are largest just below T_c^d , but appear to be absent above T_c^d , although the presence of these effects leads to some uncertainty in ascertaining the exact transition temperature.

The relaxation effect deserves further investigation. Of particular interest are: an accurate measure of the time constant, the dependence of the effects on applied electric field strength, and the extension of the observations to samples of varying degrees of deuteration. The current experimental arrangement is not suitable for exploring these effects further because of (a) the long thermal time constant of the cell and (b) the lack of automation of the experimental arrangement which renders impossible the continuous scanning of the relaxation effects over long periods of time.

(b) Measurements along the x axis

Uesu and Kobayashi (1976) have reported that the dielectric constants measured along the x and z axes in CDP are independent of temperature over the range 110-300 K. However the temperature dependence of the capacitance and conductance along the x axis for CDDP measured during a heating run, shown in Figure 6.18, does indeed show a significant anomaly, albeit much smaller than the y axis anomaly. The same sample and experimental arrangement were used for the x and y axis measurements.

Relaxation effects similar to those occurring for the y axis were observed in the range 235-242 K. T_c^d was estimated to be 246.3 ± 1 K.

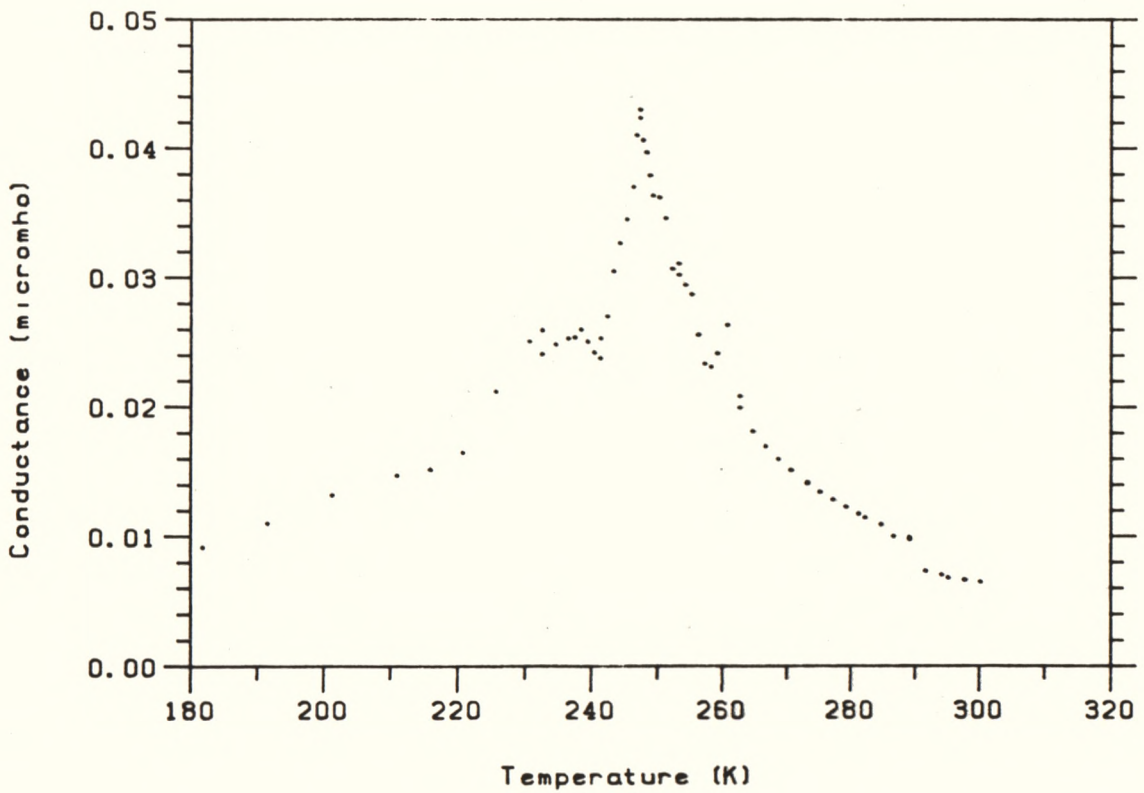
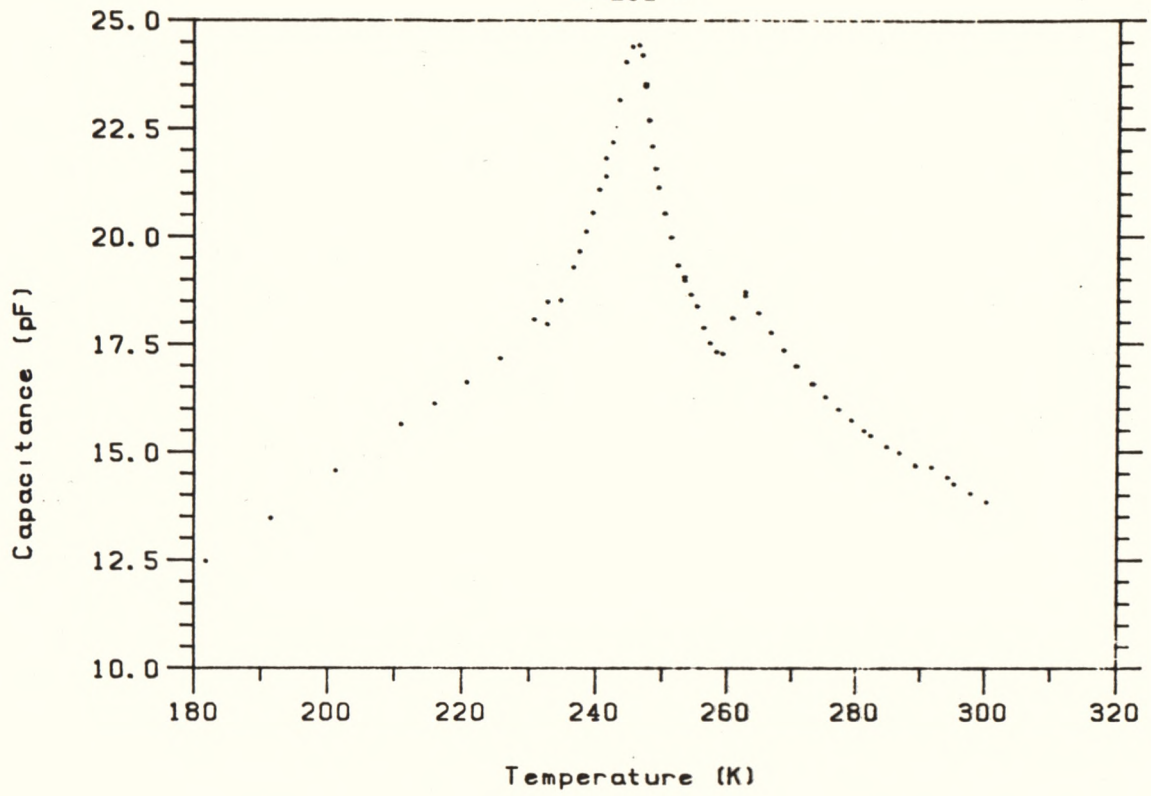


Figure 6.18. Temperature Dependences of the Capacitance and Conductance of CDDP measured along the x axis.

The discontinuity at 260 K is spurious, and was not reproducible. It was associated with an observed instability in the bridge readings. The probable cause was that the sample, as a result of handling during the ultrasonic and y axis dielectric measurements, was slightly damaged and some small (100) pieces had cleaved from the prepared surface before the sample was inserted into the cell for the x axis measurements. This slight damage caused some mechanical instability in the sample holding arrangement, so that the probable cause of the spurious effect at 260 K was a small physical change in the position of the sample.

The sample thickness was 0.560 mm and the approximate surface area of the parallel faces was 1.05 cm^2 , so that an estimate of the dielectric constant may be obtained by multiplying the capacitance (in pF) in Figure 6.18 by a factor of 6.2.

6.4.4 Discussion

6.4.4.1 $T > T_C^d$: Deviations from Curie-Weiss Behaviour

(a) Y axis measurements

Figure 6.19 shows a plot of the inverse capacitance versus temperature for the y axis measurement of dielectric constant (i.e. the data of Figure 6.16). A smoothed spline function (IMSL routine ICSSCU) has been fitted to the data. The fit shows a linear temperature dependence of inverse capacitance over the range 248-262 K. In order to gain a better estimate of the upper temperature limit of this linear region, the temperature derivative of the fit was calculated, and is also plotted in Figure 6.19. The derivative is reasonably constant over the range 250-260 K, but above 260 K shows a steady increase. Hence, in the region 248-260 K, the dielectric behaviour is well described by the usual Curie-Weiss law

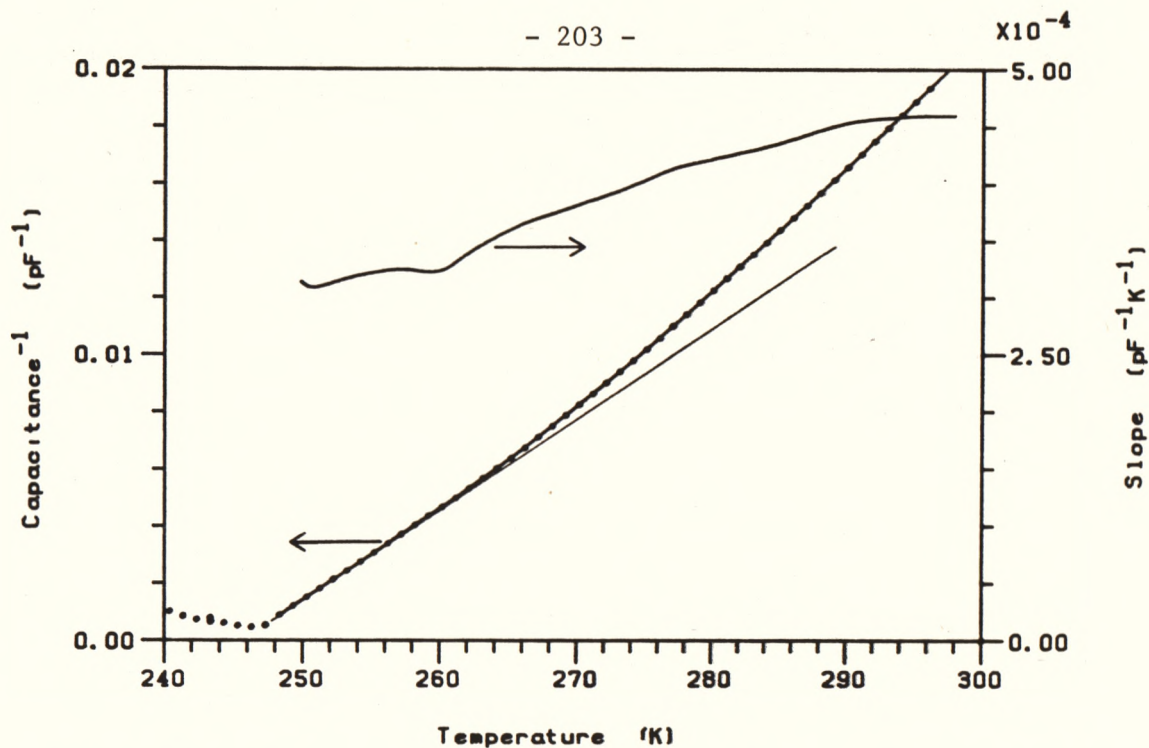


Figure 6.19. The Temperature Dependence of the Inverse Capacitance for the y axis Data of Figure 6.16. Note the increase in slope at about 260 K corresponding to the deviation of the dielectric constant from the Curie-Weiss law in this temperature region.

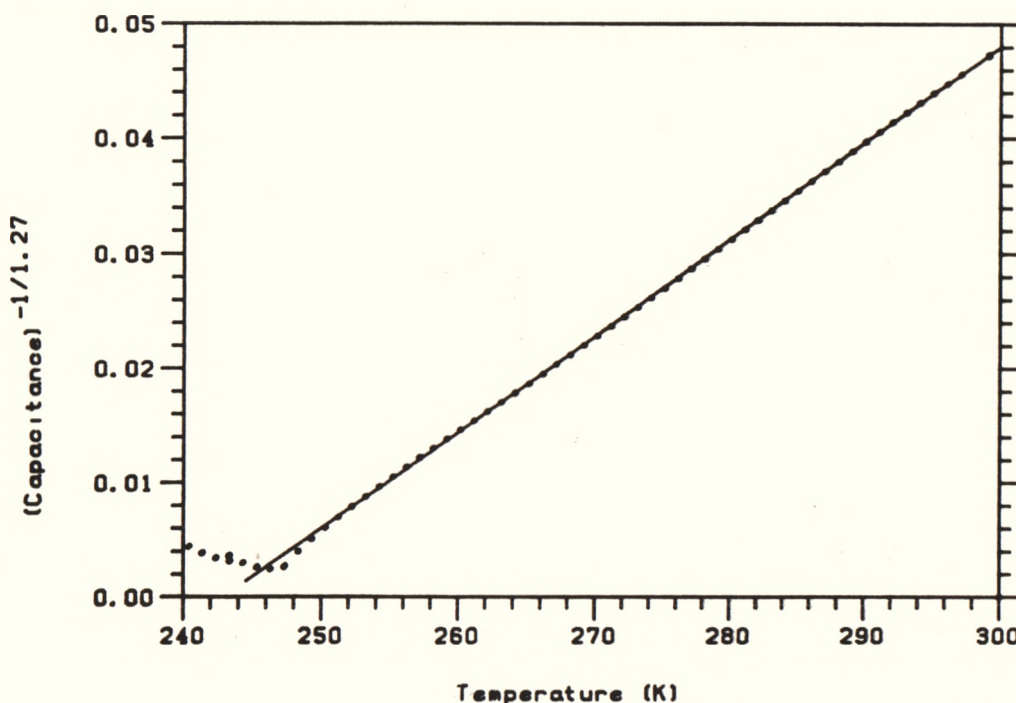


Figure 6.20. The Temperature Dependence of Inverse Capacitance Raised to the Power of 1/1.27 for the Data of Figure 6.16. In the temperature range 250-300 K the plot is linear, which indicates that, in this region, the capacitance is well described by the power law dependence $(T-T_0)^{-\kappa}$, where $\kappa = 1.27 \pm 0.02$.

$$\text{Capacitance} = k (T-T_0)^{-1}$$

where T_0 was determined to be 245.9 ± 0.2 K and $k = 3.03 \times 10^3$ pF K. If the conversion factor of 21.4 between dielectric constant and capacitance (section 6.4.3(a)) is assumed, this value of k gives a value for the Curie constant of 6.5×10^4 K.

Above 260 K, the dielectric behaviour deviates from the usual Curie-Weiss law, and in fact may be fitted to the expression

$$\text{Capacitance} = k' (T-T_0')^{-\kappa}$$

where $\kappa = 1.27 \pm 0.02$ and $T_0' = 242.9 \pm 0.2$ K (Figure 6.20). This value of κ was obtained by plotting $(\text{capacitance})^{-1/\kappa}$ versus temperature for different values of κ and choosing that value of κ which minimized χ^2 for a straight line fit in the region 250-300 K. Although difficult to see in Figure 6.20, there is a small curvature in the temperature dependence of $(\text{capacitance})^{-1/1.27}$ in the range 250-260 K, but above 260 K the linear fit is excellent.

Thus, it may be stated that above T_c^d there is a definite cross-over between a region close to T_c ($(T-T_c^d) < 13$ K) described by the Curie-Weiss law, and a region further from T_c ($13 < (T-T_c^d) < 52$ K) described by a non-classical value of the critical exponent of 1.27 ± 0.02 .

Blinc et al. (1979) have reported similar behaviour in the dielectric constant. Their measurements on CDDP showed Curie-Weiss behaviour in the region $0 < (T-T_c^d) < 4$ K and a non-classical value of the critical exponent of 1.28 ± 0.03 in the region $4 < (T-T_c^d) < 35$ K. They associated the classical Curie-Weiss behaviour with the usual long-range, dipole-dipole interactions which are adequately described by

a mean field theory, whilst the region described by a non-classical critical exponent was associated with short-range, one-dimensional type interactions. They quantified this model by proposing that the short-range intrachain coupling be described by a one-dimensional Ising model and the long-range interchain interactions be approximated by a mean field. This model yielded the following expression for the dielectric constant, ξ , above T_c^d :

$$\xi = \frac{A/T}{\exp(-a/T) - B/T} \quad (6.6)$$

where B/a measures the ratio between the strengths of the interchain and intrachain interactions, and A is a term proportional to the square of the dipole moment generated by the disordered hydrogen occupying one of its two possible equilibrium sites in the short O-H....O bond. They found that the data for a sample of CDDP (with $T_c^d = 257.44$ K) could be quantitatively described by equation (6.6) with the value of $B/a = 6 \times 10^{-4}$. This small value indicates that CDDP is very "one-dimensional".

Blinc et al. (1979) found the cross-over between the regions of 1-D and 3-D correlations in both CDDP and CDP at about 3 K above T_c , with the value of the non-classical exponent being 1.31 ± 0.1 for CDP. However, Deguchi et al. (1982(b)) have found significant deviations from the one-dimensional model in the region $0 < (T - T_c^d) < 20$ K. Whilst they assume that these deviations are due to the development of long-range, 3-D correlations close to the transition, they also found that the critical exponent in this region is different from unity (i.e. the dielectric behaviour does not follow a Curie-Weiss law or a one-dimensional Ising model in the range $0 < (T - T_c) < 20$ K). Hence, whilst the two above authors concur as to the existence of a temperature

range dominated by 1-D correlations, they differ as to the width of this region, and as to the nature of the dielectric behaviour in the region dominated by 3-D correlations. The findings of this study support the findings of Blinc et al. (1979), although the region of Curie-Weiss behaviour is considerably wider than that reported by them. At present these differences in the reported dielectric behaviour remain unresolved. It is possible that variations in the defect concentrations of the samples used may account for some of these differences. It is clear that more care will have to be taken in future to standardize the sample preparation procedure.

(b) X axis measurements

Since the dielectric constant along the x axis has been previously reported to be independent of temperature (Uesu and Kobayashi 1976), it is important to examine the possibility that the observed anomaly in Figure 6.18 was not due solely to a possible small misalignment of the sample from the x direction resulting in the observation of a component of the large y axis anomaly. From the Laue photographs taken of the specimen (see Chapter 3) the maximum possible degree of misalignment was $\pm 1^\circ$. This misalignment would result in an observed x axis anomaly of about $\sin 1^\circ \approx 1.8\%$ of the size of the y axis anomaly. In fact the magnitude of the x axis anomaly in Figure 6.18 is about 4.2% of the magnitude of the y axis anomaly, which suggests that there is a genuine anomaly in the x axis dielectric behaviour.

The existence of such a genuine anomaly was confirmed by the critical point analysis. Figure 6.21 shows a plot of inverse capacitance versus temperature for the x axis measurements of Figure 6.18. It is clear that the dielectric behaviour does not follow a Curie-Weiss law. Note that the slope of the curve decreases with increasing temperature,

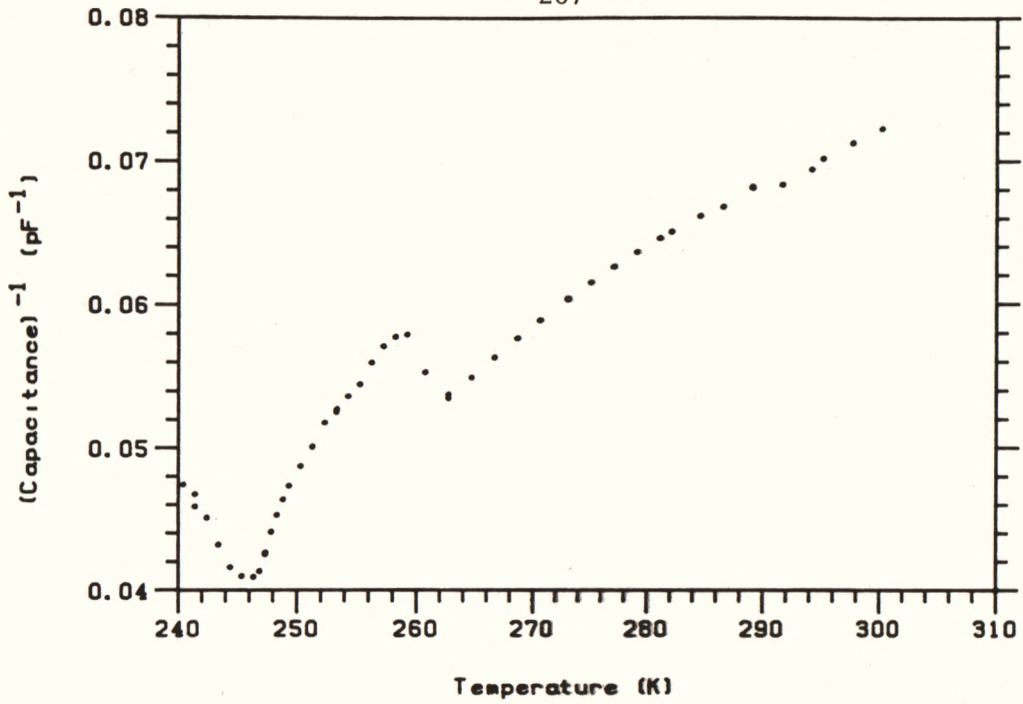


Figure 6.21. The Temperature Dependence of the Inverse Capacitance for the x axis data of Figure 6.18.

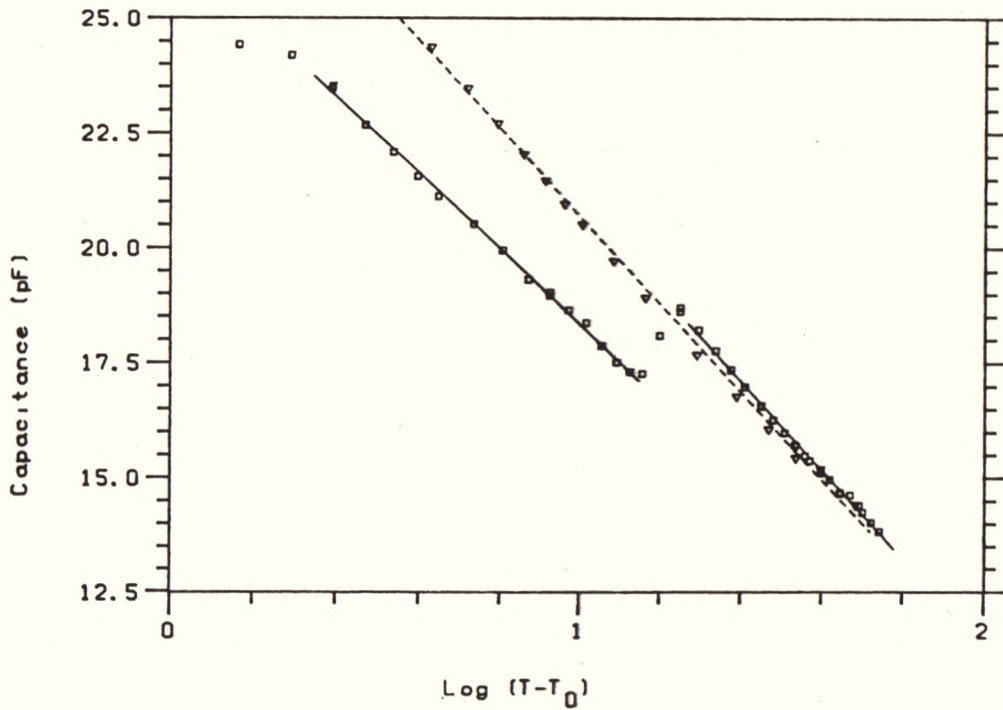


Figure 6.22. The x axis Capacitance plotted as a function of $\log (T-T_0)$. The squares and solid line fit refer to the data of Figure 6.18 (which was taken on a heating run). Data taken on a cooling run (shown by the inverted triangles and fitted by the broken line) confirm that there is a genuine log type dependence of the dielectric constant orthogonal to the ferroelectric axis.

in contrast to Figure 6.19 where the slope slowly increases. This suggests that a critical point exponent of less than unity is appropriate. Plots of (capacitance) $^{-1/\kappa}$ versus temperature for varying values of κ showed that the fit improved as $\kappa \rightarrow 0$, suggesting the possibility of a log type dependence (see Fisher (1967) wherein it is shown that $(T-T_0)^{-\kappa} \rightarrow \log (T-T_0)$ as $\kappa \rightarrow 0$).

Figure 6.22 shows a plot of capacitance versus $\log (T-T_0)$ where $T_0 = 244.9 \pm 1$ K has been chosen so as to minimize χ^2 for the straight line fit to the data. The source of the kink at $\log (T-T_0) \approx 1.1$ is the spurious anomaly at 260 K (see Figure 6.18). Due to this anomaly the slope of the straight line fit is different by about 14% below and above 260 K, but it is nevertheless reasonable to describe the data by a straight line over a decade. The log dependence was confirmed by data taken on a cooling run with $T_0 = 247.5 \pm 1$ K. This data is also shown in Figure 6.22.

Since the x axis dielectric behaviour follows a different functional form from the y axis dielectric constant, it is clear that the x axis anomaly cannot be simply due to a component of the y axis anomaly appearing in the x direction. Hence these measurements confirm the presence of a genuine dielectric anomaly in the x axis dielectric constant with a $\log (T-T_0)$ type dependence.

It would be very interesting to see if this non-classical log-type dependence could be described in the framework of the one-dimensional Ising model, which was successful in the case of the y axis behaviour. However, it is important to note that the x axis measurements do not display a region which may be thought of as dominated by 3-D, dipole-dipole interactions (as evidenced by a $(T-T_0)^{-1}$ dependence). In this regard an obvious extension to the present work would be a measurement of the dielectric behaviour along the z axis and an

examination of the dielectric properties at right angles to the ferroelectric axis as a function of deuterium content.

6.4.4.2 $T < T_c^d$: Relaxation Effects

As has already been discussed in section 6.2.4.1, Kamysheva et al. (1981) have found evidence of a very high mobility of the domain walls in CDP in the temperature region between T_c and T_f (where T_f is the freezing point of the domain structure). The width of this region of about 30 K is of the same order as the width of the temperature region in which relaxation effects were observed in CDDP in this study. Thus, the relaxation effects may be due to a rearrangement of the domain structure driven by the small measuring field (which was continuously applied to the specimen even during the overnight breaks in data collection). It is reasonable to attribute such a rearrangement to such a small field in view of the very low value of coercive field ($100\text{--}200 \text{ V cm}^{-1}$) at temperatures about 20 K below T_c , and the observed S-shaped type hysteresis curve with the coercive field close to zero at 3-5 K below T_c (Kamysheva et al. (1981)). Hence, as the sample is warmed towards T_c , the increasing rate of relaxation may be attributed to the increasing mobility of the domain walls (as evidenced by the increase in the dielectric loss seen in Figure 6.18, and as observed by Kamysheva et al. (1981)), and the reduction in the field necessary to bring about a rearrangement of the domains. With the disappearance of a permanent dipole moment above T_c , the domains may be thought of as having "dissolved", and hence no relaxation is observed above the transition temperature. An obvious necessary extension to this work is an examination of the dependence of the relaxation phenomenon on the applied electric field strength. Initial investigations showed that, as might be expected, the rate of relaxation increased markedly as the

measuring field strength was increased from 1 V cm^{-1} to 100 V cm^{-1} .

To the best of the author's knowledge, similar relaxation effects have not been reported elsewhere in the literature. This may simply be due to the fact that most authors have used continuous temperature scans rather than stabilizing the temperature for each measurement. However, Levstik et al. (1975), who used a measurement system very similar to the one used in this study in their measurements on CDP and CDDP, have also not reported any relaxation phenomena.

This non-observance by other authors of relaxation effects in CDP or CDDP may be due to differences in the defect concentration of the samples used in the measurements. The situation may be analogous to the observation of the "double" anomaly for the z-axis measurements which was only observed in one of the specimens studied. In that case the differences between specimens were attributed to the dependence of the domain structure on the defect concentration (Kamysheva et al. (1981)). As in the ultrasonic measurements this hypothesis could be tested by annealing the specimen and remeasuring its dielectric behaviour.

6.5 SUMMARY

Measurements of the ultrasonic velocity and attenuation of the longitudinal waves propagating along the x, y, and z axes in CDP revealed anomalies for all three directions, with the largest anomaly occurring for the ferroelectric y axis. The anomaly along the x axis in CDDP was found to be much smaller and broader than that for the corresponding mode in CDP. The question of whether deuteration changes the nature of the transition mechanism remains unresolved.

Only the data collected for the z axis were of sufficient quality to carry out a critical point analysis. This analysis provided evidence to suggest a cross-over between a temperature region close to T_c in which the anomaly displays a power law dependence, and a region further away from T_c in which the anomaly displays a log type dependence. The interpretation offered to explain these observations is that far away from T_c , 1-D, short-range interactions dominate the ultrasonic behaviour, whilst close to T_c the usual 3-D, long-range, dipole-dipole interactions are dominant.

These findings were compared and contrasted with the conflicting log type dependences of the anomalies found by Kanda et al. (1983) (K83), and the power law dependences with large critical exponents found by Yakushkin et al. (1981) (Y81). The above interpretation is not consistent with the theoretical basis apparently underlying the work of both K83 and Y81 that a log type dependence is evidence of 3-D interactions, whilst a power law dependence with large critical exponents is evidence of 1-D interactions.

Some of the discrepancies between the results reported by Y81, K83, and this study may be due to the different conditions under which the measurements of each study were performed. (For example, the degree of deuteration, and the application of a bias field to produce a

monodomain specimen were found to have a marked influence on the size and shape of the anomalies.) In this context the findings of this study could be viewed as possessing elements of the features reported by both Y81 and K83.

Measurements of the dielectric constant of CDDP showed that the dielectric constant is described by the usual Curie-Weiss law close to T_c , whereas, further away from T_c , the dielectric constant is described by a non-classical critical exponent of 1.27. Other studies have found that, in the region described by this non-classical critical exponent, the dielectric constant is well described by the 1-D Ising model. Hence, the results of this study constitute convincing evidence (consistent with the findings of this study for the ultrasonic measurements) of a cross-over between a temperature region close to the transition dominated by 3-D interactions, and a region further away from T_c dominated by 1-D interactions.

In contrast with the findings of previous studies, a significant anomaly was found for the dielectric constant measured orthogonal to the ferroelectric axis. This anomaly was found to have a log type dependence, and although the interpretation of this finding remains unclear, it is interesting to speculate that this may be due to 3-D deviations from the 1-D Ising model which become evident when the dielectric constant is measured orthogonal to the ferroelectric axis

The directional Grüneisen parameters (calculated from x and z axis thermal expansion coefficients measured by this study and the y axis data reported by Deguchi et al. (1981)) show that, from the thermodynamic point of view, the "one-dimensionality" of CDP increases as $T \rightarrow T_c$. The expansion measurements show no evidence of a "cross-over" as discussed above, but this may well be due to the poor temperature resolution of these measurements. (Note, however, that Nakamura et al.

(1984) have found that a systematic deviation exists between their measured y axis expansion data and the values calculated on the basis of the 1-D Ising model. They attributed these deviations to the growth of 3-D interactions close to transition.)

Finally, the observation of an unexpected second anomaly below T_c in the z axis ultrasonic measurements, and the observation of very long term relaxation effects in the dielectric constant below T_c , both suggest that CDP has a very "soft" domain structure in the ferroelectric phase.

CHAPTER 7

CONCLUSION

7.1 THE PRESENT STUDY

The elastic constant matrix of CsH_2PO_4 (CDP) has been determined using ultrasonic velocity measurements at 10 MHz. The elastic constants have been used to calculate phase and group velocity surfaces, the bulk modulus, linear compressibilities, Young's modulus surfaces and the Debye temperature. The calculations showed that CDP is a very soft material with a bulk modulus of only 5.3 GPa. Significant anisotropy was found in Young's modulus and linear compressibility, which has been successfully correlated with the known chain and layer-like structure of CDP. Despite the disordered nature of the hydrogen linking the ferroelectric y axis chain, Young's modulus for this direction was found to be much larger than that for the x or z axes. On the basis of the elastic measurements it has been concluded that, even at room temperature, CDP shows evidence of being a "one-dimensional" material.

In an attempt to elucidate the mechanism of the ferroelectric transition, measurements have been made of the temperature dependences of (a) the ultrasonic velocity and attenuation for the longitudinal modes propagating along the x, y, and z axes, (b) the expansion coefficient along the x and z directions, and (c) the dielectric constant of CDDP. The critical point analyses of both the ultrasonic and dielectric anomalies showed evidence of a cross-over between temperature regions in which the anomalies are described by different functional forms, which suggests that the transition in CDP takes place in two stages. Far away from T_c , 1-D, intrachain forces are dominant. In this region, the dielectric behaviour is well described by a 1-D Ising model.

(These observations are consistent with the room temperature elastic measurements which also suggest the dominance of 1-D type forces.) However, as $T \rightarrow T_c$, the 3-D, interchain, dipole-dipole interaction grows until it dominates the behaviour. This 3-D interaction is presumably responsible for the small displacements of the Cs and P atoms at the transition which contribute to the development of a permanent dipole moment in the ferroelectric state.

Calculations of the Grüneisen parameters based on the expansion measurements have revealed that, from the thermodynamic point of view, the degree of "one-dimensionality" increases as the transition is approached. This is consistent with the reported increase in the intrachain correlation for the hydrogen-bonded y axis chain as $T \rightarrow T_c$.

7.2 FUTURE WORK

Most of the analysis in this study has concentrated on the transition region for $T > T_c$. However, the observation of (a) a second, unexpected ultrasonic anomaly below T_c for propagation along the z axis and (b) a very long term relaxation in the dielectric constant, also below T_c , suggested that CDP has a very "soft" domain structure in the ferroelectric state. It was also noted that the size and shape of the ultrasonic anomalies are different for polydomain and monodomain specimens. Several suggestions have been made in the text as to how these domain effects could be investigated further, including the quantitative examination of the dielectric relaxation effects, a comparative analysis of the critical region of the ultrasonic anomalies for monodomain and polydomain specimens, and the use of γ -irradiation to study the effects of defects on the domain structure.

The effect of deuteration on the mechanism of the ferroelectric transition mechanism remains unclear. In order to clarify this, it will

be necessary to compare careful critical point analyses of the ultrasonic anomalies of a series of samples with varying levels of deuteration.

Looking further into the future, with automation of the ultrasonic measurement system, it may become practicable to measure the temperature dependence of the velocities of a sufficient number of modes to enable the determination of the temperature dependences of all thirteen elastic constants of CDP. It would then be possible to see if the increased correlation length along the y axis as $T \rightarrow T_c$ is reflected by changes in the anisotropy in Young's modulus and the linear compressibility. Even if it is not possible to make sufficient measurements to enable the calculation of all the elastic constants, it would still be very interesting to study the temperature dependences of some of the transverse modes, especially for propagation in the xz plane, since this plane has shown such a large degree of anisotropy in the room temperature elastic measurements.

In conclusion, it may be said that the results presented in this study constitute only one more step in the overall understanding of the lattice dynamics of CDP. The next major important step in this understanding would be a determination of the room temperature phonon dispersion curves, with special emphasis to be placed on the very damped transverse acoustic mode which propagates at 38° to the x axis in the xz plane. The initial slopes of the acoustic branches of the dispersion curves are easily calculated from the elastic constants and this should aid in the search for these branches. Nevertheless the determination of the phonon dispersion curves is likely to be very demanding due to the monoclinic symmetry of CDP.

REFERENCES

- Aleksandrov, K.S., "An Ultrasonic Pulse Method of Measuring the Elastic Moduli of Monoclinic Crystals", *Sov. Phys. Crystallogr.*, 3, 630-632, (1958).
- Baranov, A.I., Ryabkin, V.S., and Shuvalov, L.A., "Some Dielectric Properties of the $\text{Cs}(\text{H}_{1-x}\text{D}_x)_2\text{PO}_4$ Crystals", *Ferroelectrics*, 25, 471-474, (1980)
- Baranov, A.I., Shuvalov, L.A., and Yakushkin, E.D., "Some Peculiarities of Ferroelectric Ordering in CsH_2PO_4 Crystals", *Ferroelectrics*, 47, 25-31, (1983)
- Barron, T.H.K., Collins, J.G., and White, G.K., "Thermal Expansion of Solids at Low Temperatures", *Advances in Physics*, 29, 609-730, (1980)
- Blinic, R., Zeks, B., Levstik, A., Filipic, C., Slak, J., Burgar, M., Zupancic, I., Shuvalov, L.A., and Baranov, A.I., "Pseudo-One-Dimensional Ferroelectric Ordering and Critical Properties of CsH_2PO_4 and CsD_2PO_4 ", *Phys. Rev. Lett.*, 43, 231-234, (1979)
- Brown, F.C., "The Physics of Solids", 1st edition, New York, W.A.Benjamin, Inc. (1967)
- Carnahan, B., Luther, H.A., and Wilkes, J.O., "Applied Numerical Methods", 1st edition, New York, J. Wiley and Sons, 319, (1969)
- Chick, B.B., Anderson, G., and Truell, R., "Ultrasonic Attenuation Unit and its Use in Measuring Attenuation in Alkali Halides," *J. Acoust. Soc. Am.*, 32, 186-193, (1960)
- Cornelius, C.A., "A Simple Computer Method for the Orientation of Single Crystals of Any Structure Using Laue Back Reflection X-ray Photographs", *Acta Cryst.* A37, 430-436, (1981)
- Cornelius, C.A., "Electronic Transitions in Transition Metals and their Compounds", Ph.D. Thesis, Monash University, Melbourne, (1982)
- Deguchi, K., Okaue, E., Abe, K., and Nakamura, E., "Anomalous Behaviour of Spontaneous Strain in Ferroelectric Cesium Dihydrogen Phosphate, CsH_2PO_4 ", *J. Phys. Soc. Jpn.*, 50, 2783-2784, (1981)
- Deguchi, K., Okaue, E., and Nakamura, E., "Static and Dynamic Critical Properties of Dielectric Constant in Ferroelectric CsH_2PO_4 and CsD_2PO_4 ", *J. Phys. Soc. Jpn.*, 51, 349-350, (1982(a))
- Deguchi, K., Okaue, E., and Nakamura, E., "Effects of Deuteration on the Dielectric Properties of Ferroelectric CsH_2PO_4 . I. Static Dielectric Properties", *J. Phys. Soc. Jpn.*, 51, 3569-3574, (1982(b))
- Federov, F.I., "Theory of Elastic Waves in Crystals", 1st edition, New York, Plenum Press, (1968)

- Fellner-Feldegg, H., "Strukturbestimmung von CsH_2PO_4 ",
Tscherma's Mineral. Petrogr. Mitt., 3, 37-44, (1952)
- Fisher, M.E., "The Theory of Equilibrium Critical Phenomena", Reports
on Progress in Physics, 30, 615-730, (1967)
- Frazer, B.C., Semmingsen, D., Ellenson, W.D., and Shirane, G., "One
Dimensional Ordering in Ferroelectric CsD_2PO_4 and CsH_2PO_4
as Studied with Neutron Scattering", Phys. Rev. B., 20,
2745-2754, (1979)
- Fritz, I.J., "Anomalous Acoustic Behaviour of KH_2PO_4 -type Crystals
at High Pressure", Phys. Rev. B., 13, 705-712, (1976)
- Garland, C.W., "Ultrasonic Investigation of Phase Transitions and
Critical Points", in "Physical Acoustics", Vol VII, edited
by W.P. Mason and R.N. Thurston, New York, Academic Press,
Chapter 2, 51-148, (1970)
- Garland, C.W., and Novotny, D.B., "Ultrasonic Velocity and Attenuation
in KH_2PO_4 ", Phys. Rev., 177, 971-975, (1969)
- Gibbs, E.E., "Anharmonic Properties of Vanadium Based A-15
Superconductors", Ph.D. Thesis, Monash University, Melbourne,
(1983)
- Grüneisen, E., and Goens, E., "Researches on Metal Crystals III;
Thermal Expansion of Zinc and Cadmium",
Z. Phys., 29, 141-156, (1924)
- Imai, K., "Anomalous Behaviour in the Heat Capacities of Pseudo-
One-Dimensional Ferroelectrics CsH_2PO_4 and CsD_2PO_4 ",
J. Phys. Soc. Jpn., 52, 3960-3965, (1983)
- Irving, M.A., Prawer, S., Smith, T.F., and Finlayson, T.R., "The Room
Temperature Elastic Constants of Caesium Thiocyanate", Aust.
J. Phys., 36, 85-92, (1983)
- Iwata, Y., Koyano, N., and Shibuya, I., "A Neutron Diffraction Study
of the Ferroelectric Transition of CsH_2PO_4 ", J. Phys. Soc.
Jpn., 49, 304-307, (1980)
- Jona, F., and Shirane, G., "Ferroelectric Crystals", 1st edition,
Oxford, Pergamon Press, (1962)
- Kamysheva, L.N., Drozhdin, S.N., and Sidorkin, A.S., "The Freezing of
the Domain Structure in the CDP Crystal Resulting from the
Structural Reconstruction of the Domain Walls", Ferroelectrics,
31, 37-40, (1981)
- Kanda, E., Tamaki, A., Fujimura, T., "Critical Slowing Down in the One-
Dimensional Ferroelectric CsH_2PO_4 ", J. Phys. C: Solid State
Phys., 15, 3401-3410, (1982(a))

- Kanda, E., Yoshizawa, M., Yamakami, T., and Fujimura, T., "Specific Heat Study of Ferroelectric CsH_2PO_4 and CsD_2PO_4 ", J. Phys. C: Solid State Phys., 15, 6823-6831, (1982(b))
- Kanda, E., Tamaki, A., Yamakami, T., and Fujimura, T., "Study of Ferroelectric CsH_2PO_4 by the Ultrasonic Velocity and Attenuation Measurements", J. Phys. Soc. Jpn., 52, 3085-3092, (1983)
- Kasahara, M., and Tatsuzaki, I., "The Dispersion of a Sound Velocity Near the Phase Transition Point of CsD_2PO_4 ", Ferroelectrics Lett., 44, 21-26, (1982)
- Kittel, C., "Introduction to Solid State Physics", 5th edition, New York, John Wiley and Sons, Inc., (1976)
- Krupnyi, A.I., Al'chikov, V.V., and Aleksandrov, K.S., "Computer Calculation of Elasticity Tensor of Monoclinic Crystals", Sov. Phys. Crystallogr., 16, 692- 695, (1972)
- Levstik, A., Blinc, R., Kadaba, P., Cizikov, S., Levstik, I., and Filipic, C., "Dielectric Properties of CsH_2PO_4 and CsD_2PO_4 ", Solid State Commun., 16, 1339-1341, (1975)
- Lüthi, B., and Rehwald, W., "Ultrasonic Studies Near Structural Phase Transitions", in "Structural Phase Transitions I", edited by K.A.Muller and H.Thomas, Berlin, Springer-Verlag, Chapter 4, 131-184, (1981)
- McSkimin, H.J., "Pulse Superposition Method for Measuring Ultrasonic Wave Velocities in Solids", J. Acoust. Soc. Am., 33, 12-16, (1961)
- McSkimin, H.J., and Andreatch, P., "Analysis of the Pulse Superposition Method for Measuring Ultrasonic Wave Velocities as a Function Of Temperature", J. Acoust. Soc. Am., 34, 609-615, (1962)
- Matsunaga, H., Itoh, K., Nakamura, E., "X-ray Structural Study of Ferroelectric Cesium Dihydrogen Phosphate at Room Temperature", J. Phys. Soc. Jpn., 48, 2011-2014, (1980)
- Miller, S.A., editor "Ethylene and its Industrial Derivatives", 1st edition, London, Ernest Benn Ltd, (1969)
- Munn, R.W., "Role of the Elastic Constants in Negative Thermal Expansion of Axial Solids", J. Phys. C: Solid State Phys., 5, 535-542, (1972)
- Musgrave, M.J.P., "Crystal Acoustics", 1st edition, San Fransisco, Holden-Day, (1970)
- Nakamura, E., Abe, K., Deguchi, K., "Quasi-One-Dimensional Behaviour of Thermal Expansion in Ferroelectric CsH_2PO_4 ", J. Phys. Soc. Jpn., 53, 1614-1616, (1984)

- Natterman, Th., "Static and Dynamic Critical Behaviour of Uniaxial Ferroelectrics and the Phase Transition in TGS", Phys. Stat. Sol.(b), 85, 291-300, (1978)
- Neighbours, J.R., "Elastic Energy Flow in Crystals of General Symmetry", J. Appl. Phys., 44, 4816-4823, (1973)
- Nelmes, R.J., and Choudhary, R.N.P., "Structural Studies of the Monoclinic Dihydrogen Phosphates: A Neutron Diffraction Study of Paraelectric CsH_2PO_4 ", Solid State Commun., 26, 823-826, (1978)
- Nye, J.F., "Physical Properties of Crystals", 2nd edition, Oxford, Clarendon Press, (1967)
- Papadakis, E.P., "Ultrasonic Phase Velocity by the Pulse Echo-Overlap Method Incorporating Diffraction Phase Corrections", J. Acoust. Soc. Am., 42, 1045-1051, (1967)
- Papadakis, E.P., "The Measurement of Small Changes in Ultrasonic Velocity and Attenuation", Critical Reviews in Solid State Sciences CRC, 3, 373-418, (1973)
- Papadakis, E.P., "Ultrasonic Velocity and Attenuation: Measurement Methods with Scientific and Industrial Applications", in "Physical Acoustics", Vol XII, edited by W.P. Mason and R.N. Thurston, New York, Academic Press, Chapter 5, 277-374, (1976)
- Pickup, C.P., and Kemp, W.R.G., "High Precision Temperature Controller for Experimental Cryostats", Cryogenics, 9, 90-94, (1969)
- Rashkovich, L.H., Meteva, K.B., Shevchik, Ya.E., Hoffman, V.G., and Mishchenko, A.V., "Growing Single Crystals of Cesium Dihydrogen Phosphate and Some of Their Properties", Sov. Phys. Crystallogr. 22, 613-615, (1977)
- Roderick, R.L., and Truell, R., "The Measurement of Ultrasonic Attenuation in Solids by the Pulse Technique and Some Results in Steel", J. Appl. Phys., 23, 267-279, (1952)
- Rumble, S. "Raman Spectra of Cesium Dihydrogen Phosphate", Ph.D. Thesis, Monash University, Melbourne, (1983)
- Scott, J.F., "Soft Mode Spectroscopy: Experimental Studies of Structural Phase Transitions", Reviews of Modern Physics, 46, 83-128, (1974).
- Schwabl, F., "Ultrasonic Attenuation at Structural Transition above T_c ", Phys. Rev. B., 7, 2038-2046, (1973)
- Seidl, F., "Concerning the Seignetteoelectrical Behaviour of RbH_2PO_4 and CsH_2PO_4 ", Tschermaks Mineral. Petrogr. Mitt., 1, 432-435, (1950)
- Sil'vestrova, I.M., Barta, Ch., Dobrzhanskii, G.F., Belyaev, L.M., and Pisarevskii, Yu.V., "Elastic Properties of Hg_2Cl_2 Crystals", Sov. Phys. Crystallogr., 20, 221-224, (1975)

- Simpson, M., "Thermal Expansion of Dilute Magnetic Alloys", Ph.D. Thesis, Monash University, Melbourne, (1979)
- Spiegel, M.R., "Mathematical Handbook of Formulae and Tables", 1st edition, New York, McGraw-Hill, 32, (1968)
- Spörl, G., Chat, D.D., and Hegenbarth, E., "Thermal Conductivity of Pseudo-One-Dimensional Ferroelectric CsH_2PO_4 ", Phys. Stat. Sol.(a), 82, K27-31, (1984)
- "Standards on Piezoelectric Crystals", Proc. I.R.E., 37, 1378-1395, (1949)
- Todo, I., "Ultrasonic Velocity in TGSe near the Ferroelectric Phase Transition", J. Phys. Soc. Jpn., 39, 1538-1542, (1975)
- Topic, B., Rutar, V., Slak, J., Burgar, M.I., Zumer, S., and Blinc, R., "Deuteron Magnetic Resonance and Relaxation Study of the Pseudo-One-Dimensional Ferroelectric Transition in CsD_2PO_4 ", Phys. Rev. B., 21, 2695-2701, (1980)
- Truell, R., Elbaum, C., and Chick, B.B., "Ultrasonic Methods in Solid State Physics", 1st edition, New York, Academic Press, (1969)
- Uesu, Y. and Kobayashi, J., "Crystal Structure and Ferroelectricity of Cesium Dihydrogen Phosphate CsH_2PO_4 ", Phys. Stat. Sol.(a), 34, 475-481, (1976)
- White, G.K., and Collins, J.G., "Thermal Expansion of Copper, Silver and Gold at Low Temperatures", J. Low Temp. Phys., 7, 43-75, (1972)
- Yagi, T., Tokunaga, M., and Tatsuzaki, I., "Brillouin Scattering Studies of the Uniaxial Ferroelectric Phase Transition in TGS and TGSe", J. Phys. Soc. Jpn., 40, 1659-1667, (1976)
- Yakushkin, E.D., Baranov, A.I., and Shuvalov, L.A., "Critical Anomalies of the Velocity and Absorption of Sound in a Quasi-One-Dimensional Ferroelectric Material CsH_2PO_4 ", JETP Lett., 33, 24-28, (1981)
- Yasuda, N., Fujimoto, S., Okamoto, M., Shimizu, H., Yoshino, K., and Inuishi, Y., "Pressure and Temperature Dependence of the Dielectric Properties of CsH_2PO_4 and CsD_2PO_4 ", Phys. Rev. B., 20, 2755-2764, (1979)
- Yet-Chong, C., and Forrest, A.M., "A Platinum Resistance Thermometer Calibration between 2 K and 273.15 K", J. Scientific Instruments, (J. Phys. E.), 1, 839-842, (1968)
- Youngblood, R., Frazer, B.C., Eckert, J., and Shirane, G., "Neutron Scattering Study of the Pressure Dependence of Short-Range Order in CsD_2PO_4 ", Phys. Rev. B., 22, 228-235, (1980)

PUBLICATIONS

The ultrasonic measurement techniques described in this thesis have also been successfully applied to the measurement of the room temperature elastic constants of Cesium Thiocyanate. This work is described in

Irving, M.A., Prawer, S., Smith, T.F., and Finlayson, T.R.,
"The Room Temperature Elastic Constants of Caesium Thiocyanate",
Aust. J. Phys., 36, 85-92, (1983)

The work on the room temperature elastic constants of CDP is reported in

Prawer, S., Smith, T.F., and Finlayson, T.R., "The Room Temperature Elastic Constants of CsH_2PO_4 ", Aust. J. Phys., 38, 63-83, (1985)

The Room Temperature Elastic Constants of Caesium Thiocyanate

M. A. Irving, S. Praver, T. F. Smith and T. R. Finlayson

Department of Physics, Monash University, Clayton, Vic. 3168.

Abstract

The velocities of propagation of elastic waves in caesium thiocyanate have been measured along the three orthorhombic axes and normal to the (110), (011) and (101) planes using a double-transducer technique at 10 MHz. The velocities are found to be consistent with the orthorhombic crystal symmetry, and in favourable agreement with a recently published rigid-ion model calculation. The calculated elastic stiffness constants have values $c_{11} = 18.9 \pm 0.7$, $c_{22} = 20.6 \pm 1.0$, $c_{33} = 28.1 \pm 1.6$, $c_{44} = 1.96 \pm 0.05$, $c_{55} = 7.30 \pm 0.2$, $c_{66} = 3.04 \pm 0.07$, $c_{12} = 7.8 \pm 4.3$, $c_{13} = 14.8 \pm 4$ and $c_{23} = 6.3 \pm 4$ GPa. The calculated values for the adiabatic bulk modulus and the low temperature limiting value of the Debye temperature are 13.2 ± 3.5 GPa and 132 K respectively.

1. Introduction

The alkali metal thiocyanates have crystal structures consisting of spherical cations and rod-shaped anions. These substances are of interest because of order-disorder type phase transitions involving the orientation of the anions which occur just below their melting points.

Potassium thiocyanate has been extensively studied by X-ray diffraction (Klug 1933; Yamada and Watanabe 1963; Akers *et al.* 1968), thermal expansion (Sakiyama *et al.* 1963), heat capacity (Vanderzee and Westrum 1970; Kinsho *et al.* 1979), differential thermal analysis (Sakiyama *et al.* 1963; Braghetti *et al.* 1969) and spectroscopic investigations (Jones 1958; Iqbal *et al.* 1972; Dao and Wilkinson 1973; Ti *et al.* 1976; Owens 1979).

By comparison caesium thiocyanate has received little attention, as only the crystal structure for the room temperature phase (Manolatos *et al.* 1973) and a differential thermal analysis investigation of the transition under pressure (Klement 1976) have been reported.

Recently, lattice dynamical calculations based upon a rigid-ion model have been made for both potassium and caesium thiocyanate (Ti *et al.* 1978; Ti and Ra 1980a, 1980b). The model potential parameters were determined from lattice stability and static equilibrium conditions. The calculated zone centre energies for the optic modes agreed favourably with the available Raman data (Ti *et al.* 1977).

In the present paper measurements of the elastic constants for caesium thiocyanate using ultrasonic techniques are reported. These are the initial results in a more extensive study to determine the dispersion relations for this crystal using

inelastic neutron scattering. The results so far compare favourably with the initial slopes of the dispersion curves derived from the model calculations of Ti and Ra.

2. Experiment

The room temperature phase of caesium thiocyanate is orthorhombic with space group *Pnma*. Plate-like single crystals were grown from water solution by evaporation. Growth was predominantly in the plane normal to [001]. The crystals were aligned from Laue back-reflection X-ray photographs with a maximum error in orientation of one degree. Faces on opposite sides of the crystals, normal to the required propagation directions, were ground and polished using grinding papers down to 1200 grade and then 6 μm diamond grit. The final samples had thicknesses between 5 and 10 mm.

Ultrasonic velocities were measured using a double-transducer technique as described by Papadakis (1967). One transducer was excited by a 50–100 V peak-to-peak 10 MHz r.f. pulse train, and the resulting echo train was detected by a similar transducer bonded to the opposite face. The received signal was displayed on an oscilloscope which was triggered by an external oscillator with a period comparable with the round-trip travel time of the pulse in the crystal. Additional electronics made it possible to intensity-modulate the display and to trigger the transmitter coherently. The frequency of the external oscillator was then adjusted to overlap the r.f. cycles of two successive echoes displayed on the oscilloscope, and from the measured frequency the round-trip travel time was determined.

There is not one unique overlap condition, but several displaced from each other by whole r.f. cycles. The choice of the correct overlap corresponding to the true round-trip travel time was determined using McSkimin's criterion (Papadakis 1967). We believe that the cyclic mismatch of these results could be up to one r.f. cycle, because of the small acoustic impedance of the crystal and unknown bond thicknesses, which could introduce large phase delays on reflection from the transducer interface.

The transducers used were fine-ground X- and Y-cut quartz, 0.125 in (3.17 mm) in diameter and coaxially gold plated. The nominal resonance frequency of each transducer was 10 MHz. The bonding materials used were a commercially available epoxy-resin glue, '5 minute Araldite', and 'Apiezon' vacuum grease. It was found that in the case of the transverse vibrating Y-cut transducers only the solid bond obtained with Araldite provided enough mechanical coupling to generate a pulse of sufficient amplitude for the velocity to be measured. However, in the case of the longitudinal vibrating X-cut transducers, the Apiezon grease could be used.

The alignment of the transducers for the transverse measurements was done by eye relative to the appropriate crystallographic directions. Consequently, the polarization for the transverse measurements could have been in error by up to 5° from the desired direction. Such an error should only affect the amplitude of the echo signal and should not alter the measured velocity. Furthermore, this type of misalignment should result in the appearance of an echo train corresponding to the transverse mode at right angles to that being measured. This was not observed and so it was assumed that any misalignment was not significant. For all modes measured, echo trains consisting of two or more echoes were observed.

In an orthorhombic system there are nine nonzero elastic constants (Nye 1967). The six diagonal terms c_{ij} can most easily be measured along the principal crystallographic directions while the off-diagonal terms can only be measured along non-

Table 1. Ultrasonic velocities and associated elastic stiffness constants for CsSCN at 293 K

ρ is the density; l , m and n are the direction cosines for the appropriate direction; (av.) denotes that the average velocity was used in determining c_{ij}

V (km s ⁻¹)		Elastic constant (GPa)
V_{xx}	2.52 ± 0.04	$c_{11} = 18.9 \pm 0.7 = \rho V^2$
V_{yy}	2.63 ± 0.06	$c_{22} = 20.6 \pm 1.0$
V_{zz}	3.07 ± 0.08	$c_{33} = 28.1 \pm 1.6$
V_{yz}	0.81 ± 0.01	$c_{44} = 1.96 \pm 0.05$
V_{zy}	0.81 ± 0.01	
V_{xz}	1.56 ± 0.02	$c_{55} = 7.30 \pm 0.21$ (av.)
V_{zx}	1.57 ± 0.02	
V_{xy}	1.00 ± 0.01	$c_{66} = 3.04 \pm 0.07$ (av.)
V_{yx}	1.02 ± 0.01	
$V_{(110)l}$	2.40 ± 0.04	$c_{12} = 7.9 \pm 4.1$ $= [(l^2 c_{11} + m^2 c_{66} - \rho V^2)(l^2 c_{66} + m^2 c_{22} - \rho V^2)/l^2 m^2]^{1/2} - c_{66}$
$V_{(110)t}$	1.39 ± 0.02	$c_{12} = 7.6 \pm 3.5$ $= [(l^2 c_{11} + m^2 c_{66} - \rho V^2)(l^2 c_{66} + m^2 c_{22} - \rho V^2)/l^2 m^2]^{1/2} - c_{66}$
$V_{(011)l}$	2.38 ± 0.06	$c_{23} = 6.4 \pm 4.8$ $= [(m^2 c_{22} + n^2 c_{44} - \rho V^2)(m^2 c_{44} + n^2 c_{33} - \rho V^2)/n^2 m^2]^{1/2} - c_{44}$
$V_{(011)t}$	1.70 ± 0.03	$c_{23} = 6.1 \pm 2.7$ $= [(m^2 c_{22} + n^2 c_{44} - \rho V^2)(m^2 c_{44} + n^2 c_{33} - \rho V^2)/n^2 m^2]^{1/2} - c_{44}$
$V_{(101)l}$	2.96 ± 0.09	$c_{13} = 14.3 \pm 7.3$ $= [(l^2 c_{11} + n^2 c_{55} - \rho V^2)(l^2 c_{55} + n^2 c_{33} - \rho V^2)/l^2 n^2]^{1/2} - c_{55}$
$V_{(101)t}$	1.14 ± 0.02	$c_{13} = 15.2 \pm 3.9$ $= [(l^2 c_{11} + n^2 c_{55} - \rho V^2)(l^2 c_{55} + n^2 c_{33} - \rho V^2)/l^2 n^2]^{1/2} - c_{55}$

principal directions. The velocities of a longitudinal and two transverse modes were measured along each of the orthorhombic axes. These are denoted by V_{ij} where i and j indicate the directions of propagation and displacement vectors respectively (Manolatos *et al.* 1973). The velocities and the six directly derivable stiffness constants (McSkimin 1964) are listed in Table 1.

The off-diagonal constants were derived from quasi-longitudinal and quasi-transverse modes along crystal directions chosen for ease of alignment and for the partial diagonalization of the secular equation (Neighbours and Schacher 1967). These directions were normal to the crystal planes (110), (011) and (101). The velocities are labelled by these planes and a suffix, either l (longitudinal) or t (transverse), to indicate the nature of the transducer employed. The polarization of the transverse measurements was aligned parallel to the [110], [011] and [101] crystal directions respectively. Two of the modes along any off-diagonal direction are not pure, in that the displacements are neither parallel nor perpendicular to the propagation direction. These are denoted as being 'quasi-longitudinal' or 'quasi-transverse' because the deviation from pure mode behaviour was subsequently calculated to be small. The remaining mode is pure transverse with displacements perpendicular to the plane of interest. It was not measured because the velocity is only dependent on previously measured diagonal constants. The off-diagonal velocities and their functional dependence on the elastic constants (McSkimin 1964) are listed in Table 1.

To calculate the elastic constants the density of the material was measured to be 2.98 ± 0.01 g cm⁻³ at 293 K by the displacement method using chloroform. This may be compared with the X-ray value of 3.025 g cm⁻³ calculated from the lattice parameters (Manolatos *et al.* 1973).

3. Results

The ultrasonic velocities and associated elastic constants at 293 K are summarized in Table 1. The errors in the velocities are predominantly due to the one r.f. cycle uncertainty in the correct overlap condition. More velocities than needed for determining the elastic constants were measured to check the consistency of the velocity measurements. The transverse velocities V_{ij} and V_{ji} must be identical by symmetry and experimentally are equal within the quoted errors. The quasi-longitudinal and quasi-transverse velocities for the off-diagonal measurements represent the two roots of the quadratic secular equation. The off-diagonal elastic constants derived from the measurement of both roots agree, which again indicates the consistency of the data.

The quoted errors in the off-diagonal elastic constants are large, firstly because of the dependence of these constants on other moduli, and secondly on account of a significant uncertainty in the alignment of the propagation direction. It should be noted that the quoted error represents the worst possible error, and the concordance of the longitudinal and transverse off-diagonal measurements indicates a greater accuracy than shown by the quoted errors.

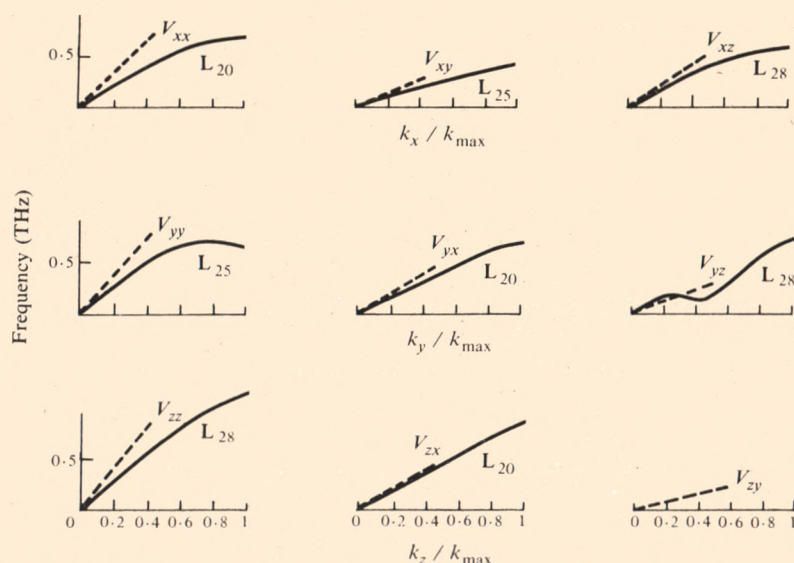


Fig. 1. Dispersion curves for the acoustic modes of CsSCN calculated by Ti and Ra (1980a). The broken line indicates the initial slopes as determined from the measured velocities.

For comparison, the ultrasonic velocities along the orthorhombic axes, together with the dispersion curves by Ti and Ra (1980a) for the acoustic modes, are presented in Fig. 1. The labelling, L_m , of the curves follows the notation adopted by Ti and Ra.

The elastic constants fully describe the elastic behaviour of the crystal. The eigenvalue problem for propagating an elastic wave can be solved using the measured constants for any arbitrary direction. Figs 2a–c show the dependence of the calculated velocities of the three modes of propagation for directions in the xz , xy and yz planes respectively. The measured velocities are also shown. These plots readily illustrate

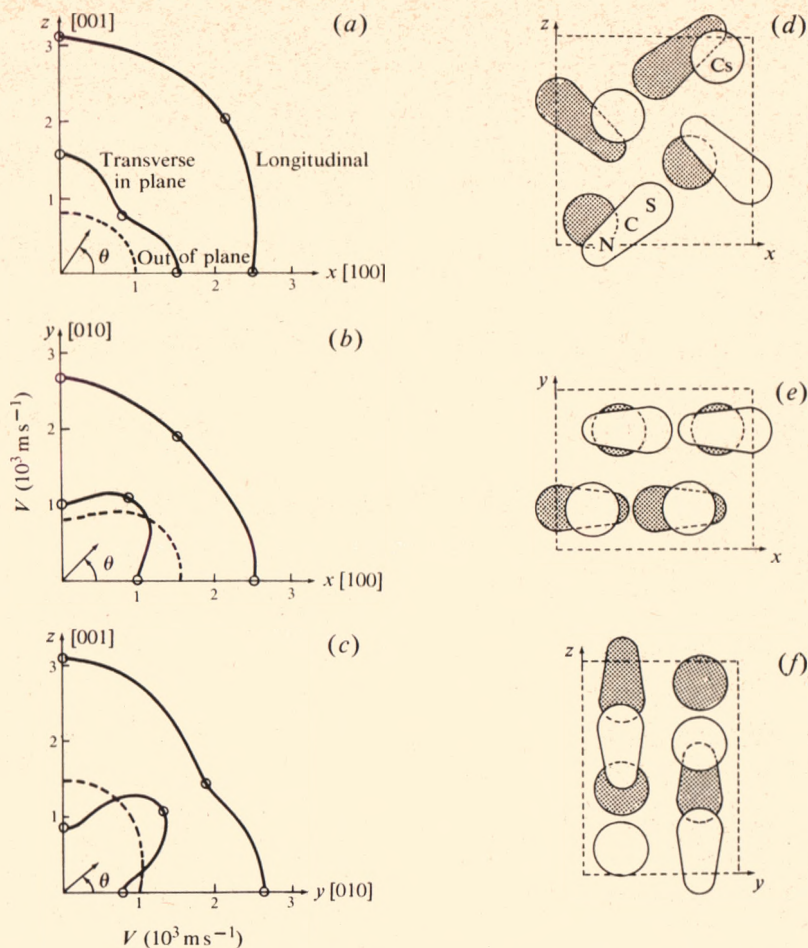


Fig. 2. Calculated velocities of propagation for acoustic modes in the xz , xy and yz planes (a-c); projections of the unit cell on the respective planes with atomic radii not drawn to scale (d-f). The actual measured velocities are shown by the open circles and the sense of θ in each plane is indicated.

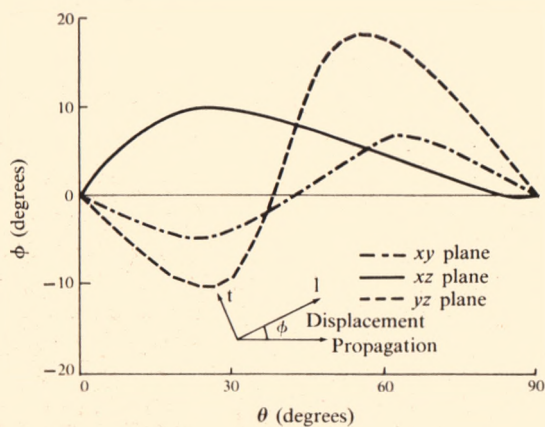


Fig. 3. Deviation from pure mode behaviour ϕ plotted against polar angle θ for the xy , xz and yz planes. The sense of ϕ is shown in the insert.

the anisotropy of the elastic behaviour. The velocity for the longitudinal mode, which is relatively isotropic, has a maximum value along the [001] direction. The minimum longitudinal and the maximum transverse velocity both occur close to the [011] direction.

Only for propagation along the principal crystallographic directions do all three elastic waves have pure modes of vibration. In any arbitrary direction within a principal plane, only the transverse wave, with polarization out of the plane, is a mode of pure vibration. The velocity for this wave is denoted by a broken curve in Figs 2a-c. The other two modes may be excited to be predominantly longitudinal or transverse in character, but the displacement vectors for such quasi-longitudinal and quasi-transverse modes will be directed at angles of ϕ and $90^\circ + \phi$ to the propagation direction respectively.

It is possible, for suitable combinations of direction cosines and elastic constants, that directions can occur for which $\phi = 0$, resulting in 'accidental' pure modes. The dependence of ϕ on the propagation direction, described by θ (see Fig. 2) in the principal planes is shown in Fig. 3, from which it is seen that 'accidental' pure modes occur in all three planes. However, whereas these pure modes occur close to the [011] and [110] directions for the xy and yz planes, the pure mode in the xz plane lies close to the z -axis.

The adiabatic bulk modulus B_s was determined from the expression

$$B_s = 1/(s_{11} + s_{22} + s_{33} + 2s_{13} + 2s_{23} + 2s_{12}),$$

where s_{ij} are the elastic compliances which were determined by inverting the c_{ij} matrix. An estimate of the worst error in B_s was determined by inverting all permutations of the various extreme values of c_{ij} , obtained by adding or subtracting the error from the value. The calculated value is 13.2 ± 3.5 GPa.

Finally, an estimate for the value of the elastic Debye temperature Θ_0^{el} was determined from the elastic constants by integrating over 5868 directions in one-quarter of the unit sphere. The result is 132 K.

4. Discussion

From Fig. 1, it can be seen that there is generally good agreement between the initial slopes of the calculated dispersion curves and the experimental velocities. These measurements represent the first experimental test of the wave-vector dependence of the calculated acoustic phonon dispersion curves for caesium thiocyanate. While the agreement lends support to the rigid-ion model and the stability criteria adopted, the acoustic modes close to the zone centre do not provide a severe test of the model. For such modes the relative changes in the positions of the atoms within the unit cell are small and therefore the effects of electronic polarization, which are not catered for in the model, will not be significant. A more rigorous test of the model requires a wider exploration of both the acoustic and optic mode branches away from the zone centre.

Major discrepancies do occur for those modes corresponding to the velocities V_{xx} and V_{yy} . In the latter case the calculated mode has negative energies. In view of the relatively low energies for this mode, the failure of the model may be due to numerical rounding errors in the eigenvalue problem for that particular symmetry group and propagation direction or, alternatively, the residual forces acting on the atoms may not be small enough to produce a valid prediction for this mode.

We note also that the mode denoted by L_{28} corresponding to V_{yz} has a pronounced dip at $k = 0.5 k_{\max}$. Since the elastic constant appropriate to this mode is identical to the mode for which the model gave negative energies, it is probable that the dip merely reflects the numerical limitations of the model. However, it is interesting to speculate that such a softening of the L_{28} mode may be responsible for the phase transition which occurs at 197°C. This transition in the related potassium compound is associated with the librational fluctuation of the NCS^- anion (Owens 1979). The calculated librational component for the L_{28} mode at $k = 0.5 k_{\max}$ is only 3% for caesium thiocyanate at room temperature. However, it is possible that this may increase as the temperature increases.

The values for the bulk modulus and Debye temperature fall within the range of values for the same parameters for other caesium ionic crystals, i.e. the caesium halides have bulk moduli which range from 14 to 26 GPa and elastic Debye temperatures from 130 to 175 K. Specific heat data for CsSCN have not been reported, however, measurements have been made by Vanderzee and Westrum (1970) for KSCN and NH_4SCN . Their values for Θ_0° are 210 and 238 K respectively where these correspond to Avogadro's number of molecular units per mole. As the value of Θ_0^{el} corresponds to Avogadro's number of atoms it is necessary to divide the values of Θ_0° by the cube root of 4 and 8 respectively for comparison with Θ_0^{el} . This gives values of 132 K (KSCN) and 119 K (NH_4SCN) which are close to the elastic value for CsSCN .

While there is marked anisotropy in the stiffness of the crystal for the propagation of transverse vibrations, the similarity of the elastic behaviour for the xy and yz planes is striking. Ultimately, the anisotropy of the elastic properties of the crystal must be related to the symmetry of the bonding within the crystal. Projections of the unit cell onto the three principal planes are shown in Figs 2d-f. From these, the planar-like stacking of the atoms along the $[010]$ direction and the similarity of the xy and yz planes are clearly seen. A detailed theoretical description of the connection between the crystal structure and the elastic properties is currently being investigated.

Acknowledgments

We are indebted to F. Ninio and S. S. Ti for a number of discussions on the above work and J. G. Collins for the use of his program to calculate Θ_0^{el} .

The support provided by an AINSE scholarship (M.A.I.) and the Vera Moore Junior Research Fellowship (S.P.) is gratefully acknowledged. The ultrasonics facility was financed in part by the ARGS and this work was supported by the Monash University Special Research Grant.

References

- Akers, C., Peterson, S. W., and Willett, R. D. (1968). *Acta Crystallogr. B* **24**, 1125.
- Braghetti, M., Berchiesi, G., and Franzosini, P. (1969). *Ric. Sci.* **39**, 576.
- Dao, N. G., and Wilkinson, G. R. (1973). *J. Chem. Phys.* **59**, 1319.
- Iqbal, Z., Sharma, L. H., and Moller, K. D. (1972). *J. Chem. Phys.* **57**, 4728.
- Jones, L. H. (1958). *J. Chem. Phys.* **28**, 1234.
- Kinsho, Y., Onodera, N., Sakiyama, M., and Seki, S. (1979). *Bull. Chem. Soc. Jpn* **52**, 395.
- Klement, W., Jr (1976). *Bull. Chem. Soc. Jpn* **49**, 2148.
- Klug, H. P. (1933). *Z. Kristallogr.* **85**, 214.
- McSkimin, H. J. (1964). 'Physical Acoustics; Principles and Methods' (Ed. W. P. Mason), Vol. 1A, pp. 271-334 (Academic: New York).

- Manolatos, S., Tillinger, M., and Post, B. (1973). *J. Solid State Chem.* **7**, 31.
- Neighbours, J. R., and Schacher, G. E. (1967). *J. Appl. Phys.* **38**, 5366.
- Nye, J. F. (1967). 'Physical Properties of Crystals', pp. 137-43 (Clarendon: Oxford).
- Owens, F. J. (1979). *Solid State Commun.* **29**, 789.
- Papadakis, E. (1967). *J. Acoust. Soc. Am.* **42**, 1045.
- Sakiyama, M., Suga, H., and Seki, S. (1963). *Bull. Chem. Soc. Jpn* **36**, 1025.
- Ti, S. S., Kettle, S. F. A., and Ra, O. (1976). *Spectrochim. Acta A* **33**, 1603.
- Ti, S. S., Kettle, S. F. A., and Ra, O. (1977). *Spectrochim. Acta A* **33**, no. 2, 111.
- Ti, S. S., and Ra, O. (1980a). *J. Chem. Phys.* **73**, 5738.
- Ti, S. S., and Ra, O. (1980b). *J. Chem. Phys.* **73**, 5749.
- Ti, S. S., Ra, O., and Kettle, S. F. A. (1978). *J. Chem. Phys.* **68**, 2638.
- Vanderzee, C. E., and Westrum, E. F. (1970). *J. Chem. Thermodyn.* **2**, 417.
- Yamada, Y., and Watanabe, T. (1963). *Bull. Chem. Soc. Jpn* **36**, 1032.

Manuscript received 22 July, accepted 17 September 1982

The Room Temperature Elastic Behaviour of CsH_2PO_4

S. Prawer, T. F. Smith and T. R. Finlayson

Department of Physics, Monash University, Clayton, Vic. 3168.

Abstract

The components of the elastic constant matrix of monoclinic caesium dihydrogen phosphate (CDP) have been determined using ultrasonic velocity measurements to be $C_{11} = 28.83 \pm 0.43$, $C_{22} = 26.67 \pm 0.37$, $C_{33} = 65.45 \pm 0.48$, $C_{44} = 8.10 \pm 0.15$, $C_{55} = 5.20 \pm 0.24$, $C_{66} = 9.17 \pm 0.22$, $C_{12} = 11.4 \pm 3.6$, $C_{13} = 42.87 \pm 1.58$, $C_{15} = 5.13 \pm 0.67$, $C_{23} = 14.5 \pm 4.4$, $C_{25} = 8.4 \pm 4.3$, $C_{35} = 7.50 \pm 0.81$ and $C_{46} = -2.25 \pm 0.31$ GPa. Calculations of the velocity surfaces, ray directions, Young's modulus surfaces and linear compressibility show marked elastic anisotropy, which has been correlated with the chain and layer-like structure of CDP.

1. Introduction

The crystal structure of ferroelectric CsH_2PO_4 ($T_c = 154$ K) was unambiguously determined to be monoclinic $P2_1/m$ by Uesu and Kobayashi (1976) rather than the orthorhombic structure earlier reported by Fellner-Feldegg (1952). On the basis of the oxygen-oxygen bond distances they suggested that the structure consists of PO_4 groups, hydrogen bonded approximately along the a and c axes as shown in Fig. 1. The hydrogen bonds along the a axis link the PO_4 groups into chains running along the b axis. These chains are cross linked by the hydrogen bond along the c axis. Thus (100) layers are formed which are bonded to each other by ionic forces involving the Cs^+ ion (see also Fig. 6a). The relative weakness of the interlayer forces is evident from the perfect cleavage that occurs along the (100) plane.

The structure was further refined by Matsunaga *et al.* (1980) who also determined the position of the hydrogen atoms. They found that the sites for the two hydrogen ions were inequivalent. The hydrogen ions associated with hydrogen bonding along the c axis were ordered at room temperature, whereas the ions along the a axis were disordered at room temperature. At T_c the ordering of this hydrogen linked the chains of PO_4 tetrahedra together along the ferroelectric b axis. Since one hydrogen is already ordered in the paraelectric state, the ferroelectric transition has been described as pseudo-one-dimensional, unlike the three-dimensional behaviour observed in the case of KH_2PO_4 (KDP) (Frazer *et al.* 1979). This one-dimensionality has been the focus to date of many of the studies on CsH_2PO_4 (CDP) (see e.g. Youngblood *et al.* 1980; Iwata *et al.* 1980; Yakushkin *et al.* 1981; Kanda *et al.* 1982, 1983).

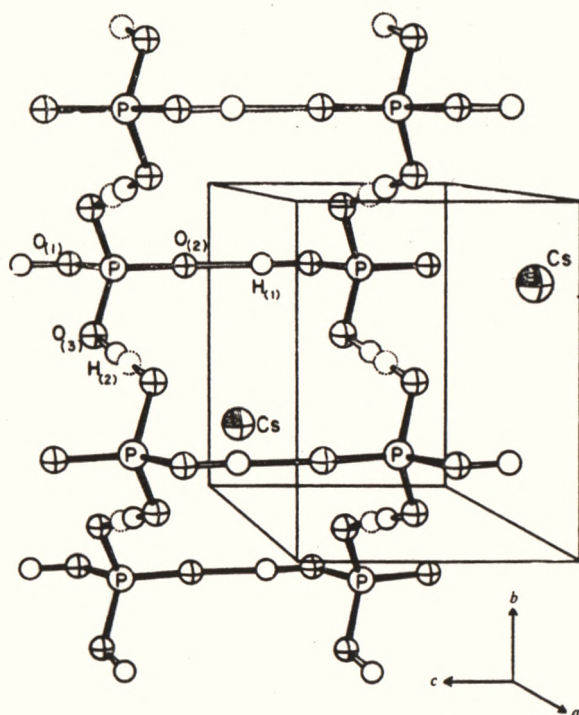


Fig. 1. Crystal structure of CsH_2PO_4 . Disorder in the hydrogen bonds along the a axis involved in chain formation is indicated by the neighbouring solid and dotted circles used to represent the proton positions. Note that adjacent PO_4 groups in the b -axis chain are not in the same cell. [From Frazer *et al.* (1979).]

The present paper does not specifically address the problem of the elastic behaviour in the vicinity of the transition but is restricted to a report of the room temperature elastic behaviour and its relationship to the crystal structure. As such, this work represents a first step in the overall understanding of the lattice dynamics of CDP.

The nature of the chain and layer like bonding can be expected to be reflected in the elastic properties of the crystal, as the elastic constants are given by the second derivative with respect to strain of the free energy. Here we report a complete determination of the elastic constant matrix of CDP, via measurements of the ultrasonic phase velocities along different crystallographic directions. There are 13 independent nonzero elastic constants C_{11} , C_{22} , C_{33} , C_{44} , C_{55} , C_{66} , C_{12} , C_{13} , C_{15} , C_{23} , C_{25} , C_{35} and C_{46} (Nye 1967) for monoclinic symmetry. Direct and simple relationships between measured velocities and elastic constants are only possible for C_{22} , C_{66} and C_{44} . All the other constants occur coupled together in more complicated relationships. Also, only measurements along the b axis yield pure elastic waves (i.e. purely transverse or purely longitudinal particle motion). Hence, the determination of all 13 elastic constants of a monoclinic system is demanding both experimentally and computationally.

The elastic constants are usually referred to an orthonormal set of axes x, y, z which have a standard orientation with respect to the crystallographic axes a, b, c (see 'Standards on Piezoelectric Crystals' 1949). The conventional arrangement is shown in Fig. 2. In order to avoid confusion, the normal notation $[\alpha, \beta, \gamma]$ will refer to directions with respect to the monoclinic axes a, b, c , and the primed notation $[l, m, n']$ will refer to directions with respect to the orthonormal set.

Once the C_{ij} matrix is known it is possible to calculate the Debye temperature, bulk modulus, linear compressibility and Young's modulus, as well as constant phase and group velocity surfaces. The dependence of the last four quantities on crystal orientation must be related to the crystal structure, although this relationship is very complex.

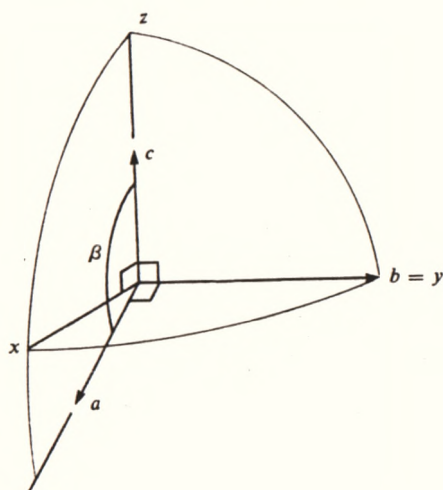


Fig. 2. Axes of monoclinic CsH_2PO_4 ($\beta = 107.742^\circ$): a and c are perpendicular to b , but not to each other, while xyz form the cartesian axes to which the elastic constants are referred.

Finally, as previously mentioned, the ferroelectric ordering in CDP is essentially of a one-dimensional nature. The elastic constants, particularly the off-diagonal elements, provide information about the cross compliance between the principal ferroelectric axis and directions at right angles to it. A knowledge of the cross compliance is essential for the description of anomalies which appear in these off-principal-axis directions.

2. Theory: Elastic Waves in Crystals

The equation of motion for particles in a crystal with displacements u_i from their mean positions is given in the index-summation convention used throughout this paper by (Brown 1967)

$$\rho \frac{\partial^2 u_i}{\partial t^2} = C_{ijkl} \frac{\partial^2 u_k}{\partial x_j \partial x_l}, \quad (1)$$

where ρ is the density and C_{ijkl} is the elastic constant tensor.

Representing a travelling wave in a crystal by the form

$$u_i = A_i \sin(\omega t - k_j x_j), \quad (2)$$

where ω is the frequency, k is the wave vector and A is the polarization vector, and substituting this into equation (1) yields

$$\rho \omega^2 A_i = C_{ijkl} k_j k_l A_k. \quad (3)$$

As dispersion effects are negligible in the long wavelength region of the ultrasonic measurements, the ultrasonic velocity V is $\omega|k|^{-1}$, where $|k| = (k_1^2 + k_2^2 + k_3^2)^{1/2}$. Equation (3) may then be written as

$$\lambda A = \rho V^2 A, \quad (4)$$

where λ is a real symmetric matrix whose components are quadratic functions of the direction cosines l, m, n of the propagation vector k . Specifically, if

$$Q = \begin{bmatrix} C_{11} & C_{66} & C_{55} & C_{56} & C_{15} & C_{16} \\ C_{66} & C_{22} & C_{44} & C_{24} & C_{46} & C_{26} \\ C_{55} & C_{44} & C_{33} & C_{34} & C_{35} & C_{45} \\ C_{56} & C_{24} & C_{34} & \frac{1}{2}(C_{23} + C_{44}) & \frac{1}{2}(C_{36} + C_{45}) & \frac{1}{2}(C_{46} + C_{25}) \\ C_{15} & C_{46} & C_{35} & \frac{1}{2}(C_{36} + C_{45}) & \frac{1}{2}(C_{13} + C_{55}) & \frac{1}{2}(C_{14} + C_{56}) \\ C_{16} & C_{26} & C_{45} & \frac{1}{2}(C_{46} + C_{25}) & \frac{1}{2}(C_{14} + C_{56}) & \frac{1}{2}(C_{12} + C_{66}) \end{bmatrix}, \quad L = \begin{bmatrix} l^2 \\ m^2 \\ n^2 \\ 2mn \\ 2ln \\ 2lm \end{bmatrix},$$

then

$$\begin{aligned} \lambda_{11} &= Q_{1j} L_j, & \lambda_{22} &= Q_{2j} L_j, & \lambda_{33} &= Q_{3j} L_j, \\ \lambda_{23} &= Q_{4j} L_j, & \lambda_{13} &= Q_{5j} L_j, & \lambda_{12} &= Q_{6j} L_j, \end{aligned}$$

where the Voigt notation has been used (Nye 1967) and $j = 1-6$.

Equation (4) indicates that ρV^2 are the eigenvalues of the matrix λ , whilst A (the polarizations) are the corresponding eigenvectors. For (4) to have non-trivial solutions it is required that

$$|\lambda_{ik} - \rho V^2 \delta_{ik}| = 0. \quad (5)$$

Hence, measurements of the three velocities (two transverse and one longitudinal) for a given propagation direction l, m, n were used to establish relationships between the elastic constants. To obtain sufficient relationships to determine all 13 elastic constants for a monoclinic material, measurements of all three velocities were required in at least six different directions (i.e. $[100]', [010]', [001]', [10n]', [110]'$ and $[011]'$). Some of the relationships were redundant and were used as internal consistency checks on the data. The procedure adopted is outlined in Section 4.

The direction of energy flow R in a crystal is, in general, not parallel to the propagation vector. Often called the ray vector, R is given by the tensor product of stress and particle velocity (Musgrave 1970) and, by assuming Hooke's law that strain is linearly proportional to stress (Nye 1967), it has been shown that its components are given by

$$R_j = C_{ijkl} \dot{u}_i \partial u_k / \partial x_l. \quad (6)$$

By assuming a wave solution of the form (2) exists, equation (6) can be written as

$$\bar{R}_j = \frac{1}{2} C_{ijkl} A_i A_k k_l \omega, \quad (7)$$

where \bar{R}_j is the time average over one period ($2\pi/\omega$) of the energy vector. As only the direction of R_j is of interest, (7) may be rewritten as

$$r_j = 2\bar{R}_j |k|^{-1} \omega^{-1} = C_{ijkl} A_i A_k p_l, \quad (8)$$

where $p_l = k_l |k|^{-1}$ are the direction cosines of the propagation vector. Then, expanding (8) and using the Voigt notation we get

$$r_1 = lQ_{1j}S_j + mQ_{6j}S_j + nQ_{5j}S_j,$$

$$r_2 = lQ_{6j}S_j + mQ_{2j}S_j + nQ_{4j}S_j,$$

$$r_3 = lQ_{5j}S_j + mQ_{4j}S_j + nQ_{3j}S_j,$$

where $j = 1-6$, and S is the column matrix

$$S = \begin{bmatrix} A_1^2 \\ A_2^2 \\ A_3^2 \\ 2A_2A_3 \\ 2A_3A_1 \\ 2A_1A_2 \end{bmatrix}. \quad (9)$$

Hence for a given propagation direction $[lmn]'$ the λ matrix was calculated and equation (4) was solved to obtain the eigenvalues (i.e. the values of ρV^2) and the eigenvectors (i.e. the polarization vector A).

Since λ is real and symmetric it has three real positive eigenvalues and three independent eigenvectors which are mutually perpendicular. In general the eigenvectors do not constitute purely transverse or purely longitudinal particle motion. In the special case that the longitudinal mode is pure, the two transverse modes are also pure. However, if only one transverse mode is pure, the remaining transverse and the longitudinal eigenvectors are not pure but are constrained to lie in a plane perpendicular to the pure transverse mode and are therefore referred to as semi-pure modes of vibration.

Once the polarization vector A was determined the matrix S could be calculated and using equation (9) the components of the ray direction r calculated.

3. Experimental

Sample Preparation

The CDP crystals used in this investigation were produced by the solvent evaporation method. The saturated solution was produced by reacting stoichiometric quantities of CsOH and H_3PO_4 which gave a saturated solution with a pH of approximately 4. The resulting crystals sometimes showed evidence of mixed growth habits which were revealed by examining the samples between crossed polarizers. In these cases, the offending section of crystal was removed before measurements were performed. It was found that lowering the pH to 2-2.5 by addition of excess H_3PO_4

eliminated this problem and gave crystals of excellent quality. Frazer *et al.* (1979) have also reported that in order to obtain good crystal growth, it was necessary to add a slight excess of H_3PO_4 to produce a starting solution with a pH of about 2.5. The crystals used for the elastic measurements varied in size and quality, but in all cases were at least 3 mm thick and the faces to which the transducers were bonded had diameters of at least 3.2 mm.

The crystals were aligned using Laue back reflection photographs with the aid of a computer program that produced simulations of Laue patterns for any given orientation (Cornelius 1981). These simulations enabled the Laue spots to be indexed, and using the actual indexed spot positions from the photograph, an estimate of the error in alignment could be calculated. This was found to be a maximum of one degree, but along the main symmetry directions the error was closer to $\pm 0.5^\circ$.

The ultrasonic measurements require two opposite faces to be polished flat and parallel to each other and perpendicular to a given crystallographic direction. CDP is brittle, heat sensitive and extremely water soluble making polishing a difficult task. However, samples were polished with faces parallel to within a tolerance of $10'$ of arc, with each surface flat to within 10 interference fringes per cm, and surface scratches less than $5\text{ }\mu\text{m}$ deep.

Velocity Measurements

The ultrasonic velocity was measured by the pulse echo overlap technique described by Papadakis (1967). A 3.18 mm (0.125 in.) diameter quartz transducer was bonded to one face of the specimen, and was excited by a 50–100 V peak-to-peak 10 MHz r.f. pulse. The returning echoes were picked up by this same transducer and displayed on a CRO. The pulse echo overlap technique involves triggering the CRO with a signal, the period of which is equal to the round trip travel time between the echoes of interest and hence overlapping the two echoes r.f. cycle for r.f. cycle on the oscilloscope screen. This enables the round trip travel time T to be determined accurately from the triggering frequency and hence, from the path-length of the specimen between the parallel faces, the velocity V of the particular mode may be calculated.

The major source of error in this technique is the choice of the correct r.f. cycle for overlap. We have used, with some success, the criterion suggested by McSkimin (1961) for the determination of the correct overlap condition. However, whereas he applied the technique to homogeneous samples such as fused silica, which gave excellent quality echo trains, not only did the present samples contain defects which resulted in poor echo train quality, but the inherent monoclinic symmetry of the system also gave rise to mixed modes which produced an echo train composed of a superposition of separate modes, each with a different velocity. In these cases determination of the correct echo for overlap was difficult and in some cases there was an ambiguity of ± 1 r.f. cycle in the overlap which gave rise to errors of the order of $\pm 1\%$ in the determined velocity.

The echo train quality, and hence the ability to determine the correct echo for overlap, is also very dependent on the quality of the bond between transducer and sample. In general, the thinner the bond the better the echo train quality. We found that Dow Corning 276-V9 resin (a thick and very viscous alpha methyl styrene fluid) was a satisfactory bonding agent for both longitudinal and transverse waves. Less

viscous bonding agents, such as silicone greases, whilst satisfactory for longitudinal waves, lacked sufficient acoustic coupling for the transverse waves. The Dow Corning 276-V9 resin has the important advantage over solid bonds (such as salol) that the crystal may be rotated *in situ* with respect to the transverse transducer to excite each one of the two transverse modes separately. This is essential in the case of a monoclinic system, because for some propagation directions the polarization of the transverse mode with respect to the crystal axes is a function of the elastic constants which are yet to be determined.

Table 1. Ultrasonic sound velocities in CsH_2PO_4

PT, pure transverse; PL, pure longitudinal; SPT, semi-pure transverse; SPL, semi-pure longitudinal; QT, quasi-transverse; QL, quasi-longitudinal

No.	Direction of wave propagation ^A	Approximate wave displacement direction	Velocity (10^3 m s^{-1})	Type
V_1	100	100	3.047 ± 0.005	SPL
V_2	100	010	1.688 ± 0.02	PT
V_3	100	001	1.133 ± 0.01	SPT
V_4	010	010	2.878 ± 0.02	PL
V_5	010	100	1.788 ± 0.02	PT
V_6	010	001	1.416 ± 0.002	PT
V_7	001	001	4.540 ± 0.01	SPL
V_8	001	010	1.586 ± 0.015	PT
V_9	001	100	1.153 ± 0.003	SPT
V_{10}	0.520, 0, -0.854	0.520, 0, -0.854	3.847 ± 0.006	SPL
V_{11}	0.520, 0, -0.854	010	1.796 ± 0.004	PT
V_{12}	0.520, 0, -0.854	0.854, 0, 0.520	0.7605 ± 0.006	SPT
V_{13}	110	110	2.982 ± 0.006	QL
V_{14}	110	001	1.683 ± 0.003	QT
V_{15}	110	110	1.307 ± 0.013	QT
V_{16}	011	011	3.622 ± 0.08	QL
V_{17}	011	011	1.980 ± 0.008	QT
V_{18}	011	100	1.409 ± 0.007	QT
V_{19}	0.252, 0.588, -0.769	0.252, 0.588, -0.769	3.686 ± 0.08	QL
V_{20}	0.252, 0.588, -0.769	Trans 1	2.014 ± 0.01	QT
V_{21}	0.252, 0.588, -0.769	Trans 2	1.219 ± 0.009	QT
V_{22}	0.698, 0, -0.716	0.698, 0, -0.716	3.217 ± 0.13	SPL
V_{23}	0.698, 0, -0.716	010	1.796 ± 0.004	PT
V_{24}	0.698, 0, -0.716	0.716, 0, 0.698	Unknown	SPT
V_{25}	0.925, 0, 0.395	0.925, 0, 0.395	3.151 ± 0.004	SPL
V_{26}	0.925, 0, 0.395	010	1.520 ± 0.004	PT
V_{27}	0.925, 0, 0.395	0.395, 0, -0.925	0.83 ± 0.03	SPT

^A Direction is with respect to xyz axes.

4. Results

The measured velocities are shown in Table 1. The wave displacement directions are approximate only, because in most instances the waves are not pure and their true displacement vectors can only be determined by calculation from the determined elastic constants. Nevertheless, experience has shown that most waves are either predominantly longitudinal or transverse in character and hence one may assume that the polarization of the exciting transducer (which is the basis for the approximate

wave displacement directions given in Table 1) is a reasonable first approximation to the actual eigenvector.

The measurement of the velocity was repeated at least twice for each mode using different specimens. An exception to this was for propagation along $[011]'$ for which the measurement was repeated by repolishing the sample to reduce its pathlength and examining a different section of the crystal. In general the consistency in the velocity between the different measurements was within ± 1 r.f. cycle ($\sim 1-2\%$). However, in some cases, particularly for semi-pure modes, the velocity data between measurements were consistent to between $0.2-0.6\%$.

The density used in the calculation was obtained by hydrostatic weighing in chloroform at 20°C and found to be $\rho = 3.22 \pm 0.04 \text{ g cm}^{-3}$, which corresponds well to the value given by Rashkovich *et al.* (1977) of $3.24 \pm 0.01 \text{ g cm}^{-3}$. The X-ray density, computed from the unit cell data given by Uesu and Kobayashi (1976), is 3.27 g cm^{-3} which also agrees well with our results.

It is possible to find C_{22} , C_{66} and C_{44} directly using pure modes. The necessary relationships are

$$C_{22} = \rho V_4^2 = 26.67 \pm 0.37 \text{ GPa}, \quad (10)$$

$$C_{66} = \rho V_2^2 = 9.17 \pm 0.22 \text{ GPa}, \quad (11)$$

$$C_{44} = \rho V_8^2 = 8.10 \pm 0.15 \text{ GPa}. \quad (12)$$

The velocities corresponding to the remaining pure modes with propagation vector along the b axis are related to the above constants by the relationship

$$\rho V_5^2 + \rho V_6^2 = C_{44} + C_{66}. \quad (13)$$

On substituting the numerical values the left- and right-hand sides of (13) agree to 3% , which is well within experimental error.

The value of C_{46} may be determined from the velocity of the last remaining pure mode propagating along the $[10n]'$ direction in the xz plane. Here, the relationship is

$$C_{46} = (\rho V_{11}^2 - l^2 C_{66} - n^2 C_{44})/2nl = -2.25 \pm 0.31 \text{ GPa}. \quad (14)$$

A consistency check may be obtained by using the relationship

$$C_{46}^2 = C_{44} C_{66} - \rho V_5^2 \rho V_6^2. \quad (15)$$

Here, the numerical agreement of the left- and right-hand sides is within 24% , which is still within experimental error. The error is large because the small value of C_{46} corresponds to subtracting nearly equal terms on the right-hand side of (15).

The relationships necessary for the determination of the remaining diagonal elastic constants and C_{15} and C_{35} are

$$C_{11} + C_{55} = \rho(V_1^2 + V_2^2) = 34.03 \pm 0.19 \text{ GPa}, \quad (16)$$

$$C_{11} C_{55} - C_{15}^2 = \rho V_1^2 \rho V_2^2 = 123.6 \pm 2.7 (\text{GPa})^2, \quad (17)$$

$$C_{33} + C_{55} = \rho(V_7^2 + V_9^2) = 70.65 \pm 0.29 \text{ GPa}, \quad (18)$$

$$C_{33}C_{55} - C_{35}^2 = \rho V_7^2 V_9^2 = 284.1 \pm 2.8 \text{ (GPa)}^2, \quad (19)$$

$$l^2 C_{11} + C_{55} + n^2 C_{33} + 2 \ln(C_{15} + C_{35}) = \rho V_{10}^2 + \rho V_{12}^2 \\ = 49.51 \pm 0.18 \text{ GPa}, \quad (20)$$

where $l^2 + n^2 = 1$.

Whilst it is possible (but tedious) to solve (16)–(20) analytically it is more convenient to solve these equations numerically using a generalized Newton–Raphson algorithm (Carnahan *et al.* 1969). The system converges to two separate solutions, depending on the starting values of the variables. One solution may be rejected as unphysical as, on substituting this set of elastic constants back into equation (4), it is found that the eigenvector corresponding to the fastest mode (i.e. the quasi-longitudinal wave) is polarized close to 90° to the propagation direction.

The errors in C_{11} , C_{55} , C_{33} , C_{15} and C_{35} were calculated by varying the right-hand sides of (16)–(20) by plus or minus the quoted error for all possible permutations and noting the maximum and minimum values of the constants which emerge when the equations are solved. This is considered to be a more realistic estimate of the error than would be obtained by solving (16)–(20) analytically and summing all possible maximum errors. In the latter case the errors calculated are unreasonably large, as no account is taken of the self-consistency requirements which do not allow worst case errors to occur independently of one another.

The value of C_{13} may then be obtained from the calculated constants above by the equation

$$\{l^2 C_{15} + n^2 C_{35} + \ln(C_{13} + C_{55})\}^2 \\ - (l^2 C_{11} + n^2 C_{55} + 2 \ln C_{15})(l^2 C_{55} + n^2 C_{33} + 2 \ln C_{35}) \\ - \rho V_{10}^2 \rho V_{12}^2 = 88.75 \pm 0.84 \text{ (GPa)}^2. \quad (21)$$

There will be two solutions for C_{13} depending on whether the positive or negative square root is taken in (21). Once again one solution has been rejected as unphysical on the criterion that the quasi-longitudinal wave travels faster than the quasi-transverse wave and is polarized closer to the propagation direction.

To obtain C_{12} , C_{25} and C_{23} , the velocities in the $[110]'$ and $[011]'$ directions were measured. The solution to the eigenvalue equation requires for the $[110]'$ direction

$$\begin{vmatrix} C_{11} + C_{66} - 2\rho V^2 & C_{12} + C_{66} & C_{15} + C_{46} \\ C_{12} + C_{66} & C_{22} + C_{66} - 2\rho V^2 & C_{25} + C_{46} \\ C_{15} + C_{46} & C_{25} + C_{46} & C_{55} + C_{44} - 2\rho V^2 \end{vmatrix} = 0, \quad (22)$$

and for the $[011]'$ direction

$$\begin{vmatrix} C_{66} + C_{55} - 2\rho V^2 & C_{46} + C_{25} & C_{46} + C_{35} \\ C_{46} + C_{25} & C_{22} + C_{44} - 2\rho V^2 & C_{44} + C_{23} \\ C_{46} + C_{35} & C_{44} + C_{23} & C_{44} + C_{33} - 2\rho V^2 \end{vmatrix} = 0. \quad (23)$$

The properties of the roots of the cubic equations (22) and (23) give us relations that may be used as consistency checks on the measured velocities. These relations are for the $[110]'$ direction

$$2\rho(V_{13}^2 + V_{14}^2 + V_{15}^2) = C_{11} + C_{22} + 2C_{66} + C_{55} + C_{44}, \quad (24)$$

and for the $[011]'$ direction

$$2\rho(V_{16}^2 + V_{17}^2 + V_{18}^2) = C_{66} + C_{55} + 2C_{44} + C_{22} + C_{33}. \quad (25)$$

On substituting the values of the constants so far determined the left- and right-hand sides of (24) and (25) agree to within 0.7% and 0.2% respectively, which is well within experimental error. The properties of the cube roots of (22) and (23) also yield, for the $[110]'$ direction,

$$\begin{aligned} & (C_{12} + C_{66})^2 + (C_{25} + C_{46})^2 \\ &= (C_{11} + C_{66})(C_{22} + C_{66}) + (C_{11} + C_{66})(C_{55} + C_{44}) + (C_{22} + C_{66})(C_{55} + C_{44}) \\ & \quad - (C_{15} + C_{46})^2 - (2\rho)^2(V_{13}^2 V_{14}^2 + V_{14}^2 V_{15}^2 + V_{13}^2 V_{15}^2), \end{aligned} \quad (26)$$

$$\begin{aligned} & (C_{55} + C_{44})(C_{12} + C_{66})^2 + (C_{11} + C_{66})(C_{25} + C_{46})^2 \\ & \quad - 2(C_{12} + C_{66})(C_{15} + C_{46})(C_{25} + C_{46}) \\ &= (C_{11} + C_{66})(C_{22} + C_{66})(C_{55} + C_{44}) - (2\rho V_{13}^2)(2\rho V_{14}^2)(2\rho V_{15}^2) \\ & \quad - (C_{22} + C_{66})(C_{15} + C_{46})^2. \end{aligned} \quad (27)$$

For the $[011]'$ direction the corresponding relationships are

$$\begin{aligned} & (C_{23} + C_{44})^2 + (C_{25} + C_{46})^2 \\ &= (C_{66} + C_{55})(C_{22} + C_{44}) + (C_{66} + C_{55})(C_{44} + C_{33}) + (C_{22} + C_{44})(C_{44} + C_{33}) \\ & \quad - (C_{46} + C_{35})^2 - (2\rho)^2(V_{16}^2 V_{17}^2 + V_{17}^2 V_{18}^2 + V_{16}^2 V_{18}^2), \end{aligned} \quad (28)$$

$$\begin{aligned} & (C_{66} + C_{55})(C_{23} + C_{44})^2 + (C_{44} + C_{33})(C_{46} + C_{25})^2 \\ & \quad - 2(C_{46} + C_{25})(C_{46} + C_{35})(C_{44} + C_{23}) \\ &= (C_{66} + C_{55})(C_{22} + C_{44})(C_{44} + C_{33}) - (2\rho V_{16}^2)(2\rho V_{17}^2)(2\rho V_{18}^2) \\ & \quad - (C_{22} + C_{44})(C_{35} + C_{46})^2. \end{aligned} \quad (29)$$

Equations (26), (27) and (28) were solved for the unknowns $C_{12} + C_{66}$, $C_{25} + C_{46}$ and $C_{23} + C_{44}$ simultaneously by a generalized Newton-Raphson algorithm. The solutions were checked by substitution into equation (29) which yielded consistency between right- and left-hand sides of better than 0.7%. The solution to (26)–(28) involves the intersection between two circles (26) and (28), and an ellipse or hyperbola (27). As such there are two sets of distinct solutions:

$$\begin{aligned} (C_{12}, C_{25}, C_{23}) &= \pm(11.4 \pm 3.6, 8.4 \pm 4.3, 14.5 \pm 4.4) \text{ GPa} \\ &= \pm(12.2 \pm 2.9, 0.95 \pm 4.2, 15.3 \pm 4.0) \text{ GPa}. \end{aligned}$$

An attempt to calculate the errors in C_{12} , C_{25} and C_{23} by solving the equations for all the possible permutations of plus or minus the quoted errors in C_{11} , C_{22} , C_{33} , C_{44} ,

C_{55} , C_{66} , C_{13} , C_{15} , C_{35} , C_{46} and the measured velocities V_{13}, \dots, V_{18} was unsuccessful. For most permutations of the errors the system of equations (26)–(28) no longer converged, as the internal consistency requirements of (24) and (25) were no longer satisfied. The uncertainties in C_{12} , C_{25} and C_{23} quoted above were calculated by restricting the errors in the velocities so that the left- and right-hand sides of (24) and (25) agreed to within 1% for all permutations of the errors in the velocities. In this case the system of equations (26)–(28) converged for most error permutations, except those extreme cases for which all the errors were either added or subtracted.

Two of the above solutions (the negative of each pair) may be rejected as unphysical by a consideration of the eigenvectors as described above. This still leaves two distinct solutions, and although the eigenvectors corresponding to each solution are different, both are physically quite reasonable. Clearly, the choice of solution has little effect on the value of C_{12} and C_{23} , but the value of C_{25} is radically changed. In order to differentiate between these solutions the velocity in a further general direction $[0.252, 0.588, -0.769]'$ was measured. The criterion

$$R_{19-21} = \sum_{i=19}^{21} (V_{\text{calc}_i} - V_i)^2 / V_i^2,$$

where V_{calc_i} are the velocities calculated for the $[0.252, 0.588, -0.769]'$ direction from the elastic constants, was used as a measure of the goodness of fit of the data. The first solution gives an R value three times smaller than for the second solution and has therefore been adopted.

The criterion

$$R_{1-18} = \sum_{i=1}^{18} (V_{\text{calc}_i} - V_i)^2 / V_i^2$$

has been calculated and a value of 1.8×10^{-3} obtained. This compares very favourably with the value of R obtained by Krupnyi *et al.* (1972) in their calculations for some monoclinic organic crystals. However, they found it necessary to employ a least squares error function to refine the elastic constants in order to reduce their value of R to less than 10^{-2} . This procedure resulted in their final value for C_{22} being lower than the directly measured value. No physical justification was offered by them for modifying a directly measured quantity as a result of numerical calculation.

Table 2. Elastic constants of CsH_2PO_4

The C_{ij} were calculated using a density of 3.22 g cm^{-3} at 20°C

ij	C_{ij} (GPa)	S_{ij} (GPa) $^{-1}$	ij	C_{ij} (GPa)	S_{ij} (GPa) $^{-1}$
11	28.83 ± 0.43	1.82	12	11.4 ± 3.6	-0.219
22	26.67 ± 0.37	0.103	13	42.87 ± 1.58	-1.17
33	65.45 ± 0.48	0.772	15	5.13 ± 0.67	0.249
44	8.10 ± 0.15	0.133	23	14.5 ± 4.4	0.138
55	5.20 ± 0.24	0.450	25	8.4 ± 4.3	-0.150
66	9.17 ± 0.22	0.117	35	7.50 ± 0.81	-0.181
			46	-2.25 ± 0.31	0.033

The complete elastic constant matrix C_{ij} is given in Table 2. The inverse of the elastic constant matrix was calculated to give the elastic compliance matrix S_{ij} which is also listed in Table 2. Quantities discussed in the following section, such as bulk modulus and linear compressibility are calculated in terms of these S_{ij} .

5. Discussion

Velocity Surfaces

Using the values of the C_{ij} matrix in Table 2, the wave velocity for any propagation direction can be calculated via equations (4) and (5). Figs 3a, 3b and 3c are polar plots of velocity versus propagation direction for propagation vectors in the xy , xz and yz planes respectively.

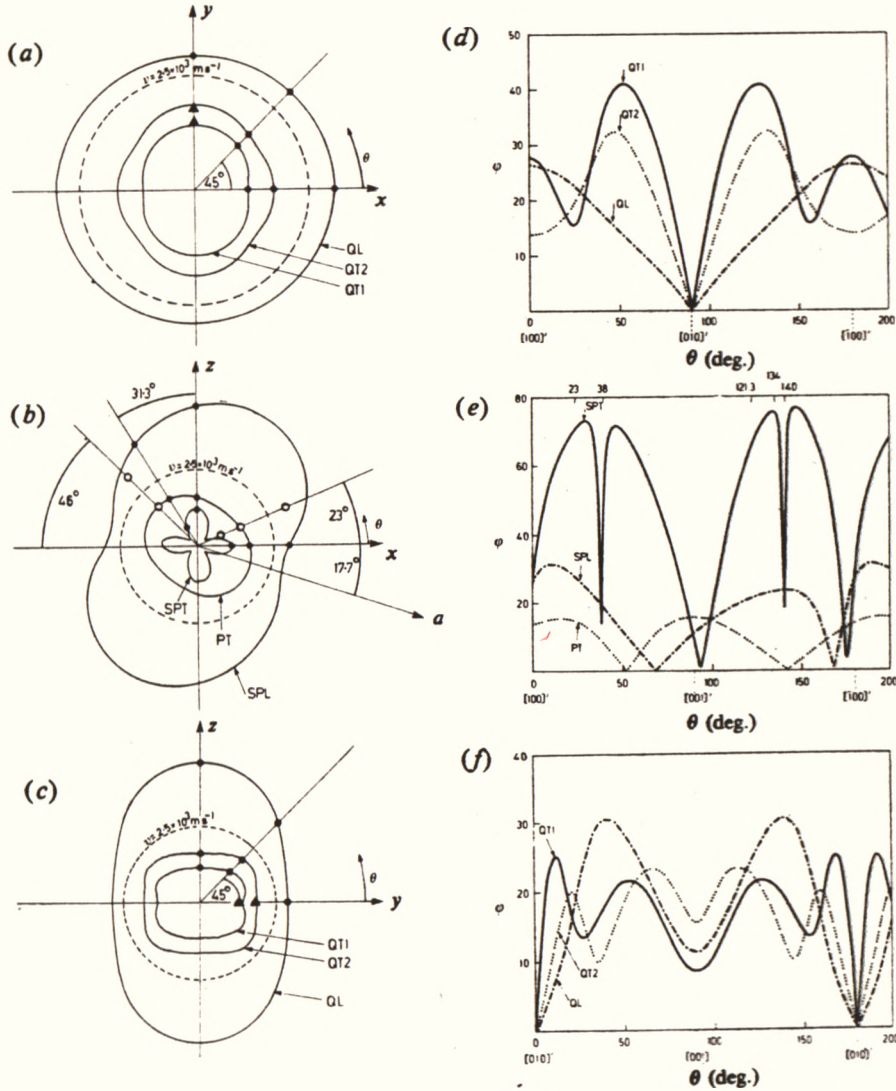


Fig. 3. Polar plots of the calculated phase velocity for the (a) xy , (b) xz and (c) yz planes, together with the absolute value ϕ of the deviation angle between the ray and propagation vectors (d)–(f), where θ is measured in the sense given in the corresponding polar plot. The solid circles show the measured velocities actually used in the calculations. The triangles represent the measured velocities for the two pure transverse (PT) waves travelling parallel to the b axis and are used as a cross-check. The open circles show other measured velocities in the xz plane.

It is immediately obvious that, for propagation directions in the xy and yz planes, the wave velocity is quite isotropic. This stands in very marked contrast to the plot for the xz plane (Fig. 3b), which displays very marked anisotropy, particularly for the semi-pure transverse (SPT) mode with the smallest velocity. The calculations predict a minimum in the velocity of this mode of $0.290 \times 10^3 \text{ m s}^{-1}$ for propagation directions making angles of 38° and 140° to the x axis. This is a remarkably low value. For comparison, Sil'vestrova *et al.* (1975) have reported a value of $0.347 \times 10^3 \text{ m s}^{-1}$ for the velocity of a transverse wave propagating in the yz plane in Calomel, which they claimed to be the 'lowest value' measured for crystals at that time. It should be pointed out, however, that Sil'vestrova *et al.* actually determined this value experimentally whilst our value is calculated from the determined elastic constants.

In an effort to check the unusual predictions arrived at from the calculations we attempted to measure the velocity of each of the three modes for other propagation directions in the xz plane. For all propagation directions in this plane, one mode is pure transverse (PT) having a polarization vector parallel to $[010]'$. The other two modes are semi-pure having polarization vectors of the form $[n0-l]'$ and $[l0n]'$. For propagation at 134° to the x axis the measured PT velocity agrees very well with the predicted value. The SPT mode, with a predicted velocity of $0.363 \times 10^3 \text{ m s}^{-1}$, could not be generated at all. It was found that, on rotating the crystal with respect to the transverse exciting transducer, the pure mode decreased in amplitude as expected, but that no other mode could be detected. Similar difficulties were encountered for the measurements of V_{12} (see Table 1), although in that case a weak mode could be detected. It was also noted that this SPT mode could be generated by a longitudinal transducer.

The failure to observe the very low velocity mode is not unexpected as such a mode would be expected to be heavily damped compared with the faster modes. However, as can be seen from Fig. 3b, the measured velocity of the semi-pure longitudinal (SPL) mode, which is strongly propagated, is significantly smaller than the predicted value in this direction. Similar results were obtained for propagation at 23° to the x axis, in that the measured pure mode velocity is very close to the predicted value and that the SPL wave velocity was significantly less than the predicted value. In this case, the SPT wave could be detected, but it was very weakly propagated and only a rough estimate of its velocity could be obtained ($V = 0.83 \times 10^3 \text{ m s}^{-1}$).

The discrepancy between the measured and calculated values of this SPL mode suggests that the severe damping of the SPT mode influences the longitudinal mode as well. The formulation of the equation of motion assumes an infinite lossless medium and therefore does not include any damping term. Normally, the introduction of such a term should have little or no influence on the velocities. However, if the damping is sufficiently severe so as to almost stop one mode from propagating at all, the nature of the eigenvalue equation can be expected to change, since the dimensionality of the problem would effectively be reduced from 3 to 2. We are currently investigating the effect that a severe damping term for one mode will have on the other measured velocities.

Ray Directions

For each direction of propagation there are three associated wave modes, each with a different velocity, polarization and ray energy propagation direction. Figs 3d,

3e and 3f show plots of the magnitude of the absolute angle between the ray direction and the propagation direction, calculated via equation (9), for the *xy*, *xz* and *yz* planes respectively.

Deviation angles of up to 70° are not unusual (see e.g. Neighbours 1973). The plots for the *xy* and *yz* planes show that there are no accidental pure modes of propagation, since the deviation angle only goes to zero for propagation along the *b* axis, which is demanded by symmetry. Once again the plot for the *xz* plane is very peculiar. The deviation angle for the SPT mode increases rapidly for propagation off the *x* axis, reaching a value of 73° at 30° from the *x* axis. With further displacement, the deviation angle decreases abruptly to a value of 14° at 38° from the *x* axis and then abruptly increases. Similar behaviour occurs for propagation directions about 140° to the *x* axis.* Note that the minima in the calculated velocities of this mode occur for the same propagation directions. The sharpness of the dip is striking. In the region of the anomalies the deviation angle changes by about 38° for a 1° change in propagation direction. Calomel (Sil'vestrova *et al.* 1975) displays similar behaviour for the transverse mode, the velocity of which has a minimum value of $0.347 \times 10^3 \text{ m s}^{-1}$ for propagation at 45° to the *x* axis in the *xy* plane.

The deviation angles for the measured velocities (V_{22} – V_{27}) in the *xz* plane can be read from Fig. 3e. It can be seen that the mode propagating at 134° to the *x* axis has a deviation angle of 76°. It is therefore not unexpected that this ray was unobserved since it must reflect off the sides of the crystal many times during its round trip. The mode at 23° has a smaller deviation angle, namely 69°, and was weakly observed. The mode at 121.3° (V_{12}) has a deviation angle of 64° and was clearly observed.†

In order to test these conclusions, measurements of the velocity for propagation at the angles in the *xz* plane at which the minima in velocity and deviation angle occur (namely 38° and 140°) would be desirable. However, such measurements would require the crystal to be aligned very precisely as even small errors in alignment will lead to large changes in the deviation angle. The crystal would also have to be of excellent quality as a mosaic spread of even 1° will lead to a gross divergence of the beam. Finally, even if the beam were propagated without a large divergence, the very low value of velocity for this mode will probably be accompanied by a high value of attenuation, making the mode difficult or impossible to observe experimentally.

Bulk Modulus, Linear Compressibility and Young's Modulus

The bulk modulus of CsH_2PO_4 was calculated via the relationship (Nye 1967) $B = \{S_{11} + S_{22} + S_{33} + 2(S_{12} + S_{23} + S_{13})\}^{-1}$. A value of 5.28 GPa was obtained using the S_{ij} matrix calculated by taking the inverse of the C_{ij} matrix in Table 2. An attempt was made to calculate the error in the bulk modulus by adding all possible permutations of the errors to the values of C_{ij} before inverting the matrix. However, for most permutations of the errors, especially those involving extreme cases where

* The eigenvectors in the *xz* plane are well behaved and do not deviate from pure mode behaviour by more than 17°.

† It should be recalled that the number of reflections off the side walls of the crystal will depend on the tangent of the deviation angle. Thus a deviation angle of 76° ($\tan 76^\circ = 4.01$) will result in about twice as many side wall reflections as a deviation of 64° ($\tan 64^\circ = 2.05$).

all the errors were either added or subtracted, the C_{ij} matrix ceased to be positive definite. Positive definiteness is the mathematical consequence of demanding a positive strain energy for lattice stability. Thus a C_{ij} matrix which is not positive definite cannot describe the elastic properties of any real material. Hence we may reject those error permutations for which the C_{ij} matrix is not positive definite as unphysical.

When the calculation was performed using only those error combinations for which the C_{ij} matrix was positive definite, the bulk modulus was found to lie in the range 0.9–16.5 GPa. This large uncertainty is due to ignoring the fact that constants are coupled in such complicated ways that the quoted errors cannot occur independently. A more sophisticated error calculation system is required—possibly a Monte Carlo method of assigning the value of C_{ij} to be used as a normally distributed variable with mean and standard deviation equal to the values and errors respectively given in Table 2.

Table 3. Bulk moduli for selected crystals

Crystal	Class	B (GPa)	Reference
CsH_2PO_4	Monoclinic	5.28	This paper
KH_2PO_4	Tetragonal	27.3	Fritz (1976)
Potassium tartrate	Monoclinic	16.8	Aleksandrov (1958)
$\text{NH}_4\text{H}_2\text{PO}_4$	Tetragonal	20.1	Fritz (1976)
CsSCN	Orthorhombic	13.2	Irving <i>et al.</i> (1983)
Calomel	Tetragonal	18.0	Sil'vestrova <i>et al.</i> (1975)

The value of B is remarkably small. For comparison, B for some other materials is shown in Table 3. These values have been calculated via the elastic constants given in the references listed. Note that Calomel, whilst displaying some similar anisotropic features to CDP in the behaviour of the velocity and ray directions, nevertheless has a value of bulk modulus comparable with the other crystals listed.

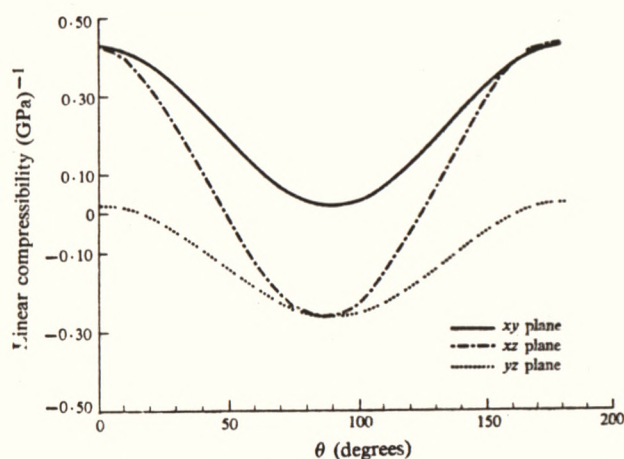


Fig. 4. Linear compressibility for directions in the xy , xz and yz planes, with θ measured as in Fig. 3.

Since CDP displays a chain-like structure it is of interest to calculate the linear compressibility K_{lmn} , which is the strain response of the crystal along a given direction $[l, m, n]'$ to the application of hydrostatic pressure. For a monoclinic system the expression is (Nye 1967)

$$K_{lmn} = (S_{11} + S_{12} + S_{13})l^2 + (S_{12} + S_{22} + S_{23})m^2 \\ + (S_{13} + S_{23} + S_{33})n^2 + (S_{15} + S_{25} + S_{35})ln.$$

A plot of linear compressibility versus direction in the xy , xz and yz planes is given in Fig. 4. Note how the compressibility along the x axis is twenty times larger than that along the y axis, and that the compressibility along the z axis is negative. Thus when hydrostatic pressure is applied to CsH_2PO_4 the crystal responds by contracting along the x axis and expanding along the z axis. By comparison the length change along the y axis is small. This further demonstrates the marked elastic anisotropy of CDP.

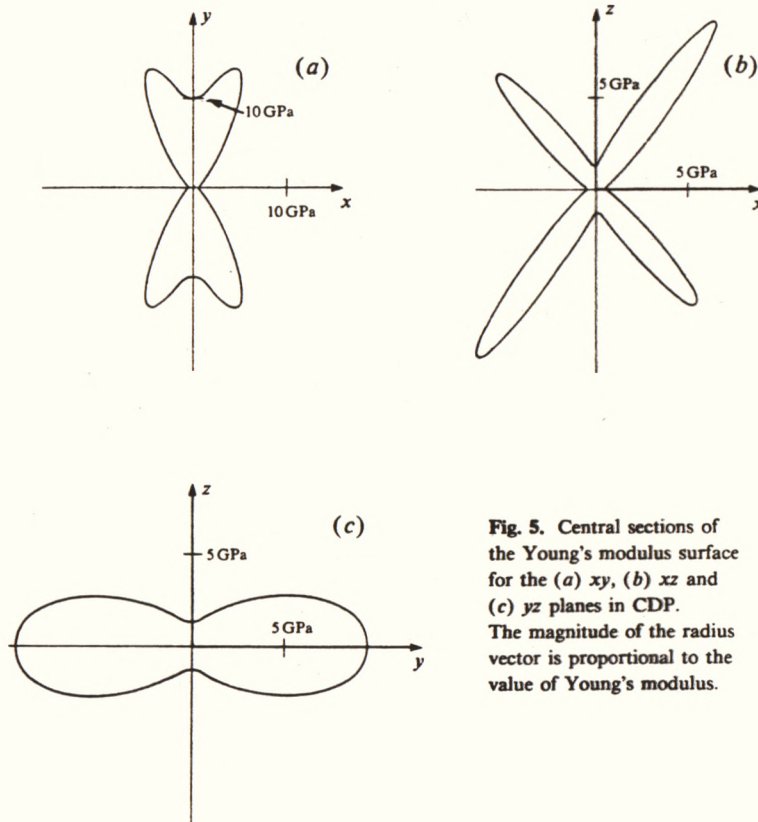


Fig. 5. Central sections of the Young's modulus surface for the (a) xy , (b) xz and (c) yz planes in CDP. The magnitude of the radius vector is proportional to the value of Young's modulus.

Finally, the central sections of the Young's modulus surface on the xy , xz and yz planes were calculated and are shown in Figs 5a, 5b and 5c respectively. In Fig. 5

the radius vector is proportional to the value of Young's modulus Y for that direction. The curves were calculated from the expression (Nye 1967)

$$\begin{aligned} Y^{-1} = & l^4 S_{11} + 2l^2 m^2 S_{12} + 2l^2 n^2 S_{13} + 2l^3 n S_{15} \\ & + m^4 S_{22} + 2m^2 n^2 S_{23} + 2lm^2 n S_{25} \\ & + n^4 S_{33} + 2ln^3 S_{35} + m^2 n^2 S_{44} + 2lm^2 n S_{46} \\ & + l^2 n^2 S_{55} + l^2 m^2 S_{66}. \end{aligned}$$

Young's modulus gives a measure of the 'stiffness' of the crystal to a uniaxial stress applied along the direction of interest. Once again the elastic behaviour is clearly very anisotropic.

Using the elastic constants in Table 2, J. G. Collins (personal communication) has calculated the elastic Debye temperature to be 134.5 K for Avogadro's number of ions. This value is consistent with an estimate from thermal conductivity data of 140 ± 10 K (Spörl *et al.* 1984).

Relationship to Crystal Structure

Much of the elastic anisotropy in CDP originates from the extremely low velocity predicted for the SPT mode for propagation in the xz plane at 38° and 140° to the x axis. This anomaly results in the sharp dip for the deviation angle between ray and wave normals for these propagation directions. It also results in the very low value for the bulk modulus, and the large anisotropies in Young's modulus and the linear compressibility. We suggest the following qualitative explanation, in terms of the known crystal structure of CDP, as to why this mode should behave anomalously.

As previously noted, CDP consists of (100) layers of hydrogen bonded PO_4 groups, the layers being held together by electrostatic attraction to the Cs^+ ions. A projection of the structure onto the (010) plane is given in Fig. 6a based on the atomic positions given by Uesu and Kobayashi (1976) and Matsunaga *et al.* (1980). The H2 hydrogen links 03-03 and 04-04 groups to form the PO_4 chains along the b axis. The H1 hydrogen cross links the chains to form the (100) layers.

Uesu and Kobayashi (1976) pointed out that nearly linear chains of Cs and P ions are formed along the $[10\bar{1}]$ direction with an interatomic distance of 4.03 \AA ($\equiv 4.03 \times 10^{-10} \text{ m}$). However, it is evident from Fig. 6a that this is an error and that the chains with close to this interatomic distance lie along the $[101]$ direction. It is also seen in Fig. 6a that there are nearly linear chains of P-01, Cs^+ , P-01 groups along the $[10\bar{1}]$ direction where the Cs_1 -P₁ separation is 5.46 \AA (with an oxygen intervening) and the Cs_1 -P₂ separation is 5.01 \AA (with no intervening atoms). Uesu and Kobayashi (1976) also pointed out that these distances are considerably longer than the K-P distance of 3.49 \AA in KDP.

If we consider a wave propagating in the xz plane at 38° to the x axis, the eigenvectors for this direction can be calculated by solving the eigenvalue equation (4). The eigenvectors lie in the xz plane and make angles of 39.9° (SPT) and 50.1° (SPL) to the x axis as shown in Fig. 6b. The third mode is PT and has polarization parallel to $[010]$. The SPT polarization is approximately parallel to the $[10\bar{1}]$ direction and makes an angle of only 1.4° with the direction joining Cs_1 and P₂.

Since there are no intervening atoms between Cs_1 and P₂ and since the eigenvectors are constrained to lie in the xz plane, the force constants associated with this mode

disordered in the room temperature phase. As a consequence of both these factors we may expect the velocity to be correspondingly small for this mode.

Irrespective of the above explanation, the correspondence of the transverse polarization for the mode propagating at 38° to the x axis to the linear Cs-P arrays and the O3-H2-O3 hydrogen bond direction seems unlikely to be coincidental. It is unfortunate that this mode is not more easily observed experimentally, for the response of the velocity of this mode to temperature through the ferroelectric ordering would be very interesting.

It has also been observed by Uesu and Kobayashi (1976) that nearly linear arrays of Cs and P atoms also occur along the $[0, \pm 1, 1]$ directions with a comparatively large Cs-P separation. However, we observed that in the yz plane the velocity of all modes is very isotropic, showing none of the peculiar effects of the xz plane. We may account for this difference by recalling that for propagation in the xz plane the eigenvectors are constrained by symmetry to lie in that plane, whereas for propagation in the yz plane no such restriction applies and in fact the eigenvectors lie considerably out of the plane. Thus the force constants for this mode will not necessarily be determined by the comparatively large Cs-P interatomic distance within the yz plane.

The anisotropy of the linear compressibility and of Young's modulus is related to the layer and chain structure of CDP. The maximum in the value of the linear compressibility and the corresponding minimum in the value of Young's modulus for the x -axis direction correspond to the weak bonding between the (100) layers. Under hydrostatic pressure these layers are forced closer together. The corresponding expansion along the c axis may be explained by a small rotation of the PO_4 tetrahedron (possibly caused by repulsion between the O1 and O2 atoms of adjacent layers), which results in an elongation of the hydrogen bonded c -axis chain. Selenium and tellurium are examples of other chain-like materials which have negative linear compressibility parallel to the chain axis (Munn 1972). Under uniaxial stress, however, the bonding in the c -axis chain is only about as strong as the interlayer bonding (see Fig. 5b).

It is surprising that the b -axis bonding is so much stronger than for the c axis (see Fig. 5c), especially in view of the disordered state of the hydrogen bonds linking this chain. This may be explained by noting that these hydrogen bonds lie nearly parallel to the a axis, so that compression of the b -axis chain would involve a bending of the bond, rather than a compression of the double well potential along its axis. The strength of the b -axis bonding is consistent with the findings of Frazer *et al.* (1979) that the correlation length along the b axis is much longer than those along the a and c axes.

The very strong anisotropy for Young's modulus in the xz plane (Fig. 5b) is correlated to the anomalous SPT mode discussed above. The maxima in Young's modulus (at 54° and 131° to the x axis) occur for directions which are almost parallel to the SPL polarization for wave propagation directions for which the SPT mode has its minimum velocity. Thus the crystal is stiffest at right angles to the $[10\bar{1}]$ Cs-P chains (see Fig. 6).

Finally, as mentioned in the Introduction, most of the studies on CDP to date have focussed on the comparison between the transition mechanism in pseudo-one-dimensional CDP, and the more familiar three-dimensional KH_2PO_4 . The plots

of Young's modulus for KH_2PO_4 (calculated from the elastic constants quoted by Fritz 1976) for the xy and yz ($\equiv xz$) planes (see Fig. 7) indicate clearly that the very anisotropic elastic behaviour in CDP is absent in the case of KH_2PO_4 . In particular, it is obvious that the elastic behaviour for the ferroelectric z axis in KH_2PO_4 is not very different from that for the other axes, in contrast to CDP for which the ferroelectric b axis is much stiffer than the a or c axes.

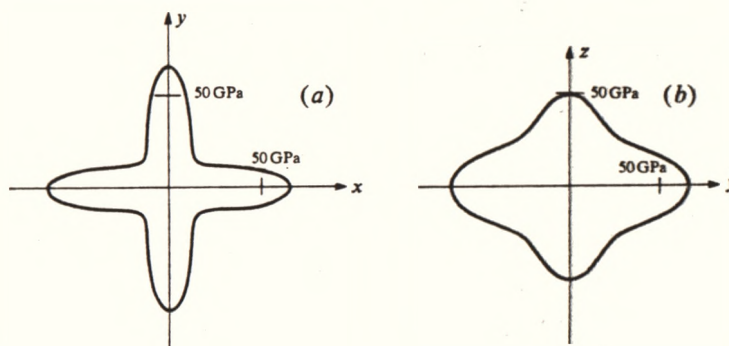


Fig. 7. Central sections of the Young's modulus surface for the (a) xy and (b) yz planes in KH_2PO_4 . The magnitude of the radius vector is proportional to the value of Young's modulus.

6. Conclusions

The elastic constant matrix of CsH_2PO_4 has been determined via ultrasonic velocity measurements. Significant anisotropy in the elastic constants was found. In particular, calculations using the matrix determined predict a very low velocity of sound ($0.290 \times 10^3 \text{ m s}^{-1}$) for the semi-pure transverse mode propagating in the xz plane at 38° to the x axis. This could not be confirmed experimentally due to the failure to propagate the mode. As the polarization direction for this mode is almost parallel to the linear Cs-P chains with a large (5.01 \AA) nearest neighbour separation and to the direction of the disordered hydrogen bond, its low velocity is attributed to the relatively weak forces acting in this direction.

The significant anisotropy found in Young's modulus and the linear compressibility reflect the weak forces between the (100) layers and show clearly that even in the paraelectric state the bonding along the b -axis chain is different to that along the c axis. Hence, the one-dimensional chain-like structure of CDP reveals itself, not only in the critical phenomena, but also in the static elastic behaviour at room temperature. These observations of the elastic anisotropy must be added to the differences in the nature of the ferroelectric transition mechanism in setting CDP apart from other members of the KH_2PO_4 family.

Acknowledgments

The authors have benefited from discussions with Drs J. G. Collins and F. Ninio. Comments by the former, particularly on the theory section, and the calculation of the elastic Debye temperature are specifically acknowledged. This work was undertaken with the support of the Australian Research Grants Scheme and the Monash

University Special Research Grants Scheme. One of us (S.P.) gratefully acknowledges the award of the Vera Moore Junior Research Fellowship.

References

- Aleksandrov, K. S. (1958). *Sov. Phys. Crystallogr.* **3**, 630.
- Brown, F. C. (1967). 'The Physics of Solids' (Benjamin: New York).
- Carnahan, B., Luther, H. A., and Wilkes, J. O. (1969). 'Applied Numerical Methods' (Wiley: New York).
- Cornelius, C. A. (1981). *Acta Crystallogr. A* **37**, 430.
- Fellner-Feldegg, H. (1952). *Tschermaks Mineral. Petrogr. Mitt.* **3**, 37.
- Frazer, B. C., Semmingsen, D., Ellenson, W. D., and Shirane, G. (1979). *Phys. Rev. B* **20**, 2745.
- Fritz, I. J. (1976). *Phys. Rev. B* **13**, 705.
- Irving, M. A., Prawer, S., Smith, T. F., and Finlayson, T. R. (1983). *Aust. J. Phys.* **36**, 85.
- Iwata, Y., Koyano, N., and Shibuya, I. (1980). *J. Phys. Soc. Jpn* **49**, 304.
- Kanda, E., Tamaki, A., Yamakami, T., and Fujimura, T. (1983). *J. Phys. Soc. Jpn* **52**, 3085.
- Kanda, E., Yoshizawa, M., Yamakami, T., and Fujimura, T. (1982). *J. Phys. C* **15**, 6823.
- Krupnyi, A. I., Al'chikov, V. V., and Aleksandrov, K. S. (1972). *Sov. Phys. Crystallogr.* **16**, 692.
- McSkimin, H. J. (1961). *J. Acoust. Soc. Am.* **33**, 12.
- Matsunaga, H., Itoh, K., and Nakamura, E. (1980). *J. Phys. Soc. Jpn* **48**, 2011.
- Munn, R. W. (1972). *J. Phys. C* **5**, 535.
- Musgrave, M. J. P. (1970). 'Crystal Acoustics' (Holden-Day: San Francisco).
- Neighbours, J. R. (1973). *J. Appl. Phys.* **44**, 4816.
- Nye, J. F. (1967). 'Physical Properties of Crystals' (Clarendon: Oxford).
- Papadakis, E. P. (1967). *J. Acoust. Soc. Am.* **42**, 1045.
- Rashkovich, L. H., Meteva, K. B., Shevchik, Ya. E., Hoffman, V. G., and Mishchenko, A. V. (1977). *Sov. Phys. Crystallogr.* **22**, 613.
- Sil'vestrova, I. M., Barta, Ch., Dobrzhanskii, G. F., Belyaer, L. M., and Pisarevskii, Yu. V. (1975). *Sov. Phys. Crystallogr.* **20**, 221.
- Spörl, G., Chat, D. D., and Hegenbarth, E. (1984). *Phys. Status Solidi (a)* **82**, K27.
- 'Standards on Piezoelectric Crystals' (1949). *Proc. Inst. Radio Eng.* **37**, 1378.
- Uesu, Y., and Kobayashi, J. (1976). *Phys. Status Solidi (a)* **34**, 475.
- Yakushkin, E. D., Baranov, A. I., and Shuvalov, L. A. (1981). *JETP Lett.* **33**, 24.
- Youngblood, R., Frazer, B. C., Eckert, J., and Shirane, G. (1980). *Phys. Rev. B* **22**, 228.

Monash University Library



33168112048414

CALL No.

H

*THESIS

P918

VOL./PT.

THE HARGRAVE LIBRARY
MONASH UNIVERSITY